2011

A Study of Cross-Flow Air Heating via a Multiport Serpentine Microchannel Heat Exchanger

Faisal Siddiqui
University of Windsor

A Study of Cross-Flow Air Heating via a Multiport Serpentine Microchannel Heat Exchanger

by

Faisal A. Siddiqui

A Thesis
Submitted to the Faculty of Graduate Studies
through Mechanical, Automotive, and Materials Engineering
in Partial Fulfillment of the Requirements for
the Degree of Master of Applied Science at the
University of Windsor

Windsor, Ontario, Canada
2011

A Study of Cross-Flow Air Heating via a Multiport Serpentine Microchannel Heat

Exchanger

by

Faisal A. Siddiqui

APPROVED BY:

_____
Dr. Randy Bowers, Outside Department Reader
Department of Engineering Materials

_____
Dr. Nader Zamani-Kashani, Internal Department Reader
Department of Mechanical Engineering

_____
Dr. Amir Fartaj, Advisor
Department of Mechanical Engineering

_____
Dr. Henry Hu, Chair of Defense
Department of Engineering Materials

January 28, 2011

Declaration of Originality

I hereby certify that I am the sole author of this thesis and that no part of this thesis has been published or submitted for publication.

I certify that, to the best of my knowledge, my thesis does not infringe upon anyone's copyright nor violate any proprietary rights and that any ideas, techniques, quotations, or any other material from the work of other people included in my thesis, published or otherwise, are fully acknowledged in accordance with the standard referencing practices. Furthermore, to the extent that I have included copyrighted material that surpasses the bounds of fair dealing within the meaning of the Canada Copyright Act, I certify that I have obtained a written permission from the copyright owner(s) to include such material(s) in my thesis and have included copies of such copyright clearances to my appendix.

I declare that this is a true copy of my thesis, including any final revisions, as approved by my thesis committee and the Graduate Studies office, and that this thesis has not been submitted for a higher degree to any other University or Institution.

Abstract

An experimental investigation is performed to determine air side forced convective heat transfer and flow characteristics of wavy fin, serpentine, multi-port slab, crossflow microchannel heat exchanger.

Experiments are conducted for 30 different operating conditions in single-phase air-to-ethylene glycol crossflow configuration. These operating conditions ($752 < Re_a < 3165$, and $23°C < T_{a,i} < 46.5°C$) yield air side Nusselt number (Nu_a), and Colburn factor (j_a) of up to 8.4 and 0.009 respectively. The Nu_a and j_a obtained in these experiments are generally higher, and friction factor, f_a is generally lower than those found in the literature. Possible explanations for the apparent discrepancies are explored.

A thorough uncertainty analysis is performed. Uncertainties in Nu_a, j_a, and friction factor f_a are approximately 4.8%, 5.2%, and 5.8% respectively. A large number of key heat exchanger performance parameters are also investigated in order to develop general correlations suitable for industrial applications and engineers.

Dedicated to –

my parents,

who are my source of eternal inspiration

Acknowledgement

First and foremost, I would like to express my sincere gratitude and thanks to my supervisor Dr. Amir Fartaj for believing in me and providing with the opportunity to work on this project. His exemplary patience, support, understanding, and tireless supervision were pivotal to the completion of this project. His resourcefulness and ability to address my questions and confusions in order to get me on track were called upon regularly. Working with him has taught me a great deal about professionalism and honorable conduct in addition to the engineering knowledge and concepts.

I would also like to thank my committee members Dr. Randy Bowers, and Dr. Nader Zamani for their advice and suggestions. Dr. Bowers' questions, suggestions, and editing of my thesis have unquestionably led to a more polished and well presented final product.

I would like to extend my gratitude to Mr. Mesbah Khan for commissioning the present lab setup. Special thanks to Mr. Sarbadaman Dasgupta for his assistance with my experiments and research efforts. His positive attitude and effervescence was particularly useful in overcoming stagnant situations and making new breakthroughs. Thanks are also extended to the following colleagues for assistance with experiments: Serena Al-Obaidi, Mohammed Saadi, Abdul Quaiyum, Mohammed Ismail, and Shahram Fotowat.

I am also thankful to the Department of Mechanical Engineering for GA opportunity, technical support provided through Mr. Andrew Jenner and Mr. Patrick Seguin and the secretarial services of Ms. Rose Gignac and Ms. Barbara Tattersall.

Last but not least, I would like to express my gratitude to my family, my dad Firoze Siddqui, mom Dilara Yasmin, and brother Tousif Siddiqui who have been a constant source of inspiration and support – emotional, moral and of course financial; particularly, my parents who have, to this date, continued to sacrifice their past and present for my future and consistently encouraged me to undertake difficult but necessary steps forward in my life.

Table of Content

List of Original Publications and Presentations

Some of the results and observations from each experimental phase of current study are disseminated and documented in the form of journal publication, conference presentations and transaction publications as follows:

Siddiqui, F. A., Dasgupta, E. S., and Fartaj, A. Experimental Investigation of Air-Side Heat Transfer and Fluid Flow Performances of Multi-Port Serpentine Crossflow Mesochannel Heat Exchanger (Paper #HFF-D-11-00055), <u>International Journal of Heat and Fluid Flow, 2011,</u> (in review).

Dasgupta, E. S., **Siddiqui, F. A.,** Quaiyum, A., Al-Obaidi, S., and Fartaj, A. 2011. Experimental Study on Air Cooling via a Multiport Mesochannel Cross-Flow Heat Exchanger, (Paper #ICNMM2011-58257). <u>9th International Conference on Nanochannels, Microchannels, and Minichannels (ICNMM),</u> June 19 - 22, Edmonton, AB, Canada. (in review)

Dasgupta, E. S., **Siddiqui, F. A.**, and Fartaj, A. Experimental study on air-side heat transfer & fluid flow characteristics of Microchannel heat exchanger in cross-flow orientation. <u>2011 SAE World Congress & Exposition, 2011</u> (Paper #11HX-0041). (accepted for publication)

Khan, M. G., **Siddiqui, F. A.**, Mosa, M. and Fartaj, A. Experimental comparative study on heat transfer performances of circular, elliptical, and microchannel heat exchangers, (Paper #162), <u>Proceedings of The Canadian Society for Mechanical Engineering Forum 2010, CSME FORUM 2010</u>, June 7-9, Victoria, BC, Canada. (published)

List of Figures

List of Tables

Nomenclature

$2A$	Two times the wavy fin amplitude. (m)
A	Area. (m^2)
A_a	Total heat transfer area in the air side. (m^2)
$A_{c,i}$	Inner cross sectional area of the microchannels. (m^2)
$A_{c,MC}$	Cross sectional area of a single microchannel. (m^2)
A_{duct}	Cross sectional area of the test chamber duct. (m^2)
$A_{Frontal,Blocked}$	Combined frontal area of all fins and slabs in the heat exchanger, which blocks air flow. (m^2)
$A_{Frontal,Fin}$	Frontal area of a single fin. (m^2)
$A_{Frontal,Fin,HX}$	Combined frontal area of all fins in the heat exchanger. (m^2)
$A_{Frontal,HX}$	Frontal area of the heat exchanger. (m^2)
$A_{Frontal,Slab}$	Frontal area of an individual slab. (m^2)
$A_{Frontal,Slab,HX}$	Combined frontal area of all heat transferring slabs in the heat exchanger. (m^2)
$A_{HT,a,HX}$	Combined available heat transfer surface area of all fins and slabs in the heat exchanger. (m^2)
$A_{HT,Fin}$	Heat transfer surface area of a single fin. (m^2)
$A_{HT,Fin,HX}$	Combined heat transfer surface area of all fins in the heat exchanger. (m^2)
$A_{HT,in,MC}$	Inner heat transfer surface area of an individual microchannel. Also known as the liquid side heat transfer surface area for one microchannel. (m^2)

$A_{HT,in,MC,HX}$	Combined inner heat transfer surface area of all microchannels within all heat transferring slabs. $\left(m^2\right)$
$A_{HT,in,MC,Slab}$	Inner heat transfer surface area of all microchannels within a slab. $\left(m^2\right)$
$A_{Min,a}$	Minimum free flow area available for air flow. $\left(m^2\right)$
$A_{NF,Slab}$	Total area of an individual slab that is not occupied by fins. It is the summation of individual areas on the slab, which are situated between two adjacent fins. $\left(m^2\right)$
$A_{NF,Slab,HX}$	Combined area of the slabs for the entire heat exchanger, which is not occupied by the fins. $\left(m^2\right)$
$A_{XS,HT,MC,HX}$	Combined cross-sectional area of all microchannels within all heat transferring slabs. $\left(m^2\right)$
$A_{XS,MC}$	Cross-sectional area of an individual microchannel. $\left(m^2\right)$
$A_{XS,MC,Slab}$	Combined cross-sectional area of all microchannels within a slab. $\left(m^2\right)$
C'	Correction factor for estimating air velocity from dynamic pressure. Depends on the Pitot static tube construction.
C_{min}	Heat capacity of the fluid with lower heat capacity. $\left(J/s.^\circ C\right)$
c_p	Specific heat. $\left(J/kg.^\circ C\right)$
$c_{p,a}$	Air specific heat. $\left(J/kg.^\circ C\right)$
C	Heat capacity. $\left(J/s.^\circ C\right)$
C^*	Heat capacity ratio.
C_{Press}	Air side dimensionless pressure coefficient.
D	Diameter. $\left(m\right)$
$D_{Hyd,a,HX}$	Theoretical hydraulic diameter on the air side for the heat exchanger. Calculated from Kays and London (1984). $\left(m\right)$
$D_{i,MC}$	Inner diameter of the microchannel. $\left(m\right)$

D_{MC}	Diameter of an individual microchannel. (m)
$D_{o,MC}$	Outer diameter of the microchannel (taken as equal to the slab height). (m)
f	Friction factor.
f_a	Air side friction factor.
F	LMTD Correction factor for multi-pass cross-flow heat exchanger.
F_p	Fin Pitch. (m)
G	Mass flux. $(kg/m^2.s)$
G_a	Air mass flux (also known as air mass velocity). $(kg/m^2.s)$
h	Convective heat transfer coefficient. $(W/m^2.{}^\circ C)$
h_a	Air side heat transfer coefficient. $(W/m^2.{}^\circ C)$
h_g	Glycol side heat transfer coefficient. $(W/m^2.{}^\circ C)$
H_{Fin}	Height of an individual fin. (m)
$H_{HX,TC}$	Height of the heat exchanger contained within square duct section of the test chamber. (m)
H_{Slab}	Height of an individual slab. It is parallel to air flow direction. (m)
HB_{avg}	Heat balance with respect to average heat transfer rate $\dot{Q}$. $(\%)$
HB_g	Heat balance with respect to glycol side heat transfer rate $\dot{Q}_g$. $(\%)$
j	Colburn factor.
j_a	Air side Colburn factor.
k	Thermal conductivity. $(W/m.{}^\circ C)$
k_{Al}	Thermal conductivity of aluminum. $(W/m.{}^\circ C)$
k_{Fin}	Thermal conductivity of the fin. $(W/m.{}^\circ C)$
k_g	Glycol thermal conductivity. $(W/m.{}^\circ C)$

K_c	Abrupt contraction pressure loss coefficient.
K_e	Abrupt expansion pressure loss coefficient.
l	Flow length. (m)
L	Fin parameter. (m)
L_λ	Wavy Fin Wavelength. (m)
L_{Fin}	Length of an individual fin in the direction of air flow. (m)
$L_{HT,MC,HX}$	Combined length of microchannels participating heat transfer for the entire heat exchanger. (m)
$L_{HT,Slab}$	The length of each slab passes participating in heat transfer. (m)
$L_{HX,TC}$	Length of the heat exchanger contained within square duct section of the test chamber (excludes serpentine portion of heat exchanger within the side covers). (m)
$\dot{m}$	Mass flow rate. (kg/s)
$\dot{m}_a$	Air mass flow rate. (kg/s)
$\dot{m}_g$	Glycol mass flow rate. (kg/s)
$\dot{m}_{g,HX}$	Glycol mass flow rate through all channels of the heat exchanger. (kg/s)
M	Fin parameter. $\left(\sqrt{1/m}\right)$
n	Number of tubes/channels.
$N_{Fin,HX}$	Total number of fins in the heat exchanger.
$N_{Fin,Slab}$	Total number of fins per slab.
$N_{FinArray,HX}$	Total number of fin arrays in the heat exchanger.
$N_{HT,Slab,HX}$	Total number of slabs in the heat exchanger participating in heat transfer.
N_{MC}	Number of microchannels.

$N_{MC,Slab}$	Total number of microchannels per slab.
NTU	Number of Transfer Units.
Nu	Nusselt number.
Nu_a	Air side Nusselt number.
Nu_g	Glycol side Nusselt number.
$p_{g,i}$	Glycol side pressure at the heat exchanger inlet. (kPa)
$p_{g,o}$	Glycol side pressure at the heat exchanger outlet. (kPa)
p_{static}	Static pressure read by the Pitot static tube. (Pa)
p_{total}	Total pressure read by the Pitot static tube. (Pa)
Pe	Péclet number.
Pe_g	Glycol side Péclet number.
Pr	Prandtl number.
Pr_a	Air side Prandtl number.
Pr_g	Glycol side Prandtl number.
$\dot{Q}$	Average heat transfer rate. $\dot{Q} = \dot{Q}_g + \dot{Q}_a .(W)$
$\dot{Q}_{max}$	Maximum possible heat transfer rate. $\dot{Q}_{max} = \dot{m}_g \, c_{p,g} \left(T_{g,i} - T_{g,o} \right).(W)$
$r_{A,HT,a2Liq}$	Ratio of air side to liquid side heat transfer area.
R_a	Air side thermal resistance. $\left({}^{\circ}C / W \right)$
R_g	Glycol side thermal resistance. $\left({}^{\circ}C / W \right)$
R_{total}	Total thermal resistance. $\left({}^{\circ}C / W \right)$
R_{wall}	Thermal conductivity of the aluminum that interfaces between glycol and air. $\left({}^{\circ}C / W \right)$
Re	Reynolds number.
Re_a	Air side Reynolds number.
S_{Fin}	Spacing between two adjacent fins. (m)

S_L	Longitudinal pitch. (m)
S_T	Transverse pitch. (m)
St	Stanton number.
St_a	Air side Stanton number.
t	Time. (s)
t_{Fin}	Thickness of an individual fin. (m)
T	Temperature. $(^{\circ}C)$
T_a	Air temperature (also taken as air bulk temperature unless mentioned otherwise). $(^{\circ}C)$
$T_{a,b}$	Air bulk temperature. $(^{\circ}C)$
$T_{a,i}$	Air inlet temperature. $(^{\circ}C)$
$T_{a,o}$	Air outlet temperature. $(^{\circ}C)$
T_g	Glycol temperature (also taken as glycol bulk temperature). $(^{\circ}C)$
$T_{g,b}$	Glycol bulk temperature. $(^{\circ}C)$
$T_{g,i}$	Glycol inlet temperature. $(^{\circ}C)$
$T_{g,o}$	Glycol outlet temperature. $(^{\circ}C)$
$T_{s,o}$	Outer surface temperature of the glycol. $(^{\circ}C)$
U	Overall heat transfer coefficient. $(W/m^2.^{\circ}C)$
UA	Heat exchanger proportionality constant (product of overall heat transfer coefficient and heat exchanger area). $(W/^{\circ}C)$
V	Velocity. (m/s)
V_a	Air flow velocity. (m/s)
V_g	Glycol flow velocity. (m/s)

V_{MC}	Velocity of the fluid flowing through the microchannel. (m/s)
W_{Slab}	Width of a slab. It is the length of slab in the direction parallel to the air flow. (m)
Z	Characteristic length. (m)
$\forall_{HT,Liq,HX}$	Volume of liquid refrigerant within the heat transferring lengths of all microchannels in the heat exchanger. (m^3)
$\forall_{HX}$	Volume of the heat exchanger actively participating in heat transfer. (m^3)
$\dot{\forall}_g$	Glycol volume flow rate. (m^3/s)

Greek Letters

α	Thermal diffusivity. (m^2/s)
β_a	Air side heat transfer surface area density. (m^2/m^3)
$\beta_{A-Liq2V-HX}$	Liquid side heat transfer surface area density. (m^2/m^3)
$\beta_{A-Liq2V-Liq}$	Liquid side heat transfer surface area per unit liquid side heat transfer volume. (m^2/m^3)
Δp	Pressure drop. (Pa)
Δp_a	Air side pressure drop. (Pa)
$\Delta p_{a,HX}$	Air side pressure drop across heat exchanger. (Pa)
$\Delta p_{Dynamic}$	Air side dynamic pressure. $\Delta p_{Dynamic} = p_{total} - p_{static}$. (Pa)
Δp_g	Glycol side pressure drop across the heat exchanger. (kPa)
Δp_{pitot}	Dynamic pressure read by the Pitot static tube. (Pa)
ΔT	Temperature difference. $(^\circ C)$

ΔT_1	Temperature difference between the two fluid streams at end (1) of the heat exchanger. $\left(^\circ C\right)$
ΔT_2	Temperature difference between the two fluid streams at end (2) of the heat exchanger. $\left(^\circ C\right)$
ΔT_a	Change in air temperature $\Delta T_a = T_{a,o} - T_{a,i}$. $\left(^\circ C\right)$
ΔT_{a-s}	Mean temperature difference between slab outer surface and air inlet. $\left(^\circ C\right)$
ΔT_g	Change in glycol temperature. $\Delta T_g = T_{g,i} - T_{g,o}$. $\left(^\circ C\right)$
ΔT_{g-s}	Mean temperature difference between slab outer surface and glycol inlet. $\left(^\circ C\right)$
ΔT_{LM}	Log mean temperature difference. $\left(^\circ C\right)$
ε	Heat exchanger effectiveness.
η	Efficiency.
η_a	Overall surface efficiency.
η_{Fin}	Fin efficiency.
λ_{Fin}	Wavy Fin Wavelength. $\left(m\right)$
μ	Dynamic viscosity. $\left(kg / m.s\right)$
μ_a	Air dynamic viscosity. $\left(kg / m.s\right)$
μ_g	Glycol dynamic viscosity. $\left(kg / m.s\right)$
ρ	Density. $\left(kg / m^3\right)$
ρ_a	Air density. $\left(kg / m^3\right)$
$\rho_{a,b}$	Air density evaluated at the average temperature. $\left(kg / m^3\right)$
$\rho_{a,i}$	Air density evaluated at the inlet temperature. $\left(kg / m^3\right)$
$\rho_{a,o}$	Air density evaluated at the outlet temperature. $\left(kg / m^3\right)$

ρ_g	Glycol density. $\left(kg / m^3 \right)$
σ	Ratio of minimum free flow area to total frontal area.
σ_a	Ratio of minimum free flow area to total frontal area for the air side.

Symbols for Uncertainty Analysis

$B_{Parameter}$	Total bias error in the parameter based on elemental bias errors $B_1, B_2, B_3...$
$P_{Parameter}$	Total precision error in the parameter based on elemental precision errors $P_1, P_2, P_3...$
$t_{v,95}$	Student t-table distribution value for degree of freedom v and 95% confidence level.
$U_{Parameter}$	Uncertainty associated with a parameter.

Abbreviations

COP	Coefficient of Performance
DAQ	Data Acquisition System
DFM	Digital Flow Meter
DNL	Differential Non Linearity
DPTD	Differential Pressure Transducer
FSO	Full Scale Output
FSR	Full Scale Range
HVAC	Heating Ventilating and Air Conditioning
LPM	Liters per minute
LSB	Least Significant Bit
PTD	Pressure Transducer
RSS	Root Sum Square
RTD	Resistance Temperature Detector

Chapter 1: Introduction

Energy is a thermodynamic quantity that is subject to a conservation law, and is known as the capacity of a physical system to do work. It can exist in many different useful forms, including kinetic, potential, elastic, thermal, gravitational, sound, light, and electromagnetic energy. Some useful work performed by energy include the sun emitting light and heat energy to grow plants, lamps using electrical energy to light houses, and cars using stored energy in gasoline to move. The development, security, and prosperity of any nation and its citizens are powered by energy. The science that deals with understanding energy concepts is known as thermodynamics. The form of energy that is of particular interest in this thesis is thermal energy or heat.

Heat is a form of energy that transfers from one system to another due to a temperature difference. Thermodynamics, however, only deals with the amount of heat transfer resulting from the process of a system moving from one equilibrium state to another; it does not indicate the duration of such processes. Heat transfer is known as the science that addresses the rate of this form of energy transfer. Engineers are concerned with heat transfer due to the applied nature of their work.

In order to properly utilize and benefit from heat energy in many industrial and residential applications, it is necessary to transfer, add, or remove heat from one system into another. A heat exchanger is a device that enables exchange of heat between two fluids that are at different temperatures, while keeping the fluids from mixing. Heat exchangers are found in such diverse applications as air conditioning, chemical processing, power generation, and automotive engine cooling.

Heat exchangers can be classified in many different ways, and into many different types. They can be classified broadly into the three following types:

(i)   regenerative heat exchangers;
(ii)   contact heat exchangers; and
(iii)   surface heat exchangers.

A contact heat exchanger runs on the principle of direct contact, mixing and sharing the heat of the two fluids. Examples of this type of heat exchanger include the de-aerator, spray condenser, and wet cooling tower. A regenerative heat exchanger works on the principle of heat storage in a suitable medium. In most cases, the same fluid is used on either side of this heat exchanger. Fluid is cycled through the regenerative heat exchanger, where it reaches a high temperature. It then goes through an external processing step and is flowed back through the heat exchanger in the opposite direction for further processing. Surface heat exchangers are the most versatile in their applications, and are therefore are most common. The two fluids are separated by a surface through which heat is transferred.

Surface heat exchangers can be further classified based on fluid flow directions as follows:

  (i)   parallel flow;
  (ii)   counter flow; and
  (iii)   cross flow.

In a parallel flow heat exchanger the two fluids flow in same direction while transferring heat. In counter flow heat exchangers, however, the two fluids flow in opposite directions while exchanging heat. In a cross flow heat exchanger, the two fluids flow perpendicular to each other while heat transfer takes place. The heat exchanger used in this study is a cross flow type micro channel heat exchanger.

In the past century, the development of heat exchanger technology for use on an industrial scale has primarily involved expensive, large, and heavy devices with high pressure drops and high power pumps. These heat exchangers rely mainly on high input power to drive the pumps to reach the large flow rates and flow velocities necessary to provide heat transfer at satisfactory rates. Low energy costs and lax environmental regulations allowed industries to operate with high energy consumption heat exchanger models in the past. In recent years however, they have been forced to look for more efficient ways of heat transfer due to energy shortages, high cost, and strict

environmental standards.   These economic, energy and environmental challenges together with need for efficient, low cost, and in some cases mobile devices, has given rise to a search for lightweight compact heat exchangers. Inventing ways to enhance heat transfer is the primary research focus for a majority of researchers in this field. Increasing the heat transfer area per unit volume, and the heat transfer coefficient, as well as lowering the approach temperatures, altering tube shapes and orientation, and enhancing flow configurations are some of the research topics associated with heat transfer enhancements.

Considerable effort has been put into researching conventional and compact heat exchangers in the past. Research on micro channel heat exchangers to enhance heat transfer is comparatively new. Pioneering work was done by Tuckerman and Pease (1981), who first showed that micro fabrication techniques used in microelectronics can also be employed to produce microchannel heat exchangers for engineering and commercial applications on a large scale. Since that work many additional researches have published important finding in this field. There is, however, considerable discrepancy in the published literature, and a general lack of consensus when it comes to the theory of micro channel heat transfer and fluid flow. Mehendale *et al.* (2000) classified the size ranges of flow channels into simple four categories based on geometrical dimensions. Some channel classifications provided by other researchers vary from his findings. Discrepancies in the published literature are also dependent on experimental uncertainty and surface roughness. Judy *et al.* (2002) found that the small dimensions of micro channels cause difficulty in accurately measuring such driving parameters as the hydraulic diameter, roughness, flow velocity, pressure drop, volume flow rates, and flow densities, which in turn lead to large experimental uncertainties. Steinke & Kandlikar (2006) demonstrated that experimental data in the low Reynolds number range exhibit large uncertainty due to errors associated with measurement of mass flow rates. It was found that for the same material and surface finish, roughness height in MCs can be significantly higher than conventional pipes.

In general micro channel heat exchangers are expected to be more effective due to higher surface area per unit volume, improved compactness, higher heat transfer coefficient, lower approach temperatures, and longer air flow dwell time over heat exchanger. The improvement in micro channel manufacturing technology has resulted in lower costs per unit and ability to mass produce. These advantages coupled with current industry need for efficient heat transfer has made research in this field very attractive. It has led to the choice of micro channel array heat exchanger as the subject of current study.

Despite the quantity of literature published in this field, the general lack of consensus and concrete correlations regarding the fluid flow and heat transfer make it difficult for micro channel heat exchangers to be utilized in industry. Thus there is a need to further investigate microchannel heat exchanger fluid flow and heat transfer characteristics to generate useful correlations for specific types of micro channel heat exchangers. Most of the previous research involved rectangular micro channel heat exchangers due to the ease of manufacturing and fabrication. Most previous research also involved water as the working fluid. Research on serpentine type micro channel heat exchangers in the published literature is scarce. In this study circular micro channels in slab and serpentine arrangements will be investigated. An important automotive coolant, 50% ethylene glycol will also be utilized, along with water as the base fluid. Proper Reynolds number ranges, which are used in many heat exchangers, will be selected for study to determine the appropriate Nusselt number and Reynolds number relationships. Heat transfer, friction factor and pressure drop characteristics, and heat exchanger performance will also be investigated.

1.1 Motivation:

Heat-transfer enhancement using small-sized heat-exchangers has gained significant research and application interest in recent years because of the need for energy efficient of heat transfer resulting from high energy costs and stringent environmental regulations. Considerable development of new micro-fabrication and manufacturing techniques has enhanced the research appeal of microchannels to achieve high performance heating and

cooling. Reduced size and lightweight thermal-fluid systems that maintain high heat transfer capability are an increasing requirement for today's industries. Microchannel heat exchangers can meet this need, for example, by replacing conventional automotive heat exchangers for engine and transmission cooling and air-conditioning systems. Micro channel heat exchangers are a good candidate for research over conventional and compact heat exchangers for the following reasons:

- Improved heat transfer and thermal performance. Micro channel heat exchangers have smaller diameters, which provide higher heat transfer coefficient, leading to improved heat transfer and thermal performance.

- Increased coil and overall unit efficiencies.

- Substantial refrigerant charge reduction. Due to small channel diameters, the channel volume is lower; and hence less refrigerant needs to be circulated in the channels.

- Reduced air-side pressure drop for a given load. A micro channel heat exchanger, for a given load, can have greater spacing, and a lower blockage ratio while maintaining a heat transfer area similar to a conventional heat exchanger. Greater spacing will lead to reduced air-side pressure drop.

- Lower tube side friction factors and pressure drop for a given load. Friction factors are related to flow velocity in both the turbulent and the laminar region. Micro channel heat exchangers can provide the same heat transfer in the laminar flow regime, which would have required conventional heat exchangers to operate in turbulent regime. Due to the low velocity in laminar regime, the friction factor and hence, the pressure drop can be lower.

- More compact and reduced coil size. Microchannel heat exchangers can provide the same amount of heat transfer area at a lower volume compared to conventional and compact heat exchangers; hence it is more compact.

- Minimal equipment cost impact. Due to the reduction in volume, a reduction in the material used, and hence the material cost, is possible.

- Increased reliability as a result of better corrosion resistance. Most microchannel heat exchangers can be manufactured from aluminum rather than cast iron or

steel. Operation in the low pressure laminar region will not deform aluminum channels. Aluminum has excellent corrosion resistance.

- Enhanced structural robustness. Structural robustness is enhanced due to the increased corrosion resistance.

Additionally, there are benefits for using micro channel heat exchangers in automotive industry.

- Reduced weight, and improved fuel economy. Vehicles with less weight will require a smaller amount of fuel for similar mileage.
- Smaller components, occupying less room under the hood. Compared to conventional radiators, micro channel radiators will occupy less volume for the same heat transfer area, and lead to compact vehicles.
- More effective cooling. Compared to traditional radiators, the same volume provides greater heat transfer area, leading to greater cooling.
- Increased component life. Flow in microchannels is usually laminar, which means uniform flow distribution and less damage to the inner tube surface from flow fluctuations.

1.2 Objectives:

Although there has been some research conducted on performance and pressure drop of micro channel heat exchangers, the majority of this research has utilized rectangular or square channels followed by circular channels. Few studies have been conducted with straight microchannel configurations, and even fewer with serpentine microchannels configuration. Research on micro channel heat exchangers using ethylene glycol as the working fluid is virtually non-existent. So far, the researchers who have studied microchannel heat exchangers have done so from the point of view of liquid flow inside the channels; they have neglected the air-side heat transfer characteristics associated with this novel technology.

These previous statements show that there is a major lack of knowledge of the fluid flow and heat transfer parameters and characteristics for serpentine microchannel heat exchangers using ethylene glycol and air as working fluids. Further exploration is required in order to accurately understand fluid flow and heat transfer behaviors of such configurations and working fluids. There is no single study on micro channels that encompasses all the major aspects of research: fluid flow, heat transfer, friction factor, pressure drop characteristics, and heat exchanger performance.

The main aim of current study thus is to conduct experiments to investigate the proposed configurations and working fluids to determine the following information.

- Heat transfer characteristics. The air-side heat transfer coefficient in the dimensionless form of the Nusselt number, Nu_a, and Colburn factor, j_a, will be obtained. Correlations of Nusselt number and Colburn factor with Reynolds number, Re_a, will be established.
- Friction Factor Characteristics.
- Pressure Drop Characteristics. Air flow pressure drop features across the heat exchangers will be analyzed and presented in dimensionless form as a function of Reynolds number.

- Heat Exchanger performance. Correlations relating *NTU* (Number of Transfer Units), effectiveness, pressure drop, and Reynolds number will be developed.
- Possible scope of improvements.
- Correlations between the obtained characteristics. Compare Nusselt number to Reynolds number, Colburn factor to Reynolds number, and friction factor to Reynolds number relationships obtained through experiments to the available literature.

In order to accomplish the objectives of this work a series of experiments using 50% ethylene glycol as the working fluid in a glycol-air cross flow mode will be conducted. The experiments will utilize a multi-port serpentine microchannel heat exchanger. A single phase working fluid condition will be used for both working fluids throughout all of the experiments. The air-side results obtained from these experiments will be compared to the available and comparable literature.

Chapter 2: Literature Review

Heat exchangers have been used in a wide variety of engineering applications and processes in the past century. They are one of the most important and major components in any industrial process that involves adding, removing or transferring heat. The importance of this device, coupled with its variety of uses, has led to extensive research aimed at optimizing performance. The air-side pressure drop, heat transfer, and fluid flow performance of conventional cross flow heat exchangers have been the subject of significant research in the past century. Much of this research involves the investigation of the heat transfer and fluid flow characteristics of finned heat exchangers.

Microchannel heat exchangers are one of the most recent developments in heat exchanger technology. As such, the available literature on this technology is relatively scarce compared to conventional heat exchangers. Tuckerman and Pease (1981) first introduced the concept of the microchannel flow passage to remove the heat from silicon integrated circuits. Microchannel research generally involves only the liquid side of Liquid-to-Air crossflow. Research on finned microchannel heat exchangers is very rare, investigations of air-side heat transfer and fluid flow investigation are virtually non-existent.

Based on the limited literature available on liquid-side, properties it is evident that micro channel heat exchangers possess superior thermal and hydraulic features, *i.e.* heat transfer coefficient, heat transfer area, approach temperature, channel geometry, arrangements and orientations, when compared to conventional and compact heat exchangers. Microchannel heat exchangers show great promise due to their larger heat transfer area per unit volume, and higher heat transfer coefficients. A brief review of selected literature on micro channel heat exchangers, their heat transfer and fluid flow features, and a comparison to conventional heat exchangers is followed by a survey of air-side investigations of conventional finned tube and plate fin heat exchangers.

2.1 Previous research on Microchannel heat exchangers

A number of studies have been conducted to examine the heat transfer and flow behaviors in microchannels. Owhaib and Palm (2004) experimentally studied single phase convective heat transfer in circular microchannels. Various available heat transfer augmentation techniques for microchannel were reviewed by Steinke and Kandlikar (2004). Morini (2004) surveyed the previous literature and experimental results of single phase convective heat transfer in microchannels. Hetsroni *et al.* (2005) conducted experiments into the heat transfer in microchannels, and compared the results to theory and numerical results with different microchannel geometries. A crossflow micro heat exchanger capable of expediting the heat transfer from liquid to gas was designed Harris *et al.* (2000). They demonstrated that such heat exchangers could be used in wide range of automotive, home heating, and aerospace applications. Kandlikar (2006) investigated and categorized various diameter flow passages; also they studied multiphase fluid flow and heat transfer characteristics in microchannels. Khan and Fartaj (2010) reviewed many potential applications of the microchannel heat exchangers, since they provide high heat transfer, reduced weight, energy, and space over traditional heat exchangers. The authors investigated the heat and fluid flow for characteristics for various working fluids in different microchannel air-to-liquid cross flow test specimens. Experiments by Khan and Fartaj (2010a) experimentally investigated the fluid flow behavior in a multi-port circular straight microchannel slab in the classical laminar flow regime.

2.1.1 Heat transfer enhancement using Microchannel heat exchangers

Several researchers have attempted to classify and compare micro channel heat exchangers to conventional heat exchangers with respect to important fluid flow and heat transfer parameters. For example, Ramshaw (1995) found that micro channel heat exchangers can significantly increase the heat exchange that can be accomplished per unit volume as an aim of process intensification. Shah (1991) stated that "a heat exchanger is referred to as a micro heat exchanger if the surface area density is above about 10,000 m^2/m^3." Mehendale *et al.* (2000) classified a hydraulic diameter of 1–100 µm as a micro-

structured exchanger, compared to a hydraulic diameter of greater than 6 mm as conventional heat exchanger.

Bier *et al.* (1990) and (1993) studied a micro channel heat exchanger with an active volume of 1 cm^3 and surface density of $14,200 \, m^2 / m^3$ and 4000 channels per cubic centimeter. They found that a volumetric thermal power of 18,000 MW/m^3 could be achieved with an overall heat transfer coefficient on the order of magnitude of 20 kW/m^{2}K and a temperature difference of 50 °C. Similar results were also reported by Kang *et al.* (2002), who used pure water as the working fluid in the laminar regime to produce a volumetric heat transfer of 5446 MW/m^3 and an overall heat transfer coefficient of 24.7 kW/m^{2}K from rectangular microchannels with 9000-µm lengths, 40-µm widths, and 200-µm depths and a surface-area density of 15,294 m^2/m^3. Luo *et al.* (2007) used a counter current micro channel heat exchanger with multi passage microchannels; there were 28 channels per plate with each channel lengthened by right angle turns to prolong residence time. The width of the channels was 200 µm, separated by borders with a thickness of 50 µm. They calculated an overall heat transfer coefficient of 5000–25,000 W/m^{2}K and a volumetric thermal power of 315 MW/m^{3}K.

Lee *et al.* (2004) presented a polymer type micro channel heat exchanger applicable to a 272 BGA multi-chip module (MCM). The fabricated heat exchanger was 300-µm in height. They found that this heat exchanger was able to reduce thermal resistance up to 89% (from 50 to 7 °C/W) by the liquid cooling method and parametric optimization. Kido (2000) from Matsushita Refrigeration Company developed a compact heat exchanger incorporating a rotary fluid pump and a special manifold. Tests on this heat exchanger showed considerable thermal resistance reductions of about 0.03 K/W; however, a very large pressure drop, low flow rates, and a low overall COP were noted.

Peng *et al.* (1994), Wang and Peng (1994), Adams *et al.* (1998) and Qu *et al.* (2000) indicated that microchannel flow can deliver up to 60 times higher heat transfer rates than conventional channels, and can easily achieve a heat flux level in excess of 100 W/cm^2. These benefits, however, are accompanied by a high fluid pressure drop of over 200 kPa.

This pressure drop is identified as the major drawback to micro channel heat exchangers. Typical conventional heat exchangers have an average heat transfer surface area per unit volume of 50 to 100 m^2/m^3, and a heat transfer coefficient of up to 5000 W/m^2K when using liquid as the working fluid.

Oh *et al.* (2003) studied the effect of the orientation of microchannel tubes, hydraulic coating, and louver pitch on the heat transfer performance of a microchannel evaporator. They found that the orientation of the microchannel tubes has a great effect on the heat transfer performance. Hrnjak and Litch (2008) studied a prototype ammonia chiller with an air cooled condenser and a plate evaporator. Two aluminum condensers were evaluated in the chiller: one with a parallel tube arrangement between headers and ''microchannel'' tubes (hydraulic diameter D_h = 0.7 mm); and the other with a single serpentine ''macrochannel'' tube (D_h = 4.06 mm). They found that the microchannel charge was an average of 53% less than for the serpentine. The ''microchannel'' condenser charge per heat transfer capacity ratio was around 76% less than for the ''macrochannel'' serpentine condenser. The experiments showed that refrigerant charge is directly proportional to the hydraulic diameter, and that by using smaller hydraulic diameters and a lower refrigerant charge, higher heat transfer capacity is achievable. Qi *et al.* (2009) studied two retrofitted compact and high efficiency microchannel evaporator and subcooling condenser. The authors compared them with currently used baseline heat exchangers in mobile air conditioning. They found a volume reduction of 17.2% and 15.1%, and a weight reduction of 2.8% and 14.9% for the microchannel evaporator and condenser, respectively.

2.1.2 Microchannel heat exchanger geometry improvements

Microchannel heat exchangers typically find applications in the electronics industry. However, electronics cooling applications restrict how the system can be designed. Several researchers have investigated and optimized microchannel heat exchanger geometry. One notable study was conducted by Kandlikar and Upadhye (2005). They generated channel optimization plots for a microchannel heat exchanger designed to cool

a chip with dimensions 10mm x 10mm. Their generated optimization plot was able to accurately determine various channel geometrical parameters, including an optimal number of channels for a maximum allowable chip temperature of 360K and inlet fluid temperature of 300K. They also investigated the effect of split flow arrangement, and found that such arrangement provides a substantial pressure drop reduction.

2.1.3 Effect of Microchannel enhancement

A number of investigators have focused on the application of certain enhancements to microchannels. As mentioned in the previous section Kandlikar and Upadhye (2005) analyzed the effect of splitting flow arrangements using enhanced, offset strip-fin geometry to obtain a significant pressure drop reduction. Kandlikar and Grande (2004) reviewed liquid cooling with internal flow channels; they stated that three dimensional microchannels, which use microstructures or grooves in channels and channel surfaces, can achieve significant increases in single phase cooling. Colgan *et al.* (2005) compared various offset fin geometries using multiple heat exchanger zones and optimized cooler fin designs. They found that a unit thermal resistance of 10.5 C-m^2/W from the cooler surface to the inlet water can be achieved while maintaining a fluid pressure drop of less than 35 kPa.

2.2 Air side investigations of conventional crossflow heat exchangers

For conventional heat exchangers the air-side thermal resistance generally accounts for 90% of total thermal resistance (Wang, 2000). Hence the evaluation of air side appropriate heat transfer and fluid flow correlations for the heat exchanger is being considered imperative. Many researchers have investigated the air-side heat transfer and fluid flow characteristics of conventional and compact cross flow heat exchangers. A sample of the literature is summarized below in terms of the air-side operating flow regimes, fin types used, correlations developed, as well as the effect of fin types, fin parameters, *i.e.* fin height, width, length, and spacing, and also flow regimes on air-side fluid flow and heat transfer characteristics.

Wang *et al.* (2000) focused on the data reduction methodology for the air-side performance of finned tube heat exchangers and recommended specific data reduction methods for obtaining the air-side performance of fin-and-tube heat exchangers. The authors recommended that energy balance (*i.e.* difference in the magnitude of heat transfer rates) between the air-side and liquid side should be less than 5% for accurate results. The authors advised that future researchers utilize proper selection of established effectiveness NTU relationships for analyzing any particular heat exchanger, along with the calculation of the friction factor in a manner that would negate entrance and exit losses.

Dong *et al.* (2007a) studied experimentally a total of 11 wavy fin and flat tube crossflow heat exchangers across a range of air-side Reynolds number between 800-6500. The heat exchangers of varying fin pitches, lengths, and heights were subjected to a constant tube-side water flow rate. They reported that friction (*f*) and Colburn (*j*) factors decreased with increasing Reynolds number. It was also reported that an increase in fin spacing increases the *f* and *j* factors for a given Reynolds number; the *f* factor as function of Reynolds number did not vary with fin height. The authors also developed heat transfer and pressure drop correlations for wavy fins, which were reported to be more than 95% accurate in predicting those parameters.

Nuntaphan *et al.* (2005) studied 23 crimped spiral crossflow heat exchangers for the effects of tube diameter, fin spacing, tube pitch, and tube arrangement. The authors reported that increasing the fin height increased the pressure drop and decreased the heat transfer coefficient significantly for an in-line arrangement. However the effect was found to be not so drastic when examining a staggered fin arrangement because its air-flow blockage pressure drop term dominated other pressure drop contributions. They also reported smaller fin spacings led to lower heat transfer coefficients.

Tang *et al.* (2009) investigated the air-side heat transfer and the friction factor of 12-row, 18-mm finned heat exchangers. The authors investigated a range of air-flow Reynolds numbers between 4000 and 10000; they found that crimped spiral type fins provide

higher heat transfer and pressure drop compared to plain, slit types of fins. They also found that slit fin heat exchangers perform better compared to other heat exchangers at higher Reynolds number ranges.

De Paepe *et al.* (2005) investigated the performance of several plate-fin types for 30 different air-side Reynolds numbers between 400 and 1600. The authors developed a Reynolds number vs. *j* factor correlation, which can predict *j* factors using surface temperature measurements with only 13% error.

Paeng *et al.* (2009) measured the forced convective heat transfer of plate fin-tube heat exchangers at air-side Reynolds numbers between 1082 and 1649. The authors then numerically computed the average air-side Nusselt number. They found errors of less than 6% when the numerically computed value was compared with experimental values, hence demonstrating the suitability of the particular numerical model used.

Dong *et al.* (2007) studied air-side heat transfer and pressure drop characteristics for 16 types of offset, strip fin, flat tube, heat exchangers over air-side Reynolds numbers between 500 and 7500. The authors developed correlations for the *j* factor and *f* factor against Reynolds number using regression analysis, which predicted 95% of the *j* factor and 90% of the *f* factor experimental data within ±10%.

Huzayyin *et al.* (2007) investigated the effect operating conditions for wavy finned tubes. The operating conditions included air temperature, air relative humidity, and evaporator pressure on such air-side performance as cooling capacity, pressure drop, and heat transfer coefficient. The authors found that increasing the air inlet temperature, air coil face velocity, and air inlet relative humidity resulted in a decrease in the air temperature drop across the coil. They also reported that the pressure drop across the coil increases with an increase in the inlet air relative humidity, and the coil face velocity.

Dong *et al.* (2008) analyzed the air-side heat transfer and pressure drop characteristics of 9 louver-finned, flat tube heat exchangers of varying fin spacing and length. The authors

reported j and f factors over a Reynolds number range between 500 and 6500. They reported an increase in air side heat transfer coefficient (h_a) and pressure drop (Δp) with a decrease in fin spacing and length; fin spacing had a greater influence on the thermal hydraulic characteristics of the louvered fins.

Khan *et al.* (2004) investigated an elliptical tube array heat exchanger with air-side Reynolds numbers between 10,000 and 33,000. Results showed that an increase in the heat transfer rate and Nusselt number depended on an increase in the air-side Reynolds number according to a power law relation. The dimensionless pressure drop coefficient was seen to reduce from 0.33 to 0.16, *i.e.* from a Reynolds number 10,000 to 20,000, and remained constant at this level.

Wang *et al.* (2000a) studied the air-side thermal-hydraulic characteristics of 18 different fin-tube heat exchangers with a plain fin configuration. The authors reported that for a given number of tube rows, the heat transfer characteristics were greatly dependent on fin pitch. It was found that for up to two rows, the heat transfer performance increased with a decrease in fin pitch, while for four or more rows, the effect of fin pitch was negligible. It was also found that for a given fin pitch, friction performance was not significantly altered by the number of tube rows.

Park *et al.* (2009) studied the air-side thermal-hydraulic performance of a flat-tube aluminum heat exchanger constructed with serpentine louvered, wavy, and plain fins. Both dry and wet conditions were investigated. The authors found that fin spacing has a significant influence on f and j factors, as they decrease with decrease in fin spacing. This effect is seen to be more pronounced at high Reynolds numbers. The authors reported that for louvered fin heat exchangers, fin spacing has greater influence on the f factor under wet conditions than at dry conditions. It was also found that under wet conditions, louver spacing has greater influence on performance than at dry conditions.

Tang and Yang (2005) experimentally investigated the thermal performances of single-row fin-and-tube heat exchanger. The authors found the leading thermal resistance on the air side.

The convective heat transfer is mainly influenced by boundary layer separation effects and by wake interactions suggested by Incropora and Dewitt (2002). Tao *et al.* (2006) performed three dimensional numerical simulations to investigate the local heat transfer coefficient and fin efficiency of wavy fin-and-tube heat exchangers for laminar flow. They observed that the local Nusselt number in the wake region was very low that would lead to weak convective heat transfer in this region. Similar results were obtained by Tian *et al.* (2009) during numerical studies on wavy fin-and-tube heat exchangers which had three-row round tubes in staggered or in-line arrangements.

Taler (2005) developed a numerical model for predicting the heat transfer correlations for crossflow compact heat exchangers, and computed air side heat transfer coefficient from overall thermal resistance. The author chose to implement their numerical model for a double row, two-pass automotive radiator in laminar flow region. The major and minor diameters of the oval shaped tubes were 11.82mm and 6.35mm respectively. His numerical simulation revealed that the regions behind the tubes contributed very small to the performance of the heat exchanger. The heat transfer rate was observed very low in the second row due to presence of the wakes in the front and behind the tube.

El-Shaboury and Ormiston (2005) numerically studied on forced-convection heat transfer of crossflow in banks of plain tubes in square and non-square inline arrangements. They found that the heat transfer rate around the first tube in the bundle was always higher than the tubes following it.

2.3 Uncertainty in Microchannel heat exchangers

Kandlikar (2006) divides the uncertainties or errors in micro channel heat exchangers into three groups: uncertainties inherent to fluid properties; uncertainties relative to micro

channel geometric characteristics; and uncertainties due to flow rate measurements. While most of these uncertainties are within an acceptable range, they tend to become unmanageable for cross section dimensions. For example uncertainties in hydraulic diameters are magnified to the fourth power in the calculation of flow rate. Kandlikar also finds that for a measurement inaccuracy of only 10-nm across a depth of 1.0-µm produces an error of 4% in the estimation of flow rate. For a rectangular micro channel heat exchanger of height *a* and width *b*, a major influence on the overall uncertainty comes from the uncertainty in measurement of *a* and *b*.

Lower Reynolds numbers tend to exhibit large uncertainties due to the errors associated with flow rate measurements. Uncertainties in the overall calculation can be also introduced as a result of uncertainties in channel dimensions, flow rate measurements, entrance and exit losses, and the developing region effects. Steinke and Kandlikar (2006) analyzed the uncertainties in the experimental measurements of Nusselt number. Uncertainties in surface temperature measurement and flow channel dimensions also contribute to the overall uncertainty. Uncertainties in geometrical measurements also play a role in introducing uncertainties to the friction factor estimation. It is also found that smaller diameter tubes tend to have higher overall uncertainty in general due to the relative difficulty in measuring small heat transfer rates accurately.

2.4 Summary of literature review

From the above-provided description of past research, it is evident that there is a great scatter of results and findings in the available literature. Such literature is found to be either on analysis of liquid side of microchannel heat exchangers, or an air-side of finned conventional heat exchangers. An air-side investigation of a microchannel heat exchanger does not exist; published investigations of microchannel heat exchangers utilizing ethylene glycol were not found.

A great portion of the research on microchannel has used water as the base fluid, including Mala *et al.* (1999), Weilin *et al.* (2000), Wu *et al.* (2003), Peng *et al.* (1994),

Peng *et al.* (1994a), Yu *et al.* (1995), Jiang *et al.* (1995), Papautsky *et al.* (1999), Wilding *et al.* (1994). Few researchers have used fluids other than water as the working fluid. Hegab *et al.* (2002) used R134a; Pfahler *et al.* (1989) using propanol; Pfahler *et al.* (1991) using silicone oil and isopropyl alcohol; and Judy *et al.* (2002) used methanol and isopropanol. No published literature was found using ethylene glycol in micro channels. Of the surveyed literature, none dealt with glycol in small diameter channels, except for Jokar *et al.* (2005), who used larger hydraulic diameters ranging between 2.6 and 4.1 mm. This diameter range, however, does not fall in the micro channel category.

Researchers also investigated various channel shapes, the three most frequent of which are rectangular, trapezoidal, circular cross sections. Most publications tend to use rectangular microchannels due to the relative ease of manufacturing such channels. These publications include Peng *et al.* (1994), Peng *et al.* (1994a), Jiang *et al.* (1995), Papautsky *et al.* (1999), Hegab *et al.* (2002), Pfahler *et al.* (1989), Pfahler *et al.* (1991), Wu *et al.* (1998), Arkilic *et al.* (1994), Arkilic *et al.* (1997), Shih *et al.* (1996) etc. Researchers who used circular channels include Mala *et al.* (1999), Yu *et al.* (1995), Judy *et al.* (2002), Chung *et al.* (2002), and Choi *et al.* (1991). Research done on trapezoidal cross section channels include Weilin *et al.* (2000), Wu *et al.* (2003), Wilding *et al.* (1994), Pfahler *et al.* (1991), and Harley *et al.* (1995) etc.

Several publications found deviations from classical laminar flow heat transfer and fluid flow theory because the hydrodynamic and thermal developing and developed regions were not considered properly. Available air-side finned heat exchanger research by Dong *et al.* (2007), Nuntaphan *et al.* (2005), De Paepe *et al.* (2005), Paeng *et al.* (2009), Huzayyin *et al.* (2007), Wang *et al.* (1999), Park *et al.* (2009), and Tang *et al.* (2009) involved various fin types. The air-side Reynolds number is these experiments ranged from 400 to 10,000, and showed the effect of fin height, width, length, flow regimes, and environmental conditions, on heat transfer and fluid flow parameters as well as heat exchanger performances.

Previous air side research by Wang (2000), and Tang and Yang (2005) have found that thermal resistance on the air side of the air-to-liquid heat exchanger dominates the total thermal resistance (composed of air, liquid, and wall thermal resistances). In some cases the air side thermal resistance reached up to 90% of the total thermal resistance.

Conventional heat exchangers employing in-line or staggered tube row configuration develop regions of low fluid velocity behind the rows. This area is called wake region. El-Shaboury and Ormiston (2005), Taler (2005), Tao *et al.* (2007), and Tian *et al.* (2009) performed numerical analysis of in-line tube row configurations. These studies have all found that heat transfer rate for second and subsequent rows are adversely affected by wake region resulting relatively lower heat transfer rates when compared to the first row.

2.5 Scope of current study

A large number of articles in the published literature have been carefully examined; their research scope and findings were compiled and provided in this chapter. After reviewing this literature, and in light of the previous work, a finned multi-port circular microchannel heat exchanger was studied experimentally. 68 circular microchannels, 1 mm in diameter, situated parallel to each other, were fabricated inside the serpentine slab structure. The heat exchanger was made of aluminum, and was attached inside a 305-mm x 305-mm x 600-mm Plexiglas test chamber. The serpentine slab was oriented to provide a 0° air flow angle of attack. The air flow was perpendicular to the channel lengths and parallel to the structure width. Placing the slabs in this orientation also ensured a longer air dwell time over them, and optimized heat transfer. A single-phase 50% ethylene glycol-water mixture was used as the working fluid in a series of experiments against air under similar cross flow condition. The air Reynolds number ranged between 750 and 3165. The glycol Reynolds number range was held fairly constant at 200 ± 5. These Reynolds number ranges were chosen because they were found to be applicable for current micro channel heat exchangers. Through experimental study on these heat exchangers, an air-side Reynolds number vs. Nusselt number relationship will be examined. Also general fluid

flow, heat transfer, and pressure drop characteristics, as well as heat exchanger parameters will be examined.

Chapter 3: Experimental Setup and Methodology

3.1 Microchannel heat exchanger research facility

This detailed study of microchannel heat exchanger was undertaken in the University of Windsor's Microchannel Research Facility, room B05, of Essex Hall. It is a state-of-the-art research facility, whose sole focus is microchannel and microchannel heat exchanger research and development; it is a one-of-a-kind in southwestern Ontario. The research facility is composed of a closed loop thermal wind tunnel with a built-in heat exchanger for heating and cooling the air flow. It has an external water supply system for the heat exchanger, several types of microchannel heat exchangers, a data acquisition system utilizing LabVIEW, and numerous measurement devices. The detailed schematic of the experimental setup and the research facility including all major components is presented in Figure 3.1.

3.2 Research facility apparatus

A large number of apparatus are utilized in a typical test run; the major equipment and sub-systems are illustrated in Figure 3.1 schematic and Figure 3.2 photograph. The entire experimental setup consists of sub-systems such as: thermal wind tunnel, working fluid tank, gear pump (glycol-side), piston pump (air-side), circulation heater, city water supply, and data acquisition system. Each of these sub-systems is composed of multiple components. The details of each of these sub-systems and their components are described as follows.

3.2.1 Thermally insulated wind tunnel

The closed loop thermal wind tunnel houses a built-in heat exchanger and a detachable test section. It is 544 cm long, 75 cm wide and 164 cm high, and is the largest component in the research facility. The wind tunnel has 1-cm thick wall and a contraction ratio of 6.5.

Legend

1. Test Fluid
2. Gear Pump
3. Circulation Heater
4. Relief Valve
5. Needle Valve
6. Digital Flow Meter
7. Microchannel HX Inlet RTD
8. Microchannel HX Inlet PTD
9. Microchannel Heat Exchanger
10. Microchannel HX Outlet RTD
11. Microchannel HX Outlet PTD
12. Impeller Flow Meter
13. Test Fluid Mass Collection Bucket
14. Thermal Wind Tunnel
15. Hydraulic Oil Piston Pump
16. Hydraulic Motor & Fan
17. Wind Tunnel Heat Exchanger
18. Pitot Static Tube
19. Air Inlet Temp. Thermocouple Grid
20. Air Outlet Temp. Thermocouple Grid
21. City Hot Water Supply
22. City Cold Water Supply
23. Hot Water Header
24. Cold Water Header
25. Mixing Chamber for Auxiliary Supply
26. Mixing Chamber for WT. HX. Supply
27. Wind Tunnel HX Inlet Supply Line
28. Wind Tunnel HX Drainage Line
29. Drain
30. Air Differential PTD
31. Air Velocity Measurement PTD
32. FlowKinetics FKT Pressure/Flow DAQ
33. Terminal Block (96 Signal Inputs)
34. Signal Conditioner (SCXI Modules)
35. PC with NI DAQ Card + LabView

Figure 3.1: Microchannel heat exchanger research facility & experimental setup schematic
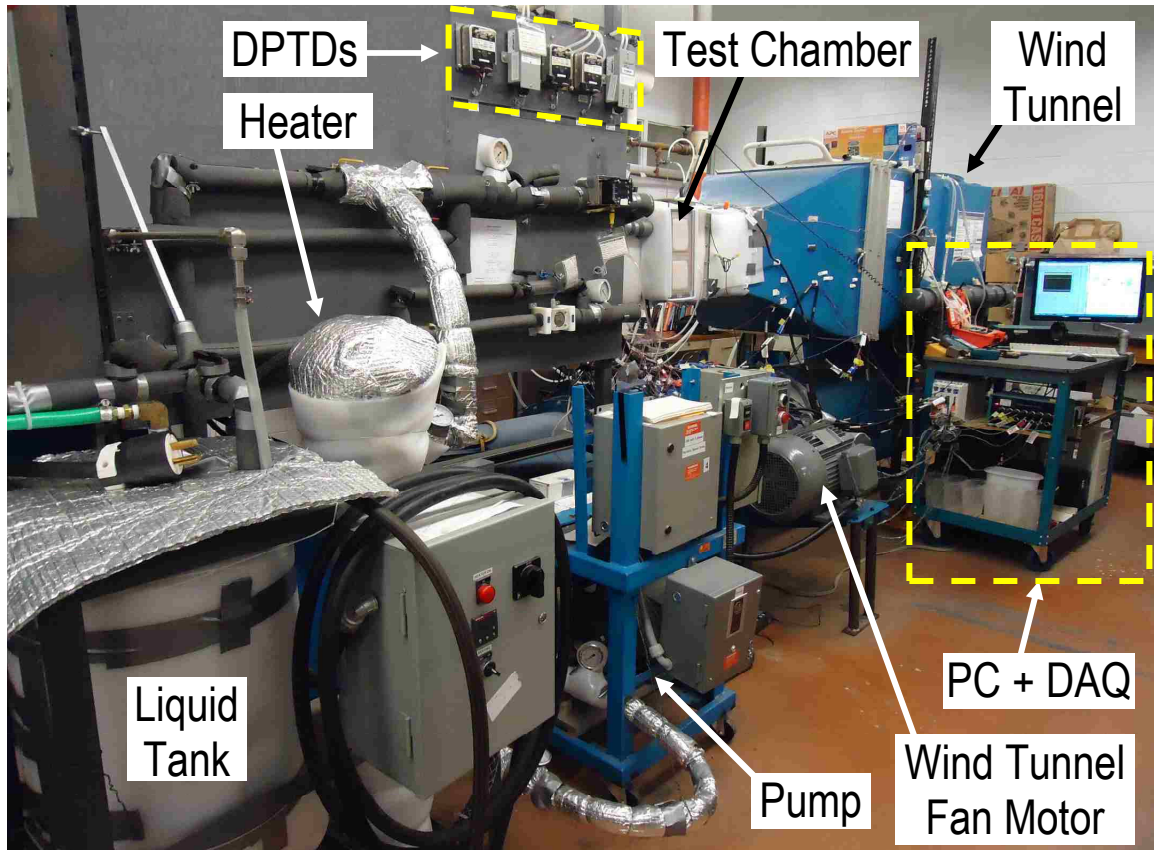
Figure 3.2: Microchannel heat exchanger research facility

Air circulation through the wind tunnel is accomplished by utilizing a blower that is driven by a hydraulic piston pump, the details of which are provided in section 3.2.6. The direction of air-flow inside the wind tunnel is shown in Figure 3.3. Maximum recorded average air velocities inside the wind tunnel of up to 30 m/s are possible in the absence of a test heat exchanger inside the test section. Experiments with the serpentine microchannel heat exchanger in place revealed that an air flow velocity of up to 11 m/s is achievable. It is dependent on frontal area and blockage ratio of the heat exchanger. The built-in tubular heat exchanger is situated at the upstream side of air passage inside the tunnel duct. This heat exchanger draws water from external water supply and is used to heat, cool, and control the air temperature as required by the parameters of the experiment. The built-in heat exchanger is robust enough to handle the full flow rate supplied by the city, and in experimental runs has been demonstrated to handle flow rates in excess of 42 liters per minute.
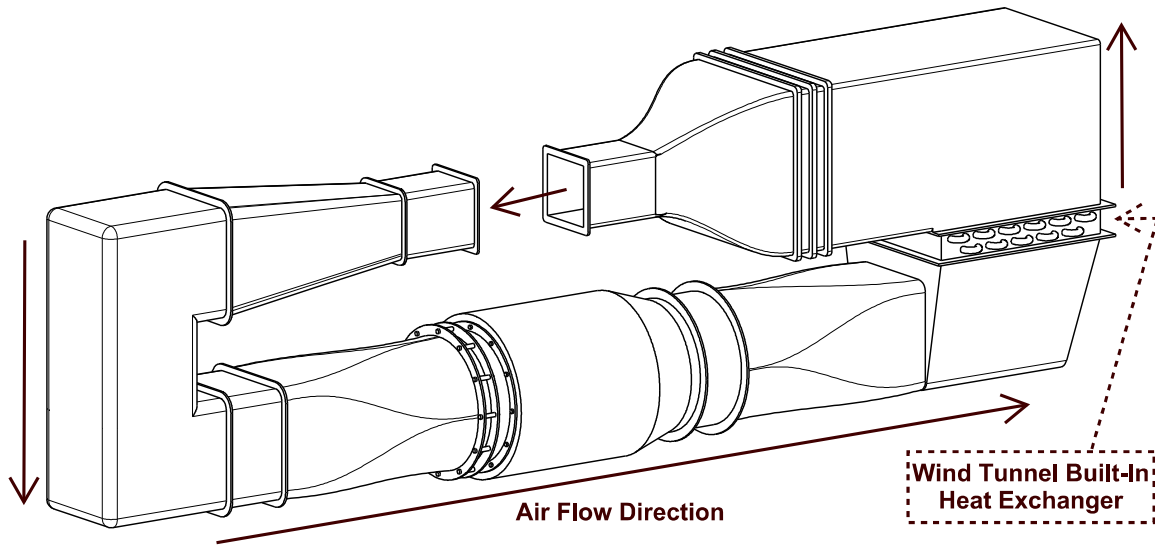
Figure 3.3: Wind tunnel with air flow direction

3.2.2 Test chamber

The fully assembled test chamber is shown in Figure 3.4. It has a length of 600 mm, width of 305 mm, and depth of 305 mm. The test chamber is constructed of Plexiglas with thermal conductivity of 0.19 W/m.°C. It is constructed in such a way that it will fit snuggly onto the wind tunnel's loading platform. The test chamber is a square cross section duct that matches the attaching portion of the wind tunnel. This arrangement ensures uniformity of air flow into the test chamber from the wind tunnel, hence eliminating any adverse effects related to air flow fluctuations. It is fabricated with screw holes for attaching to the wind tunnel. The roof of the test chamber has a removable lid which aids with both the in attaching process to the wind tunnel, as well as maintenance. After attaching the test chamber to the wind tunnel, the inner wall of the test chamber is taped with the wind tunnel to ensure flow uniformity and to reduce flow fluctuations. The test chamber also has a docking port on its roof for placing a Pitot tube or a hot wire anemometer for velocity and pressure measurements. A series of holes are regularly spacing on the top and side walls of the test chamber, making it possible to insert a Pitot tube. The holes traverse across the cross section of test chamber to measure air flow pressure and velocity in accordance with log-Tchebycheff method. Sections of Plexiglas

were also attached to the outside of the bottom wall of the test chamber for structural robustness.
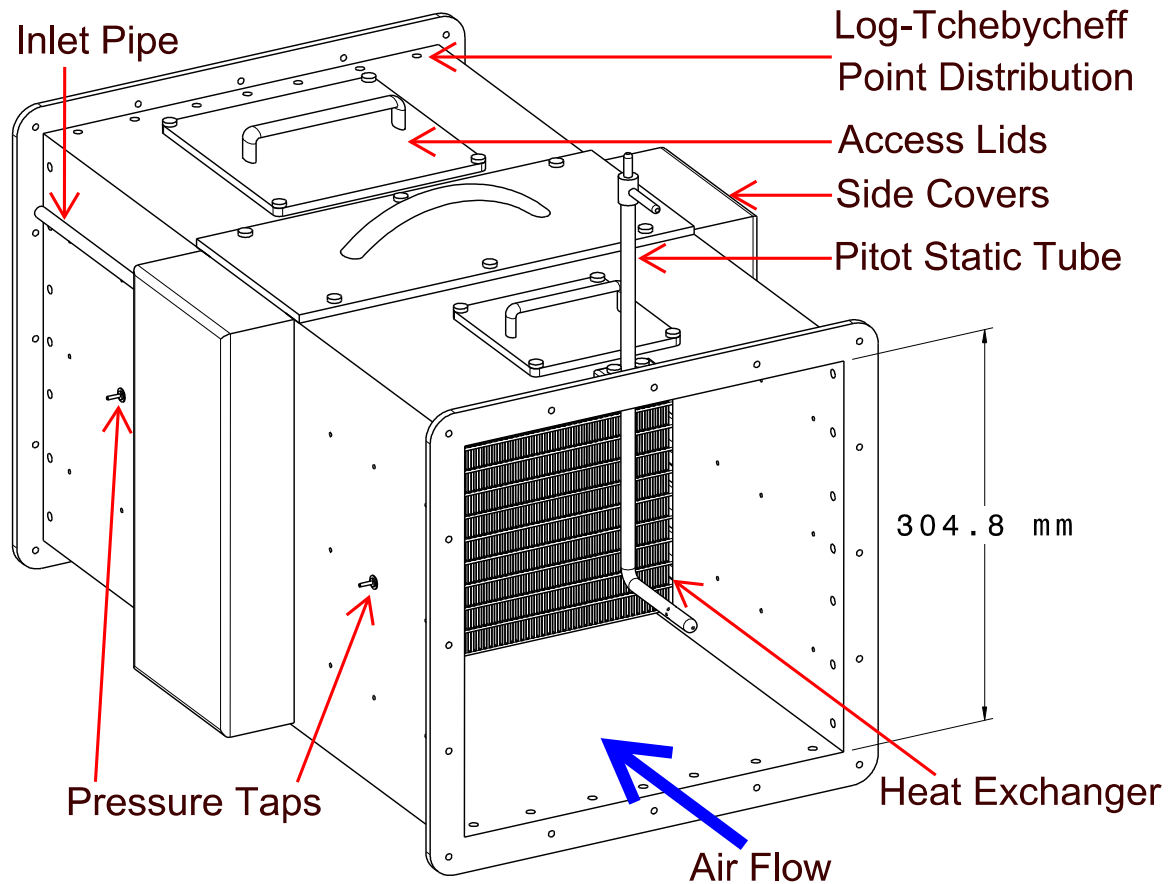
Figure 3.4: Fully assembled test chamber

3.2.3 Serpentine Microchannel heat exchanger

The serpentine microchannel heat exchanger, Figure 3.5, is constructed of aluminum. It is 305 mm wide, 285 mm high, and has a frontal area of 0.08669 m^2. The depth of the microchannel heat exchanger in direction parallel to air flow is 100 mm. The microchannel slabs and fins, which alternate in the construction of the heat exchanger, are also 100 mm wide. The microchannel heat exchanger consists of inlet and exit pipes, an inlet and an exit major header, and three inlet and three exit minor headers. The function of the major inlet and exit headers is to accumulate the liquid flowing from inlet pipe and minor exit headers, respectively, and to send the liquid flow into the minor inlet headers and exit pipe, respectively. The minor inlet and exit headers receive the liquid

flowing into them from the major inlet header and microchannels, respectively, and send the flowing liquid into the microchannels and major exit header respectively. The flow regime achievable in this heat exchanger with the existing equipment was in the laminar region.
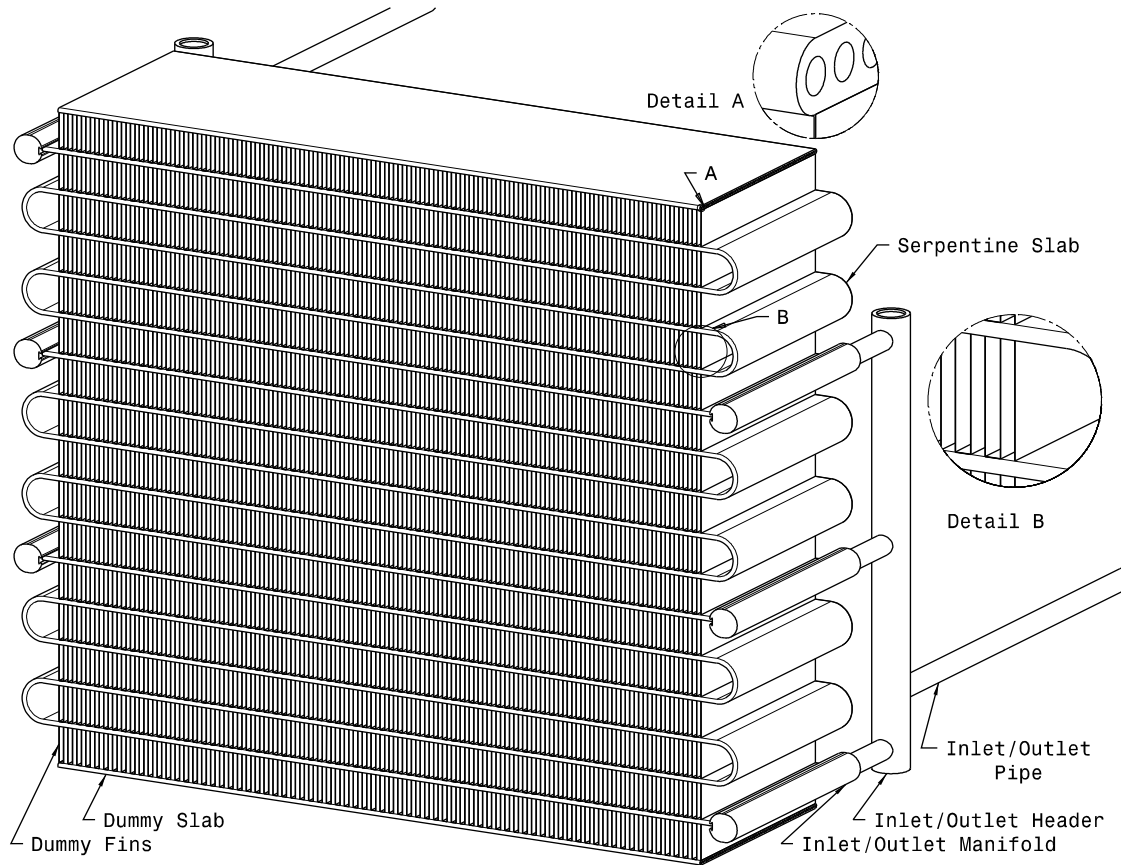
Figure 3.5: Microchannel heat exchanger used in this study

3.2.3.1 Microchannel arrangement within the heat exchanger slab

An illustration of the serpentine microchannel slab is shown in Figure 3.6. The serpentine slab houses a total of 68 microchannels. Each of these equally spaced microchannels is 1 mm in diameter, and the distance between the centers of the first and last microchannels in this series is 98 cm. The radius of the fillets at the ends of the slab width is 1 mm, giving the total width of 100 mm as previously mentioned.
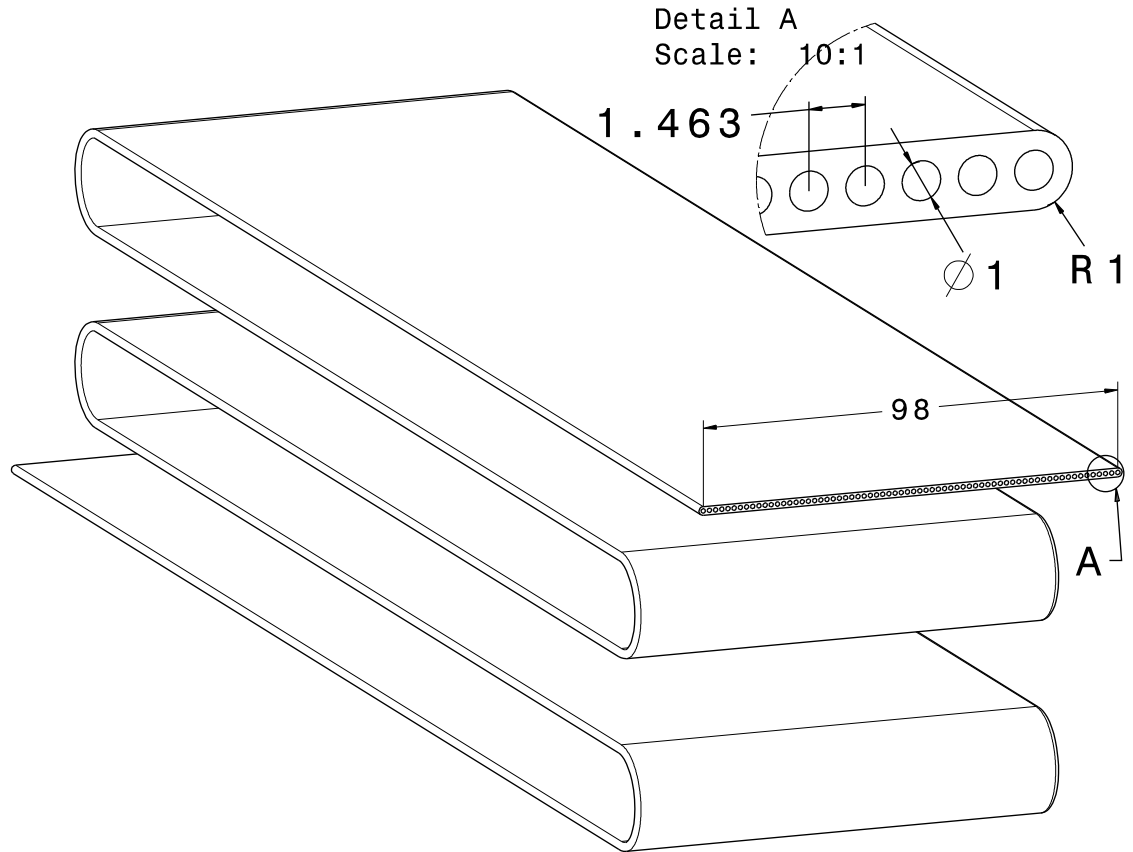
Figure 3.6: Microchannel serpentine section with channel arrangements

3.2.3.2 Heat exchanger serpentine slab arrangement

The microchannel heat exchanger consists of 3 serpentine microchannel slabs. The serpentine slabs are essentially one large (1838 mm) straight slab bent into five slab segments of alternate flow directions. The outer segments are each 370 mm long, the three middle segments are each 320 mm long. The three serpentine slabs therefore make up 15 slabs of alternate flow directions, perpendicular to the air flow direction. The effective heat transfer length of these 15 slabs is limited by the cross section of the test chamber to be 305 mm each. An illustration of the slab arrangement is shown in Figure 3.7. As seen in this figure, the slab inlets and exits are connected to the minor inlet and exit headers.
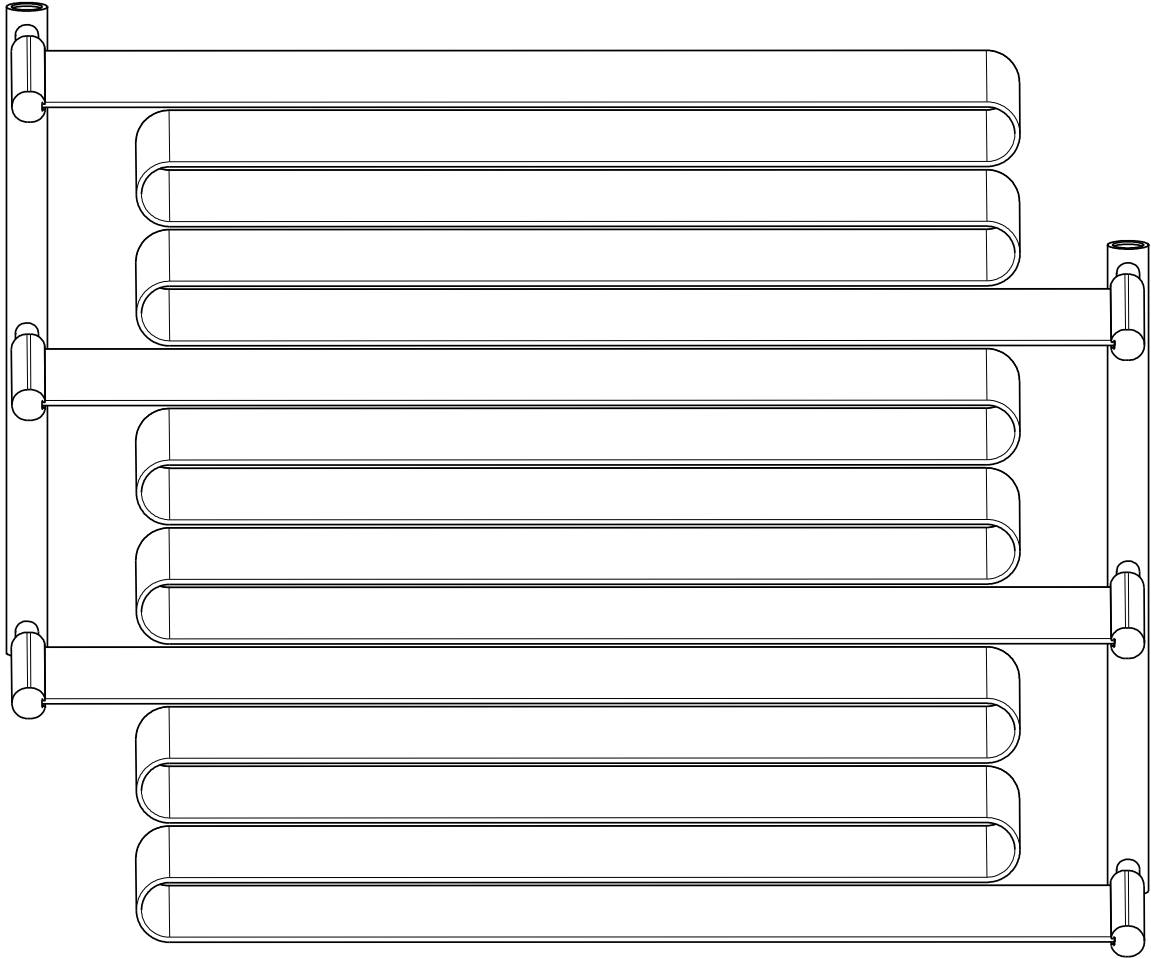
Figure 3.7: Slab arrangement within microchannel heat exchanger

3.2.3.3 Heat exchanger fin arrangement

The fins of this microchannel heat exchanger are fabricated from large pieces of thin aluminum sheet. A total of 14 such sheets are placed alternately between the microchannel slabs. The sheets are 98 mm wide in the direction parallel to the air flow. They are bent at right angles to create the geometry shown in Figure 3.8. The fin top and bottom surfaces shown in Figure 3.8 are attached to the slab to aid heat transfer from the slab to the fins. As such, the fins and slab together create rectangular blocks of flow area through which air can pass without mixing in the transverse direction. The fins are on average 18 mm high, and are manufactured to have a density of 12 fins per 25.4 mm (1 inch). The center of one fin to the center of another therefore is 2.12 mm as shown in Figure 3.8. The total length of the finned area is 12 inches, and the total number of fins in this length is 144 ± 0.3.
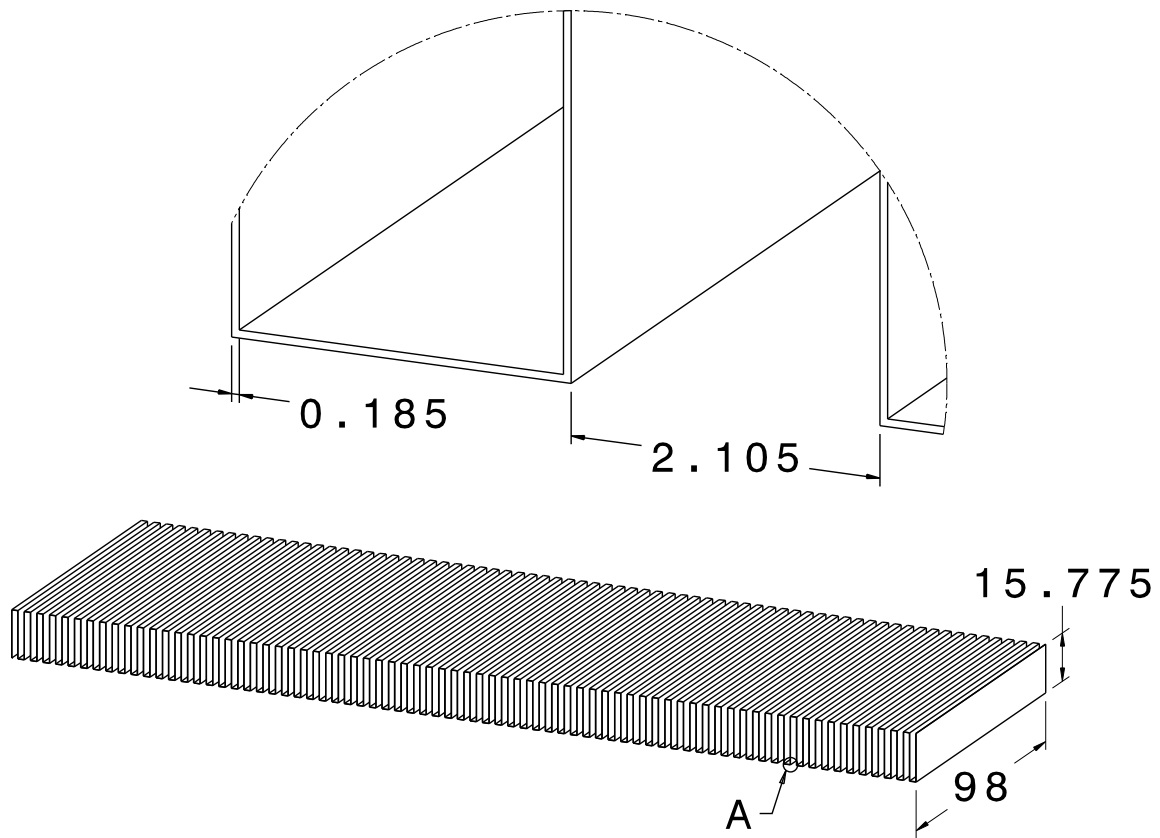
Figure 3.8: Microchannel heat exchanger fin

3.2.4 Circulation immersion heater with PID controller

The heater used in this experiment is a circulation immersion heater, Model # MFLI606X2818, from Wattco, Figure 3.9. It is furnished with a removable flange, threaded nozzles, drain plugs, insulation, and mounting brackets, which allow it to be easily incorporated into the existing research facility sub-systems. The heater is 4" 150 lb flanged steel vessel with 38.1 mm (1-1/2 inch) inlet and outlet. It is capable of providing up to 6 kW. It has a heating element watt density of 4.6 W/cm^2, which classifies it as a medium range watt density heater; low watt density is preferred for longer heater life.
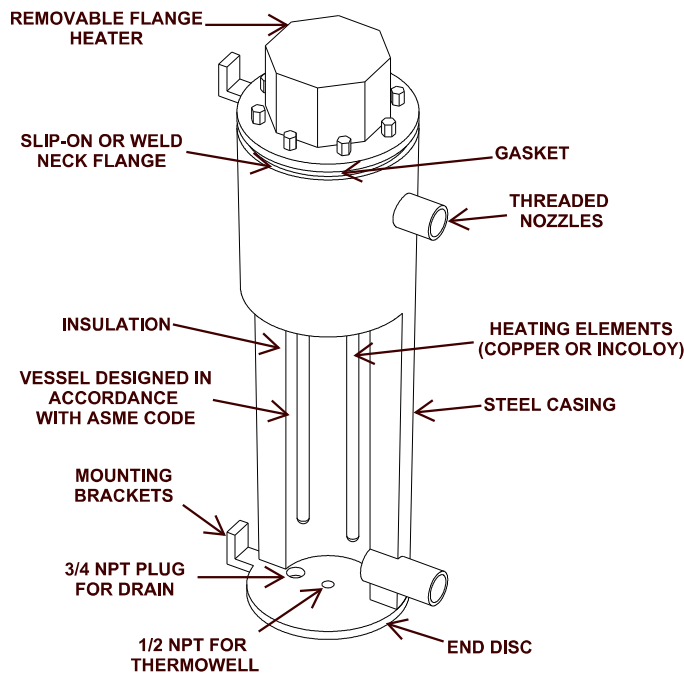
Figure 3.9: Circulation immersion heater with various components

The heater is controlled via a 1/16 DIN Series SD Controller, Model # SD6C-HJAA-AARG. It is furnished with an auto tuning feature, an on-off control, and a proportional integral derivative (PID) control. The on-off control switches the output to either full on or full off, depending on the input, set point, and hysteresis. The auto tuning feature allows the controller to measure the system response to determine effective settings for PID control. PID control provides more accurate control than on-off control. It adjusts

output when the temperature is within a proportional band by lowering the output power when the process temperature is close to the set point. For the experimental runs, the PID control and auto tuning feature were turned on for more accurate temperature control.

3.2.5 Gear pump with variable speed step motor

The pump utilized in the research facility is a positive displacement bronze gear pump from Omega, Model # FPUGR202-RCB. It is suitable for pumping water, oils, and certain solvents, and can provide outputs at a relatively constant flow rate regardless of the outlet pressure. This pump is capable of handling fluids with a viscosity of 21,630 cSt (100,000 SSU), and can provide up to 689 kPa gage (100 psig) pressure. It is powered by an external motor capable of up to 1725 rpm. The pump is connected by the shaft to a 3-phase, 230 V, variable-speed external motor, which can be controlled a frequency controller. By controlling the frequency, the speed of the motor and hence the liquid flow rate can be controlled.

3.2.6 Hydura piston pump for air circulation

A Hydura piston pump, Model # PVQ 06LS, circulated air through the wind tunnel. It works in conjunction with a Hydura variable displacement motor, Model # HB5-31. The variable speed motor is controlled through a needle valve, which facilitates manual adjustment displacement, and hence both the flow rate and the velocity of the air flow.

3.3 Research facility instrumentation and data acquisition

Temperature on the air-side and on the surface of the heat exchanger slabs was measured by thermocouples. The 50% glycol-water mixture temperature measurement was conducted using appropriate RTDs. The strategic location and arrangement of these thermocouples and RTDs and their specification is detailed below.

3.3.1 Temperature measurement arrangements

Thermocouples used on the surface of heat exchanger in various locations. These T-type thermocouples were placed on the bends, minor headers, and inlet and exit pipes of the heat exchanger. They provide both surface temperature measurements for further analysis, as well as a general trend of surface temperature along the heat exchanger slabs.

The air-side inlet temperature was measured by placing a grid of 9 equally spaced thermocouples on the wind tunnel duct, 3-5 mm from the inlet of the test chamber. It was anticipated that the air temperature variation in the test chamber exit cross section would be greater because of the presence of the heat exchanger. To take this variation into account, 25 equally spaced thermocouples were arranged in a grid and placed on the wind tunnel duct 3-5 mm from the exit of the test chamber. The thermocouple inlet and exit grids are shown in Figure 3.10 together with dimensions in dual units (mm and inch respectively). They were placed on the wind tunnel rather than test chamber since they will not require removal when removing the test chamber to change test heat exchangers. The close proximity of these thermocouples to the test chamber inlet and exit eliminates any incorrect temperature profile representation.
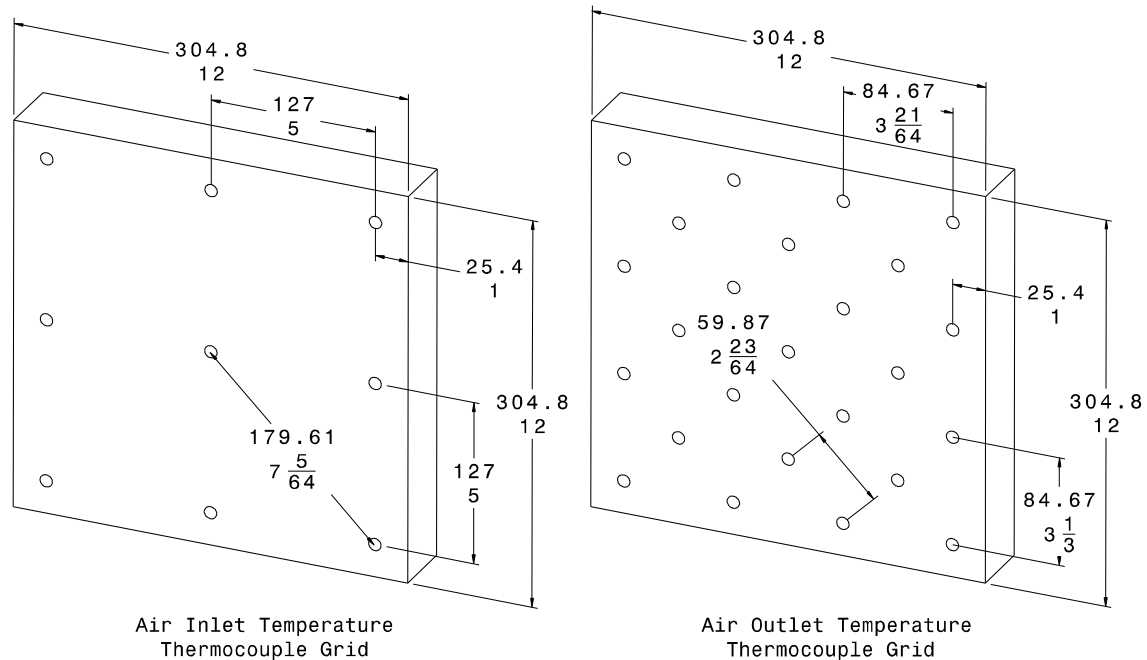
Figure 3.10: Thermocouple arrangements at the inlet and exit of test chamber

Resistance temperature detectors account for the predictable change in the electric resistance of some materials with changing temperature. Omega ultra precise immersion RTD sensors are used in the experiments. They are constructed of 100 ohm platinum with an accuracy of 1/10 DIN, and have a temperature range of -100 to 400 °C (-148 to 752 °F). The probe diameter is 6 mm (1/4 inch); the probe length is 51 mm (2 inch). It is furnished with mounting threads for ease of integration into the existing liquid piping network. The RTDs are located in both the inlet and the exit pipes of the heat exchanger to measure the glycol-water temperature. Figure 3.11 illustrates the RTD.
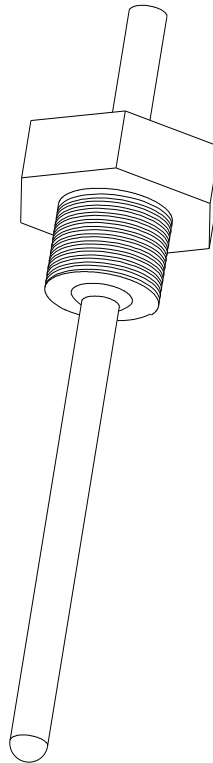
Figure 3.11: Ultra precise RTD

3.3.2 Pressure measurement arrangements

The pressure measurement on the air-side of the heat exchanger was accomplished with the aid of a FlowKinetics pressure acquisition system as well as differential pressure transducers (DPTDs). The glycol-flow pressure was measured using Omega pressure

transducers of an appropriate range. The details of these measurement systems are discussed below.

Pressure Ports

Sensor Storage

LCD Screen

Controls

Battery
Compartment

Power Adapter

PC Port

Relative Humidity
Sensor

Pitot Probe
(optional)

Temperature sensor
(K-Type thermocouple)

Silicone Tubing
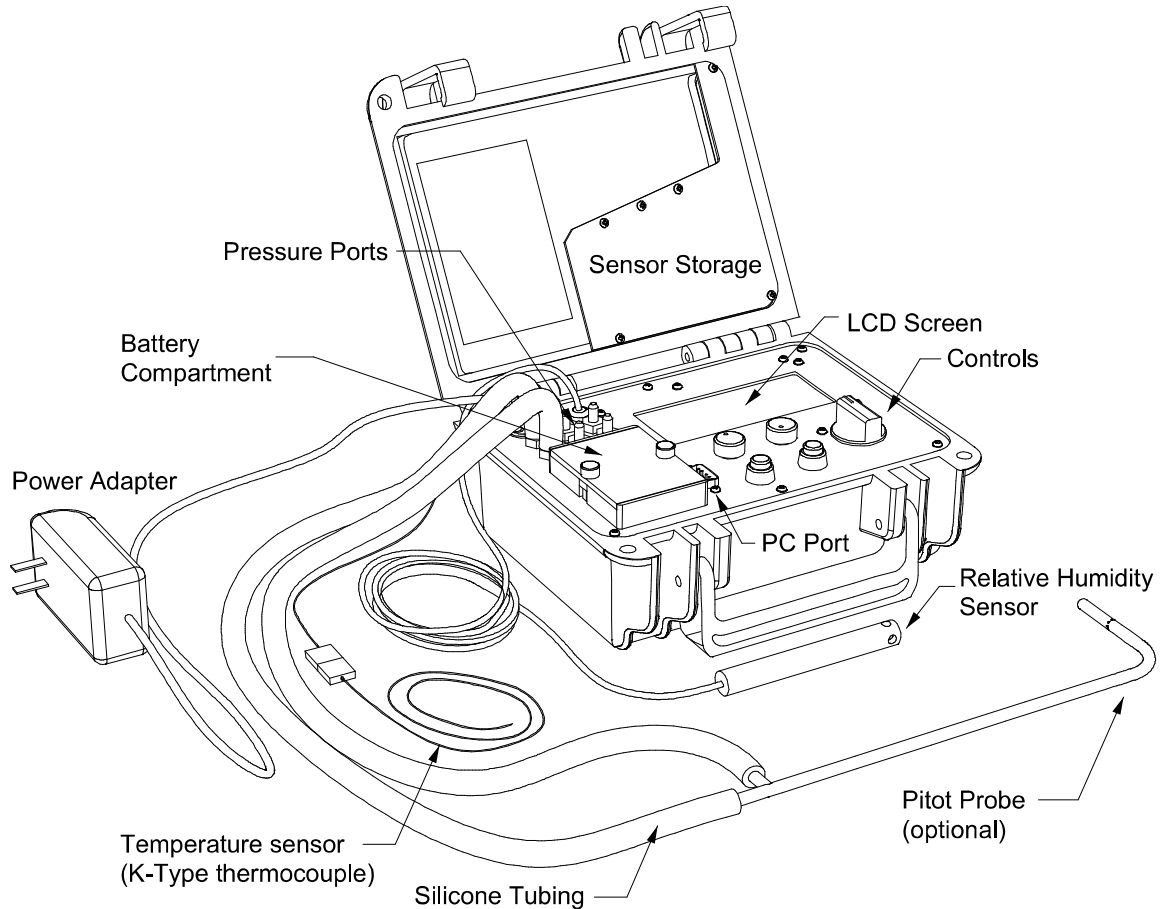
Figure 3.12: FlowKinetics flow and pressure acquisition system (Courtesy: FlowKinetics)

The FlowKinetics FKT series flow measurement / pressure acquisition system was utilized in conjunction with a Pitot static tube for measuring the air-side pressures. It is a portable, micro-processor-based pressure acquisition system that is capable of measuring: up to three different independent pressures, current atmospheric pressure, gas temperature, relative humidity, and gas density. This system and its accessories are shown in Figure 3.12. The flow measurement and pressure acquisition system, Model # FKT-3DP1A-0.4-5-1, accommodates K-type thermocouple sensors, and relative humidity sensors. It also has pressure ports for accommodating pressure differential readings from the test chamber pressure taps. The pressure ports are also connected with the Pitot static

tube, Model # P012A, to measure pressure differentials and to compute flow velocities. The Pitot static tube (Pitot probe) has a 317.5 mm (12.5 inches) insertion length, and a probe diameter of 3 mm (1/8 inches). It can accommodate a maximum temperature of 426 °C (800 °F). It is illustrated in Figure 3.12.

The glycol-side pressure readings were facilitated by Omega's PX Series pressure transducer, Model # PX-277, Figure 3.13. It has a stainless steel fitting and body, and has a broad temperature compensated range of -20 to 80 °C. This pressure transducer can read pressures between 0 and 100 psig, and outputs 0-5 DC volts. The relation between the pressure readings and output voltage is linear. It is furnished with a DIN plug connector for ease of removing and attaching DAQ wires.
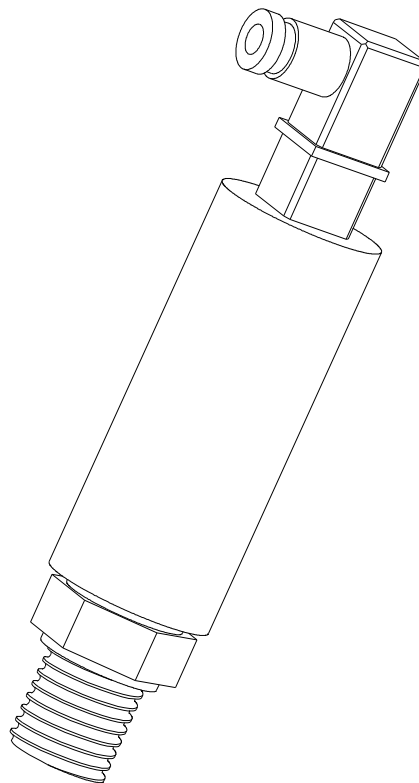
Figure 3.13: Omega PX series pressure transducer

3.3.3 Personal computer & DAQ hardware

The data acquisition system is composed of a custom built computer operating with Microsoft Windows XP Professional 5.01.2600 Service Pack 3, v.3311. It is furnished with an Intel Pentium 4 processor, 2800 MHz speed, 512 MB RAM, and a 16 inch LG Monitor. A National Instrument data acquisition card, Model # PCI 6052E, is installed in the PC, which is connected to an SCXI Module signal conditioner. The SCXI Module is capable of handling up to 128 channels. It is connected with a terminal block, Model # SCXI 1303, which is capable of reading up to 96 signal inputs simultaneously from the various measurement sensors mentioned in previous sections.

3.3.4 Other hardware and monitoring devices

Additional hardware and monitoring devices support the data acquisition system. These devices are not involved in actual measurements and acquisition, but rather facilitate the data acquisition process. An Omega Digital Thermometer, Model # HH506R, is used in conjunction with a T-type thermocouple to monitor and maintain the temperature of glycol in the liquid tank. An Omega multi-function digital manometer, Model # HHP 2025, with a range of 0 to 200 kPa, measures the absolute pressure in the experimental facility prior to experiments to ensure a uniform experimental environment across all experimental runs. A TSI VelociCalc air velocity meter, Model # 8345, with a range of 0 to 30 m/s, is used in conjunction with a telescopic hot wire probe to monitor the velocity, flow rate, and temperature of the air flow through the test chamber. It helps to achieve and maintain the flow conditions as per the set test conditions.

An Omega dual thermocouple and RTD calibrator, Model # CL543, with an accuracy of ± 0.2 °C calibrated the RTDs and thermocouples used in the lab. An APC UPS, Model # BR1200LCD, was used to protect the sensitive equipment from power surges and fluctuations. It also provides up to 100 minutes of back up power to the PC and other equipment in case of power outage. An HP power supply, Model # 721A, with a range of 0 to 30V) was used to provide constant 24±2 DC volts to the devices/sensors in the lab

that require an excitation voltage to operate. It automatically limits peak current flow to the set nominal value, thereby preventing accidental current surges.

3.3.5 LabView version 8

LabVIEW (Laboratory Virtual Instrumentation Engineering Workbench) from National Instruments is a visual programming language platform and development environment. Its use includes, but is not limited to, data acquisition, instrument control, and industrial automation. It is compatible with wide variety of operating systems including Microsoft Windows, UNIX, Linux, and Mac OS X. Using intuitive graphical icons and wires that resemble flowcharts, LabVIEW was used to develop a sophisticated measurement system for the research facility. It offers integration with up to thousands of hardware devices, including the National Instrument data acquisition card, NI-PCI-6052E multi-function I/O Board, installed in the PC.

3.4 Experimental methods and operating conditions

In all of the experiments, the 50% ethylene glycol-water mixture was passed through the channels of the microchannel heat exchanger, and the air flow was oriented perpendicular to the liquid flow across the heat exchanger through the finned spaces. The flow arrangement is therefore of the crossflow type. The experiments investigated the fluid flow and heat transfer phenomenon associated with the heating of air. Air flows at six different temperatures lower than the glycol-water mixture temperature were blown across the heat exchanger. The liquid at a higher temperature flowed through the channels concurrently with the external air flow. The air approach temperature for all experiments therefore was lower than the microchannel slab/fin surface temperature; the slab/fin surface temperature was lower than the glycol-water flow temperature.

The wind tunnel built-in heat exchanger located upstream from the test heat exchanger was used to heat the air inside the wind tunnel. It was used to achieve, adjust, and maintain the free stream inlet temperature to the test chamber. A mixing chamber was

connected to the hot and cold city water supply at its inlet, and to the built-in heat exchanger at its outlet. The lowest and highest air temperatures were achieved using the 100% cold and 100% hot water supply, respectively. Intermediate air temperatures were achieved by passing a mixture at the appropriate proportion of cold and hot water through the built in heat exchanger for 30 minutes, while air was being circulated through the wind tunnel at the same time. It ensured stability of both air-flow velocity and temperature. Slight fluctuations of air-flow temperature in the experimental runs can be explained in terms of city supply water flow fluctuations.

The circulation heater mentioned previously was the source of heating for the glycol-water mixture passing through the heat exchanger. The glycol-water temperature was set at the desired level by using the Watlow temperature controller; it was maintained at that level through the use of PID control. The operating principle of this PID control was mentioned previously.

While the glycol-water flow temperature and flow velocities were maintained, the air-flow temperature and velocities generated a set of unique heat transfer and fluid flow data. These data were then used to observe the effect of flow and temperature variation on the heat transfer and fluid flow characteristics. The inlet and exit temperatures, flow velocities of glycol-water and air, and the outer surface temperatures were the major parameters to be monitored. The experimental operating conditions are tabulated below.

Table 3.1: Experimental operating conditions and controlling parameters

Controlling Parameters					
50% Glycol-Water Mixture			**Air**		
Inlet Temperature $\left(T_{g,i}\right)$ **[°C]**	**Mass Flow Rate** $\left(\dot{m}_g\right)$ **[kg/s]**	**Reynolds Number**	**Inlet Temperature** $\left(T_{a,i}\right)$ **[°C]**	**Velocity** $\left(V_a\right)$ **[m/s]**	**Reynolds Number**
74±1	0.0345 ± 0.005	200 ± 5	23	3, 5, 7, 9, and 11	854 – 3165
			28		825 – 3081
			33		813 – 3006
			38		790 – 2918
			43		768 – 2859
			46.5		752 – 2787

3.5 Data collection process

Six different air temperatures between 23 °C and 46.5 °C were considered for analysis. For each of these air temperatures, five different air velocities steps between 3m/s to 11 m/s, 750 < Re_a < 3165, were investigated against a constant flow rate and temperature of glycol-water mixture. The glycol-side mass flow rate was approximately 0.0345 ± 0.005 kg/s, which corresponds to a Reynolds number of 200 ± 5. The Reynolds number is based on the microchannel inner diameter.

All experiments commenced by starting the gear pump and adjusting its variable speed motor to circulate the glycol-water mixture through the channels of test heat exchanger. Then the Hydura piston pump was started and its needle valve was adjusted to circulate the air flow through the wind tunnel and across the test chamber and test heat exchanger. With glycol flowing through the test heat exchanger, the circulation heater is started and set to the operating condition. While the air flow is being stabilized, the water supply is also started. The circulation heater quickly heats the glycol-water mixture to the required

value. Air velocity and temperature are stabilized simultaneously over approximately 30 minutes.

After one of the six particular air-side operating temperatures was achieved and stabilized, five different air-side velocities were tested, one at a time, against the constant flow and temperature glycol-water mixture through the heat exchanger to collect the necessary data for the respective operating conditions. As such a total of unique 30 data sets for air heating were collected for analysis. Stability of the system, flow velocity and temperatures were well maintained both on the glycol side and on the air side, despite flow fluctuations in the city water supply to the built-in heat exchanger. To eliminate any adverse effects of these variations, three to four sets of each experimental run were conducted; the mean of only the most stable data sets were utilized in the analysis.

3.5.1 Calibration

Ideally the calibration process should be implemented under the same conditions applied during testing. Therefore prior to each experiment, the temperature readings of all monitoring thermocouples, as well as inlet and exit thermocouples and RTDs on both the air-side and glycol-side, were calibrated according to the thermocouple and RTD calibrator mentioned previously. These values were recorded and entered into the National Instrument LabView Data Acquisition System so that the experimental values would provide the most accurate representation.

3.5.2 Working fluid temperature measurements

Because the air and glycol-water mixture working fluids utilized in the heat exchanger operated along different cross sections, different methods and temperature measurement in differing configurations needed to be applied. The following sections illustrate these methods.

3.5.2.1 Air temperature measurements

As mentioned earlier, two planes of 9 and 25 thermocouples for both inlet and exit temperature measurement and acquisition were located along the wind tunnel duct just outside of the test chamber. After approximately 30 minutes of circulating air through the wind tunnel and test chamber, the flow and other parameters had stabilized to the required operating temperature, and data acquisition was begun. Thermocouples at the approach upstream and downstream of the test section measured the air temperature. Data were then recorded at a rate of 1 kHz for a duration of 180 to 200 seconds and averaged to get the average temperature at the particular location of the thermocouple. The average temperature of different thermocouples on this plane was then averaged to determine the plane temperature profile. A similar method was applied on the downstream plane. These temperature profiles both at the upstream and downstream were found to be fairly uniform; upstream temperatures were noted to be more uniform than the downstream values.

The temperatures recorded from the nine thermocouples upstream of the heat exchanger were then averaged as follows to represent a uniform temperature applicable at the center of the duct cross section:

$$T_{a,i} = \frac{1}{N} \sum_{J=1}^{N} \left[\frac{1}{n} \sum_{j=1}^{n} \left[T_{a,i} \right] \right], \text{ where } N = 9 \text{ and } n = \text{total samples at } 1\,kHz \text{ over } 180 - 200\,\text{sec}$$

(3.1)

Air inlet temperature distribution profile at the wind tunnel inlet cross section for the operating condition involving target air flow of $5\,m/s$ at $38\,°C$ is shown in Figure 3.14. The temperature distribution is found to be fairly uniform with temperature variations within $3\,°C$. Nine equally spaced thermocouples were used to acquire the temperature readings resulting in an average air inlet temperature of $38.27\,°C$. The figure shows large parts of the cross section with temperature $37 < T_{a,i} < 38.5\,°C$, which is expected if the uniform temperature distribution is to result in an average temperature of 38.27. Temperature at the outer edges of the cross section is slightly higher than the rest of the cross section. This deviation could also have been caused due to back flow or uneven

mixing at that region. The magnitude of this variation however, is within the typical range of uncertainty for thermocouples.
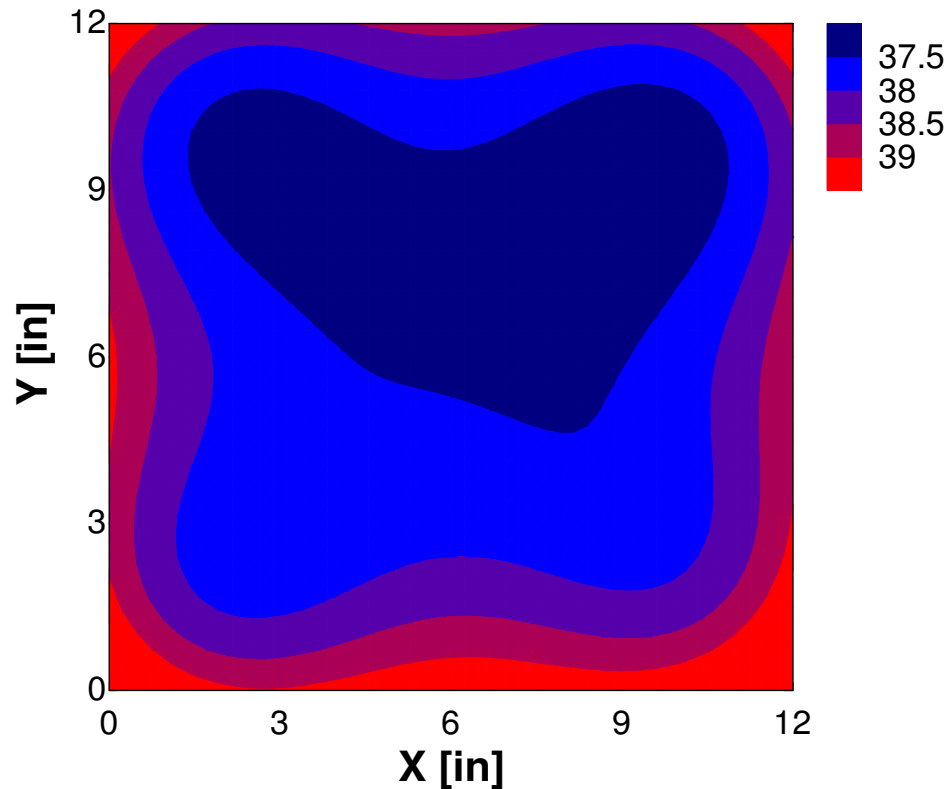
Figure 3.14: Temperature profile at the test chamber inlet cross section ($T_{a,i}$=38.27°C)

Figure 3.15 illustrates the outlet air temperature distribution at the wind tunnel outlet cross- section for the same operating condition as above. Unlike the inlet cross section temperature distribution, this cross section presents a wide range of temperatures and uneven temperature distribution. The temperature distribution was anticipated to be non-uniform at this cross section due to air flow through the cross flow heat exchanger. Therefore a total of 25 thermocouples were employed here, and their readings resulted in an average outlet temperature of $45.11 \, °C$. The hot liquid in the heat exchanger entered through left hand side (*i.e.* X=0), and exited on the right hand side (*i.e.* X=12) after passing through several bends and flowing side to side several times. The temperature distribution therefore illustrates a higher temperature on the left hand side as air flowing

through this region which was exposed to the highest surface temperature of the heat exchanger.
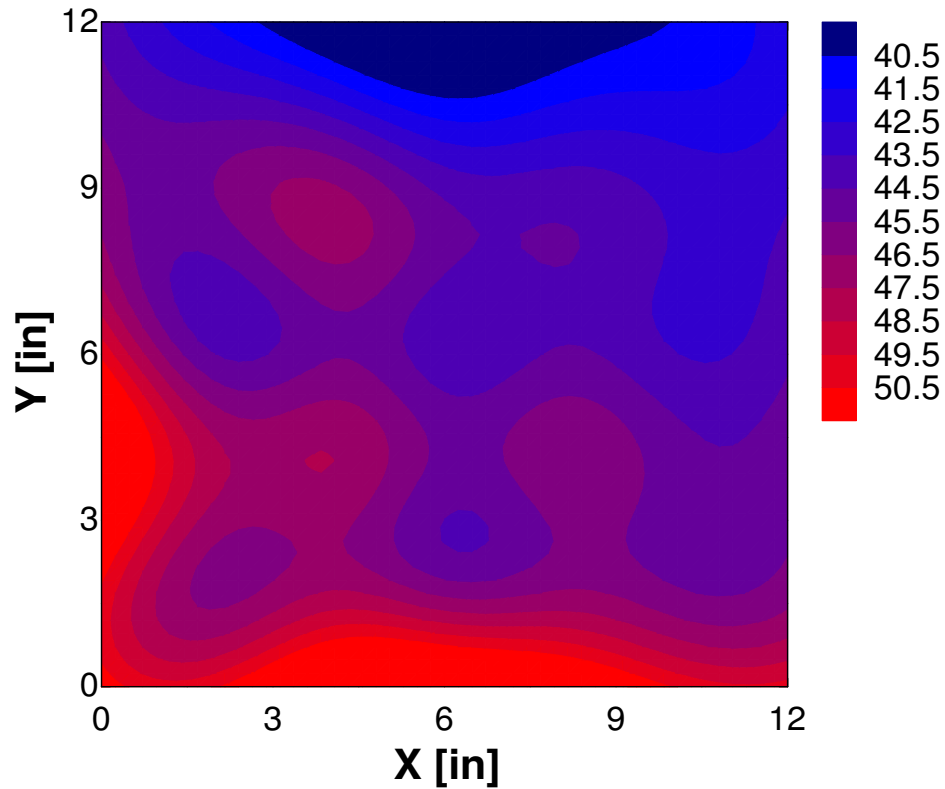
Figure 3.15: Temperature profile at the test chamber outlet cross section ($T_{a,o}$=45.11°C)

Data from the 25 thermocouples were recorded and averaged as follows to provide the best possible representation:

$$T_{a,o} = \frac{1}{N}\sum_{J=1}^{N}\left[\frac{1}{n}\sum_{j=1}^{n}\left[T_{a,o}\right]\right], \text{ where } N = 25 \text{ and } n = total\ samples\ at\ 1\,kHz\ over\ 180-200\,sec$$

(3.2)

The deviation from this mean downstream temperature to any thermocouple temperature reading on the downstream plane was found to be less than 5% in most cases. The average of the mean temperatures from these thermocouples for data analysis purpose was therefore deemed acceptable.

The mean temperature difference between the air inlet and outlet temperatures was evaluated as:

$$\Delta T_a = T_{a,i} - T_{a,o} \qquad (3.3)$$

The mean temperature difference between slab outer surface and air inlet was evaluated as follows:

$$\Delta T_{a-s} = T_{a,i} - T_{s,o} \qquad (3.4)$$

3.5.2.2 Glycol-water mixture temperature measurements

Unlike the air side flow, which takes place in a 305 x 305 mm duct, the glycol-water flow takes place in narrow tubes and microchannels. It is not therefore feasible to place thermocouples inside the tube as it would interfere with the flow and heat transfer. Hence RTDs were used because they did not adversely affect the flow and pressure drop characteristics. An RTD was placed at the pipe inlet to the heat exchanger to measure the inlet temperature; another was placed at the outlet pipe of the heat exchanger to measure the exit temperature. These RTDs were connected to the DAQ and their temperature readings were recorded at a frequency of 1 kHz for a duration of approximately 180 to 200 seconds.

The glycol-water mixture inlet temperature was determined by taking the average of all the samples collected during this period of time as follows:

$$T_{g,i} = \frac{1}{n} \sum_{j=1}^{n} \left[T_{g,i} \right], \text{ where } n = \text{total samples at } 1\, kHz \text{ over } 180 - 200\sec \qquad (3.5)$$

A similar method was applied for the temperature readings from the outlet RTD. Hence the glycol outlet temperature was obtained as follows:

$$T_{g,o} = \frac{1}{n} \sum_{j=1}^{n} \left[T_{g,o} \right], \text{ where } n = \text{total samples at } 1\, kHz \text{ over } 180 - 200\sec \qquad (3.6)$$

The mean temperature difference between glycol-water mixture inlet and outlet temperatures was evaluated as:

$$\Delta T_g = T_{g,i} - T_{g,o} \tag{3.7}$$

3.5.3 Surface temperature measurements

The microchannel slab surface temperature was measured by thermocouples strategically placed on the bend of the heat exchanger. Every bend of the microchannel slab had a total of 2 or 3 thermocouples located along the direction of the air flow to measure the effect of temperature both along the length and the width of the slab. Again each thermocouple measurement was recorded by the DAQ at 1 kHz for the duration of test, and the average of these samples was taken to be the average temperature reading of the particular thermocouple. The average outside surface temperature ($T_{s,o}$) for the whole length of a single serpentine slab is taken to be the average of all thermocouples on that slab. The whole heat exchanger is consisted of three such serpentine slabs.

Therefore the average surface temperature ($T_{s,o}$) is obtained through the following equation:

$$T_{s,o} = \frac{1}{N} \sum_{J=1}^{N} \left[T_{s,o} \right], \text{ where } N = \text{total thermocouples on the slab} \tag{3.8}$$

The variation of surface temperatures along the length of the serpentine slab was found to be fairly linear. This averaging method was therefore found acceptable.

3.5.4 Working fluid flow and pressure drop measurements

As mentioned earlier, because the two working fluids for this heat exchanger have different thermophysical properties and operate along different cross sections, they required different temperature measurement methods. The measurement of their flow characteristics and pressure drops also needed different methods and apparati. The

instrumentation section described the devices used for these purposes. The following sections illustrate the methods.

3.5.4.1 Air flow and pressure drop measurements

The air flow measurements included the air velocity and mass flow rate; the pressure drop was measured across the microchannel slab array. As mentioned in the instrumentation section, the flow measurement and pressure acquisition system was used in conjunction with pressure taps (see Figure 3.4) located on both sides of the test heat exchanger. Specifically they were located on the side walls of the test chamber, and at the middle between the top and bottom wall, to measure the pressure difference. This accurate pressure acquisition system provides the pressure readings in pascal (Pa).

3.5.4.2 Approach air velocity measurements (V_a)

The air approach velocity was measured in conjunction with a Pitot static tube. The dynamic pressure was acquired by the Pitot static tube, the static and total pressure ports of which were connected to the acquisition system. Pressure readings were used to calculate the difference in pressure (Δp_{pitot}) between the static and total pressure ports.

The mean air-side dynamic pressure difference for all of the experimental runs was evaluated as per the following equation:

$$\Delta p_{pitot} = \frac{1}{n} \sum_{j=1}^{n} \left[\Delta p_{pitot} \right]_{j}, \ where \ n = 4 \ to \ 5 \ repeats \tag{3.9}$$

Using the dynamic pressure difference, the mean inlet velocity is evaluated according to:

$$V_a = C' \sqrt{\frac{2\Delta p_{pitot}}{\rho_a}}, \tag{3.10}$$

Where, C' is a correction factor that depends on the Pitot tube construction, particularly the spacing of the holes. For current experiments it is taken as 1.

3.5.4.3 Air-side mass flow rate estimation

After determining approach air mean velocity at the test chamber inlet from the dynamic pressure, the mean velocity of air was used to estimate the air-side mass flow rate. The air-side mass flow rate across the heat exchanger was obtained using principle of conservation of mass and is expressed as follows:

$$\dot{m}_a = \rho_a A_{duct} V_a,$$
(3.11)

A_{duct} is the constant cross section area of test chamber.

3.5.4.4 Air-side pressure drop across tube array measurement ($\Delta p_{a,HX}$)

Pressure taps were drilled at various locations in the side walls of the test chamber as seen in Figure 3.4. These strategically placed pressure tap locations at the top, bottom and middle provide a wide variety of options for testing the pressure drop across the array at different locations and different distances from the test heat exchanger. The middle row of pressure taps used to measure the air-side pressure drop across the array. It is second farthest from the heat exchanger as shown in Figure 3.4.

3.5.4.5 Glycol-water mixture flow and pressure drop measurements

A different set of equipment and a different methodology were used to measure and record the glycol mass flow rate, velocity, and pressure drop across the microchannel heat exchanger. The following sections elaborate further on these measurements.

3.5.4.6 Glycol mass flow rate measurements ($\dot{m}_g$)

The mass flow rate of glycol through the microchannel heat exchanger was measured during each experimental run even though the flow conditions for glycol were not altered. The mass flow rate measurement was accomplished by collecting the glycol exiting from the heat exchanger outlet. The duration over which glycol was collected was also recorded.

The mass flow rate was calculated by dividing mass collected by time duration as follows:

$$\dot{m}_g = \frac{1}{n} \sum_{j=1}^{n} \left[\frac{\dot{m}_g}{t} \right]_j, \; where \; n = 4 \; to \; 5 \; repeats \tag{3.12}$$

3.5.4.7 Glycol velocity estimation (V_g)

Using the conservation of mass principle and the mass flow rate obtained from the previous section, the glycol flow velocity was calculated as follows:

$$V_g = \frac{\dot{m}_g}{\rho_g A_{c,i}}, \tag{3.13}$$

$A_{c,i}$ is the inner cross section area of the microchannels.

3.5.4.8 Glycol pressure drop measurements (Δp_g)

The pressure drop measurements for glycol required a device that would not adversely affect the flow of glycol. Therefore a Pressure Transducer (PTD) was placed at the pipe inlet to the heat exchanger to measure the inlet pressure in pascals (Pa); another was placed at the outlet pipe of the heat exchanger to measure the exit pressure of same unit.

These PTDs were connected to the DAQ and their pressure readings were recorded at a frequency of 1 kHz for duration of the experiment.

The glycol-water mixture inlet pressure was determined by taking the average of all the samples collected during the experiment as follows:

$$p_{g,i} = \frac{1}{n} \sum_{j=1}^{n} \left[p_{g,i} \right], \text{ where } n = \text{total samples at } 1\,kHz \text{ over } 180 - 200\,\text{sec} \qquad (3.14)$$

A similar method was also applied for the temperature readings from the outlet RTD. The glycol outlet pressure was obtained as follows:

$$p_{g,o} = \frac{1}{n} \sum_{j=1}^{n} \left[p_{g,o} \right], \text{ where } n = \text{total samples at } 1\,kHz \text{ over } 180 - 200\,\text{sec} \qquad (3.15)$$

The pressure difference between the inlet and outlet pressures across the heat exchanger equals the pressure drop on the glycol side and is expressed as follows:

$$\Delta p_g = p_{g,i} - p_{g,o} \qquad (3.16)$$

3.6 Uncertainty of measurement for the apparatus

The overall experimental setup is composed of various components necessary to generate meaningful results and analysis. These components include but not limited to the list shown in Table 3.2

Table 3.2: Apparati contributing to the uncertainty

Pressure Gages	Liquid Tank
Air Compressor	Pump (In-line)
Temperature Gage	Heater (In-line)
Closed Loop Wind Tunnel	Flexible Hose
Micro Channel Heat Exchanger	Digital Flow Meter
Proportional Pressure Relief Valve	Impeller Flow Meter
Resistance Temperature Detector (RTDs)	Data Acquisition System
Closed Loop Pipe Network for water circulation	Pressure Transducers (PTDs)

This research endeavor attempted to formulate and evaluate where possible the uncertainties inherent in the various instruments and measurement systems. These uncertainties would propagate through the calculations along with other uncertainties. These other uncertainties pertaining to the fluid properties, the micro channel geometrical characteristics, and the flow rate measurements. By obtaining meaningful data sets under varying geometrical characteristics, flow rate measurements, and fluid properties, the calculation and interpretation of uncertainties in many heat transfer parameters will be performed. Measurement errors, bias and precision errors, design stage uncertainty analysis, error propagation, and multiple measurement uncertainty analysis can be elaborated.

Chapter 4: Theoretical Considerations and Data Reduction

The methodology for thermal and hydraulic performance analysis of current heat exchanger is presented in this chapter. The fundamental concepts of fluid flow and heat transfer are illustrated as part of this data reduction methodology.

4.1 Evaluation of thermophysical properties of the glycol-water and air

The thermophysical properties of air include the density, viscosity, thermal conductivity, specific heat, Prandtl number, enthalpy, thermal diffusivity, and thermal expansion coefficient. They were evaluated at the bulk temperatures for the 50% glycol-water mixture and for the air.

The bulk temperature for the air side was evaluated as the arithmetic average of the air inlet and outlet temperatures.

$$T_{a,b} = \frac{T_{a,i} + T_{a,o}}{2} \tag{4.1}$$

The bulk temperature for the 50% glycol-water mixture was evaluated as the arithmetic average of the glycol-water inlet and outlet temperatures.

$$T_{g,b} = \frac{T_{g,i} + T_{g,o}}{2} \tag{4.2}$$

4.2 Key assumptions

The following assumptions were considered for the reduction of the current experimental data.

1. Air flow across the heat exchanger is in steady state.
2. Air condensation on the heat exchanger surface is insignificant.
3. Radiative heat transfer between the heat exchanger and the air is negligible.

4. Radiative heat transfer between the test chamber and the room is negligible.

5. Conductive heat transfer between the heat exchanger and the room is negligible.

6. The changes in fluid temperature and velocity at heat exchanger inlet and outlet are assumed negligible for significantly altering the operating condition.

7. The working fluid streams experienced little or no change in velocities and elevations. Therefore kinetic and potential energy changes are negligible.

8. Axial heat conduction along the slab (i.e. along the direction of glycol flow), is usually insignificant and can be considered negligible.

4.3 Dimensionless fluid flow and heat transfer parameters

A dimensionless number is one that describes a particular physical system, and is considered a pure number without any physical units. Such numbers are not affected by any change in units of measurement. A set of dimensionless numbers are used extensively in the study of fluid mechanics and heat transfer analysis because they can relate and generalize relationships between different parameters. Heat transfer and fluid flow conditions can be related in terms of non-dimensional parameters such as the Nusselt number, Nu, or Stanton number, St, Reynolds number, Re, and Prandtl number, Pr. A list of dimensionless numbers used in present analysis, along with a brief explanation of each is presented below.

4.3.1 Reynolds number

Osborn Reynolds (1842-1912), was British Scientist famous for demonstrating that a combination of parameters can be successfully characterize fluid flow regimes, namely laminar and turbulent. This combination is a dimensionless number and is known as the Reynolds number, Re. It is also defined as the ratio of inertial forces to viscous forces in a particular flow regime, and is illustrated as follows:

$$\mathrm{Re} = \frac{\text{Inertia force}}{\text{Viscous force}} = \frac{\rho V Z}{\mu} \tag{4.3}$$

where, $\rho =$ fluid density, $V =$ velocity, $\mu =$ viscosity, and $Z =$ characteristic length.

When viscous forces dominate inertial forces, the result is a smaller Reynolds number and smooth flow. Such a flow regime is called laminar flow. When inertial forces dominate viscous forces, the result is a higher Reynolds number and disordered motion within the flow. It is known as turbulent flow.

4.3.2 Prandtl number

The Prandtl number, Pr, is named after Ludwig Prandtl (1875-1953) of Germany. He was famous for introducing the concept of boundary layer. The Prandtl number is the ratio of momentum diffusivity to thermal diffusivity for a fluid.

$$Pr = \frac{\text{Momentum diffusivity}}{\text{Thermal diffusivity}} = \frac{\mu c_p}{k} \tag{4.4}$$

where, $c_p =$ fluid specific heat, and $k =$ thermal conductivity.

The Prandtl number is also a measure of the relative development of the velocity boundary to the thermal boundary. The flow velocity of a fluid has significant bearing on the temperature profile. The temperature profile in turn significantly influences the rate of heat conduction from a surface. For fluids such as air, where $Pr < 1$, the thermal boundary layer is thicker relative to velocity boundary layer; hence heat is quickly dissipated from the fluid. For $Pr \gg 1$, heat dissipates very slowly.

4.3.3 Nusselt number

German engineer Wilhelm Nusselt (1882-1957), was famous for developing a dimensional analysis of heat transfer without prior knowledge of Buckingham π theorem. The Nusselt number, Nu, is named after him. It is a dimensionless representation of the heat transfer coefficient, h, and is the ratio of convective to conductive heat transfer for any particular fluid.

$$Nu = \frac{\text{Convection heat transfer rate}}{\text{Conduction heat transfer rate}} = \frac{hZ}{k} \tag{4.5}$$

The Nusselt number is greater where the convective heat transfer dominates conductive heat transfer. Such conditions are desirable, and are characterized by enhanced heat transfer within the fluid; heat is transferred by convection through the layers of a fluid in motion as opposed to a fluid at rest.

4.3.4 Stanton number

The Stanton number, St, is named after a British engineer, Sir Thomas Edward Stanton (1865-1931). This dimensionless number is the ratio of heat convection to the enthalpy rate change of a fluid, whose temperature is approaching that of the adjacent solid surface. The Stanton number is especially significant where the axial heat conduction of the fluid is negligible. It is inversely related to the Reynolds number, similar to the pressure drop and the friction factor. This dimensionless number also relates three very important parameters for heat transfer and fluid flow, namely the Nusselt number, Reynolds number, and Prandtl number for any flow condition and geometry.

$$St = \frac{\text{Heat convection}}{\text{Enthalpy rate change}} = \frac{h}{Gc_p} = \frac{h}{\rho V c_p} = \frac{Nu}{\text{Re Pr}} \qquad (4.6)$$

where, $G = $ mass flux.

4.3.5 Péclet number

The Péclet number, Pe, is named after French physicist Jean Claude Eugène Péclet (1793-1857). It is of significant importance in the study of transport phenomena in fluid flows, and is the ratio of the rates of advection and diffusion for a physical quantity by the flow. The Péclet number in the context of diffusion of heat is defined as the product of the Reynolds number and the Prandtl number. It is given as follows:

$$Pe = \frac{\text{Rate of advection}}{\text{Rate of diffusion}} = \frac{ZV}{\alpha} = \frac{ZV}{\left(\dfrac{k}{\rho c_p}\right)} = \text{Re Pr} \qquad (4.7)$$

where, $\alpha = $ thermal diffusivity.

4.3.6 Colburn factor for convective heat transfer

The Colburn factor, j, is essentially a modified Stanton number. It takes into account moderate variations in the fluid Prandtl number.

$$j = St \, Pr^{2/3} \tag{4.8}$$

4.4 Data reduction objectives

The main objective of the current study is to investigate the air side heat transfer and flow characteristics of a multi-pass, multi-port, serpentine microchannel heat exchanger. Hence the purpose of data reduction is to evaluate the air-side factors that pertain to the core of the heat exchanger. These factors are: the overall thermal resistance (R_{total}), effectiveness (ε), NTU, Nusselt number (Nu_a), Colburn factor (j_a), Reynolds number (Re_a) pressure drop (Δp_a), friction factor (f_a).

One assumption made for data analysis is to treat the ethylene glycol - water mixture as an incompressible Newtonian fluid. As such, the liquid side properties are independent of pressure and can be viewed as functions of temperature only. The test-liquid is assumed to be uniformly distributed through all the channels because the manifold diameter is ten times larger than a single channel. The flow of air through the finned spaces over the slab is also assumed to be uniform with no blockage, turbulence, fluctuations, or back pressure. The glycol-water mixture and air temperatures in the core section of heat exchanger are assumed to be the average of their respective inlet and exit temperatures. The thermodynamic properties of the air and the test-liquid in the heat exchanger core section are therefore evaluated based on these average temperatures. The fundamental variables for the liquid and the air side were measured at an optimum steady state for all operating conditions.

4.5 Data reduction

The mass flow rate of both the 50% ethylene glycol-water mixture and the air through the heat exchanger was calculated using the following equations,

$$\dot{m}_{g,HX} = \dot{\forall}_g \, \rho_g \tag{4.9}$$

$$\dot{m}_a = \dot{m}_{a,HX} = \rho_a V_a A_{Min,a} \tag{4.10}$$

Here V_a is calculated from equation (4.11), which was derived from equation (3.10) for $C'=1$,

$$V_a = \sqrt{\frac{2\Delta p_{Dynamic}}{\rho_a}} \tag{4.11}$$

Since each of the three inlet manifolds supply liquid to 68 channels, the total number of independent channels carrying fluid is 204. The glycol-water mixture flow velocity and Reynolds number were evaluated using the principle of mass conservation ($\dot{m} = \rho V A$) as shown in the following equations.

$$\left. \begin{aligned} \dot{m}\Big|_{MC} = \dot{m}_g = \rho A V\big|_{MC} = \frac{\dot{m}_{g,HX}}{3(68)}\bigg|_{MC} \\[2ex] \Rightarrow V_{MC} = \frac{\dot{m}_{g,HX}}{204\rho A_{c,MC}} = \frac{4\dot{m}_{g,HX}}{204\pi\rho D_{MC}^2} = \frac{\dot{m}_{g,HX}}{51\pi\rho D_{MC}^2} \end{aligned} \right\} \tag{4.12}$$

$$\mathrm{Re}_g = \mathrm{Re}\big|_{MC} = \frac{\rho D V}{\mu}\bigg|_{MC} = \left(\frac{\rho_g D}{\mu_g}\right)_{MC}\left(\frac{\dot{m}_{g,HX}}{51\pi\rho_g D_{MC}^2}\right) = \frac{\dot{m}_{g,HX}}{51\pi\mu_g D_{MC}} \tag{4.13}$$

The air side mass velocity into the heat exchanger core is calculated based on the minimum free flow area through the fin and slab arrays.

$$G_a = \frac{\dot{m}_a}{A_{Min,a}} \tag{4.14}$$

The air side Reynolds number is therefore evaluated using the Reynolds number definition in conjunction with the core mass velocity.

$$\text{Re}_a = \left(\frac{\rho V D}{\mu} \right)_a = \frac{\frac{\rho V A_{Min,a}}{A_{Min,a}} D_{Hyd,a,HX}}{\mu_a} = \frac{\frac{\dot{m}_a}{A_{Min,a}} D_{Hyd,a,HX}}{\mu_a} = \frac{G_a D_{Hyd,a,HX}}{\mu_a} \qquad (4.15)$$

The heat transfer rates of liquid and air due to forced convection are evaluated by the following equations respectively.

$$\dot{Q}_g = \dot{m}_g \, c_{p,g} \left(T_{g,i} - T_{g,o} \right) \qquad (4.16)$$

$$\dot{Q}_a = \dot{m}_a \, c_{p,a} \left(T_{a,o} - T_{a,i} \right) \qquad (4.17)$$

The heat transfer rate for both the liquid side and the air side fell within ±3% of each other. Therefore, an arithmetic average of the air-side and waterside heat transfer rates was defined as the overall heat transfer rate as per Rugh *et al.* (1992).

$$\dot{Q} = \frac{\dot{Q}_g + \dot{Q}_a}{2} \qquad (4.18)$$

In theory, the heat released by liquid and absorbed by air should be the same. In reality, however, it is never achieved due to such extraneous factors as heat leakages, system response lag/errors, and experimental errors. The difference between the heat absorbed by air and released by the liquid can be expressed as a percent and is defined as the heat balance. The following two equations illustrate the heat balance calculation method with respect to glycol heat transfer rate ($\dot{Q}_g$), and glycol-air average heat transfer rate ($\dot{Q}$) respectively.

$$HB_g = \left[\frac{\dot{Q}_g - \dot{Q}_a}{\dot{Q}_g} \right] \times 100 \qquad (4.19)$$

$$HB_{avg} = \left[\frac{\dot{Q}_g - \dot{Q}_a}{\dot{Q}} \right] \times 100 \qquad (4.20)$$

The average heat balance percentages are found in the present study to be well within the acceptable margin ($\pm15\%$) recommended by ASME PTC 30-1991.

The overall thermal resistance, R_{total}, was calculated using the overall heat transfer rate.

$$R_{total} = R_g + R_{wall} + R_a = \frac{1}{UA} = \frac{F\Delta T_{LM}}{\dot{Q}} \tag{4.21}$$

The correction factor, F, pertaining to crossflow heat exchangers was taken from Bowman *et al.* (1940). Based on the experimental operating conditions and temperature loadings, F is found to be constant at 0.98. The log mean temperature difference (ΔT_{LM}) for counter flow used in conjunction with F is determined based on the following equation.

$$\Delta T_{LM} = \frac{\Delta T_1 - \Delta T_2}{\ln\left(\dfrac{\Delta T_1}{\Delta T_2}\right)} \tag{4.22}$$

In this equation,

$$\Delta T_1 = T_{g,i} - T_{a,o} \tag{4.23}$$

$$\Delta T_2 = T_{g,o} - T_{a,i} \tag{4.24}$$

The overall thermal resistance (R_{total}) for the current test heat exchanger has three components: air side (R_a), wall side (R_{wall}), and glycol-water side (R_g).

$$R_{total} = \frac{1}{UA} = \frac{F\Delta T_{LM}}{\dot{Q}} = R_a + R_{wall} + R_g = \frac{1}{(\eta hA)_a} + \frac{\ln\left(\dfrac{D_{o,MC}}{D_{i,MC}}\right)}{2\pi k_{Al}l} + \frac{1}{(hA)_g} \tag{4.25}$$

The overall surface efficiency is evaluated to properly represent the air side fin arrays. It is expressed by the following equation.

$$\eta_a = 1 - \frac{A_{HT,Fin,HX}}{A_{HT,a,HX}}\left(1 - \eta_{Fin}\right) \tag{4.26}$$

In this equation,

$$A_{HT,a,HX} = A_{HT,Fin,HX} + A_{NF,Slab,HX} \tag{4.27}$$

Shah and Sekulic (2003) defined the fin efficiency for wavy fins of uniform cross-section. This definition is found suitable for fins in current heat exchanger and is therefore adopted and expressed in the following equation.

$$\eta_{Fin} = \frac{\tanh(ML)}{ML} \tag{4.28}$$

In this equation,

$$M = \sqrt{\frac{2h_a}{k_{Fin}t_{Fin}}} \tag{4.29}$$

$$L = \frac{H_{Fin}}{2} - t_{Fin} \tag{4.30}$$

The heat transfer coefficient is the amount of heat transferred through a unit area of a medium over a unit time, for a unit temperature difference between the medium boundaries. Accurate measurement and surface temperature readings are required in order to calculate the respective fluid side heat transfer coefficients. The current heat exchanger geometry poses a considerable challenge for properly measuring the surface temperatures for both the finned surfaces as well as the microchannel slab located between arrays of fins.

The heat transfer coefficient for the glycol-water mixture is therefore primarily evaluated by first evaluating the Nusselt number, using the Gnielinski correlation for thermally developing and hydrodynamically developed flow in smooth circular tube as referenced in Kakaç and Liu (2002).

$$Nu_g = \sqrt[3]{3.66^3 + 1.61^3 \left(\frac{Pe_g D_{MC}}{L_{HT,MC,HX}} \right)} \tag{4.31}$$

$$Pe_g = \mathrm{Re}_g \, \mathrm{Pr}_g \tag{4.32}$$

$$\mathrm{Pr}_g = \frac{\mu_g c_{p,g}}{k_g} \tag{4.33}$$

Therefore the heat transfer coefficient for the glycol-water mixture is obtained from the definition of Nusselt number.

$$h_g = \frac{Nu_g k_g}{D_{MC}} \tag{4.34}$$

The air side heat transfer coefficient is obtained through an iterative process, utilizing expressions for the overall thermal resistance, and the fin and surface efficiencies.

1. The thermal resistances are calculated.

$$R_{total} = \frac{1}{UA} = \frac{F \Delta T_{LM}}{\dot{Q}} \tag{4.35}$$

$$R_{wall} = \frac{\ln\left(\dfrac{D_{o,MC}}{D_{i,MC}}\right)}{2\pi k_{Aluminium} L_{HT,MC,HX}} \tag{4.36}$$

$$R_g = \frac{1}{h_g A_{HT,in,MC,HX}} \tag{4.37}$$

2. Set: $\eta_a = 1$, and enter it into Eq. (4.38), which is obtained by rearranging Eq.(4.25), to solve for h_a:

$$h_a = \frac{1}{\eta_a A_{HT,a,HX}\left[R_{total} - R_{wall} - R_g\right]} \tag{4.38}$$

3. Enter h_a obtained from Eq. (4.38) into Eq.(4.29) to solve for M

4. Enter M obtained from Eq. (4.29) into Eq. (4.28) to solve for η_{Fin}

5. Enter η_{Fin} obtained from Eq.(4.28) into Eq.(4.26) to solve for η_a

6. Enter η_a obtained from Eq. (4.26) into Eq. (4.38) to solve for h_a

7. Loop through steps $2 - 6$ with new η_a, h_a, and η_{Fin}, for 3 ~ 4 trials to obtain final values for η_{Fin}, η_a, and h_a.

Measurement of the surface temperature in the present study was accomplished using 56 strategically-placed thermocouples on un-finned exposed surfaces, around the serpentine

bends, and at the heat exchanger inlet and exit tube surfaces just before and after the test section boundary. The average of the measured surface temperatures for each of the individual operating condition was used to compute a secondary set of heat transfer coefficients for both the glycol-water mixture and for the air for validation purposes only. It is shown as follows.

$$h_g = \frac{\dot{Q}_g}{A_{HT,in,MC,HX}\left(T_g - T_s\right)} \tag{4.39}$$

$$h_a = \frac{\dot{Q}_a}{\eta_a A_{HT,a,HX}\left(T_s - T_a\right)} \tag{4.40}$$

The results obtained using this secondary approach were compared to the heat transfer coefficient primary evaluation method outlined above. The two results were found to agree with each other within ±5%.

The heat exchanger effectiveness is the ratio of the actual heat transfer rate to the theoretical heat transfer rate of a heat exchanger with infinite heat transfer area. For the microchannel heat exchanger it is evaluated based on the following equation.

$$\varepsilon = \frac{\dot{Q}}{\dot{Q}_{max}} = \frac{\dot{Q}}{\left(\dot{m}c_p\right)_{min} \Delta T_{max}} = \frac{\dot{Q}}{\left(\dot{m}c_p\right)_g \left(T_{g,i} - T_{a,i}\right)} \tag{4.41}$$

The Number of Transfer Units (*NTU*), which is a measure of heat exchanger performance, was computed by using the following expression.

$$NTU = \frac{UA}{C_{min}} \tag{4.42}$$

In this equation,

$$UA = \frac{1}{R_{total}} \tag{4.43}$$

$$C_{min} = \dot{m}_{g,HX}\, c_{p,g} \tag{4.44}$$

The Stanton number, the dimensionless heat transfer characteristic that measures the ratio of heat transfer into a fluid to the thermal capacity of the fluid was evaluated for air side of the present heat exchanger.

$$St_a = \frac{h_a}{G_a c_{p,a}} \tag{4.45}$$

The Colburn factor for the air side (j_a) which modifies the Stanton number to consider moderate variations in the fluid Prandtl number, is defined as follows.

$$j_a = St_a \, Pr_a^{2/3} \tag{4.46}$$

The Reynolds number is the ratio of the inertia forces to the viscous forces of a fluid. For air flow through the heat exchanger finned areas, it is determined from the following relationship.

$$Re_a = \left(\frac{\rho V D}{\mu}\right)_a = \frac{G_a D_{Hyd,a,HX}}{\mu_a} \tag{4.47}$$

Wang *et al.* (2000) recommended a method to compute the fanning friction factor at the core of heat exchanger; it does not require calculation of the entrance and exit losses. This relationship is based on the pressure drop equation proposed by Kays and London (1984). It takes into account the area contraction ratio, as well as the fluid inlet, exit, and average densities. This relation is expressed as follows.

$$f_a = \left(\frac{A_{Min,a}}{A_{HT,a,HX}}\right)\left(\frac{\rho_{a,b}}{\rho_{a,i}}\right)\left[\frac{2\Delta p_{a,HX}\rho_{a,i}}{G_a^2} - \left(1+\sigma_a^2\right)\left(\frac{\rho_{a,i}}{\rho_{a,o}}-1\right)\right] \tag{4.48}$$

where,

$$\sigma_a = \frac{A_{Min,a}}{A_{Frontal,HX}} \tag{4.49}$$

Chapter 5: Results and Discussion

The primary objectives of the present study were to obtain the air-side heat transfer (*i.e.* $\dot{Q}$, Nu_a, j_a), fluid flow (*i.e.* $\Delta p_{a,HX}$, f_a), and heat exchanger performance (ε, NTU, UA, η_{Fin}) characteristics, as well as develop general correlations to compare with previously published works. To accomplish these objectives, the experiments in the present study utilized heating of air under varying operating conditions.

The air was subjected to a wide range of flow and temperature conditions while the temperature and flow conditions on the glycol-water side was maintained at a constant level. For the air heating process, the hot inlet glycol-water entered the microchannels at $T_{g,i} = 74 \pm 1°C$; and the cold air-side flow was varied at 23, 28, 33, 38, 43, and 46.5 $\pm 0.2°C$. The glycol mass flow rate was $0.0345 \pm 0.005 kg/s$, which translates to a Reynolds number of $\text{Re}_g = 200 \pm 5$. The air-side flow rate was varied such that the nominal flow velocity condition upstream of the heat exchanger was 3, 5, 7, 9, or 11 m/s at each of the temperature levels. These combinations translate to a nominal Reynolds number range of 752 to 3165 for Re_a.

In this chapter, the effect of several different parameters on the heat transfer rate, Nusselt number, NTU and effectiveness, Colburn j factor, and friction factor have been discussed. The results and observations of these sets of experiments have been reviewed and are accepted for publication.

The following sections discuss the effect of several different parameters on heat transfer and fluid flow characteristics. These parameters include the effect of Reynolds number on heat transfer rate, Nusselt number, and pressure drop; the effect of temperature on heat transfer and Nusselt number; the effect of temperature and Reynolds number on NTU and effectiveness.

5.1 Heat transfer characteristics

In this section the air side heat transfer characteristics of the microchannel heat exchanger will be discussed. General correlations for different inlet temperature levels will also be developed. The parameters closely scrutinized in this section include the heat balance between the two fluids, heat transfer rate, dimensionless temperature, Nusselt number and Colburn j factor.

5.1.1 Heat balance (HB) in the experiment

Figure 5.1 shows the heat balance between glycol and air, calculated with respect to $\dot{Q}_g$ and $\dot{Q}$.
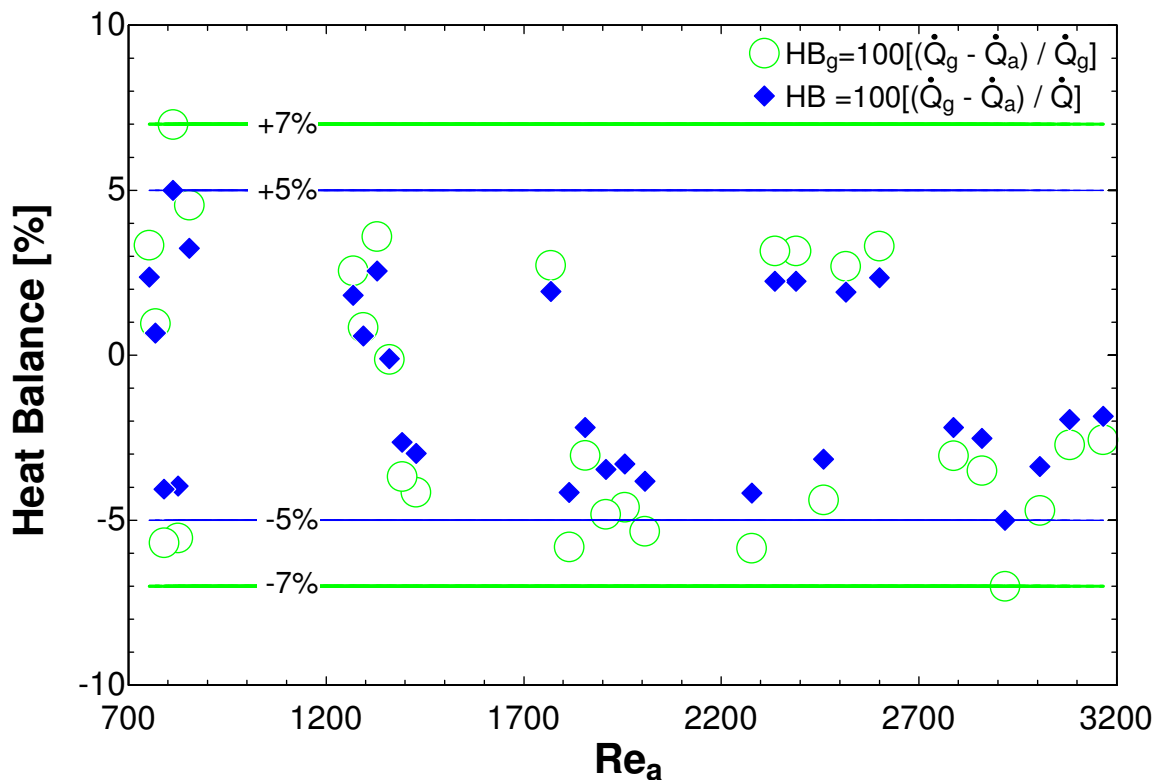
Figure 5.1: The effect of air side Reynolds number on heat balance between ethylene glycol-water mixture and air in the present study

The $\dot{Q}_a$ is found to vary within ±5% from $\dot{Q}$, and ±7% from $\dot{Q}_g$. Both levels of variation for the entire set of collected data and operating conditions are within the acceptable level of ±15% as set by ASME PTC 30-1991. Such level of accuracy can be attributed to the significant amount of insulation accompanying the piping and flow network, test chamber, and sensors. Since the liquid side temperature is measured using highly accurate RTDs, the heat transfer rates calculated for glycol-water mixture regarded as having greater credibility. As the heat balance between glycol-water and air lies well within the acceptable range, the collected data is therefore found reliable for further heat transfer analysis.

5.1.2 Effect of Reynolds number on heat transfer rate

The heat transfer rate ($\dot{Q}$) is evaluated in Chapter 4 is plotted against Re_a in Figure 5.2.
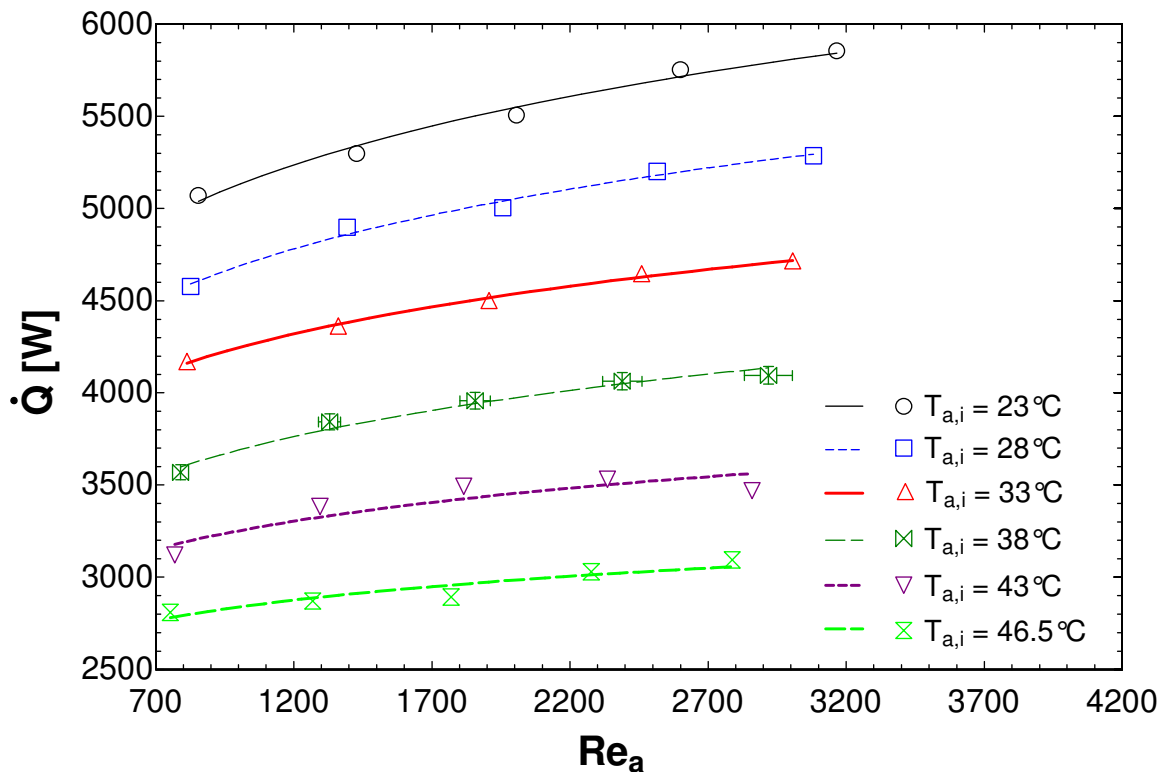
Figure 5.2: The effect of air side Reynolds number on average heat transfer rate

The $\dot{Q}$ increases with increasing in Re_a with power law relationship. The curves in this plot are best described by equations of the form $\dot{Q} = x \, \mathrm{Re}_a^y \quad [0 < y < 1 \text{ and } x > 0]$, which suggest a decreasing slope with increase in Re_a, and is evident in Figure 5.2. This increase in $\dot{Q}$ is attributed to the increase in convective heat transfer with Reynolds number. The highest heat transfer for a given $T_{a,i}$ is found for the highest Re_a. Higher heat transfer rates ($\dot{Q}$) are found at lower air inlet temperature for a particular Reynolds number (Re_a) due to larger inlet temperature differential between the two fluids. The average heat transfer rate is a function of both the air and glycol-water solution heat transfer rates. The curves for average heat transfer rate therefore closely reflect the state of air side heat transfer rate. The diminishing positive slope for $\dot{Q}$ can be explained by the same phenomenon occurring on the air side. The relative increase in air side heat transfer rate as a function of Reynolds number diminishes due to formation and development of thicker boundary layer at higher Re_a. Thick boundary layers inhibit heat transfer.

5.1.3 Effect of Reynolds number on dimensionless temperature

The effect of Reynolds number (Re_a) on non-dimensional temperature ($\Delta T_a / T_{a,i}$) is shown in the Figure 5.3. The dimensionless temperature decreases with increasing frontal air velocity *i.e.* Re_a in the power law relationship with negative exponent. The value of non-dimensional temperature is higher at lower temperature for a particular Reynolds number due to higher temperature difference at lower air inlet temperature. The data can be regarded as credible when the data points can be closely approximated with their curve fit.
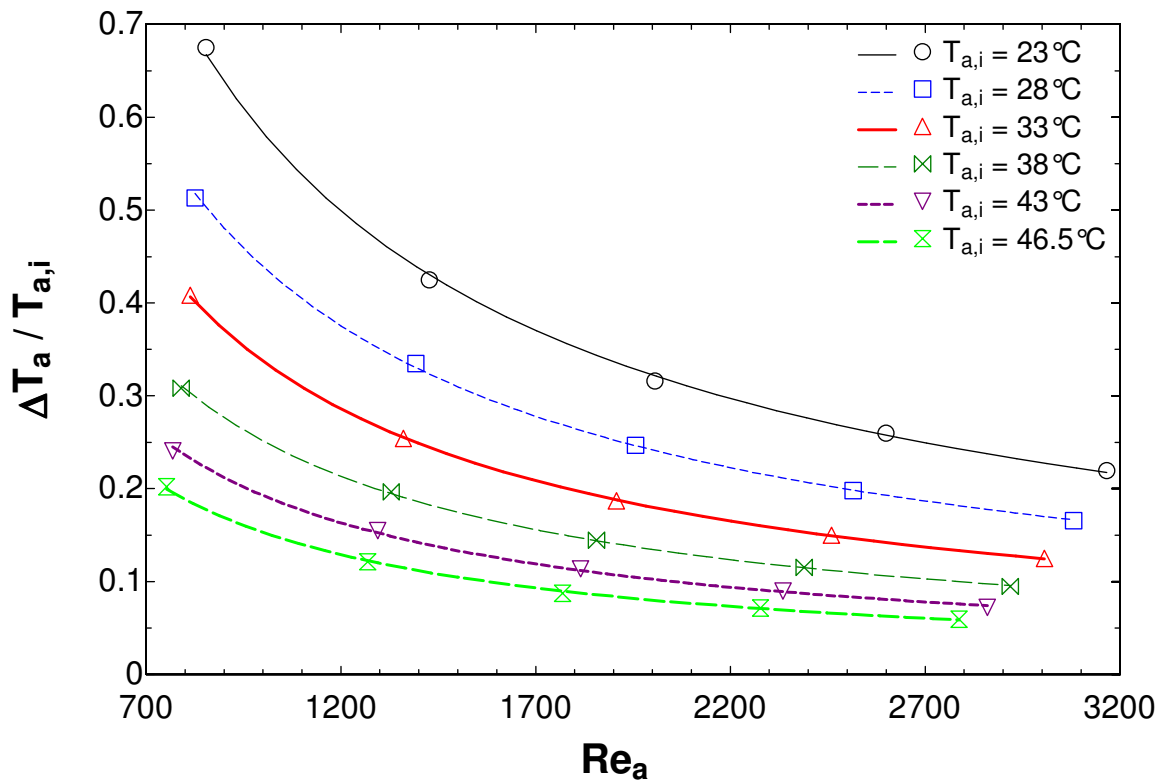
Figure 5.3: The effect of air side Reynolds number on its dimensionless temperature

5.1.4 Effect of Reynolds number on Nusselt number

Air side Nusselt number (Nu_a) is computed for all temperature levels at different frontal air velocities. The effect of air side Reynolds number (Re_a) on Nusselt number (Nu_a) is shown in Figure 5.4. As expected, the Nusselt number (Nu_a) increase non-linearly with increase of Re_a since convective heat transfer increases with increasing Reynolds number. The slopes of the curves in this figure also demonstrate a decreasing slope with increase in Re_a, which is characteristic of power law of $Nu_a = x\,Re_a^y$ $\left[0 < y < 1 \text{ and } x > 0\right]$, form. The Nusselt number (Nu_a) for a given air-side Reynolds number increases as the inlet air temperature ($T_{a,i}$) rises. A general Nu_a-Re_a correlation capable of predicting Nu_a within ±10% has been obtained in the present study by combining all different temperatures as

$$Nu_a = 0.845\,Re_a^{0.2736} \tag{5.1}$$

As the air inlet temperature is increased from one level to another, the bulk temperature of air also increased. The viscosity of any gas increases with increase in its bulk temperature. Therefore as the bulk temperature of air is increased its viscosity also increased. This in turn reduces the Re_a for a given velocity as the air inlet temperature is increased. This fact in conjunction with all other experimental conditions being kept constant would yield the same Nu_a at lower Re_a for the higher $T_{a,i}$ levels. The same principle applies to several other parameters such as ε, NTU, UA, and $\Delta p_{a,HX}$.
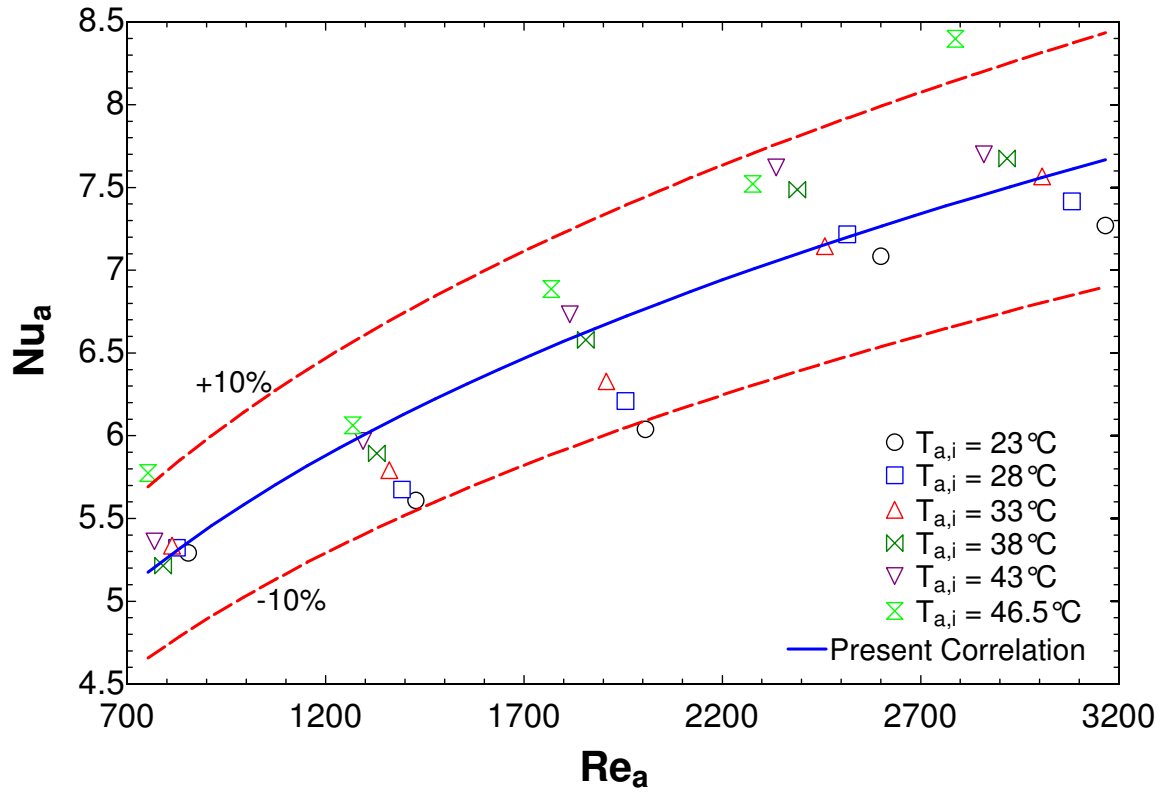
Figure 5.4: The effect of air side Reynolds number on dimensionless heat transfer coefficient Nusselt number

5.1.5 Effect of Reynolds number on Colburn *j* factor

Air side Colburn factor (j_a) are computed for all temperature levels at different frontal air velocities. The effect of air side Reynolds number (Re_a) on Colburn factor (j_a) is illustrated in Figure 5.5. The figure indicates that the Colburn factor (j_a) decreases with increasing Reynolds number (Re_a) and its value is higher at higher air inlet temperatures ($T_{a,i}$) for a given Re_a. The j_a is found to decrease with the power-law relationship with an increase in Re_a at a given $T_{a,i}$, and is modeled with $j_a = x\,\mathrm{Re}_a^y \;\left[y < 0 \text{ and } x > 0 \right]$. A general $j_a - \mathrm{Re}_a$ correlation capable of predicting j_a within $\pm 10\%$ has been obtained from present study by combining all six different temperatures and is found to be

$$j_a = 0.948\,\mathrm{Re}_a^{-0.7266} \tag{5.2}$$
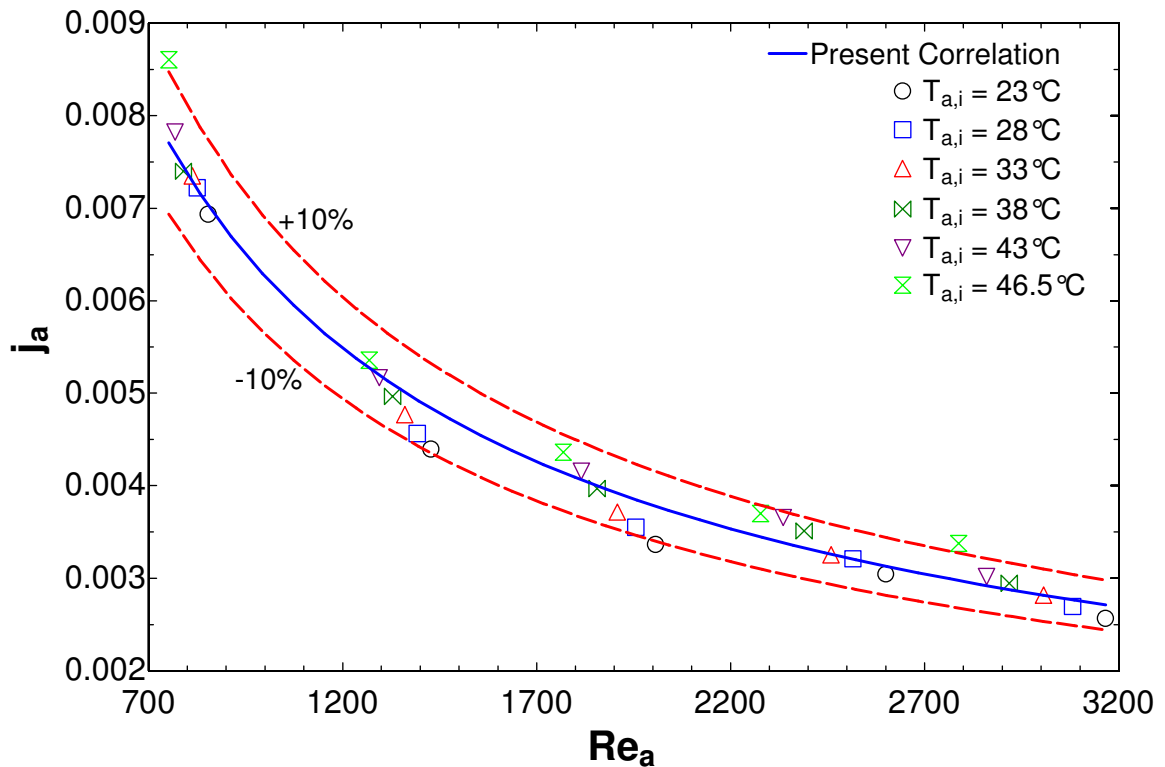
Figure 5.5: The effect of air side Reynolds number on Colburn *j* factor

5.2 Fluid flow characteristics

The following few sections will closely scrutinize the air side fluid flow characteristics of the microchannel heat exchanger. Accompanying general correlations at each different inlet temperature levels will also be developed. The parameters investigated in this section include the pressure drop across heat exchanger, friction factor, and dimensionless pressure coefficient.

5.2.1 Effect of Reynolds number on pressure drop

The pressure drop ($\Delta p_{a,HX}$) across the heat exchanger core are plotted against the air side Reynolds number (Re_a) in Figure 5.6. The figure shows a power-law relationship of increased slope, and hence described in the form of $\Delta p_{a,HX} = x\,\mathrm{Re}_a^y \quad [y > 1 \text{ and } x > 0]$. The air side Reynolds number (Re_a) is based on the hydraulic diameter which is evaluated for air side matrix flow passages suggested by Kays and London (1984). Pressure drops and friction factors are evaluated for all predefined temperature levels (23 to $46.5°C$) at different air velocities corresponding Reynolds number range from 752 to 3165. This figure shows the effects of air side Reynolds numbers and air inlet temperatures on air side pressure drops. The air side pressure drops increase with increasing Reynolds number in non-linear manner. The figure also shows a little difference in pressure drop across heat exchanger for different $T_{a,i}$ at lower Re_a. A general $\Delta p_{a,HX}$ - Re_a correlation capable of predicting $\Delta p_{a,HX}$ within ±10% has been obtained in the present study by combining all different temperatures as

$$\Delta p_{a,HX} = 0.0016\,\mathrm{Re}_a^{1.592} \tag{5.3}$$
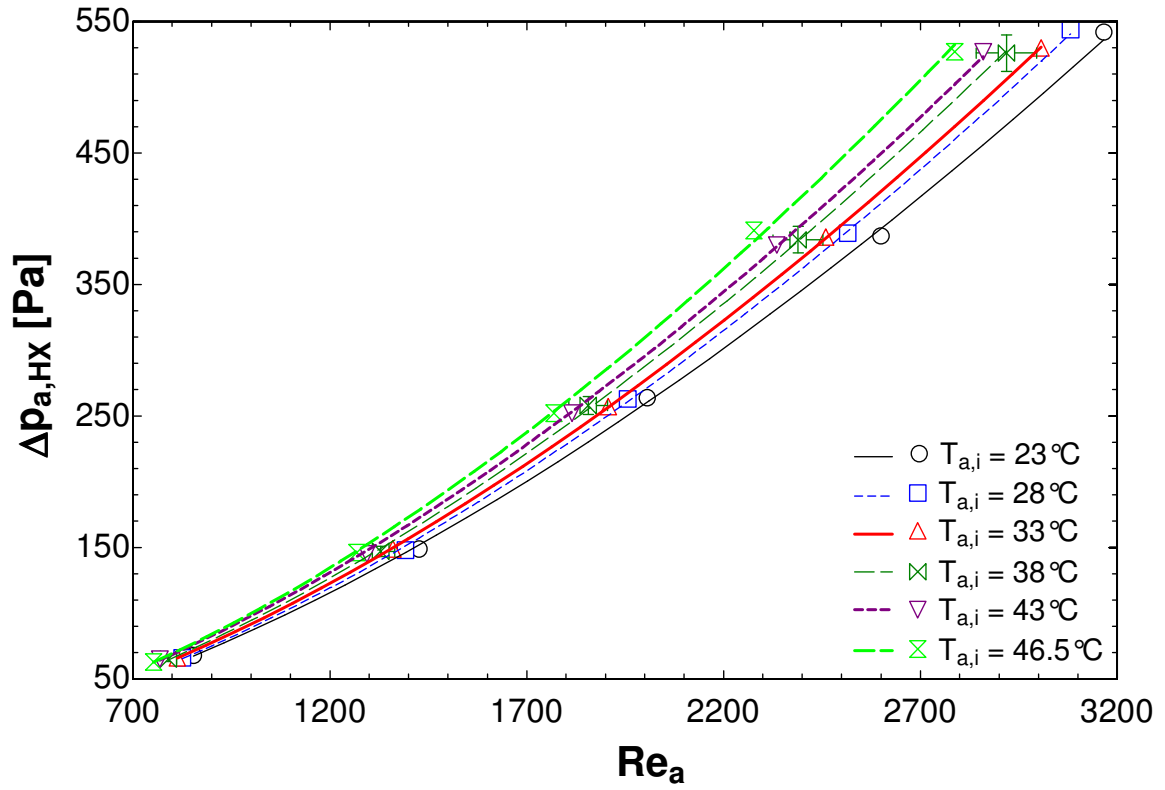
Figure 5.6: The effect of air side Reynolds number on pressure drop across heat exchanger core

5.2.2 Effect of Reynolds number on friction factor

Figure 5.7 is generated to show f_a as a function of Re_a. The $f - \text{Re}_a$ data for each $T_{a,i}$ is best fit with power-law with negative exponent and decreasing slope, and in the form of $f_a = x\,\text{Re}_a^y$ $[y < 0 \text{ and } x > 0]$. Hence f_a decreases with increasing Re_a. The rate of decrease in f_a is greater at Re_a increase originating in lower compared to higher end of Re_a spectrum. The plot also illustrates that f_a decreases slightly (3 – 4%) with an increase in air inlet temperature ($T_{a,i}$) at the same Re_a. The effect of temperature here is therefore found to be insignificant. A general $\text{Re}_a - f_a$ correlation capable of predicting f_a within ±5% has been obtained from the present study by combining all temperature levels as follows.

$$f_a = 0.775\,\text{Re}_a^{-0.374} \tag{5.4}$$
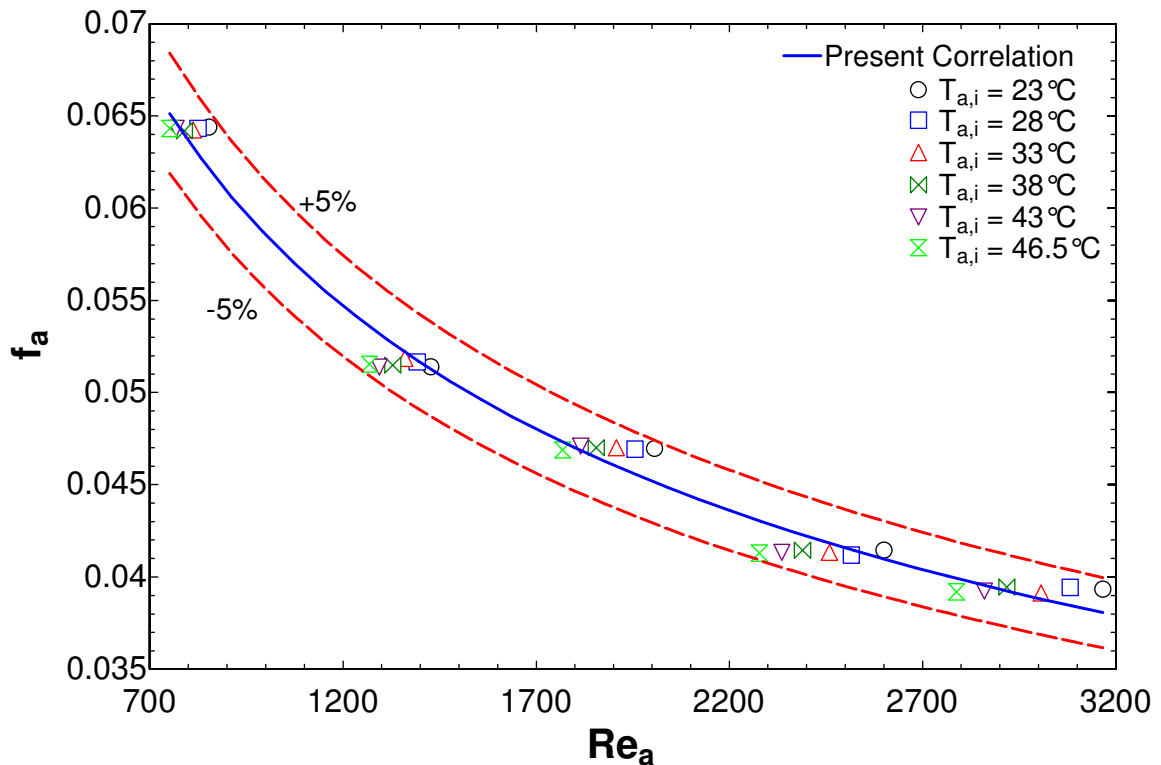
Figure 5.7: The effect of air side Reynolds number on heat exchanger core friction factor

5.3 Heat exchanger performance characteristics

This section will illustrate various performance parameters pertaining to the current heat exchanger. The investigation will yield general correlations at every different inlet temperature levels. The parameters closely scrutinized in this section include the effectiveness, *NTU*, surface temperature, fin efficiency, and $UA-$value.

5.3.1 Effect of Reynolds number on effectiveness

The effectiveness, ε, is determined in Chapter 4, and its variation is shown in Figure 5.8 with respect to Re_a. The figure illustrates a monotonic increase in effectiveness with increase in Re_a. The increase in ε with respect to Re_a is accompanied by a decreasing slope, and is modeled by equation $\varepsilon = x\,\text{Re}_a^y \quad [0 < y < 1 \text{ and } x > 0]$. The increase in ε over a range of Re_a at the higher Re_a would therefore be lower in comparison to the corresponding range at lower Re_a. For a given Re_a, the ε is observed to be greater with increase in $T_{a,i}$, as it is accompanied by decrease in $\dot{Q}_{max}$, which is inversely proportional to ε. The effectiveness ranged from 81.2% to 94.8% is observed in the experiment. A general ε-Re_a correlation capable of predicting ε within ±4% has been obtained in the present study by combining all different temperatures as

$$\varepsilon = 0.435\,\text{Re}_a^{0.096} \tag{5.5}$$
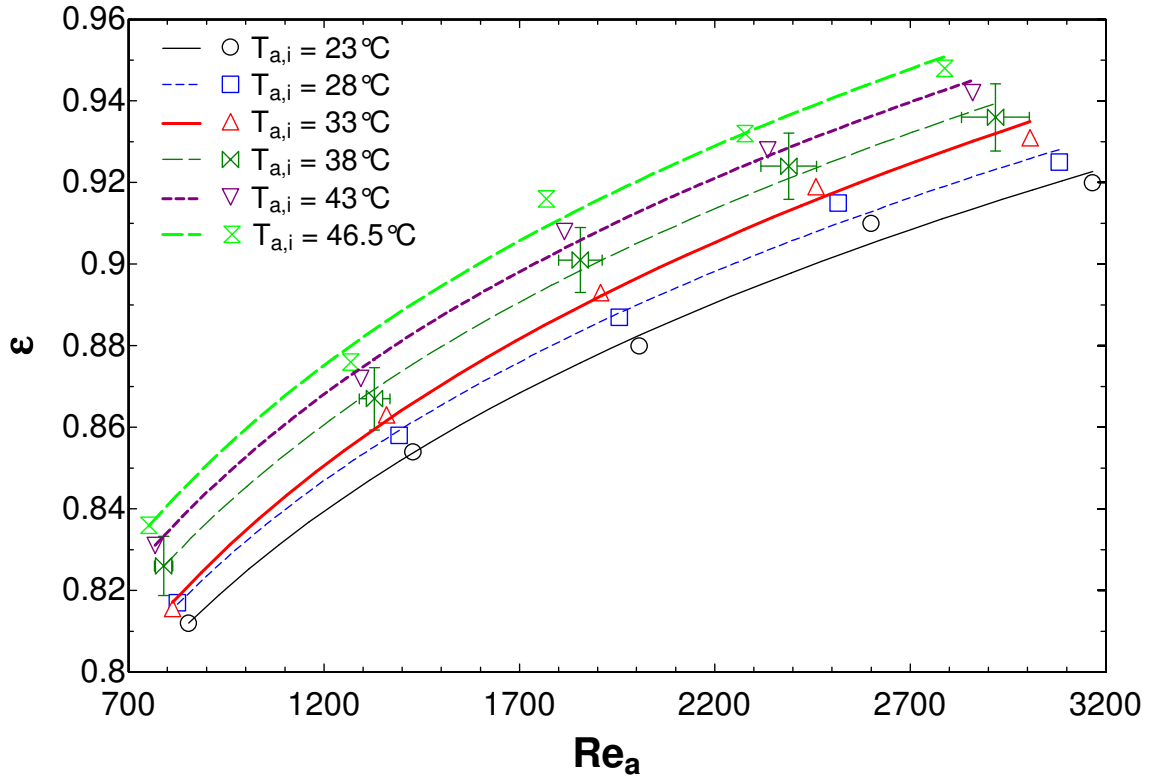
Figure 5.8: The effect of air side Reynolds number on heat exchanger effectiveness

5.3.2 Effect of Reynolds number on *UA* – value

The effect of air side Reynolds number (Re_a) on *UA* is plotted in Figure 5.9. The *UA* value is the inverse of R_{total} and is the measure of how well heat is transferred through the heat exchanger. By determining *UA* value for a particular heat exchanger, its overall heat transfer coefficient both inside (U_i), and outside (U_o) slabs/tubes surfaces can be determined. The figure shows *UA* value increases with increase in Re_a at a given temperature in a non-linear basis, which is best modeled by power-law relationship of the form $UA = x\,\text{Re}_a^y \quad \left[0 < y < 1 \text{ and } x > 0\right]$. The *UA* value also increases with $T_{a,i}$ for a given Re_a. A general *UA*-Re_a correlation capable of predicting *UA* within ±7% has been obtained in the present study by combining all different temperatures as

$$UA = 70.582\,\text{Re}_a^{0.196} \tag{5.6}$$
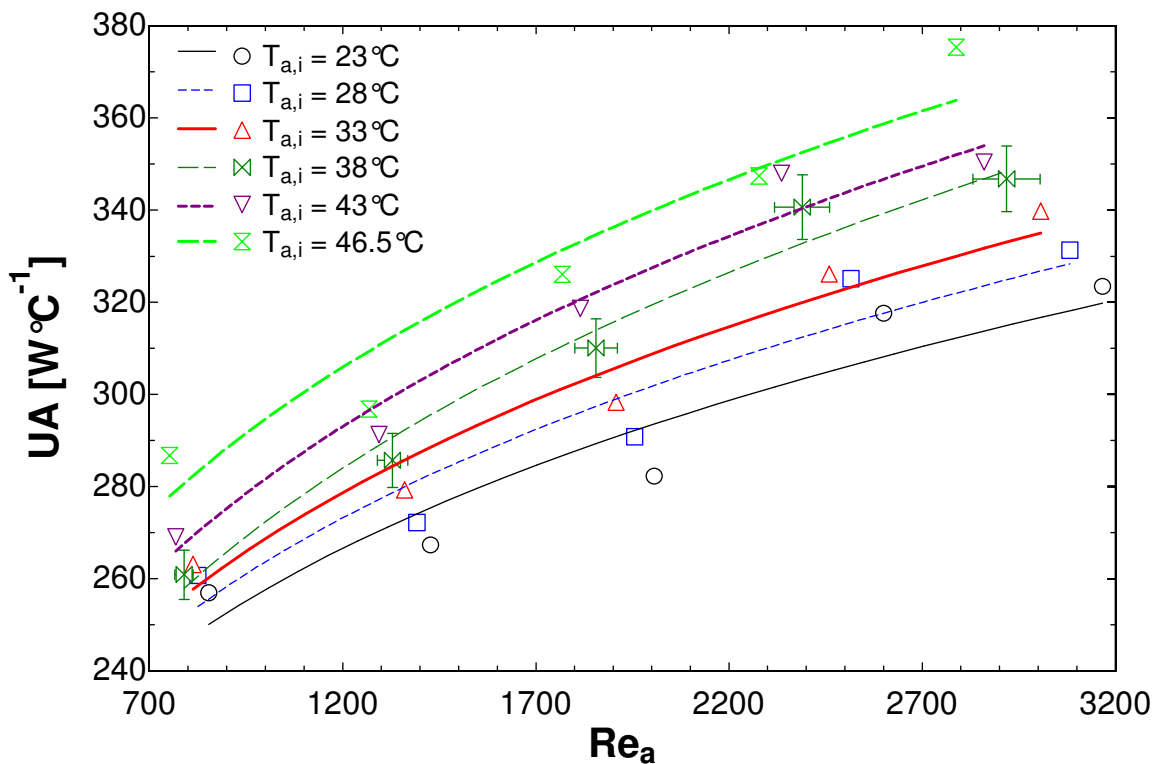
Figure 5.9: The effect of air side Reynolds number on heat exchanger *UA*-value

5.3.3 Effect of Reynolds number on fin efficiency

The fin efficiency (η_{Fin}), of the present heat exchanger as a function of Re_a is plotted in Figure 5.10. The figure shows that fin efficiency of current heat exchanger is fairly high and ranging from 93.2% to 95.8% over the set operating conditions.
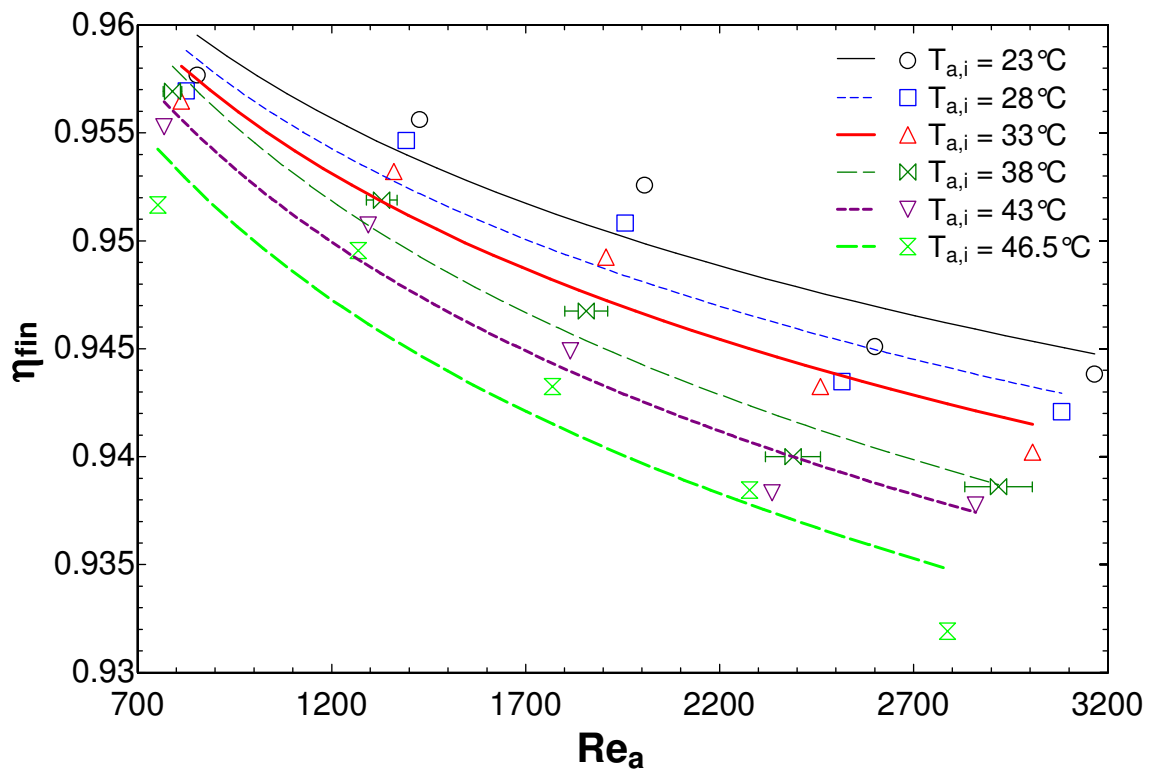
Figure 5.10: The effect of air side Reynolds number on fin efficiency

The data for all $T_{a,i}$ level is best fit by negative exponent power-law relationship and modeled with $\eta_{Fin} = x\,\mathrm{Re}_a^y \quad [y < 0 \text{ and } x > 0]$. The fin efficiency decreases with increase in Re_a. The decreasing negative slope means the drop in fin efficiency is higher at lower end of Re_a range. The figure also illustrates higher fin efficiency is possible for a given Re_a through decrease in $T_{a,i}$, as the fins can transfer heat more effectively to the comparatively cooler air. A general η_{Fin}-Re_a correlation capable of predicting η_{Fin} within $\pm 1\%$ has been obtained in the present study by combining all different temperatures as

$$\eta_{Fin} = 1.047\,\mathrm{Re}_a^{-0.013} \tag{5.7}$$

5.3.4 Effect of pressure drop on effectiveness

Figure 5.11 illustrates effectiveness as a function of pressure drop across the heat exchanger. The figure shows an increase in ε is associated with an increase in pressure drop. The data shows a trend, which is best fit with power-law curve of the form as $\varepsilon = x\Delta p_{a,HX}^{y}$ $[0 < y < 1 \text{ and } x > 0]$. This means the effectiveness can be increased by the same amount at the higher end of effectiveness spectrum at a cost of greater increase in pressure drop across heat exchanger. This relationship provides engineers with a challenge to deduce proper effectiveness and pressure drop requirements for a particular application. The figure also shows that effectiveness at a given pressure drop across the heat exchanger increases with increase in $T_{a,i}$.
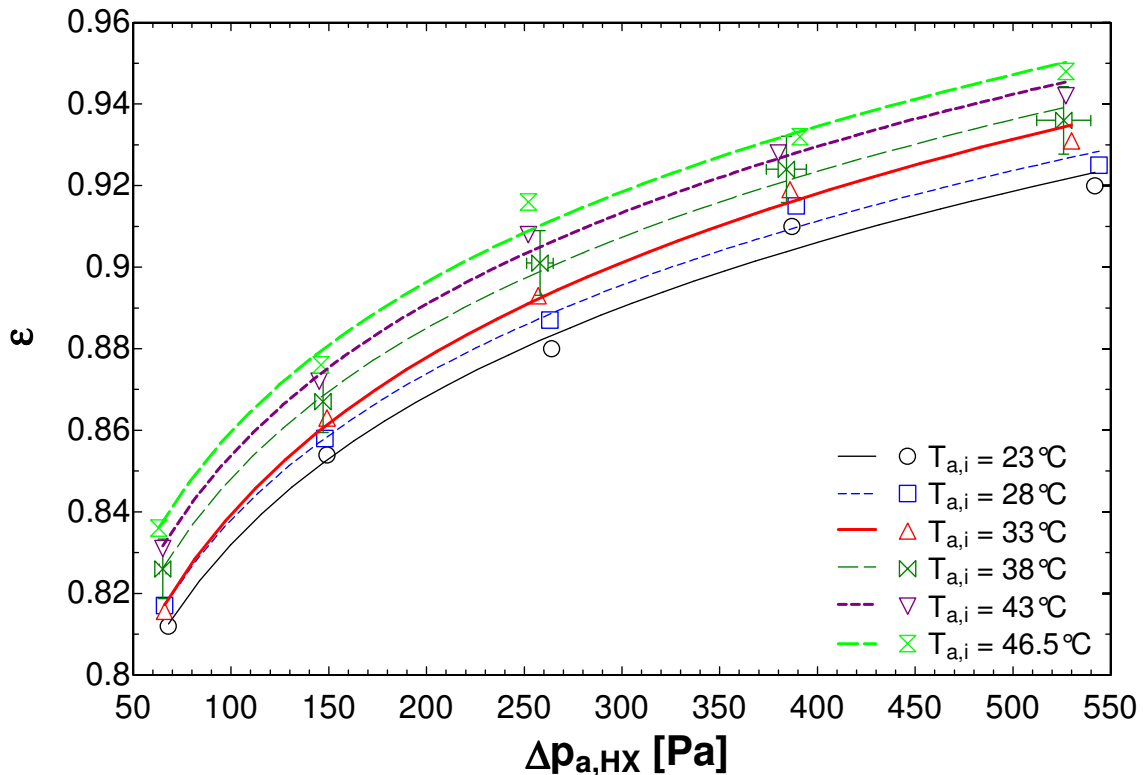
Figure 5.11: The effect of air side pressure drop across heat exchanger core on heat exchanger effectiveness

A general ε - $\Delta p_{a,HX}$ correlation capable of predicting ε within ±2.5% has been obtained in the present study by combining all different temperatures as

$$\varepsilon = 0.637\Delta p_{a,HX}^{0.0061} \tag{5.8}$$

5.3.5 Relationship between C^*, effectiveness, and *NTU*

The effect of heat capacity rate ratio (C^*) on effectiveness (ε), and Number of Transfer Unit (NTU) is plotted in Figure 5.12. Both the ε, and NTU decreases with increase in C^* in power law manner. The relationship for both $\varepsilon - C^*$, and $NTU - C^*$ is modeled with negative exponent power-law of the form $\varepsilon = xC_a^{*y}$ $\left[y < 0 \text{ and } x > 0 \right]$, and $NTU = xC_a^{*y}$ $\left[y < 0 \text{ and } x > 0 \right]$ respectively. The increase in C^* translates into a decrease in Re_a, since $C^* = C_g / C_a$ while C_g is kept constant. At lower C^* (or higher Re_a), both the ε, and NTU are greater for a given $T_{a,i}$. The NTU is also found to be greater at higher $T_{a,i}$ for a given C^* (or Re_a). The ε-C^* relationship also illustrates an increase in heat exchanger ε with increase in $T_{a,i}$ for a given C^* value, as increase in $T_{a,i}$ is accompanied by decrease in $\dot{Q}_{max}$, which is inversely proportional to ε.
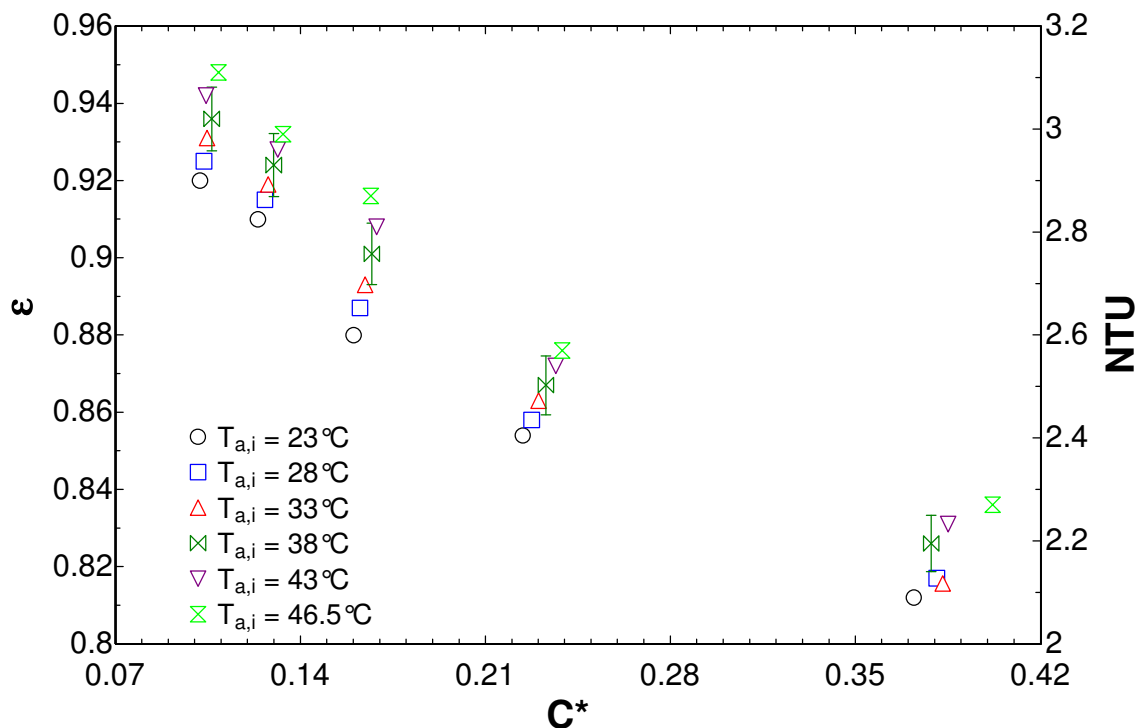
Figure 5.12: The relationship between heat capacity, effectiveness, and *NTU*

5.3.6 Heat exchanger surface temperature

The heat exchanger slab surface temperature is shown in Figures 5.13 – 5.18. Figure 5.13, 5.14, and 5.15 illustrate the top, bottom, and middle serpentine sections of the heat exchanger respectively for the operating condition $23°C$ and $3\,m/s$. The figures illustrate a large gradient of surface temperature from the glycol side inlet at $X = 0mm$ to the outlet at $X = 1800mm$. The air first makes contact with the section at $Y = 0mm$ and flows over the slab until it exits from $Y = 100mm$. The figures also show that it takes a longer axial distance (*i.e.* $X -$ direction) for the top section surface temperature to drop to the same temperature of middle or bottom slab. This suggests a lack of uniformity of the air pressure and flow entering the heat exchanger at $3\,m/s$.
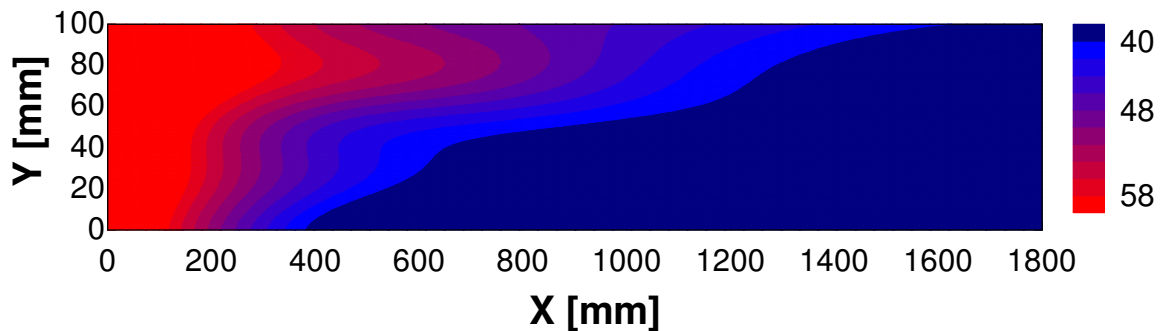
Figure 5.13: Surface temperature of the top serpentine section at 23 °C, 3 m/s.
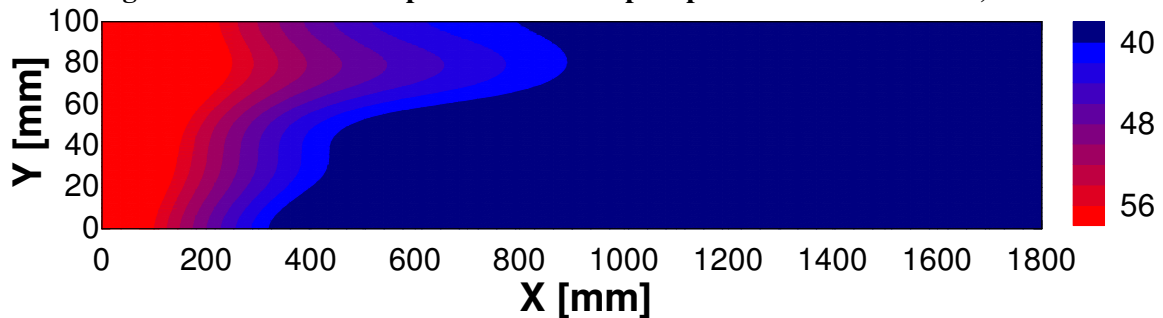
Figure 5.14: Surface temperature of the middle serpentine section at 23 °C, 3 m/s.
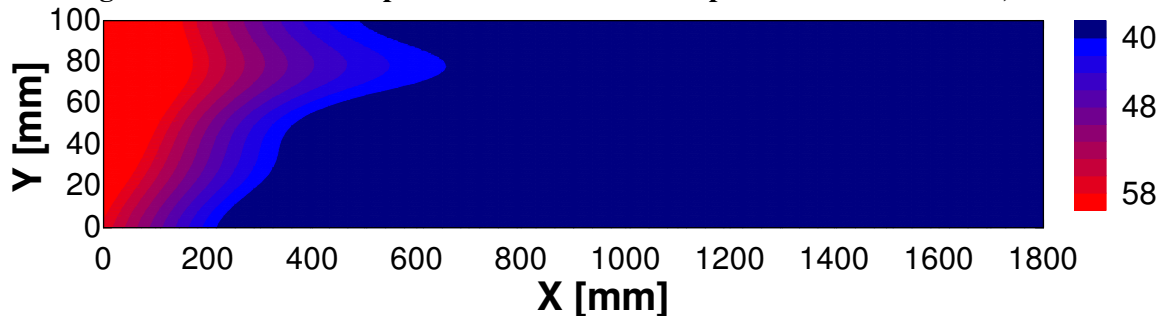
Figure 5.15: Surface temperature of the bottom serpentine section at 23 °C, 3 m/s.

The lack of uniformity of the air pressure and flow is however, the case when the operating condition is on the other extreme at $46.5\,^{\circ}C$ and $11\,m/s$ as illustrated in Figures 5.16-5.18. Figures 5.16, 5.17, and 5.18 illustrate the top, middle, and bottom serpentine section surface temperature for the operating condition at $46.5\,^{\circ}C$ and $11\,m/s$.
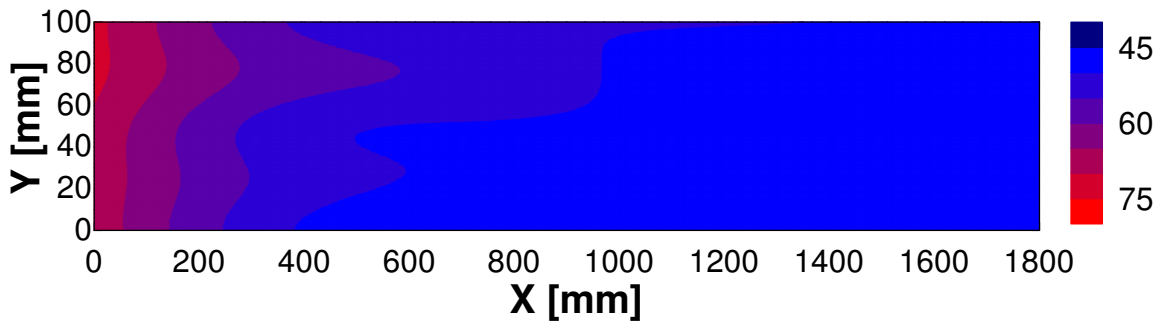
Figure 5.16: Surface temperature of the top serpentine section at 46.5 °C, 11 *m/s*.
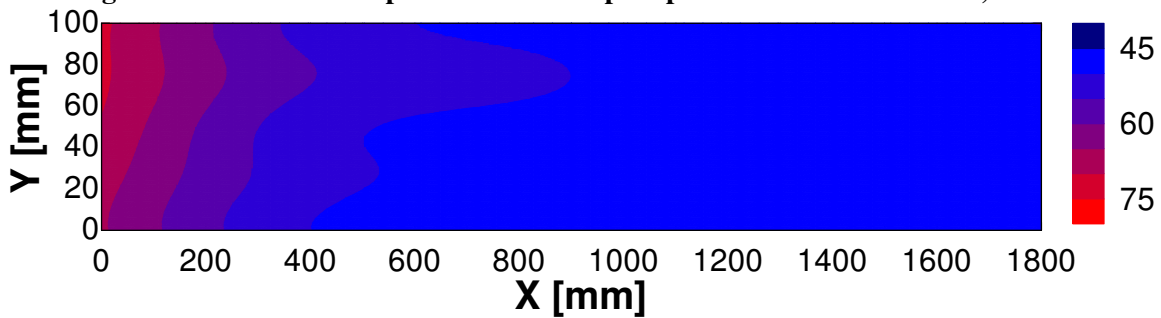
Figure 5.17: Surface temperature of the middle serpentine section at 46.5 °C, 11 *m/s*.
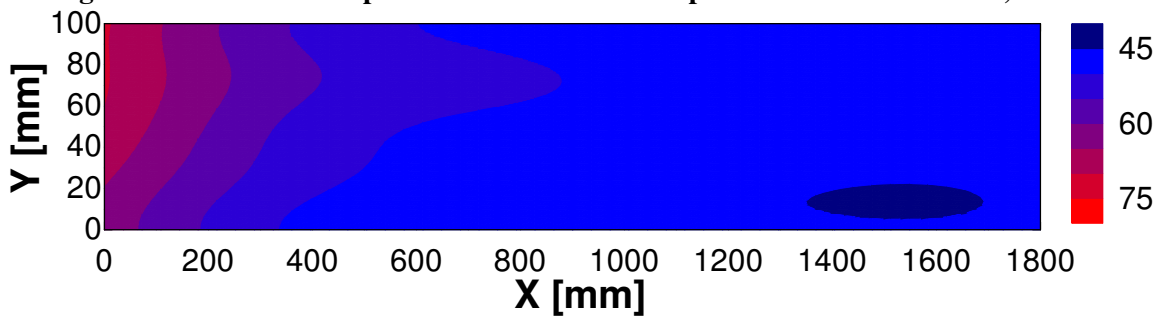
Figure 5.18: Surface temperature of the bottom serpentine section at 46.5 °C, 11 *m/s*.

At this operating condition the sections reach the lowest temperature level faster than the previously mentioned operating condition. In each operating condition higher temperature is observed at $Y = 100mm$ to the outlet at $Y = 0mm$. One reason for this is that the air first makes contact with the slab at $Y = 0mm$ removes heat from the slab surface and become warmer. The temperature difference between the warm air and rest of

the slab thus becomes smaller, which leads to reduced heat removal closer to $Y = 100mm$. Another reason for the higher temperature close to $Y = 100mm$ as oppose to $Y = 0mm$ is seen due to the presence of boundary layer. Boundary layer develops and thickens along the direction air flow. Thus the thickness of boundary layer would be greater closer to $Y = 100mm$ compared to $Y = 0mm$. Since boundary layer is not conducive to heat transfer, less heat is removed at its thickest portion (*i.e.* closer to $Y = 100mm$). It can be also seen from Figures 5.13-5.18, that with the exception of top section surface at $23°C$ and 3 *m/s*, the surface temperature stabilizes after about $X = 650mm$ to $X = 1000mm$, which corresponds to 2 to 3 pass within each of the serpentine section. The magnitude of drop in surface temperature along the X direction is higher for 11 *m/s* compared to that 3 *m/s*.

5.4 Comparison with other studies and models

In this section, comparison will be made between other studies and heat exchanger models to illustrate the heat transfer and fluid flow enhancements made possible through the use of microchannel slabs compared to others. Slab vs. inline tube arrangement performances, as well as Nusselt number, friction factor and Colburn j factor will be compared.

5.4.1 Nusselt number comparison

The effect of air side Reynolds number on air side Nusselt number in the current study is compared to another similar plate fin-tube type heat exchanger of larger tube diameter from Taler (2005) in Figure 5.19. The heat exchanger developed by Taler (2005) employed mono-ethylene glycol solution, and was an inline, double row, two-pass, plate finned heat exchanger of comparable dimension to the present heat exchanger. The figure shows that the Nu_a value of current study is higher compared to Taler (2005) for same Re_a range. This further illustrates the heat transfer superiority of microchannel slab over inline tubes.
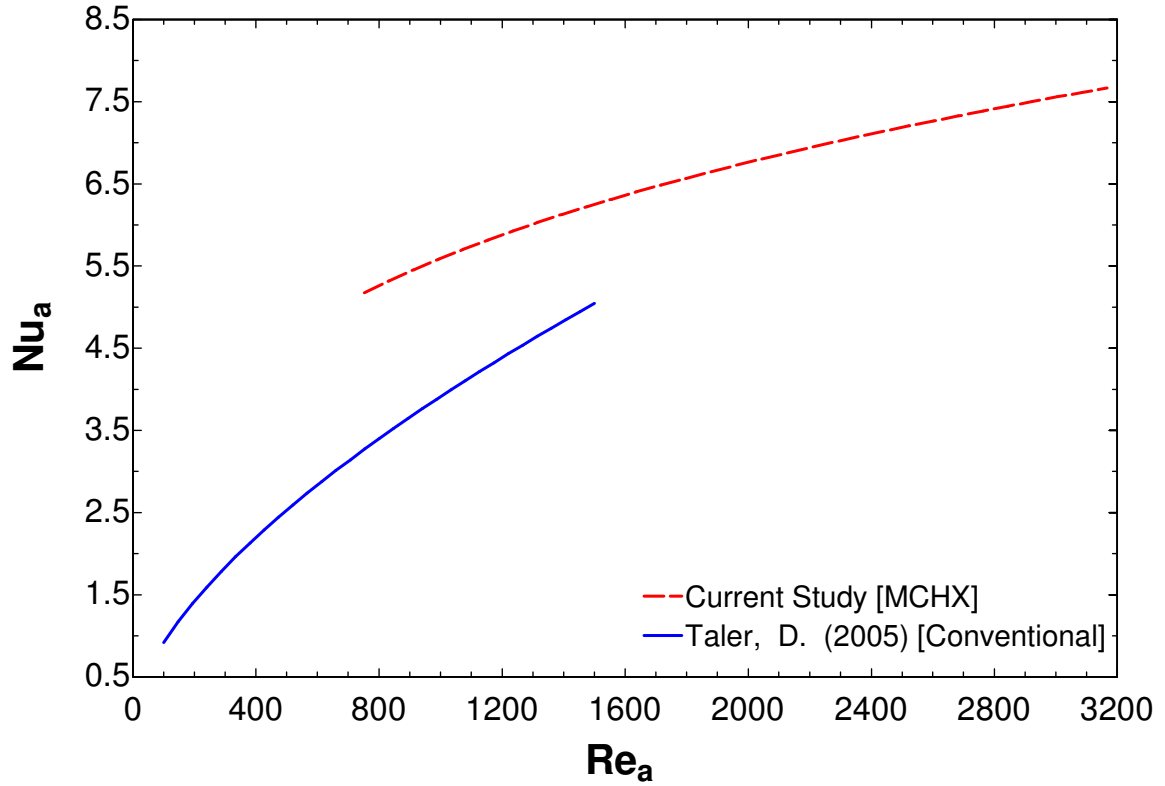
Figure 5.19: Comparison of air side dimensionless heat transfer coefficient Nusselt number between present study and Taler (2005)

5.4.2 Colburn factor comparison

Figure 5.20 compares the Colburn factor for heat convection, (j_a) for present study with same fin-tube heat exchanger from Taler (2005). The constructions of these heat exchangers are similar in general except for present heat exchanger's much smaller channel diameter as well as slab geometry. The j_a value is higher in the current study compared to Taler (2005) over the same Reynolds number range. It indicates that the microchannel heat exchanger in the current study has superior performance with respect to convection heat transfer.
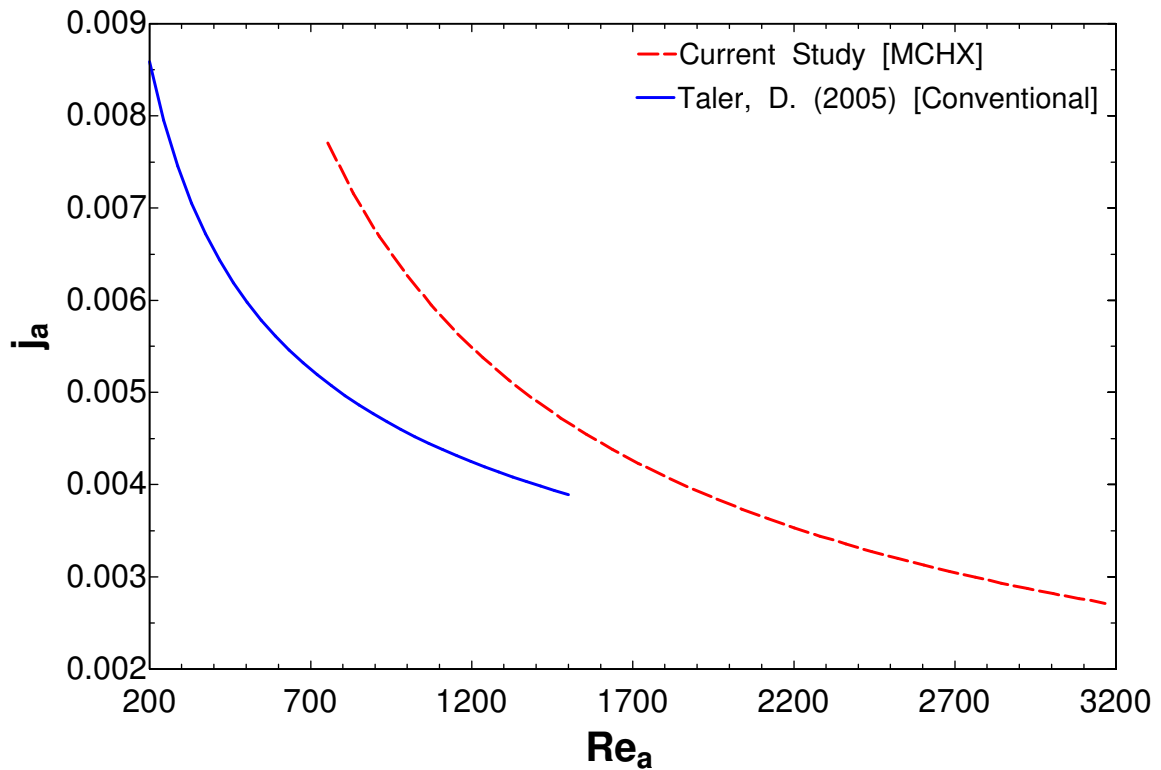
Figure 5.20: Comparison of air side Colburn *j* factor for heat convection correlation developed in present study to Taler (2005)

5.4.3 Friction factor comparison

Figure 5.21 illustrates the comparison between two heat exchangers. These are the heat exchangers used in the current study and in Dong *et al.* (2007). The air side of the wavy fin and flat tube conventional heat exchanger from Dong *et al.* (2007) is as like as the air side of current heat exchanger. The correlation for friction factor in present study was derived based on the computation method by Kays and London (1984) is illustrated in Chapter 4. This method does not require calculation of the entrance and exit losses and takes into account the area contraction ratio, as well as the fluid inlet, exit, and average densities. The friction factor correlation provided in Dong *et al.* (2007), which takes into account the various fin dimensions was derived based on another method from Kays and London (1984). The correlation developed by Dong *et al.* (2007) and accompanying Kays and London (1984) method is given in that order as follows.

$$f_a = 1.16 \, \mathrm{Re}_a^{-0.309} \left(\frac{F_p}{H_{Fin}} \right)^{0.3703} \left(\frac{F_p}{2A} \right)^{-0.25} \left(\frac{L_{Fin}}{L_\lambda} \right)^{-0.1152} \tag{5.5}$$

$$f = \left(\frac{A_{Min,a}}{A_{HT,a,HX}} \right) \left(\frac{2\Delta p_{a,HX}}{\rho V_{max}^2} - K_c - K_e \right) \tag{5.6}$$

This method takes into account the entrance and exit pressure losses, and treats air as incompressible fluid with constant density according to average air temperature. Using these correlations, the friction factor for both heat exchangers were plotted and compared. The present heat exchanger shows lower friction effect than Dong *et al.* (2007) for a given Re_a in this figure. It is found that present heat exchanger minimizes the friction factor.
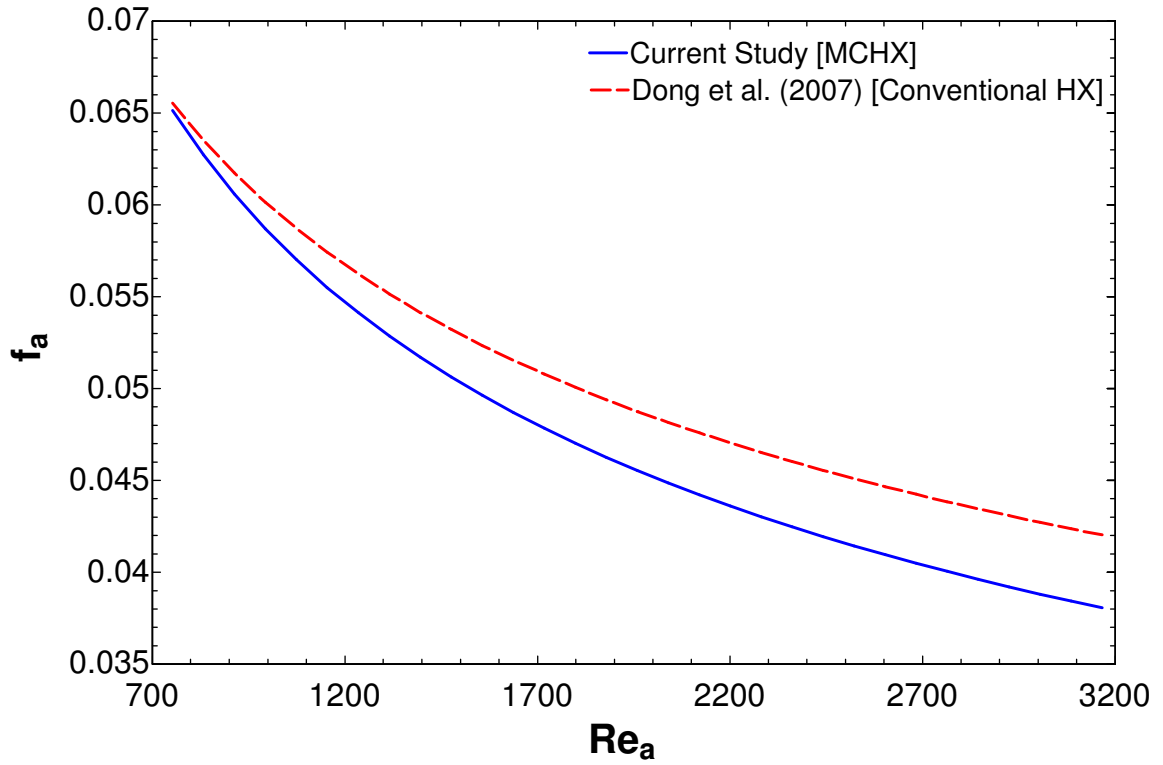
Figure 5.21: Comparison of friction factor between the heat exchanger from present study Dong *et al.* (2007) as function of air side Reynolds number

5.4.4 Slab vs. inline tube comparison

Flow over tube banks in crossflow orientation is very common in many industrial applications. In the conventional heat exchangers the tube rows arrangement of a bank is usually met by either inline or staggered in the direction of flow as shown by Figure 5.22 (a). A wake region is formed behind the tube when fluid is flowing over the tube. The tube diameter, transverse pitch (S_T) and longitudinal pitch (S_L) are playing vital role for heat transfer; the smaller values of S_T / S_L are adversely affected in heat transfer.

However, the effect of wake region behind the tube is insignificant for multi-port microchannel slab geometry shown in Figure 5.22 (b). The heat exchanger used in the current study is built up by multi-port microchannel slab. The multi-port microchannel slab, which offers flat heat transfer areas at the top and the bottom faces of each slab, has no gap in between the flow channels for fluid interaction. This allows the flowing air to make very good contact heating surfaces, increases dwell time, and provides almost uniform temperature distribution throughout the heat exchanger core. Thus it expected to lead to higher heat transfer over the conventional heat exchangers of isolated tube rows.
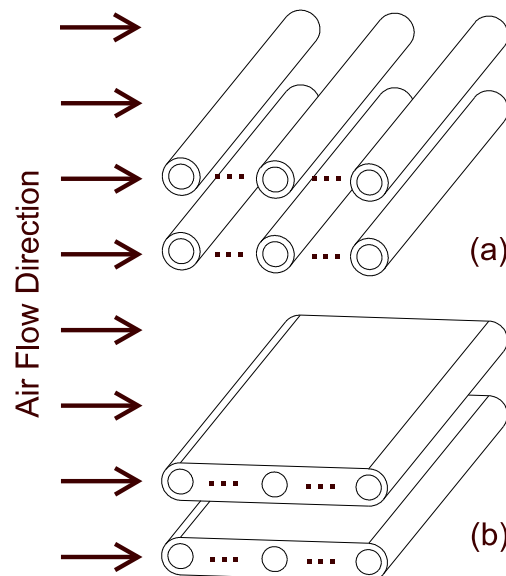
Figure 5.22: (a) In-line tube arrangement, (b) Slab arrangement

The Nusselt number and Colburn j factor correlations developed in the present study were compared with correlations developed by Taler (2005) earlier in Figures 5.19, and 5.20. The figures demonstrated that the correlations for the present heat exchanger provided higher Nusselt number, and Colburn j factor and therefore superior heat transfer performance over the flow regime considered. It was also mentioned in Chapter 2 that the author through his numerical simulation found the regions behind the tubes contributed very little to the performance of the heat exchanger. Due to the underperformance of this region inside the heat exchanger the overall performance of the heat exchanger was adversely affected.

The fluid mean velocity is one of the key driving forces behind convection heat transfer. The convection heat transfer increases with the increase mean flow velocity. The underperformance of the region behind the tubes can therefore be explained in terms of flow velocity. The flow velocity behind a row of tube is particularly low in comparison to the velocity over or under the tube as shown by the numerical simulation by FLUENT in Figure 5.23. In this figure the arrows are the fluid particle velocity vector. Their direction represents the flow direction of fluid particles in a particular location. The length of the arrows conveys the relative magnitude of the flow velocity.
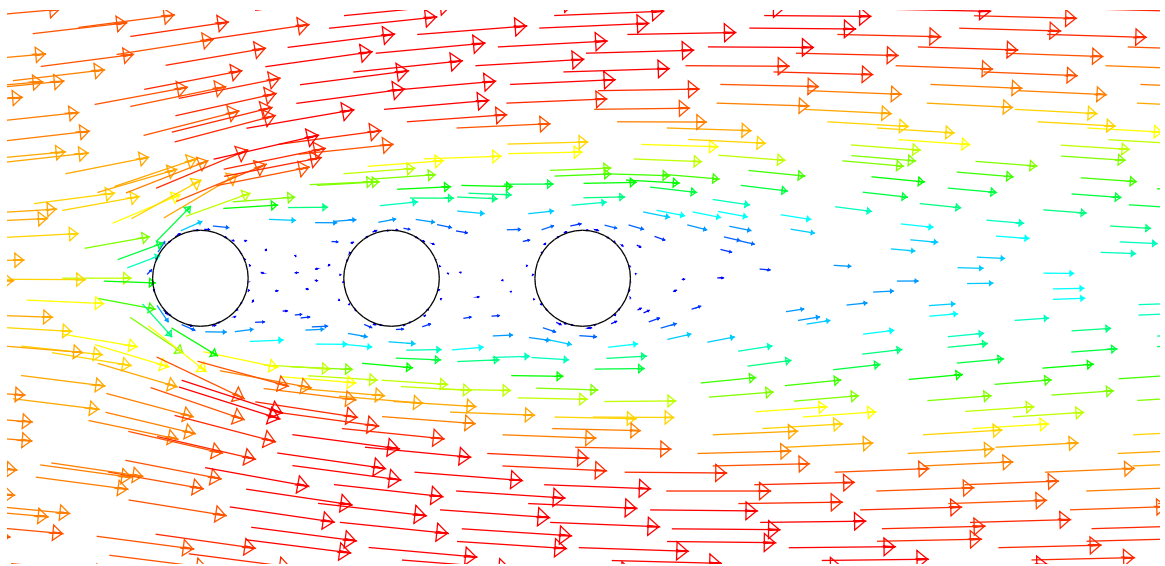
Figure 5.23: Numerical simulation of flow velocity around tube rows

The fluid makes contact and flows past the first tube with relatively high velocity. The fluid velocity interacting with the second and third row is therefore significantly lower. This adverse effect on the subsequent rows of tubes becomes more acute with the increase in number of rows. The heat transfer performance of the subsequent rows therefore diminishes significantly.

The effect of low flow velocity in the wake region is not as significant for of a slab and channel geometry. In Figure 5.24, a numerical simulation is presented to illustrate this point. In this simulation the fluid, flow regime, and velocity is kept identical to that of Figure 5.23. To maintain similarity the slab is given the same frontal area (*i.e.* projected slab cross section area in the direction of air flow) as the tubes. This slab can accommodate three channels of diameter equal to tube diameter of Figure 5.23. It can be seen that only one wake region forms only behind the slab. The flow velocity immediately next to the slab is about the same magnitude of that in Figure 5.23. The Newtonian fluid makes a good contact with the slab surface and has longer dwell time.
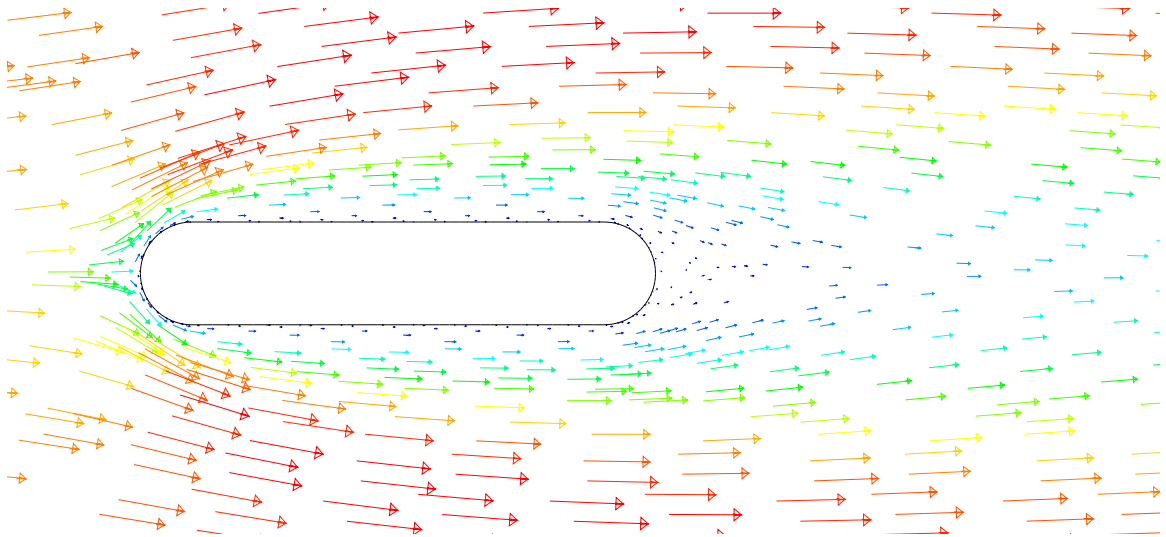
Figure 5.24: Numerical simulation of flow velocity around a slab

One advantage of this geometry over circular tube is difference the way conduction heat transfer takes place. The conduction heat transfer is much uniform in this case compared

to the in-line model. Liquids can transfer heat to the inner surface of channels within aluminum slab by convection. This heat will conduct from the inner surface of channels to outer surface of slab through conduction. Since all channels are contained within the slab and are not separated by fluid wake regions, the heat will conduct from location of higher temperature to lower temperature (*i.e.* from the back to the front of the slab where it is met with higher fluid velocity). This difference in conduction heat transfer provides the slab with much effective means of heat transfer as heat can conduct from inner channel surface to outer slab surface based on temperature difference and not limited by low velocity wakes.

Chapter 6: Conclusions and Recommendations

The main objective of the present study was to investigate air side forced convection heat transfer and fluid flow characteristics, microchannel heat exchanger performance characteristics, and comparison of results obtained to the available literature. In order to successfully meet these objectives cold air was blown over the external surface of a prototype finned, multi-port, serpentine microchannel heat exchanger. The heat exchanger was fixed with inside a Plexiglas test chamber, which was attached to a close loop calorimetric wind tunnel. Both the air flow velocity and temperature were varied over a wide range to produce 30 unique operating conditions. Both the temperature and flow velocity of the 50% glycol-water solution refrigerant used inside the test chamber were maintained constant for all experimental runs. The air side inlet temperatures investigated in this study was set at 23, 28, 33, 38, 43, $46.5°C$. At each of these temperature levels the air flow velocity was varied at five different levels between 3 to $11 m/s$ with an increment of 2 m/s, which translate into Reynolds number ranging between 752-3165. The glycol-water solution temperature and mass flow rate was kept constant at $74°C$ and 0.0345 kg/s producing a Reynolds number of 200. The conclusions and recommendations from the present study are presented in this chapter.

6.1 Conclusions
The main objectives in this study were to ascertain the heat transfer, and fluid flow characteristics of microchannel heat exchanger, its performances, and making comparisons with available literature. In this study many of these characteristics are given in dimensionless form, which is particularly useful in comparing with other studies or use of present data in future studies. The heat transfer, fluid flow, heat exchanger performance, and comparisons deduced from the analysis of results are presented below.

- The air side flow Reynolds number was found to be the main controlling parameters for influencing heat transfer. The heat transfer rate also increases in power law manner with an increase in Reynolds number.

- Both the dimensionless temperature coefficient and the Colburn j factor were seen to decrease with increase in Reynolds number while the opposite was noticed for Nusselt number. All increases and decreases were monotonic and are modeled best with a power law relationship. The overall correlations obtained for determining Nusselt number and Colburn j factor to within ±10% is provided as follows.

$$Nu_a = 0.845 \, \text{Re}_a^{0.274}$$

$$j_a = 0.948 \, \text{Re}_a^{-0.727}$$

- The Reynolds number was the main controlling parameter which influenced the pressure drop across heat exchanger array. The pressure drop across heat exchanger increased monotonically with increase in Reynolds number and was best modeled as power law relationship.

- With regards to friction factor, the air flow Reynolds number was the primary parameter of influence. The friction factor decreased with an increase Reynolds number in power law manner. The general correlation obtained by unifying all data for estimating the friction factor as a function of Reynolds number is given as follows.

$$f_a = 0.775 \, \text{Re}_a^{-0.374}$$

- The UA-value as function of Reynolds number was also seen to increase with a power law relationship of decreasing positive slope. The variation of UA was found to be significant with change in Reynolds number. A general correlation for estimating UA value of the heat exchanger at a given Reynolds number is given as follows.

$$UA = 70.582 \, \text{Re}_a^{0.196}$$

- The fin efficiency was found to decrease with an increase in the Reynolds number. The decrease however was found to be minuscule for the range of Reynolds number being considered. The general correlation developed for obtaining fin efficiency at a given Reynolds number is given as the following.

$$\eta_{Fin} = 1.047 \, \mathrm{Re}_a^{-0.013}$$

- The effectiveness of the heat exchanger as function of pressure drop across heat exchanger was seen to increase with a power law relationship of decreasing positive slope. The variation of effectiveness was found to be significant with change in Reynolds number.

- Both the effectiveness and NTU was found to decrease with an increase in heat capacity ratio. The decrease in effectiveness and NTU with respect to heat capacity ratio was found to be significant but not great. The general correlations developed for obtaining effectiveness within ±2.5% and NTU within ±5% at a given heat capacity ratio are given as the following.

$$\varepsilon = 0.750 C^{*-0.099}$$

$$NTU = 1.788 C^{*-0.200}$$

- It is seen that at low air flow velocity or Reynolds number, there is a flow maldistribution through the heat exchanger array, which was suggested based on the temperature contour. With the exception of top surface at 3 m/s air velocity, the slab temperature tended to stabilize after 2 to 3 passes, and remained virtually constant at that temperature until it exited the slabs. At 3 m/s the top slab surface temperature stabilized in the final pass of the five pass serpentine slab. The difference is likely due to the difference in flow pressure experienced by the slabs at low Reynolds number.

- When the air flow temperature and velocity was increased, the relative difference between the slab surface temperature contours diminished. All three slab temperatures stabilized at or after approximately 3 passes. This reduction in temperature contour difference can be explained by the relatively uniform pressures experienced by all three slabs at this flow rate.

- The correlations developed for dimensionless heat transfer parameters such as Nusselt number and Colburn j factor, and dimensionless fluid flow parameter such as friction factor in this study was compared with available correlation from similar heat exchangers. The general trends for these three parameters tend to agree well with the correlations chosen for comparison.

- The slab presents enhanced heat transfer by reducing the effect of wake region common to in-line and staggered tube configuration. The present geometry provides better heat transfer performances by mitigating wake region adverse effects, providing longer air dwell time, and effective conduction heat transfer mechanism between from inner surface of channels inside the slab to outer surface of the slab.

- Comparison between the correlation for present heat exchanger and wavy finned flat tube heat exchanger, reveled a general agreement in friction factor trend and magnitude. The present heat exchanger also demonstrated a reduction in friction factor hence indicating lower pumping power requirements.

- It was found that the microchannel slab fin construction of the present heat exchanger provides significant heat transfer enhancements when compared with in-line tube fin heat exchangers. This difference was attributed to the formation of low fluid velocity wake regions behind the tubes of in-line heat exchanger. The rate of convection heat transfer is dependent on fluid velocity. The wake region reduced the heat transfer performance of in-line heat exchanger by creating these low velocity regions. This effect was found insignificant for slab with channels as

it is characterized by uniform conduction heat transfer from channel inner surface to slab outer surface. The heat from the outer slab surface is then transferred to the external flow without being adversely affected by the wake region.

This study provides several important relationships and correlations pertaining to the heat transfer, fluid flow, and performance characteristics for multi-port microchannel slab fin heat exchanger. It can therefore be considered to be of significant importance to heating, cooling, refrigeration, HVAC industries. One of the primary concerns for the industrial application is associated costs and benefit. Some form of tradeoff (i.e. fluid flow and pumping power to heat transfer rate) between the parameters discussed is usually associated with achieving the optimum cost benefit ratio. The characteristics, relationships, and correlations in this study would help in such decision making for a particular industrial application.

6.2 Recommendations

The observations from the present study will assist in further research efforts, and investigations in the field of heat transfer and thermo fluids. A large number of correlations were developed for heat transfer, fluid flow and heat exchanger characteristics for the present heat exchanger model. These correlations may prove useful to the industrial applications and heat exchanger engineers/designers. The results and conclusions deduced here can be verified and improved by broadening the range of heat transfer and flow regimes. They can also be improved through designing new heat exchangers with different fin, slab, channel dimensions and spacing, orientations, and shape.

The present study can be expanded by several means. They are:
- Investigation of air cooling using the present heat exchanger.
- Theoretical study involving second law of thermodynamics analysis of the present heat exchanger.

- Comparison of current results with those from in-line and staggered tube fin heat exchanger within similar operating conditions.

- Numerical analysis of the present heat exchanger within the same experimental conditions.

- Investigating heat transfer and fluid flow of multi-row slab-fin heat exchanger.

- Investigating effect spacing between the following: channel, fin, rows of slab.

There were various limitations present in the present experimental setup. Therefore future researchers utilizing the present experimental setup would be well advised to make the following modifications in order for to achieve more accurate and efficient data collection.

- Increasing the size of liquid tank to several times the present capacity would ensure stable temperature of fluid flow through the heat exchanger and would enable longer duration of un-interrupted data collection.

- Using a chiller to replace the presently used city water supply system would greatly increase the stability of the water used to cool the air flowing inside the wind tunnel.

- Use of infrared camera or thermochromic liquid crystal material to measure the slab surface, air inlet and outlet temperatures would significantly increase the accuracy of air temperature measurement.

- Implementing a high power electric motor to run the wind tunnel fan instead of hydraulic pump would greatly stabilize the air flow inside the wind tunnel, as well as provide a greater range of flow velocity.

- Replacing the presently used gear pump with a higher capacity pump would enable the researcher to study operating conditions involving turbulent flow through the microchannel.

- Replacing current 6 *kW* heater in favor of higher capacity would enable study of greater range of heat transfer.

References

Arkilic, E. B., Breuer, K. S. and Schmidt, M. A. (1994). "Gaseous flow in microchannels." Application of Microfabrication to Fluid Mechanics **197**: 55-66.

Arkilic, E. B., Schmidt, M. A. and Breuer, K. S. (1997). "Gaseous slip flow in long microchannels." Journal of Microelectromechanical Systems **6**(2): 167-178.

Bier, W. (1990). "Manufacturing and testing of compact micro heat exchangers with high volumetric heat transfer coefficients." American Society of Mechanical Engineers, Dynamic Systems and Control Division (Publication) DSC **19**(1): 189-197.

Bier, W., Keller, W., Linder, G., Seidel, D., Schubert, K. and Martin, H. (1993). "Gas to gas heat transfer in micro heat exchangers." Chemical Engineering and Processing: Process Intensification **32**(1): 33-43.

Bowman, R. A., Mueller, A. C. and Nagle, W. M. (1940). "Mean temperature difference in design." Transactions of the ASME **62**(1): 283-294.

Choi, S. B., Barron, R. F. and Warrington, R. O. (1991). Fluid Flow and Heat Transfer in Microtubes. Micromechanical Sensors, Actuators, and Systems. Atlanta, Georgia, ASME. **DSC-32:** 123-134.

Chung, P. M. Y., Kawaji, M. and Kawahara, A. (2002). "Characteristics of Single-Phase Flow in Microchannels." ASME Conference Proceedings **2002**(36150): 1219-1228.

Colgan, E. G., Furman, B., Gaynes, M., Graham, W., LaBianca, N., Magerlein, J. H., Polastre, R. J., Rothwell, M. B., Bezama, R. J., Choudhary, R., Martson, K., Toy, H., Wakil, J., Zitz, J. and Schmidt, R. (2007). "A practical implementation of silicon microchannel coolers for high power chips." IEEE transactions on components and packaging technologies **30**(2): 218-225.

De Paepe, M., Willems, A. and Zenner, A. (2005). "Experimental Determination of the Heat Transfer Coefficient of a Plate-Fin Heat Exchanger." Heat Transfer Engineering **26**(7): 29 - 35.

Dong, J., Jiangping, C. and Zhijiu, C. (2008). "Thermal-hydraulic performance of novel louvered fin using flat tube cross-flow heat exchanger." Frontiers of Energy and Power Engineering in China **2**(1): 99-106.

Dong, J., Jiangping, C., Zhijiu, C. and Yimin, Z. (2007). "Air-side thermal hydraulic performance of offset strip fin aluminum heat exchangers." Applied Thermal Engineering **27**(2): 306-313.

Dong, J., Jiangping, C., Zhijiu, C., Yimin, Z. and Wenfeng, Z. (2007a). "Heat transfer and pressure drop correlations for the wavy fin and flat tube heat exchangers." Applied Thermal Engineering **27**(11): 2066-2073.

Editorial (1991). "Journal of Fluids Engineering: Policy on reporting uncertainties in experimental measurements and results." Transactions of the ASME, Journal of Fluids Engineering **113**: 313-314.

Editorial (1993). "Journal of Heat Transfer: Policy on reporting uncertainties in experimental measurements and results." Transactions of the ASME, Journal of Heat Transfer **115**: 5-6.

El-Shaboury, A. M. F. and Ormiston, S. J. (2005). "Analysis of Laminar Forced Convection of Air Crossflow in In-Line Tube Banks with NonSquare Arrangements." Numerical Heat Transfer, Part A: Applications: An International Journal of Computation and Methodology **48**(2): 99 - 126.

Harley, J. C., Huang, Y., Bau, H. H. and Zemel, J. N. (1995). "Gas flow in micro-channels." Journal of Fluid Mechanics **284**: 257-274.

Harris, C., Despa, M. and Kelly, K. (2000). "Design and fabrication of a cross flow micro heat exchanger." Journal of Microelectromechanical Systems **9**(4): 502-508.

Hegab, H. E., Bari, A. and Tim, A. (2002). "Friction and convection studies of R-134a in microchannels within the transition and turbulent flow regimes." Experimental Heat Transfer **15**(4): 245-259.

Hetsroni, G., Mosyak, A., Pogrebnyak, E. and Yarin, L. P. (2005). "Heat transfer in micro-channels: Comparison of experiments with theory and numerical results." International Journal of Heat and Mass Transfer **48**(25): 5580-5601.

Hrnjak, P. S. and Litch, A. D. (2008). "Microchannel heat exchangers for charge minimization in air-cooled ammonia condensers and chillers." International Journal of Refrigeration **31**(4): 658-668.

Huzayyin, A. S., Nagle, S. A. and Elattar, H. F. (2007). "Air-side performance of a wavy-finned-tube direct expansion cooling and dehumidifying air coil." International Journal of Refrigeration **30**(2): 230-244.

Incropera, F. P. and DeWitt, D. P. (2002). Introduction to Heat Transfer. New York, John Willy and Sons.

Jiang, X. N., Zhou, Z. Y., Yao, J., Li, Y. and Ye, X. Y. (1995). Micro-fluid Flow In Microchannel. The 8th International Conference on Solid-State Sensors and Actuators, 1995 and Eurosensors IX. Transducers '95., Stockholm, Sweden.

Jokar, A., Hosni, M. H. and Eckels, S. J. (2005). "Correlations for heat transfer and pressure drop of glycol-water and air flows in minichannel heat exchangers." ASHRAE Transactions(1): 213-224.

Judy, J., Maynes, D. and Webb, B. W. (2002). "Characterization of frictional pressure drop for liquid flows through microchannels." <u>International Journal of Heat and Mass Transfer</u> **45**(17): 3477-3489.

Kakaç, S. and Liu, H. (2002). <u>Heat exchangers: selection, rating, and thermal design</u>. New York, CRC Press.

Kandlikar, S. G. (2006). <u>Heat Transfer and Fluid Flow in Minichannels and Microchannels</u>. Burlington, Elsevier Science Ltd.

Kandlikar, S. G. and Grande, W. J. (2004). "Evaluation of single phase flow in microchannels for high heat flux chip cooling-thermohydraulic performance enhancement and fabrication technology." <u>Heat Transfer Engineering</u> **25**(8): 5-16.

Kandlikar, S. G. and Upadhye, H. R. (2005). "Extending the heat flux limit with enhanced microchannels in direct single-phase cooling of computer chips." <u>IEEE SEMI-THERM Symposium</u> **21**: 8-15.

Kang, S. W., Chen, Y. T. and Chang, G. S. (2002). "The manufacture and test of (110) orientated silicon based micro heat exchanger." <u>Tamkang Journal of Science and Engineering</u> **5**(3): 129-136.

Kays, W. M. and London, A. L. (1984). <u>Compact Heat Exchangers</u>. New York, McGraw-Hill.

Khan, M., Fartaj, A. and Ting, D. S. K. (2004). "An experimental characterization of cross-flow cooling of air via an in-line elliptical tube array." <u>The International journal of heat and fluid flow</u> **25**(4): 636-648.

Khan, M. G. and Fartaj, A. (2010). "A review on microchannel heat exchangers and potential applications." <u>International Journal of Energy Research</u>.

Khan, M. G. and Fartaj, A. (2010a). <u>Heat Transfer Experiments of Ethylene Glycol-Water Mixture in Multi-Port Serpentine Meso-Channel Heat Exchanger Slab</u>. 3rd Joint US-European Fluids Engineering Summer Meeting (FEDSM) and 8th International Conference on Nanochannels, Microchannels, and Minichannels (ICNMM), Montreal, Quebec, CANADA, ASME.

Kido, O., Fujimoto, M., Inamori, S., Uetsuji, T. and Morishita, K. (2000). "Heat Transfer Enhancement Utilizing the Rotation of an Impeller on Thermoelectric Module." <u>Nippon Dennetsu Shinpojiumu Koen Ronbunshu</u> **37**(2): 407-408.

Lee, H., Jeong, Y., Shin, J., Baek, J., Kang, M. and Chun, K. (2004). "Package embedded heat exchanger for stacked multi-chip module." <u>Sensors and Actuators A: Physical</u> **114**(2-3): 204-211.

Luo, L., Fan, Y. and Tondeur, D. (2007). "Heat Exchanger: From Micro - to Multi - Scale Design Optimization." <u>International Journal of Energy Research</u> **31**(13): 1266-1274.

Mala, G. M. and Li, D. (1999). "Flow characteristics of water in microtubes." <u>The International journal of heat and fluid flow</u> **20**(2): 142-148.

Mehendale, S. S., Jacobi, A. M. and Shah, R. K. (2000). "Fluid Flow and Heat Transfer at Micro- and Meso-Scales With Application to Heat Exchanger Design." <u>Applied Mechanics Reviews</u> **53**(7): 175-193.

Morini, G. (2004). "Single-phase convective heat transfer in microchannels: A review of experimental results." <u>International journal of thermal sciences</u> **43**(7): 631-651.

Nuntaphan, A., Kiasiriroat, T. and Wang, C. C. (2005). "Air side performance at low Reynolds number of cross-flow heat exchanger using crimped spiral fins." <u>International Communications in Heat and Mass Transfer</u> **32**(1-2): 151-165.

Oh, S. K., Ko, C. S., Iang, D. Y., Sa, Y. C., Oh, S. Y. and Chung, B. Y. (2003). An experimental study on the wet performance of flat tube heat exchangers. <u>Proceedings of the SAREK 2003, Summer Annual Conference</u>**:** 262-267.

Owhaib, W. and Palm, B. (2004). "Experimental investigation of single-phase convective heat transfer in circular microchannels." <u>Experimental Thermal and Fluid Science</u> **28**(2): 105-110.

Paeng, J. G., Kim, K. H. and Yoon, Y. H. (2009). "Experimental measurement and numerical computation of the air side convective heat transfer coefficients in a plate fin-tube heat exchanger." <u>Journal of mechanical science and technology</u> **23**(2): 536-543.

Papautsky, I., Gale, B. K., Mohanty, S. K., Ameel, T. A. and Frazier, A. B. (1999). <u>Effects of rectangular microchannel aspect ratio on laminar friction constant</u>. SPIE Conference on Microfluidic Devices and Systems II, Santa Clara, CA.

Park, Y. G. and Jacobi, A. M. (2009). "The Air-Side Thermal-Hydraulic Performance of Flat-Tube Heat Exchangers With Louvered, Wavy, and Plain Fins Under Dry and Wet Conditions." <u>Journal of heat transfer</u> **131**(6): 1-13.

Peng, X. F., Peterson, G. P. and Wang, B. X. (1994). "Heat transfer characteristics of water flowing through microchannels." <u>Experimental Heat Transfer</u> **7**(4): 265-283.

Peng, X. F., Peterson, G. P. and Wang, B. X. (1994a). "Frictional flow characteristics of water flowing through rectangular microchannels." <u>Experimental Heat Transfer</u> **7**(4): 249-264.

Pfahler, J., Harley, J., Bau, H. and Zemel, J. (1989). "Liquid transport in micron and submicron channels." <u>Sensors and Actuators A: Physical</u> **22**(1-3): 431-434.

Pfahler, J., Harley, J., Bau, H. and Zemel, J. (1991). "Gas and liquid flow in small channels." <u>Micromechanical Sensors, Actuators, and Systems</u> **ASME DSC-32**: 49-60.

Qi, Z., Zhao, Y. and Chen, J. (2009). "Performance enhancement study of mobile air conditioning system using microchannel heat exchangers." <u>International Journal of Refrigeration</u> **30**: 1-12.

Qu, W., Mala, G. M. and Li, D. (2000). "Heat transfer for water flow in trapezoidal silicon microchannels." <u>International Journal of Heat and Mass Transfer</u> **43**(21): 3925-3936.

Ramshaw, C. (1995). <u>Process Intensification in the Chemical Industry</u>. London, Mechanical Engineering Publications Ltd.

Rugh, J. P., Pearson, J. T. and Rarnadhyani, S. (1992). "A study of a very compact heat exchanger used for passenger compartment heating in automobiles." <u>Compact Heat Exchangers for Power and Process Industries, Heat Transfer Division. ASME</u> **201**: 15-24.

Shah, R. K. (1991). Compact Heat Exchanger Technology and Applications. <u>Heat Exchange Engineering: Compact Heat Exchangers: Techniques of Size Reduction</u>. E. A. Foumeny and P. J. Heggs. London, Ellis Horwood Ltd. **2:** 1-23.

Shah, R. K. and Sekulic, D. P. (2003). <u>Fundamentals of Heat Exchanger Design</u>. New Jersey, John Wiley & Sons.

Shih, J. C., Ho, C. M., Liu, J. and Tai, Y. C. (1996). "Monatomic and polyatomic gas flow through uniform microchannels." <u>ASME MEMS</u> **DSC-59**: 197-203.

Steinke, M. and Kandlikar, S. G. (2004). "Review of single-phase heat transfer enhancement techniques for application in microchannels, minichannels and microdevices." International Journal of Heat and Technology **22**(2): 3-11.

Steinke, M. E. and Kandlikar, S. G. (2006). "Single-phase liquid friction factors in microchannels." International journal of thermal sciences **45**(11): 1073-1083.

Taler, D. (2005). "Prediction of heat transfer correlations for compact heat exchangers." International Journal of Heat and Mass Transfer **69**(3): 137-150.

Tang, L. H., Zeng, M. and Wang, Q. W. (2009). "Experimental and numerical investigation on air-side performance of fin-and-tube heat exchangers with various fin patterns." Experimental Thermal and Fluid Science **33**(5): 818-827.

Tang, S. and Yang, K. T. (2005). "Thermal performance of a single-row fin-and-tube heat exchanger." Journal of thermal science **14**(2): 172-180.

Tao, Y. B., He, Y. L., Huang, J., Wu, Z. G. and Tao, W. Q. (2007). "Numerical study of local heat transfer coefficient and fin efficiency of wavy fin-and-tube heat exchangers." International journal of thermal sciences **46**(8): 768-778.

Tian, L., He, Y., Tao, Y. and Tao, W. (2009). "A comparative study on the air-side performance of wavy fin-and-tube heat exchanger with punched delta winglets in staggered and in-line arrangements." International journal of thermal sciences **48**(9): 1765-1776.

Tuckerman, D. B. and Pease, R. F. W. (1981). "High-performance heat sinking for VLSI." IEEE Electron Device Letters **2**(5): 126-129.

Wang, B. X. and Peng, X. F. (1994). "Experimental investigation on liquid forced-convection heat transfer through microchannels." International Journal of Heat and Mass Transfer **37**(1): 73-82.

Wang, C. C. (2000). "Recent Progress on the Air-side Performance of Fin-and-Tube Heat Exchangers." International Journal of Heat Exchangers **1**(1): 49-76.

Wang, C. C. and Chi, K. Y. (2000a). "Heat transfer and friction characteristics of plain fin-and-tube heat exchangers, part I: New experimental data." International Journal of Heat and Mass Transfer **43**(15): 2681-2691.

Weilin, Q., Mala, G. M. and Dongqing, L. (2000). "Pressure-driven water flows in trapezoidal silicon microchannels." International Journal of Heat and Mass Transfer **43**(3): 353-364.

Wilding, P., Pfahler, J., Bau, H., Zemel, J. and Kricka, L. (1994). "Manipulation and flow of biological fluids in straight channels micromachined in silicon." Clinical chemistry **40**(1): 43-47.

Wu, H. Y. and Cheng, P. (2003). "Friction factors in smooth trapezoidal silicon microchannels with different aspect ratios." International Journal of Heat and Mass Transfer **46**(14): 2519-2525.

Wu, S., Mai, J., Zohar, Y., Tai, Y. C. and Ho, C. M. (1998). "A suspended microchannel with integrated temperature sensors for high-pressure flow studies." The Eleventh Annual International Workshop on Micro Electro Mechanical Systems, 1998. MEMS 98. Proceedings.: 87-92.

Yu, D., Warrington, R., Barron, R. and Ameel, T. (1995). An experimental investigation of fluid flow and heat transfer in microtubes. Proceedings of the ASME/JSME Thermal Engineering Conference, ASME. **1:** 523-530.

Appendix – A: Key Sensors and DAQ Specifications

Data Acquisition (DAQ) Card: NI-PCI-6052E

Supplied by: National Instruments Corporation

Purpose: Used to interface between the signal conditioner and the PC in order to D/A & A/D Signals, and to aid the DAQ software acquire the data at appropriate sampling rate.

Analog Input Characteristics

    Number of channels: 16 single-ended or 8 differential (software-selectable per channel)

    Type of A/D converter (ADC): Successive approximation

    Resolution: 16 bits

    Max sampling rate: 333 kS/s

    Input signal ranges (Bipolar): ±10 V, ±5 V, ±2.5 V, ±1 V, ±500 mV, ±250 mV, ±100 mV, ±50 mV

    Input signal ranges (Unipolar): 0 to 10 V, 0 to 5 V, 0 to 2 V, 0 to 1 V, 0 to 500 mV, 0 to 200 mV, 0 to 100 mV

Analog Output Characteristics

    Number of channels: 2 voltage

    Resolution & Max sampling rate: 16 bits

    Type of D/A converter (DAC): Double-buffered, multiplying

Analog Transfer Characteristics

    Relative accuracy: ±1.5 LSB (Least Significant Bit) typical

    Differential Non Linearity (DNL): ±0.5 LSB typical, ±1.0 LSB max

    Offset error (Pregain after calibration): ±1.0 µV max

Stability

    Recommended warm-up time: 15 minutes

Signal Conditioner Module: SCXI-1102

Supplied by: National Instruments Corporation

Purpose: Used to provide high accuracy thermocouple measurements by acquiring millivolt, volt, 0 to 20 mA, and 4 to 20 mA signals. Also provides high accuracy RTD measurements acquiring capability when used in conjunction with SCXI-1581 current excitation module.

Analog Input Characteristics

Number of channels: 32 Differential

Input signal ranges: ±100 mV @ gain = 100, or ±10 V @ gain = 1.

Analog Transfer Characteristics

Nonlinearity: 0.005% FSR

Offset error:

300 µV max after, or 600 µV before calibration @ gain = 1.

15 µV max after, or 100 µV before calibration @ gain = 100.

Gain error (relative to calibration reference):

0.015% of reading max after, or 0.04% of reading before calibration @ gain = 1.

0.020% of reading max after, or 0.1% of reading before calibration @ gain = 1.

Stability

Recommended warm-up time: 20 minutes

Offset temperature coefficient: 20 µV/°C @ gain = 1, 1 µV/°C @ gain = 100

Physical

Dimension: 18.8 cm × 17.2 cm

Weight: 611 g (24.6 oz)

Current Excitation Module: SCXI-1581

Supplied by: National Instruments Corporation

Purpose: Used to provide 32 channels of highly accurate and stable 100 µA current excitation to applications requiring such fixed current excitation. Such current excitation enables high accuracy RTD resistance measurements.

Input

  Input signal ranges: ±100 mV @ gain = 100, or ±10 V @ gain = 1.

Excitation

  Number of channels: 32 single ended outputs

  Current output: 100 µA

  Accuracy: ±0.05%

  Temperature drift: ±5 ppm/°C

Stability

  Recommended warm-up time: 10 minutes

Physical

  Dimension: 18.8 cm × 17.2 cm

  Weight: 731 g (25.8 oz)

Environmental

  Operating temperature: 0 to 50 °C

  Storage temperature: –20 to 70 °C

  Relative humidity: 10 to 90%

Liquid Inlet Pressure Transducer (PTD): PX219-015G5V (0-5 V, 0-103 kPa)

Supplied by: Omega Engineering Incorporated

Purpose: Used to obtain the inlet pressures of 50% glycol-water solution and transmit to the data acquisition system.

Accuracy: 0.25% FS (including linearity, hysteresis and repeatability)

Operating Temperature: -54 to 121°C (-65 to 250°F)

Compensated Temperature: -20 to 80°C (-4 to 176°F)

Thermal Effects: 0.04% FS/°C (0.02% FS/°F)

Proof Pressure: 150%

Burst Pressure: 300% range max

Response Time: 2 ms typical

Weight: 128 g (4.5 oz)

Electrical Connections: DIN 43650 plug connector

Voltage Output

    Excitation: 24 Vdc @ 15 mA

    Output: 0 to 5 Vdc or 0 to 10 Vdc, ±1.5% FSO, 3-wire. Currently set to 0-5 V.

    5 Vdc Output: 7 to 35 Vdc

    10 Vdc Output: 12 to 35 Vdc

    Zero Balance: 0 Vdc ±2% FSO

4 to 20 mA Output

    Excitation: 24 Vdc (7 to 35 Vdc) reverse polarity protected

    Output: 4 to 20 mA (2-wire) ±1% FSO

    Zero Balance: 4 mA ±2% FSO

    Max Loop Resistance: 50 x (supply voltage - 10) Ω

Liquid Outlet Pressure Transducer (PTD): PX309-005G5V (0-5V, 0-34 kPa)

Supplied by: Omega Engineering Incorporated

Purpose: Used to obtain the outlet pressures of 50% glycol-water solution and transmit to the data acquisition system.

Accuracy: ±0.25% FS BSL at 25ºC; includes linearity, hysteresis and repeatability

Operating Temperature: -40 to 85°C (-40 to 185°F)

Compensated Temperature: 0 to 50°C (32 to 122°F) for ≤5 psi range

Proof Pressure: 300% or 20psi, whichever is greater for <50 psig range

Burst Pressure: 500% of capacity or 25 psi, whichever is greater

Response Time: <1 ms typical

Weight: 154 g (5.4 oz)

Electrical Connections: 1.5 m (5') 3 Conductor cable

Voltage Output

    Excitation: 9-30 Vdc reverse polarity and over-voltage protected

    Output: 0 to 5 Vdc or 0 to 10 Vdc, ±1.5% FSO, 3-wire. Currently set to 0-5 Vdc

    5 Vdc Output: 7 to 35 Vdc

    10 Vdc Output: 12 to 35 Vdc

    Zero Balance: 0 Vdc ±2% FSO; ±4% for 1 and 2 psi ranges

4 to 20 mA Output

    Excitation: 9-30 Vdc reverse polarity and over-voltage protected

    Output: 4 to 20 mA (2-wire) ±1% FSO

    Zero Balance: 4 mA ±2% FSO; ±4% for 1 and 2 psi ranges

    Max Loop Resistance: 50 x (supply voltage - 10) Ω

Gas Differential Pressure Transducer (DPTD): PTDD PX277-01D5V (0-10 V)

Supplied by: Omega Engineering Incorporated

Purpose: Used to obtain the air dynamic pressures in conjunction with Pitot static probe located upstream of the heat exchanger array, and transmit to the data acquisition system.

Excitation: 12 to 35 Vdc

Output: 0 to 5 or 0 to 10 Vdc selectable. Currently set to 0-10 Vdc range

Accuracy: ±1.0% FS

Operating Temperature: -18 to 80°C (0 to 175°F)

Compensated Temperature: -4 to 65°C (25 to 150°F)

Thermal Effects: 0.02%FS/°C (±0.0125%FS/°F)

Proof Pressure: 10 psi

Selectable Range (inch H$_2$O): 0 to 1.0, 0 to 0.5, 0 to 0.25, -0.5 to 0.5, -0.25 to 0.25, -0.125 to 0.125. Currently set to 0 to 1.0 inch H$_2$O.

Media Compatibility: Clean dry air or inert gas

Pressure Fittings: 0.2" hose barbs (3⁄16" Tygon tubing recommended)

Termination: Screw terminal block

Enclosure: Enamel coated, 18 GA steel, NEMA-4 (IP-65) rated

Weight: 454 g (1.0 lb)

Gas Differential Pressure Transducer (DPTD): PTDD PX277-05D5V (0-10 V)

Supplied by: Omega Engineering Incorporated

Purpose: Utilized in obtaining the differential pressure across the heat exchanger in conjunction with pressure taps located in the middle of test chamber walls at the opposite sides of the heat exchanger.

Excitation: 12 to 35 Vdc

Output: 0 to 5 or 0 to 10 Vdc selectable. Currently set to 0-10 Vdc range

Accuracy: ±1.0% FS

Operating Temperature: -18 to 80°C (0 to 175°F)

Compensated Temperature: -4 to 65°C (25 to 150°F)

Thermal Effects: 0.02%FS/°C (±0.0125%FS/°F)

Proof Pressure: 10 psi

Selectable Range (inch H$_2$O): 0 to 5.0, 0 to 2.5, 0 to 1.25, -2.5 to 2.5, -1.25 to 1.25, 0.625 to 0.625. Currently set to 0 to 5.0 inch H$_2$O.

Media Compatibility: Clean dry air or inert gas

Pressure Fittings: 0.2" hose barbs (3⁄16" Tygon tubing recommended)

Termination: Screw terminal block

Enclosure: Enamel coated, 18 GA steel, NEMA-4 (IP-65) rated

Weight: 454 g (1.0 lb)

Gas Flow Measurement/Pressure Acquisition System: FKT-3DP1A-0.4-5-1

Supplied by: FlowKinetics^{TM} LLC

Purpose: Used to obtain simultaneous measurement of concurrent independent differential pressures, atmospheric pressure, temperature, relative humidity, density, and velocity of the gas being tested.

Pressure Connectors: Accepts 3.175 mm (1/8 inch) ID flexible tubing.

Differential Pressure Transducers

    Accuracy: ±0.1% typical (±0.22% max) FS at 25°C

    Media: Clean, dry, non-corrosive gases.

    Auto-zero feature eliminates Zero offset and zero temperature shift effects.

Absolute Pressure Transducer

Media: Clean, dry, non-corrosive gases.

Range: 15 to 115 kPa (2.2 to 16.7 psi)

Accuracy: ±0.5% FS typical (0 to 85°C).

    Includes effects of linearity, temperature and pressure hysteresis, zero temperature shift and span temperature shift.

Damping: User selectable from 1 to 64 data averages.

Temperature (detachable probe)

    Type: K-type wire thermocouple.

    Range: -73°C to 482°C (-100°F to 900°F).

    Accuracy: ±1°C (±1.8°F) typical at 25°C

Relative Humidity (detachable probe)

 Range: 0% to 99% Relative Humidity

 Storage: 0 to 90% Relative Humidity

 Accuracy: ±2% typical @ 25°C

 Hysteresis and Repeatability: ±1.3% typical

 Stability: ±1% typical

 Response time: 15 sec in slow moving air at 25°C

 Temperature Range: -40°C to 85°C (-40°F to 185°F)

 Probe size: Cylinder 100 mm (4 in) long with a diameter of 13 mm (0.5 in).

 Cable length: 150 cm (60 in)

Display

 Description: 4 line large character variable contrast alphanumeric LCD

 Viewing area: 102 mm (4.02 in) by 41.5 mm (1.63 in)

 Pressure units: kPa, inH2O, mmHg, and psi.

 Velocity units: m/s, ft/s and ft/min.

 Temperature units: °C and °F

 Density: kg/m^3 and lb/ft^3

 Humidity: Percent relative humidity

Output: RS232 serial port interface, 9 pin connector. USB adapter available.

Physical

 Dimension: 22.1 cm × 19.1 cm × 9.9 cm

 Weight: 1.33 kg (46.9 oz)

Environmental

 Operating temperature: 0 to 50 °C

 Storage temperature: –10 to 60 °C

Liquid Digital Flow Meter (DFM): 04004SN1-XXX (0.4-5.3LPM)

Supplied by: Proteus Industries Incorporated

Purpose: Utilized to obtain the flow rate of 50% glycol-water solution and transmit to the data acquisition system.

Flow Measurement Capability

    Accuracy: ± 1% FS.

    Linearity: ± 1.5% FS from 0.1 to 1.0x the flow range.

    Repeatability: ± 1% FS from 0.1 to 1.0x the flow range.

Temperature Measurement Capability

    Accuracy: ± 3% FS.

    Linearity: ± 1% FS from 0.1 to 1.0x the temperature range.

    Repeatability: ± 0.5% FS from 0.1 to 1.0x the temperature range.

Pressure Measurement Capability

    Accuracy: ± 3% FS.

    Linearity: ± 1% FS from 0.1 to 1.0x the pressure range.

    Repeatability: ± 0.5% of FS from 0.1 to 1.0x the pressure range.

Electrical Specifications

    Power Requirements: 24 ± 10% VDC, 200 mA

    Over-Voltage Protection: Resettable thermal fuse turns unit OFF if input > 29 Vdc.

    Electrical Connection: 2 m 8/24 AWG PVC insulated cable, rated 1.5 A at 36 Vdc.

    Switch Type: Relay Closure, Normally Open and Normally Closed contacts.

    Relay Rating: SPDT, 1 A at 48 Vdc.

Appendix – B: Key Heat Exchanger Dimensions
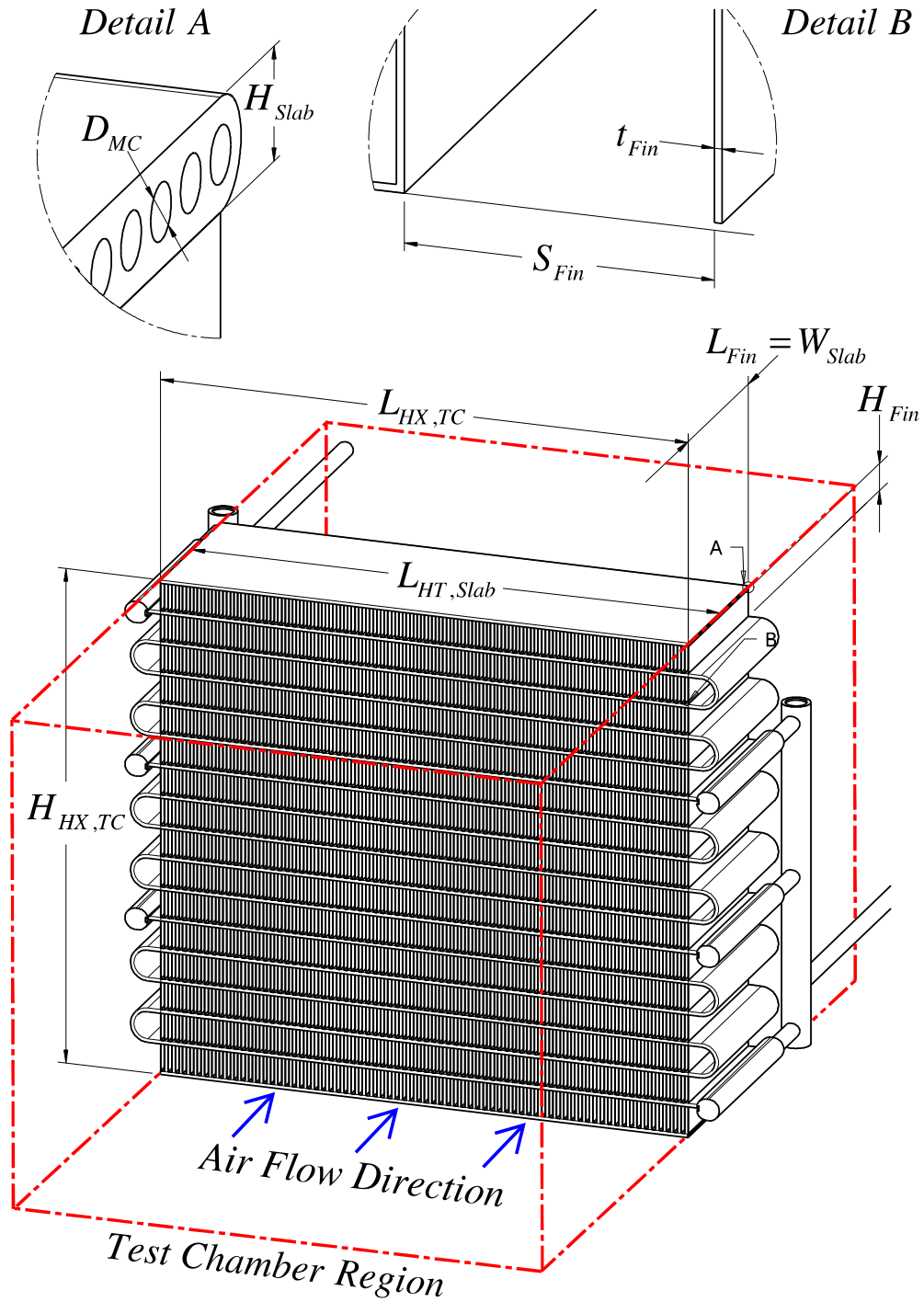
Figure B.1: Key elementary heat exchanger dimensions

Table B.1: Key heat exchanger dimensions

Dimensions	Brief Description and Calculation Formulae	Nominal Value	Uncertainty (%)
$L_{HT,Slab}\,[m]$	The length of each slab passes participating in heat transfer. It is perpendicular to the direction of air flow.	0.3048	± 0.15
$W_{Slab}\,[m]$	Width of a slab. It is the length of slab in the direction parallel to the air flow.	0.100	± 0.20
$H_{Slab}\,[m]$	Height of an individual slab. It is parallel to air flow direction.	0.002	± 0.50
$N_{Fin,Slab}$	Total number of fins per slab.	144	± 0.30
$A_{Frontal,Slab}\,[m^2]$	Frontal area of an individual slab. Evaluated as: $A_{Frontal,Slab} = L_{HT,Slab}H_{Slab}$	6.096×10^{-4}	± 0.52
$N_{HT,Slab,HX}$	Total number of slabs in the heat exchanger participating in heat transfer.	15	± 0
$A_{Frontal,Slab,HX}\,[m^2]$	Combined frontal area of all heat transferring slabs in the heat exchanger. Evaluated as: $A_{Frontal,Slab,HX} = N_{HT,Slab,HX}A_{Frontal,Slab}$	9.144×10^{-3}	± 0.52

Note: Nominal values are shown up to 3 decimal points in this table. Greater accuracy is used in all calculations. Using these values to calculate subsequent parameters may result in slight discrepancy.

Table B.1: Key heat exchanger dimensions (continued)…

Dimensions	Brief Description and Calculation Formulae	Nominal Value	Uncertainty (%)
$N_{FinArray,HX}$	Total number of fin arrays in the heat exchanger.	16	$\pm\,0$
$N_{Fin,HX}$	Total number of fins in the heat exchanger. Evaluated as: $$N_{Fin,HX} = N_{FinArray,HX}\,N_{Fin,Slab}$$	2304	$\pm\,0.30$
$t_{Fin}\,[m]$	Thickness of an individual fin.	1.850×10^{-4}	$\pm\,16$
$H_{Fin}\,[m]$	Height of an individual fin.	1.579×10^{-2}	$\pm\,0.25$
$L_{Fin}\,[m]$	Length of an individual fin in the direction of air flow.	0.100	$\pm\,0.20$
$S_{Fin}\,[m]$	Spacing between two adjacent fins.	2.107×10^{-3}	$\pm\,2.01$
$A_{HT,Fin}$ $[m^2]$	Heat transfer surface area of a single fin. Evaluated as: $$A_{HT,Fin} = 2H_{Fin}\left(L_{Fin}+t_{Fin}\right)+L_{Fin}S_{Fin}$$	3.372×10^{-3}	$\pm\,0.33$

Note: Nominal values are shown up to 3 decimal points in this table. Greater accuracy is used in all calculations. Using these values to calculate subsequent parameters may result in slight discrepancy.

Table B.1: Key heat exchanger dimensions (continued)…

Dimensions	Brief Description and Calculation Formulae	Nominal Value	Uncertainty (%)
$A_{HT,Fin,HX}$ $\left[m^2\right]$	Combined heat transfer surface area of all fins in the heat exchanger. Evaluated as: $A_{HT,Fin,HX} = N_{Fin,HX} A_{HT,Fin}$	7.771	± 0.45
$A_{Frontal,Fin}$ $\left[m^2\right]$	Frontal area of a single fin. Evaluated as: $A_{Frontal,Fin} = H_{Fin} t_{Fin}$	2.921×10^{-6}	± 16
$A_{Frontal,Fin,HX}$ $\left[m^2\right]$	Combined frontal area of all fins in the heat exchanger. Evaluated as: $A_{Frontal,Fin,HX} = N_{Fin,HX} A_{Frontal,Fin}$	6.730×10^{-3}	± 16
$A_{Frontal,Blocked}$ $\left[m^2\right]$	Combined frontal area of all fins and slabs in the heat exchanger, which blocks air flow. Evaluated as: $A_{Frontal,Blocked} = A_{Frontal,Fin,HX} + A_{Frontal,Slab,HX}$	1.587×10^{-2}	± 6.79

Note: Nominal values are shown up to 3 decimal points in this table. Greater accuracy is used in all calculations. Using these values to calculate subsequent parameters may result in slight discrepancy.

Table B.1: Key heat exchanger dimensions (continued)…

Dimensions	Brief Description and Calculation Formulae	Nominal Value	Uncertainty (%)
$L_{HX,TC}\,[m]$	Length of the heat exchanger contained within square duct section of the test chamber (excludes serpentine portion of heat exchanger within the side covers).	0.3048	± 0.15
$H_{HX,TC}\,[m]$	Height of the heat exchanger contained within square duct section of the test chamber.	0.287	± 0.25
$A_{Frontal,HX}$ $[m^2]$	Frontal area of the heat exchanger. Evaluated as: $A_{Frontal,HX} = L_{HX,TC} H_{HX,TC}$	8.748×10^{-2}	± 0.29
$A_{Min,a}$ $[m^2]$	Minimum free flow area available for air flow. Evaluated as: $A_{Min,a} = A_{Frontal,HX} - A_{Frontal,Blocked}$	7.160×10^{-2}	± 1.55

Note: Nominal values are shown up to 3 decimal points in this table. Greater accuracy is used in all calculations. Using these values to calculate subsequent parameters may result in slight discrepancy.

Table B.1: Key heat exchanger dimensions (continued)…

Dimensions	Brief Description and Calculation Formulae	Nominal Value	Uncertainty (%)
$A_{NF,Slab}$ $\left[m^2\right]$	Total area of an individual slab that is not occupied by fins. It is the summation of individual areas on the slab, which are situated between two adjacent fins. Evaluated as: $$A_{UF,Slab} = 2W_{Slab}\left(L_{HT,Slab} - N_{Fin,Slab}t_{Fin}\right)$$	$5.557{\times}10^{-2}$	$\pm\,1.55$
$A_{NF,Slab,HX}$ $\left[m^2\right]$	Combined area of the slabs for the entire heat exchanger, which is not occupied by the fins. Evaluated as: $$A_{NF,Slab,HX} = N_{HT,Slab,HX}\,A_{NF,Slab}$$	0.834	$\pm\,1.55$
$A_{HT,a,HX}$ $\left[m^2\right]$	Combined available heat transfer surface area of all fins and slabs in the heat exchanger. Evaluated as: $$A_{HT,a,HX} = A_{HT,Fin,HX} + A_{NF,Slab,HX}$$	8.604	$\pm\,0.43$

Note: Nominal values are shown up to 3 decimal points in this table. Greater accuracy is used in all calculations. Using these values to calculate subsequent parameters may result in slight discrepancy.

Table B.1: Key heat exchanger dimensions (continued)…

Dimensions	Brief Description and Calculation Formulae	Nominal Value	Uncertainty (%)
$D_{Hyd,a,HX}\ [m]$	Theoretical hydraulic diameter on the air side for the heat exchanger. Calculated from Kays and London (1984). Evaluated as: $D_{Hyd,a,HX} = 4W_{Slab}\left(A_{Min,a} / A_{HT,a,HX}\right)$	$3.325{\times}10^{-3}$	$\pm\,1.62$
$\sigma_a\ [-]$	Minimum free flow to frontal area ratio for the air side. Evaluated as: $\sigma_a = A_{Min,a} / A_{Frontal,HX}$	0.819	$\pm\,1.57$
$\forall_{HX}\ \left[m^3\right]$	Volume of the heat exchanger actively participating in heat transfer. It is also the volume of the heat exchanger contained within the square duct section of the test chamber. Evaluated as: $\forall_{HX} = H_{HX,TC}L_{HX,TC}W_{Slab}$	$8.739{\times}10^{-3}$	$\pm\,0.35$

Note: Nominal values are shown up to 3 decimal points in this table. Greater accuracy is used in all calculations. Using these values to calculate subsequent parameters may result in slight discrepancy.

Table B.1: Key heat exchanger dimensions (continued)…

Dimensions	Brief Description and Calculation Formulae	Nominal Value	Uncertainty (%)
β_a $\left[m^2 / m^3 \right]$	Air side heat transfer surface area density. Evaluated as: $\beta_a = A_{HT,a,HX} / \forall_{HX}$	985	± 12.35
$D_{MC} \left[m \right]$	Diameter of an individual microchannel.	0.001	± 3.48
$N_{MC,Slab}$	Total number of microchannels per slab.	68	± 0
$L_{HT,MC,HX} \left[m \right]$	Combined length of microchannels participating heat transfer for the entire heat exchanger Evaluated as: $L_{HT,MC,HX} = L_{HT,Slab} N_{MC,Slab} N_{HT,Slab,HX}$	311	± 0.15
$A_{XS,MC}$ $\left[m^2 \right]$	Cross-sectional area of an individual microchannel. Evaluated as: $A_{XS,MC} = \left(\pi / 4 \right) D_{MC}^2$	8.016×10^{-7}	± 6.96

Note: Nominal values are shown up to 3 decimal points in this table. Greater accuracy is used in all calculations. Using these values to calculate subsequent parameters may result in slight discrepancy.

Table B.1: Key heat exchanger dimensions (continued)…

Dimensions	Brief Description and Calculation Formulae	Nominal Value	Uncertainty (%)
$A_{XS,MC,Slab}$ $\left[m^2 \right]$	Combined cross-sectional area of all microchannels within a slab. Evaluated as: $A_{XS,MC,Slab} = N_{MC,Slab} A_{XS,MC}$	5.451×10^{-5}	$\pm\, 6.96$
$A_{XS,HT,MC,HX}$ $\left[m^2 \right]$	Combined cross-sectional area of all microchannels within all heat transferring slabs. Evaluated as: $A_{XS,HT,MC,HX} = N_{HT,Slab,HX} A_{XS,MC,Slab}$	8.177×10^{-4}	$\pm\, 6.96$
$A_{HT,in,MC}$ $\left[m^2 \right]$	Inner heat transfer surface area of an individual microchannel. Also known as the liquid side heat transfer surface area for one microchannel. Evaluated as: $A_{HT,in,MC} = \pi D_{MC} L_{HT,Slab}$	9.674×10^{-4}	$\pm\, 3.49$
$A_{HT,in,MC,Slab}$ $\left[m^2 \right]$	Inner heat transfer surface area of all microchannels within a slab. Evaluated as: $A_{HT,in,MC,Slab} = N_{MC,Slab} A_{HT,in,MC}$	6.578×10^{-2}	$\pm\, 3.49$

Note: Nominal values are shown up to 3 decimal points in this table. Greater accuracy is used in all calculations. Using these values to calculate subsequent parameters may result in slight discrepancy.

Table B.1: Key heat exchanger dimensions (continued)…

Dimensions	Brief Description and Calculation Formulae	Nominal Value	Uncertainty (%)
$A_{HT,in,MC,HX}$ $\left[m^2 \right]$	Combined inner heat transfer surface area of all microchannels within all heat transferring slabs. Evaluated as: $$A_{HT,in,MC,HX} = N_{HT,Slab,HX} A_{HT,in,MC,Slab}$$	0.987	± 3.49
$r_{A,HT,a2Liq}$ $[-]$	Ratio of air side to liquid side heat transfer area. Evaluated as: $$r_{A,HT,a2Liq} = A_{HT,a,HX} / A_{HT,in,MC,HX}$$	8.720	± 3.51
$\beta_{A-Liq2V-HX}$ $\left[m^2 / m^3 \right]$	Liquid side heat transfer surface area density. Evaluated as: $$\beta_{A-Liq2V-HX} = A_{HT,in,MC,HX} / \forall_{HX}$$	113	± 12.82
$\forall_{HT,Liq,HX}$ $\left[m^3 \right]$	Volume of liquid refrigerant within the heat transferring lengths of all microchannels in the heat exchanger. Evaluated as: $$\forall_{HT,Liq,HX} = A_{XS,HT,MC,HX} L_{HT,Slab}$$	2.492×10^{-4}	± 6.97

Note: Nominal values are shown up to 3 decimal points in this table. Greater accuracy is used in all calculations. Using these values to calculate subsequent parameters may result in slight discrepancy.

Table B.1: Key heat exchanger dimensions (continued)…

Dimensions	Brief Description and Calculation Formulae	Nominal Value	Uncertainty (%)
$\beta_{A-Liq2V-Liq}$ $\left[m^2 / m^3 \right]$	Liquid side heat transfer surface area per unit liquid side heat transfer volume. Evaluated as: $\beta_{A-Liq2V-Liq} = A_{HT,in,MC,HX} \, / \, \forall_{HT,Liq,HX}$	3959	± 7.79

Note: Nominal values are shown up to 3 decimal points in this table. Greater accuracy is used in all calculations. Using these values to calculate subsequent parameters may result in slight discrepancy.

Appendix – C: Uncertainty Analysis

A large number of fluid flow and heat transfer parameters as well as heat exchanger performance parameters have been discussed in chapters 4 and 5. In this appendix, an evaluation method of uncertainty associated with these parameters is presented. Uncertainties in this appendix are evaluated by considering a sample experimental run (not one of the 30 different operating conditions). This analysis is intended to provide the reader with an insight into available uncertainty analysis methods and their appropriate uses. It can also be used as a guide for researchers with similar experiment based research work. The parameters discussed in this thesis can be considered as part of different levels (*i.e.* first level, second level, third level and so on) for the purpose of uncertainty analysis. The uncertainties associated with first level parameter can be considered as the elemental uncertainties. Uncertainties in various dimensions, temperature, and pressure measurements can be attributed to this group. The second level parameters are considered to be a function of the first level parameters. An example of such parameter is the bulk fluid temperatures, which are the functions of the fluids inlet and outlet temperatures. Third level parameters are functions of second level parameters and so on.

This appendix will show that uncertainties are introduced in the first level parameters such as heat exchanger dimension, fluid inlet and outlet temperature, and pressure measurements by the elemental errors in the form of bias, and precision errors in measuring equipments such as digital caliper, sensors such as PTDs, DPTDs, and RTDs, and data acquisition components such as DAQ card, and signal conditioners. Uncertainties from these first level parameters then propagates into uncertainties of second level parameters such as flow and heat exchanger areas, volumes, bulk temperatures etc. Such uncertainties would then propagate further into third level such as heat transfer rates, Reynolds numbers etc. The relative uncertainties of few key fluid flow and heat transfer parameters for a trial run are tabulated in Table C.7. The following sections will discuss a comprehensive method of uncertainty analysis and propagation which has yielded the results in Table C.7.

C.1 Methods for uncertainty analysis

The broad range of uncertainty evaluation techniques can be classified into several methods. They pertain to uncertainty analysis methods for measurement tools, physical properties, and heat transfer and fluid flow parameters. They are as follows.

Method 1: Measurement tools and DAQ components.

Measurement tools include digital caliper, and DAQ components include RTDs, PTDs, DPTDs, DAQ card, and signal conditioner. Manufacturers of these equipments provide various specifications including but not limited to accuracy, linearity, drifts, hysteresis, and repeatability. These elemental errors, with the exception of repeatability are considered bias. Repeatability pertains to limits of precision error. Further precision error is found through experiments for the data collected. The scatter in data provides a standard deviation, which contributes to precision error. Once all possible elemental sources of bias (*i.e. B_1, B_2, ..., B_n*) and precision (*i.e. P_1, P_2, ..., P_n*) errors are found, the bias and precision errors are evaluated by taking Root Sum Square (RSS) of their respective sources as follows.

$$B = \pm\sqrt{B_1^2 + B_2^2 + ... + B_n^2} \qquad\qquad (C.1)$$

$$P = \pm\sqrt{P_1^2 + P_2^2 + ... + P_n^2} \qquad\qquad (C.2)$$

The overall uncertainty of the equipment is then found through RSS of the bias and precision error as follows.

$$U = \pm\sqrt{B^2 + P^2} \qquad\qquad (C.3)$$

Method 2: Fluid physical properties.

The experimental data for each operating condition is collected over a period of 3 to 4 minutes with a sampling rate of 1 kHz. This results in a data set comprising of 180,000 to

240,000 samples. The average fluid temperatures for these individual samples are evaluated and the lowest and highest values are identified. The fluid properties such as density, viscosity, specific heat, conductivity etc. are evaluated at both of these values of temperature. The uncertainties in these physical properties are then evaluated based on properties at these temperatures as follows.

$$U_{Property_{fluid}} = \frac{1}{2} \left\| \left[Property_{fluid} @ T_{b,fluid,max} \right] - \left[Property_{fluid} @ T_{b,fluid,min} \right] \right\| \qquad (C.4)$$

An exception to this is the Prandtl number, which is a function of few physical properties mentioned above and as such fall into method 3.

Method 3: Certain lengths, areas, volumes, and Heat transfer and fluid flow parameters.

The heat transfer and fluid flow parameters such as heat transfer rate, mass flow rate, Reynolds number, and many others discussed in chapters 4, and 5 are functions of lower level parameters. The uncertainties of these lower level parameters propagate into these higher level parameters based on how they are related through the functions relating them. These relationships are gauged through partial differentiation of the relating function with respect to the lower level parameters. The uncertainties in these higher level heat transfer and fluid flow parameters are then evaluated using the RSS of the individual products of partial derivatives, and uncertainties of the lower level parameters constituting them. For example if Y is dependent on X_1, X_2, ..., X_n and so on… then the uncertainty of Y is determined using the RSS as follows.

$$U_Y = \sqrt{ \left(\frac{\partial Y}{\partial X_1} U_{X_1} \right)^2 + \left(\frac{\partial Y}{\partial X_2} U_{X_2} \right)^2 + \ldots\ldots + \left(\frac{\partial Y}{\partial X_n} U_{X_n} \right)^2 } \qquad (C.5)$$

The relative uncertainty is defined as

$$\frac{U_Y}{Y} = \sqrt{\frac{\left(\frac{\partial Y}{\partial X_1}U_{X_1}\right)^2 + \left(\frac{\partial Y}{\partial X_2}U_{X_2}\right)^2 + \ldots\ldots + \left(\frac{\partial Y}{\partial X_n}U_{X_n}\right)^2}{\left[f\left(X_1, X_2, \ldots, X_n\right)\right]^2}} \qquad \text{(C.6)}$$

C.2 Uncertainty in dimension measurements

The heat exchanger dimensions and their corresponding uncertainties are obtained in two different ways. A digital caliper is used to measure the heat exchanger dimensions smaller than the range of the caliper. Few dimensions that exceed the maximum range of the caliper measurement are obtained from the manufacturer. The following sections discuss uncertainties of heat exchanger dimensions.

C.2.1 Uncertainty inherent to digital caliper

The digital caliper introduces a constant bias error into the measurements taken using it. This bias error composed of two elemental errors. They are errors resulting from the caliper accuracy, and resolution. The accuracy, resolution, and bias errors are calculated as follows.

$$B_{Accuracy} = \pm 2.54 \times 10^{-5}\,m \qquad \text{(C.7)}$$

$$B_{Resolution} = \frac{1}{2}B_{Accuracy} = \pm 1.27 \times 10^{-5}\,m \qquad \text{(C.8)}$$

$$B_{Digital\ Caliper} = \sqrt{B_{Accuracy}^2 + B_{Resolution}^2} = \pm 2.84 \times 10^{-5}\,m \qquad \text{(C.9)}$$

The uncertainties in length measurements utilizing the digital caliper involve both bias and precision error. The precision error is estimated through a set of measurements. Details of precision error estimation are given in section C.2.3.

C.2.2 Uncertainty information from heat exchanger manufacturer

The nominal values and corresponding uncertainties for some of the basic lengths are obtained from the heat exchanger manufacturer. There are two categories for choosing the manufacturer supplied data over the digital caliper measurement. They are chosen if:

(1) The lengths exceed the range of the digital caliper.

(2) The uncertainty value supplied by the manufacturer is smaller than the bias error inherent to the digital caliper.

A 95% confidence level is assumed for the uncertainties provided by the manufacturer. These parameters include the heat exchanger length, and height, slab height, fin thickness among others.

C.2.3 Uncertainty in heat exchanger dimensions

Measurements involving digital caliper are subjected to both the bias error inherent to digital caliper and a precision error based on repeated measurements of the same length parameter in different locations within the heat exchanger. These measurements include the width of the slab (W_{Slab}), number of fins per slab ($N_{Fin,Slab}$), fin height (H_{Fin}), fin length (L_{Fin}), fin spacing (S_{Fin}), and microchannel diameter (D_{MC}). They are recorded and tabulated in Table C.1. Once these basic lengths are measured and their uncertainties are determined using method 1, the nominal values and uncertainties other lengths, areas, and volumes are calculated based on mathematical relationships relating them. Since these lengths, areas, and volumes are function of lower level length parameters, the uncertainties for them are calculated from method 3. The following is the uncertainty analysis for few the key heat exchanger dimensions.

Table C.1: Heat exchanger measurements using digital caliper

No.	W_{Slab} (m)	$N_{Fin,Slab}$	H_{Fin} (m)	L_{Fin} (m)	S_{Fin} (m)	D_{MC} (m)
1	0.0994791	142	0.0157226	0.0997458	0.0022098	0.0010414
2	0.1002411	143	0.0157734	0.099822	0.002032	0.0010287
3	0.0995553	144	0.0157988	0.1004062	0.0020066	0.0009779
4	0.099695	144	0.0157353	0.0996442	0.0020828	0.0010033
5	0.1005332	142	0.0156972	0.0999744	0.0021082	0.0010668
6	0.1004443	144	0.0157734	0.0997077	0.0020701	0.0009779
7	0.099822	144	0.0157861	0.0993775	0.0021336	0.0010033
8	0.0995553	143	0.0157734	0.1002792	0.0022225	0.0010287
9	0.1003046	144	0.0158242	0.1000125	0.002032	0.0010668
10	0.100711	144	0.0158242	0.0998855	0.0020701	0.0009525
11	0.0998855	142	0.0157353	0.1002919	0.0020955	0.0009271
12	0.0997585	143	0.0157607	0.1000125	0.0021971	0.0009271
13	0.0996569	144	0.0158623	0.0997966	0.002032	0.0010287
14	0.0998093	144	0.0159004	0.099949	0.002032	0.0010414
15	0.1000887	144	0.0158623	0.0992378	0.002032	0.0009906
16	0.0997204	144	0.0157861	0.0992505	0.0021336	0.0009652
17	0.0995172	144	0.0157607	0.0994029	0.0020447	0.0010795
18	0.0997585	144	0.0157226	0.0997712	0.0020447	0.0010287
19	0.1002665	144	0.0158115	0.0996823	0.0021082	0.0009779
20	0.0999998	144	0.0158496	0.1004316	0.0021209	0.001016
21	0.0994537	143	0.0158623	0.0995553	0.0022225	0.0009779
22	0.0996061	144	0.0157353	0.0996315	0.0021717	0.0010287
23	0.0997458	144	0.0157353	0.0998474	0.0020955	0.0010287
24	0.0994029	145	0.0157099	0.0997839	0.0020955	0.0010287
25	0.099949	146	0.0157861	0.1006983	0.0020955	0.0009906
26	0.10033	144	0.0158623	0.1005459	0.0021082	0.0009525
27	0.0993013	143	0.0157861	0.1003554	0.0021463	0.0010414
28	0.0993902	143	0.0157988	0.1000252	0.0021717	0.0009906
29	0.0993648	144	0.0158877	0.0999363	0.0021082	0.0009525
30	0.100076	144	0.0157734	0.1002411	0.0021082	0.001016

Table C.1: Heat exchangers measurements using digital caliper (continued…)

No.	$W_{Slab}\,(m)$	$N_{Fin,Slab}$	$H_{Fin}\,(m)$	$L_{Fin}\,(m)$	$S_{Fin}\,(m)$	$D_{MC}\,(m)$
31	0.0993521	146	0.015748	0.1003935	0.0022225	0.0010414
32	0.1006094	144	0.0158877	0.0997839	0.0022098	0.0009398
33	0.0999871	145	0.0156972	0.1005205	0.0021971	0.0009398
34	0.100711	144	0.0157099	0.0998855	0.0019939	0.0010287
35	0.0999744	143	0.0157099	0.0999236	0.002032	0.0010414
36	0.1001649	143	0.0157353	0.1000379	0.0019812	0.0009525
37	0.0993521	144	0.0157734	0.1005332	0.0021971	0.0010541
38	0.0998855	145	0.0157353	0.0993394	0.0021971	0.0010033
39	0.0998855	144	0.0157988	0.1005586	0.0020701	0.0009525
40	0.1007237	146	0.0157988	0.1006221	0.0020066	0.001016
41	0.0993394	144	0.0157861	0.0993775	0.0020955	0.0010541
42	0.0994918	145	0.0158623	0.1004316	0.0021971	0.0009779
43	0.0997966	143	0.0157099	0.0998855	0.0019939	0.0010795
44	0.1001141	143	0.0157734	0.0997712	0.0020447	0.0010668
45	0.100076	144	0.0158623	0.10033	0.0021463	0.0010795
46	0.1001903	145	0.0157861	0.0996315	0.0020828	0.0010668
47	0.0997204	145	0.0158242	0.0995299	0.0021717	0.0009906
48	0.1006094	143	0.0157226	0.0993648	0.0021971	0.0010414
49	0.1001014	145	0.0157861	0.0996442	0.002159	0.0010414
50	0.1000379	144	0.0157734	0.0995934	0.0021717	0.0010668
51	0.0992505	145	0.0157988	0.100203	0.002032	0.0010541
52	0.0992886	144	0.0156972	0.1007491	0.0021717	0.0009652
53	0.0992632	146	0.0158242	0.1003554	0.0020193	0.0010287
54	0.0993902	146	0.015748	0.0992378	0.0021971	0.0009779
55	0.1003046	144	0.0157861	0.099695	0.0019939	0.0009398
56	0.1006348	144	0.0158496	0.1001649	0.002159	0.0010668
57	0.0997839	145	0.0159004	0.1006094	0.0022225	0.0010033
58	0.1004951	145	0.0158115	0.1004062	0.0020066	0.0009652
59	0.099568	143	0.0158369	0.0997585	0.0021082	0.0010287
60	0.100203	143	0.0157861	0.0996315	0.0019939	0.001016

For each of these parameters a total of 60 measurements are taken as evident from Table C.1. Based on these 60 measurements, the student t – distribution for 95% confidence level is found to be $t_{N,95\%} = 2$. Using this value, and standard deviation of the readings, the precision error for each of these parameters is computed in the following manner.

$$P_{W_{slab}} = \pm t_{N,95\%} S_{W_{slab}} \approx \pm 2 \frac{S_{W_{slab}}}{\sqrt{N}} \qquad \left[\because N = 60\right] \tag{C.10}$$

$$P_{N_{Fin,Slab}} = \pm t_{N,95\%} S_{N_{Fin,Slab}} \approx \pm 2 \frac{S_{N_{Fin,Slab}}}{\sqrt{N}} \qquad \left[\because N = 60\right] \tag{C.11}$$

$$P_{H_{Fin}} = \pm t_{N,95\%} S_{H_{Fin}} \approx \pm 2 \frac{S_{H_{Fin}}}{\sqrt{N}} \qquad \left[\because N = 60\right] \tag{C.12}$$

$$P_{L_{Fin}} = \pm t_{N,95\%} S_{L_{Fin}} \approx \pm 2 \frac{S_{L_{Fin}}}{\sqrt{N}} \qquad \left[\because N = 60\right] \tag{C.13}$$

$$P_{S_{Fin}} = \pm t_{N,95\%} S_{S_{Fin}} \approx \pm 2 \frac{S_{S_{Fin}}}{\sqrt{N}} \qquad \left[\because N = 60\right] \tag{C.14}$$

$$P_{D_{MC}} = \pm t_{N,95\%} S_{D_{MC}} \approx \pm 2 \frac{S_{D_{MC}}}{\sqrt{N}} \qquad \left[\because N = 60\right] \tag{C.15}$$

The overall uncertainty in each of these parameters is therefore found by RSS of their individual precision and digital caliper bias as follows.

$$U_{W_{slab}} = \pm \sqrt{B^2_{Digital\ Caliper} + P^2_{W_{slab}}} \tag{C.16}$$

$$U_{N_{Fin,Slab}} = \pm \sqrt{B^2_{Digital\ Caliper} + P^2_{N_{Fin,Slab}}} \tag{C.17}$$

$$U_{H_{Fin}} = \pm \sqrt{B^2_{Digital\ Caliper} + P^2_{H_{Fin}}} \tag{C.18}$$

$$U_{L_{Fin}} = \pm \sqrt{B^2_{Digital\ Caliper} + P^2_{L_{Fin}}} \tag{C.19}$$

$$U_{S_{Fin}} = \pm \sqrt{B^2_{Digital\ Caliper} + P^2_{S_{Fin}}} \tag{C.20}$$

$$U_{D_{MC}} = \pm \sqrt{B^2_{Digital\ Caliper} + P^2_{D_{MC}}} \tag{C.21}$$

Once the individual uncertainties of each of these basic heat exchanger parameters are found and additional uncertainty information from heat exchanger manufacturer is received, the uncertainty evaluation of other parameters proceeds according to method 3 in the following manner.

The expression for the frontal area of an individual slab is given as follows.

$$A_{Frontal,Slab} = L_{HT,Slab} H_{Slab} \tag{C.22}$$

Its uncertainty is calculated as follows.

$$U_{A_{Frontal,Slab}} = \pm \sqrt{\left(\frac{\partial A_{Frontal,Slab}}{\partial L_{HT,Slab}} U_{L_{HT,Slab}} \right)^2 + \left(\frac{\partial A_{Frontal,Slab}}{\partial H_{Slab}} U_{H_{Slab}} \right)^2} \tag{C.23}$$

Where,

$$\frac{\partial A_{Frontal,Slab}}{\partial L_{HT,Slab}} = H_{Slab} \tag{C.24}$$

$$\frac{\partial A_{Frontal,Slab}}{\partial H_{Slab}} = L_{HT,Slab} \tag{C.25}$$

The expression for the combined frontal area of all heat transferring slabs in the heat exchanger is given as follows.

$$A_{Frontal,Slab,HX} = N_{HT,Slab,HX} A_{Frontal,Slab} \tag{C.26}$$

Its uncertainty is calculated as follows.

$$U_{A_{Frontal,Slab,HX}} = \pm \sqrt{\left(\frac{\partial A_{Frontal,Slab,HX}}{\partial N_{HT,Slab,HX}} U_{N_{HT,Slab,HX}} \right)^2 + \left(\frac{\partial A_{Frontal,Slab,HX}}{\partial A_{Frontal,Slab}} U_{A_{Frontal,Slab}} \right)^2} \tag{C.27}$$

Where,

$$\frac{\partial A_{Frontal,Slab,HX}}{\partial N_{HT,Slab,HX}} = A_{Frontal,Slab} \tag{C.28}$$

$$\frac{\partial A_{Frontal,Slab,HX}}{\partial A_{Frontal,Slab}} = N_{HT,Slab,HX} \tag{C.29}$$

The expression for the total number of fins in the heat exchanger is given as follows.

$$N_{Fin,HX} = N_{FinArray,HX} N_{Fin,Slab} \tag{C.30}$$

Its uncertainty is calculated as follows.

$$U_{N_{Fin,HX}} = \pm \sqrt{\left(\frac{\partial N_{Fin,HX}}{\partial N_{FinArray,HX}} U_{N_{FinArray,HX}} \right)^2 + \left(\frac{\partial N_{Fin,HX}}{\partial N_{Fin,Slab}} U_{N_{Fin,Slab}} \right)^2} \tag{C.31}$$

Where,

$$\frac{\partial N_{Fin,HX}}{\partial N_{FinArray,HX}} = N_{Fin,Slab} \tag{C.32}$$

$$\frac{\partial N_{Fin,HX}}{\partial N_{Fin,Slab}} = N_{FinArray,HX} \tag{C.33}$$

The expression for the heat transfer surface area of a single fin is given as follows.

$$A_{HT,Fin} = 2H_{Fin} \left(L_{Fin} + t_{Fin} \right) + L_{Fin} S_{Fin} \tag{C.34}$$

Its uncertainty is calculated as follows.

$$U_{A_{HT,Fin}} = \pm\sqrt{\left(\frac{\partial A_{HT,Fin}}{\partial H_{Fin}}U_{H_{Fin}}\right)^2 + \left(\frac{\partial A_{HT,Fin}}{\partial L_{Fin}}U_{L_{Fin}}\right)^2 + \left(\frac{\partial A_{HT,Fin}}{\partial t_{Fin}}U_{t_{Fin}}\right)^2 + \left(\frac{\partial A_{HT,Fin}}{\partial S_{Fin}}U_{S_{Fin}}\right)^2}$$

(C.35)

Where,

$$\frac{\partial A_{HT,Fin}}{\partial H_{Fin}} = 2\left(L_{Fin} + t_{Fin}\right)$$

(C.36)

$$\frac{\partial A_{HT,Fin}}{\partial L_{Fin}} = 2H_{Fin} + S_{Fin}$$

(C.37)

$$\frac{\partial A_{HT,Fin}}{\partial t_{Fin}} = 2H_{Fin}$$

(C.38)

$$\frac{\partial A_{HT,Fin}}{\partial S_{Fin}} = L_{Fin}$$

(C.39)

The expression for the combined heat transfer surface area of all fins in the heat exchanger is given as follows.

$$A_{HT,Fin,HX} = N_{Fin,HX}A_{HT,Fin}$$

(C.40)

Its uncertainty is calculated as follows.

$$U_{A_{HT,Fin,HX}} = \pm\sqrt{\left(\frac{\partial A_{HT,Fin,HX}}{\partial N_{Fin,HX}}U_{N_{Fin,HX}}\right)^2 + \left(\frac{\partial A_{HT,Fin,HX}}{\partial A_{HT,Fin}}U_{A_{HT,Fin}}\right)^2}$$

(C.41)

Where,

$$\frac{\partial A_{HT,Fin,HX}}{\partial N_{Fin,HX}} = A_{HT,Fin}$$

(C.42)

$$\frac{\partial A_{HT,Fin,HX}}{\partial A_{HT,Fin}} = N_{Fin,HX} \tag{C.43}$$

The expression for the frontal area of a single fin is given as follows.

$$A_{Frontal,Fin} = H_{Fin} t_{Fin} \tag{C.44}$$

Its uncertainty is calculated as follows.

$$U_{A_{Frontal,Fin}} = \pm \sqrt{\left(\frac{\partial A_{Frontal,Fin}}{\partial H_{Fin}} U_{H_{Fin}} \right)^2 + \left(\frac{\partial A_{Frontal,Fin}}{\partial t_{Fin}} U_{t_{Fin}} \right)^2} \tag{C.45}$$

Where,

$$\frac{\partial A_{Frontal,Fin}}{\partial H_{Fin}} = t_{Fin} \tag{C.46}$$

$$\frac{\partial A_{Frontal,Fin}}{\partial t_{Fin}} = H_{Fin} \tag{C.47}$$

The expression for the combined frontal area of all fins in the heat exchanger is given as follows.

$$A_{Frontal,Fin,HX} = N_{Fin,HX} A_{Frontal,Fin} \tag{C.48}$$

Its uncertainty is calculated as follows.

$$U_{A_{Frontal,Fin,HX}} = \pm \sqrt{\left(\frac{\partial A_{Frontal,Fin,HX}}{\partial N_{Fin,HX}} U_{N_{Fin,HX}} \right)^2 + \left(\frac{\partial A_{Frontal,Fin,HX}}{\partial A_{Frontal,Fin}} U_{A_{Frontal,Fin}} \right)^2} \tag{C.49}$$

Where,

$$\frac{\partial A_{Frontal,Fin,HX}}{\partial N_{Fin,HX}} = A_{Frontal,Fin} \tag{C.50}$$

$$\frac{\partial A_{Frontal,Fin,HX}}{\partial A_{Frontal,Fin}} = N_{Fin,HX} \tag{C.51}$$

The expression for the combined frontal area of all fins and slabs in the heat exchanger, which blocks air flow is given as follows.

$$A_{Frontal,Blocked} = A_{Frontal,Fin,HX} + A_{Frontal,Slab,HX} \tag{C.52}$$

Its uncertainty is calculated as follows.

$$U_{A_{Frontal,Blocked}} = \pm\sqrt{\left(\frac{\partial A_{Frontal,Blocked}}{\partial A_{Frontal,Fin,HX}}U_{A_{Frontal,Fin,HX}}\right)^2 + \left(\frac{\partial A_{Frontal,Blocked}}{\partial A_{Frontal,Slab,HX}}U_{A_{Frontal,Slab,HX}}\right)^2} \tag{C.53}$$

Where,

$$\frac{\partial A_{Frontal,Blocked}}{\partial A_{Frontal,Fin,HX}} = 1 \tag{C.54}$$

$$\frac{\partial A_{Frontal,Blocked}}{\partial A_{Frontal,Slab,HX}} = 1 \tag{C.55}$$

The expression for the frontal area of the heat exchanger is given as follows.

$$A_{Frontal,HX} = L_{HX,TC}H_{HX,TC} \tag{C.56}$$

Its uncertainty is calculated as follows.

$$U_{A_{Frontal,HX}} = \pm \sqrt{\left(\frac{\partial A_{Frontal,HX}}{\partial L_{HX,TC}} U_{L_{HX,TC}} \right)^2 + \left(\frac{\partial A_{Frontal,HX}}{\partial H_{HX,TC}} U_{H_{HX,TC}} \right)^2} \qquad (C.57)$$

Where,

$$\frac{\partial A_{Frontal,HX}}{\partial L_{HX,TC}} = H_{HX,TC} \qquad (C.58)$$

$$\frac{\partial A_{Frontal,HX}}{\partial H_{HX,TC}} = L_{HX,TC} \qquad (C.59)$$

The expression for the minimum free flow area available for air flow is given as follows.

$$A_{Min,a} = A_{Frontal,HX} - A_{Frontal,Blocked} \qquad (C.60)$$

Its uncertainty is calculated as follows.

$$U_{A_{Min,a}} = \pm \sqrt{\left(\frac{\partial A_{Min,a}}{\partial A_{Frontal,HX}} U_{A_{Frontal,HX}} \right)^2 + \left(\frac{\partial A_{Min,a}}{\partial A_{Frontal,Blocked}} U_{A_{Frontal,Blocked}} \right)^2} \qquad (C.61)$$

Where,

$$\frac{\partial A_{Min,a}}{\partial A_{Frontal,HX}} = 1 \qquad (C.62)$$

$$\frac{\partial A_{Min,a}}{\partial A_{Frontal,Blocked}} = -1 \qquad (C.63)$$

The expression for the total area of an individual slab that is not occupied by fins is given as follows.

$$A_{NF,Slab} = 2W_{Slab}\left(L_{HT,Slab} - N_{Fin,Slab}t_{Fin}\right) \tag{C.64}$$

Its uncertainty is calculated as follows.

$$U_{A_{NF,Slab}} = \pm\sqrt{\begin{array}{l}\left(\dfrac{\partial A_{NF,Slab}}{\partial W_{Slab}}U_{W_{Slab}}\right)^2 + \left(\dfrac{\partial A_{NF,Slab}}{\partial L_{HT,Slab}}U_{L_{HT,Slab}}\right)^2 + \\[2em] \left(\dfrac{\partial A_{NF,Slab}}{\partial N_{Fin,Slab}}U_{N_{Fin,Slab}}\right)^2 + \left(\dfrac{\partial A_{NF,Slab}}{\partial t_{Fin}}U_{t_{Fin}}\right)^2\end{array}} \tag{C.65}$$

Where,

$$\frac{\partial A_{NF,Slab}}{\partial W_{Slab}} = 2\left(L_{HT,Slab} - N_{Fin,Slab}t_{Fin}\right) \tag{C.66}$$

$$\frac{\partial A_{NF,Slab}}{\partial L_{HT,Slab}} = 2W_{Slab} \tag{C.67}$$

$$\frac{\partial A_{NF,Slab}}{\partial N_{Fin,Slab}} = -2W_{Slab}t_{Fin} \tag{C.68}$$

$$\frac{\partial A_{NF,Slab}}{\partial t_{Fin}} = -2W_{Slab}N_{Fin,Slab} \tag{C.69}$$

The expression for the combined area of the slabs for the entire heat exchanger, which is not occupied by the fins, is given as follows.

$$A_{NF,Slab,HX} = N_{HT,Slab,HX}A_{NF,Slab} \tag{C.70}$$

Its uncertainty is calculated as follows.

$$U_{A_{NF,Slab,HX}} = \pm \sqrt{\left(\frac{\partial A_{NF,Slab,HX}}{\partial N_{HT,Slab,HX}} U_{N_{HT,Slab,HX}} \right)^2 + \left(\frac{\partial A_{NF,Slab,HX}}{\partial A_{NF,Slab}} U_{A_{NF,Slab}} \right)^2}$$ (C.71)

Where,

$$\frac{\partial A_{NF,Slab,HX}}{\partial N_{HT,Slab,HX}} = A_{UF,Slab}$$ (C.72)

$$\frac{\partial A_{NF,Slab,HX}}{\partial A_{NF,Slab}} = N_{HT,Slab,HX}$$ (C.73)

The expression for the combined available heat transfer surface area of all fins and slabs in the heat exchanger is given as follows.

$$A_{HT,a,HX} = A_{HT,Fin,HX} + A_{NF,Slab,HX}$$ (C.74)

Its uncertainty is calculated as follows.

$$U_{A_{HT,a,HX}} = \pm \sqrt{\left(\frac{\partial A_{HT,a,HX}}{\partial A_{HT,Fin,HX}} U_{A_{HT,Fin,HX}} \right)^2 + \left(\frac{\partial A_{HT,a,HX}}{\partial A_{NF,Slab,HX}} U_{A_{NF,Slab,HX}} \right)^2}$$ (C.75)

Where,

$$\frac{\partial A_{HT,a,HX}}{\partial A_{HT,Fin,HX}} = 1$$ (C.76)

$$\frac{\partial A_{HT,a,HX}}{\partial A_{NF,Slab,HX}} = 1$$ (C.77)

The expression for the theoretical hydraulic diameter for air side of the heat exchanger is given as follows.

$$D_{Hyd,a,HX} = 4W_{Slab}\left(A_{Min,a} / A_{HT,a,HX}\right) \tag{C.78}$$

Its uncertainty is calculated as follows.

$$U_{D_{Hyd,a,HX}} = \pm\sqrt{\left(\frac{\partial D_{Hyd,a,HX}}{\partial W_{Slab}}U_{W_{Slab}}\right)^2 + \left(\frac{\partial D_{Hyd,a,HX}}{\partial A_{Min,a}}U_{A_{Min,a}}\right)^2 + \left(\frac{\partial D_{Hyd,a,HX}}{\partial A_{HT,a,HX}}U_{A_{HT,a,HX}}\right)^2} \tag{C.79}$$

Where,

$$\frac{\partial D_{Hyd,a,HX}}{\partial W_{Slab}} = 4\left(A_{Min,a} / A_{HT,a,HX}\right) \tag{C.80}$$

$$\frac{\partial D_{Hyd,a,HX}}{\partial A_{Min,a}} = 4\left(W_{Slab} / A_{HT,a,HX}\right) \tag{C.81}$$

$$\frac{\partial D_{Hyd,a,HX}}{\partial A_{HT,a,HX}} = -4W_{Slab}\left(A_{Min,a} / A_{HT,a,HX}^2\right) \tag{C.82}$$

The expression for the minimum free flow to frontal area ratio for the air side is given as follows.

$$\sigma_a = A_{Min,a} / A_{Frontal,HX} \tag{C.83}$$

Its uncertainty is calculated as follows.

$$U_{\sigma_a} = \pm\sqrt{\left(\frac{\partial \sigma_a}{\partial A_{Min,a}}U_{A_{Min,a}}\right)^2 + \left(\frac{\partial \sigma_a}{\partial A_{Frontal,HX}}U_{A_{Frontal,HX}}\right)^2} \tag{C.84}$$

Where,

$$\frac{\partial \sigma_a}{\partial A_{Min,a}} = 1 / A_{Frontal,HX} \tag{C.85}$$

$$\frac{\partial \sigma_a}{\partial A_{Frontal,HX}} = -A_{Min,a} / A_{Frontal,HX}^2 \tag{C.86}$$

The expression for the volume of the heat exchanger actively participating in heat transfer is given as follows.

$$\forall_{HX} = H_{HX,TC} L_{HX,TC} W_{Slab} \tag{C.87}$$

Its uncertainty is calculated as follows.

$$U_{\forall_{HX}} = \pm \sqrt{\left(\frac{\partial \forall_{HX}}{\partial H_{HX,TC}} U_{H_{HX,TC}}\right)^2 + \left(\frac{\partial \forall_{HX}}{\partial L_{HX,TC}} U_{L_{HX,TC}}\right)^2 + \left(\frac{\partial \forall_{HX}}{\partial W_{Slab}} U_{W_{Slab}}\right)^2} \tag{C.88}$$

Where,

$$\frac{\partial \forall_{HX}}{\partial H_{HX,TC}} = L_{HX,TC} W_{Slab} \tag{C.89}$$

$$\frac{\partial \forall_{HX}}{\partial L_{HX,TC}} = H_{HX,TC} W_{Slab} \tag{C.90}$$

$$\frac{\partial \forall_{HX}}{\partial W_{Slab}} = H_{HX,TC} L_{HX,TC} \tag{C.91}$$

The expression for the air side heat transfer surface area density is given as follows.

$$\beta_a = A_{HT,a,HX} / \forall_{HX} \tag{C.92}$$

Its uncertainty is calculated as follows.

$$U_{\beta_a} = \pm \sqrt{\left(\frac{\partial \beta_a}{\partial A_{HT,a,HX}} U_{A_{HT,a,HX}}\right)^2 + \left(\frac{\partial \beta_a}{\partial \forall_{HX}} U_{\forall_{HX}}\right)^2} \tag{C.93}$$

Where,

$$\frac{\partial \beta_a}{\partial A_{HT,a,HX}} = 1/\forall_{HX} \tag{C.94}$$

$$\frac{\partial \beta_a}{\partial \forall_{HX}} = -A_{HT,a,HX}/\forall_{HX}^2 \tag{C.95}$$

The expression for the combined length of microchannels participating heat transfer for the entire heat exchanger is given as follows.

$$L_{HT,MC,HX} = L_{HT,Slab} N_{MC,Slab} N_{HT,Slab,HX} \tag{C.96}$$

Its uncertainty is calculated as follows.

$$U_{L_{HT,MC,HX}} = \pm \sqrt{\left(\frac{\partial L_{HT,MC,HX}}{\partial L_{HT,Slab}} U_{L_{HT,Slab}}\right)^2 + \left(\frac{\partial L_{HT,MC,HX}}{\partial N_{MC,Slab}} U_{N_{MC,Slab}}\right)^2 + \left(\frac{\partial L_{HT,MC,HX}}{\partial N_{HT,Slab,HX}} U_{N_{HT,Slab,HX}}\right)^2} \tag{C.97}$$

Where,

$$\frac{\partial L_{HT,MC,HX}}{\partial L_{HT,Slab}} = N_{MC,Slab} N_{HT,Slab,HX} \tag{C.98}$$

$$\frac{\partial L_{HT,MC,HX}}{\partial N_{MC,Slab}} = L_{HT,Slab} N_{HT,Slab,HX} \tag{C.99}$$

$$\frac{\partial L_{HT,MC,HX}}{\partial N_{HT,Slab,HX}} = L_{HT,Slab} N_{MC,Slab} \tag{C.100}$$

The expression for the cross-sectional area of an individual microchannel is given as follows.

$$A_{XS,MC} = (\pi / 4) D_{MC}^2 \qquad \text{(C.101)}$$

Its uncertainty is calculated as follows.

$$U_{A_{XS,MC}} = \pm \sqrt{\left(\frac{\partial A_{XS,MC}}{\partial D_{MC}} U_{D_{MC}} \right)^2} \qquad \text{(C.102)}$$

Where,

$$\frac{\partial A_{XS,MC}}{\partial D_{MC}} = (\pi / 2) D_{MC} \qquad \text{(C.103)}$$

The expression for the combined cross-sectional area of all microchannels within a slab is given as follows.

$$A_{XS,MC,Slab} = N_{MC,Slab} A_{XS,MC} \qquad \text{(C.104)}$$

Its uncertainty is calculated as follows.

$$U_{A_{XS,MC,Slab}} = \pm \sqrt{\left(\frac{\partial A_{XS,MC,Slab}}{\partial N_{MC,Slab}} U_{N_{MC,Slab}} \right)^2 + \left(\frac{\partial A_{XS,MC,Slab}}{\partial A_{XS,MC}} U_{A_{XS,MC}} \right)^2} \qquad \text{(C.105)}$$

Where,

$$\frac{\partial A_{XS,MC,Slab}}{\partial N_{MC,Slab}} = A_{XS,MC} \qquad \text{(C.106)}$$

Faisal A. Siddiqui. M.A.Sc. Thesis 2011. Dept of Mechanical, Automotive, and Materials Engineering, University of Windsor, Canada

147

$$\frac{\partial A_{XS,MC,Slab}}{\partial A_{XS,MC}} = N_{MC,Slab} \tag{C.107}$$

The expression for the combined cross-sectional area of all microchannels within all heat transferring slabs is given as follows.

$$A_{XS,HT,MC,HX} = N_{HT,Slab,HX} A_{XS,MC,Slab} \tag{C.108}$$

Its uncertainty is calculated as follows.

$$U_{A_{XS,HT,MC,HX}} = \pm \sqrt{\left(\frac{\partial A_{XS,HT,MC,HX}}{\partial N_{HT,Slab,HX}} U_{N_{HT,Slab,HX}}\right)^2 + \left(\frac{\partial A_{XS,HT,MC,HX}}{\partial A_{XS,MC,Slab}} U_{A_{XS,MC,Slab}}\right)^2} \tag{C.109}$$

Where,

$$\frac{\partial A_{XS,HT,MC,HX}}{\partial N_{HT,Slab,HX}} = A_{XS,MC,Slab} \tag{C.110}$$

$$\frac{\partial A_{XS,HT,MC,HX}}{\partial A_{XS,MC,Slab}} = N_{HT,Slab,HX} \tag{C.111}$$

The expression for the inner heat transfer surface area of an individual microchannel is given as follows.

$$A_{HT,in,MC} = \pi D_{MC} L_{HT,Slab} \tag{C.112}$$

Its uncertainty is calculated as follows.

$$U_{A_{HT,in,MC}} = \pm \sqrt{ \left(\frac{\partial A_{HT,in,MC}}{\partial D_{MC}} U_{D_{MC}} \right)^2 + \left(\frac{\partial A_{HT,in,MC}}{\partial L_{HT,Slab}} U_{L_{HT,Slab}} \right)^2 } \qquad \text{(C.113)}$$

Where,

$$\frac{\partial A_{HT,in,MC}}{\partial D_{MC}} = \pi L_{HT,Slab} \qquad \text{(C.114)}$$

$$\frac{\partial A_{HT,in,MC}}{\partial L_{HT,Slab}} = \pi D_{MC} \qquad \text{(C.115)}$$

The expression for the inner heat transfer surface area of all microchannels within a slab is given as follows.

$$A_{HT,in,MC,Slab} = N_{MC,Slab} A_{HT,in,MC} \qquad \text{(C.116)}$$

Its uncertainty is calculated as follows.

$$U_{A_{HT,in,MC,Slab}} = \pm \sqrt{ \left(\frac{\partial A_{HT,in,MC,Slab}}{\partial N_{MC,Slab}} U_{N_{MC,Slab}} \right)^2 + \left(\frac{\partial A_{HT,in,MC,Slab}}{\partial A_{HT,in,MC}} U_{A_{HT,in,MC}} \right)^2 } \qquad \text{(C.117)}$$

Where,

$$\frac{\partial A_{HT,in,MC,Slab}}{\partial N_{MC,Slab}} = A_{HT,in,MC} \qquad \text{(C.118)}$$

$$\frac{\partial A_{HT,in,MC,Slab}}{\partial A_{HT,in,MC}} = N_{MC,Slab} \qquad \text{(C.119)}$$

The expression for the combined inner heat transfer surface area of all microchannels within all heat transferring slabs is given as follows.

$$A_{HT,in,MC,HX} = N_{HT,Slab,HX} A_{HT,in,MC,Slab} \qquad \text{(C.120)}$$

Its uncertainty is calculated as follows.

$$U_{A_{HT,in,MC,HX}} = \pm \sqrt{\left(\frac{\partial A_{HT,in,MC,HX}}{\partial N_{HT,Slab,HX}} U_{N_{HT,Slab,HX}} \right)^2 + \left(\frac{\partial A_{HT,in,MC,HX}}{\partial A_{HT,in,MC,Slab}} U_{A_{HT,in,MC,Slab}} \right)^2} \qquad \text{(C.121)}$$

Where,

$$\frac{\partial A_{HT,in,MC,HX}}{\partial N_{HT,Slab,HX}} = A_{HT,in,MC,Slab} \qquad \text{(C.122)}$$

$$\frac{\partial A_{HT,in,MC,HX}}{\partial A_{HT,in,MC,Slab}} = N_{HT,Slab,HX} \qquad \text{(C.123)}$$

The expression for the ratio of air side to liquid side heat transfer area is given as follows.

$$r_{A,HT,a2Liq} = A_{HT,a,HX} / A_{HT,in,MC,HX} \qquad \text{(C.124)}$$

Its uncertainty is calculated as follows.

$$U_{r_{A,HT,a2Liq}} = \pm \sqrt{\left(\frac{\partial r_{A,HT,a2Liq}}{\partial A_{HT,a,HX}} U_{A_{HT,a,HX}} \right)^2 + \left(\frac{\partial r_{A,HT,a2Liq}}{\partial A_{HT,in,MC,HX}} U_{A_{HT,in,MC,HX}} \right)^2} \qquad \text{(C.125)}$$

Where,

$$\frac{\partial r_{A,HT,Air2Liq}}{\partial A_{HT,Air,HX}} = 1 / A_{HT,in,MC,HX} \qquad \text{(C.126)}$$

$$\frac{\partial r_{A,HT,Air2Liq}}{\partial A_{HT,in,MC,HX}} = -A_{HT,Air,HX} \,/\, A_{HT,in,MC,HX}^2 \tag{C.127}$$

The expression for the liquid side heat transfer surface area density is given as follows.

$$\beta_{A-Liq2V-HX} = A_{HT,in,MC,HX} \,/\, \forall_{HX} \tag{C.128}$$

Its uncertainty is calculated as follows.

$$U_{\beta_{A-Liq2V-HX}} = \pm\sqrt{\left(\frac{\partial \beta_{A-Liq2V-HX}}{\partial A_{HT,in,MC,HX}} U_{A_{HT,in,MC,HX}}\right)^2 + \left(\frac{\partial \beta_{A-Liq2V-HX}}{\partial \forall_{HX}} U_{\forall_{HX}}\right)^2} \tag{C.129}$$

Where,

$$\frac{\partial \beta_{A-Liq2V-HX}}{\partial A_{HT,in,MC,HX}} = 1 \,/\, \forall_{HX} \tag{C.130}$$

$$\frac{\partial \beta_{A-Liq2V-HX}}{\partial \forall_{HX}} = -A_{HT,in,MC,HX} \,/\, \forall_{HX}^2 \tag{C.131}$$

The expression for the volume of liquid refrigerant within the heat transferring lengths of all microchannels in the heat exchanger is given as follows.

$$\forall_{HT,Liq,HX} = A_{XS,HT,MC,HX} L_{HT,Slab} \tag{C.132}$$

Its uncertainty is calculated as follows.

$$U_{\forall_{HT,Liq,HX}} = \pm\sqrt{\left(\frac{\partial \forall_{HT,Liq,HX}}{\partial A_{XS,HT,MC,HX}} U_{A_{XS,HT,MC,HX}}\right)^2 + \left(\frac{\partial \forall_{HT,Liq,HX}}{\partial L_{HT,Slab}} U_{L_{HT,Slab}}\right)^2} \tag{C.133}$$

Where,

$$\frac{\partial \forall_{HT,Liq,HX}}{\partial A_{XS,HT,MC,HX}} = L_{HT,Slab} \tag{C.134}$$

$$\frac{\partial \forall_{HT,Liq,HX}}{\partial L_{HT,Slab}} = A_{XS,HT,MC,HX} \tag{C.135}$$

The expression for the liquid side heat transfer surface area per unit liquid side heat transfer volume is given as follows.

$$\beta_{A-Liq2V-Liq} = A_{HT,in,MC,HX} / \forall_{HT,Liq,HX} \tag{C.136}$$

Its uncertainty is calculated as follows.

$$U_{\beta_{A-Liq2V-Liq}} = \pm\sqrt{\left(\frac{\partial \beta_{A-Liq2V-Liq}}{\partial A_{HT,in,MC,HX}} U_{A_{HT,in,MC,HX}}\right)^2 + \left(\frac{\partial \beta_{A-Liq2V-Liq}}{\partial \forall_{HT,Liq,HX}} U_{\forall_{HT,Liq,HX}}\right)^2} \tag{C.137}$$

Where,

$$\frac{\partial \beta_{A-Liq2V-Liq}}{\partial A_{HT,in,MC,HX}} = 1 / \forall_{HT,Liq,HX} \tag{C.138}$$

$$\frac{\partial \beta_{A-Liq2V-Liq}}{\partial \forall_{HT,Liq,HX}} = -A_{HT,in,MC,HX} / \forall_{HT,Liq,HX}^2 \tag{C.139}$$

All the uncertainties and nominal values of key heat exchanger dimensions used and calculated from the above equations have been tabulated in appendix B.

C.3 Uncertainty in data acquisition components

The following sections illustrate the bias errors inherent to various data acquisition components. The measurements taken with these DAQ components will involve both these bias errors and precision errors resulting from all the measurements taken at 1 kHz over the data collection duration (*i.e.* 3-4 minutes).

C.3.1 Uncertainty inherent to data acquisition card

The DAQ card contributes a bias error to the measurements of the collected data. A set of elemental errors comprise this bias error. These errors are contributed by Least Significant Bit (LSB), Relative accuracy, Differential Non Linearity (DNL), and offset error. These elemental bias error sources and the uncertainty inherent to the DAQ card (*i.e.* its bias error) calculated through RSS are shown as follows.

$$B_1 = LSB = \frac{\text{Peak to Peak Voltage}}{2^{\text{\# of Bits}}} = \frac{\left[50 - (-50)\right] \times 10^{-3} V}{2^{16}} = 1.523 \times 10^{-6} V$$

$$B_2 = \text{Relative Accuracy} = \pm 1.5 LSB = 2.289 \times 10^{-6} V$$

$$B_3 = \text{Differential Non Linearity} = DNL_{DAQ-Card} = \pm 0.5 LSB = 7.629 \times 10^{-7} V$$

$$B_4 = \text{Offset Error} \left(\text{Pre Gain, Post Calibration}\right) = \pm 1.0 \times 10^{-6} V$$

$$\therefore B_{DAQ-Card} = \sqrt{B_1^2 + B_2^2 + B_3^2 + B_4^2} = 3.025 \times 10^{-6} V \qquad (C.140)$$

C.3.2 Uncertainty inherent to signal conditioner

The SCXI signal conditioner is situated upstream of DAQ card in the signal stream. Since it conditions the signal to appropriate form for DAQ card to interpret, any errors of signal conditioning will influence the measurement of the collected data. The bias error

contributed by the signal conditioner includes two elemental errors. These are Differential Non Linearity, and offset error. The uncertainty inherent to the signal conditioner (*i.e.* its bias error) is calculated through RSS, of these elemental errors as follows.

$$B_1 = \text{Differential Non Linearity } = \pm 0.005\% FSR = \pm \frac{0.005}{100}\left[50 - (-50)\right] \times 10^{-3}V = 5 \times 10^{-6}V$$

$$B_2 = \text{Offset Error} = \pm 1.5 \times 10^{-6}V$$

$$\therefore B_{SCXI} = \sqrt{B_1^2 + B_2^2} = 5.22 \times 10^{-6}V \qquad\qquad (C.141)$$

C.3.3 Uncertainty inherent to terminal block

The terminal block is integrated with the signal conditioner and in absence of adequate accuracy information; its uncertainty is not calculated individually. It is assumed that the uncertainties of signal conditioner account for the terminal block as well. Hence on an individual basis the terminal block is assigned an uncertainty of zero.

C.3.4 Overall uncertainty in data acquisition components

The overall uncertainty in data acquisition component is therefore computed through the RSS of the individual uncertainties from section C.3.1 to C.3.3. It is presented as follows.

$$\therefore B_{DAQ-System} = \sqrt{B_{DAQ-Card}^2 + B_{SCXI}^2} = 6.033 \times 10^{-6}V \qquad\qquad (C.142)$$

C.4 Uncertainty in glycol temperatures (inlet, outlet, bulk, ΔT_g)

The uncertainties in glycol temperature measurements are contributed by the bias errors of the temperature measurement sensors (*i.e.* RTDs), random errors due to scatter of the

data collected, as well as the DAQ component uncertainties. Detail methodology of this uncertainty estimation is provided in the following sections.

RTD   Terminal Block Signal Conditioner DAQ Card
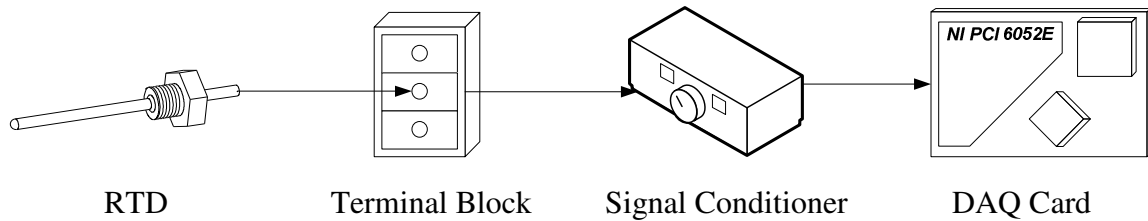
Figure C.1: Signal stream for RTD temperature measurement

C.4.1 Uncertainty inherent to liquid side RTDs

The bias error associated with the inlet and outlet Ultra Precise RTDs have been supplied by their manufacturer Omega Engineering. The bias error as a function of temperature is provided as follows.

$$B_{RTD} = \pm \frac{1}{10} \Big[0.3 + 0.005 \big| T \left({}^{\circ}C \right) \big| \Big] \tag{C.143}$$

C.4.2 Random errors in glycol temperature measurement

The random errors in glycol inlet and outlet temperature measurement are found based on the scatter of the data. This random error is presented in terms of precision error. The precision error is found by knowing three information. They are:

 (1) Total number of temperature samples collected.

 (2) Standard deviation of the temperature samples acquired.

 (3) Student t-distribution value based on the total number of samples.

Once these three information are known, the precision error in inlet and outlet glycol temperature measurement is found through the following equation.

$$P_{RTD} = \pm t_{N,95\%} S_{\overline{T}} \approx \pm 1.96 \frac{S_{T,RTD}}{\sqrt{N}} \quad [\because N \geq 1000] \tag{C.144}$$

C.4.3 Overall uncertainty in glycol temperature measurement

The overall uncertainty in glycol inlet and outlet temperature measurement due to RTD alone is therefore given by the RSS of bias and precision errors as follows.

$$U_{RTD} = \pm \sqrt{B_{RTD}^2 + P_{measurement}^2} = \pm \sqrt{\left[\frac{1}{10}\left(0.3 + 0.005|T|\right)\right]^2 + \left(1.96\frac{S_{T,RTD}}{\sqrt{N}}\right)^2} \tag{C.145}$$

The sensitivity of the inlet and outlet RTD measurement (Volts/unit temperature) is calculated by differentiating the RTD voltage-temperature equation, to find the slope at the inlet and outlet temperatures from the following equations.

RTD Temperature – Resistance Equation:

$$R_T = R_o \left[1 + AT + BT^2\right] \tag{C.146}$$

Where,

$$R_o = 100\Omega$$
$$A = 3.9080 \times 10^{-3}$$
$$B = -5.8019 \times 10^{-7}$$
$$I_{Excitation} = 100 \times 10^{-6} A$$

RTD Voltage Output:

$$V_{RTD} = I_{Excitation} R_T = I_{Excitation} R_o \left[1 + AT + BT^2\right] \tag{C.147}$$

Therefore, RTD Sensitivity:

$$K = \frac{\partial V_{RTD}}{\partial T} = I_{Excitation} R_o \left[A + 2BT\right] = 3.908 \times 10^{-5} - 1.1604 \times 10^{-8} T \tag{C.148}$$

Using the sensitivity of the RTDs, the uncertainty of the DAQ components can be translated from voltage to $°C$ as follows.

$$
\begin{aligned}
U_{DAQ} &= \pm 6.033 \times 10^{-6} V = \pm \frac{6.033 \times 10^{-6} V}{K_{RTD}} \quad °C \\
&= \pm \frac{6.033 \times 10^{-6}}{3.908 \times 10^{-5} - 1.1604 \times 10^{-8} T} \quad °C
\end{aligned}
\tag{C.149}
$$

Hence the overall uncertainty in the nominal inlet and outlet glycol temperature acquired is therefore calculated through RSS of the individual uncertainties of RTD and DAQ component by the following.

$$
\begin{aligned}
\therefore U_{T,Glycol} &= \pm \sqrt{U_{DAQ}^2 + U_{RTD}^2} \\
&= \pm \sqrt{\left(\frac{6.033 \times 10^{-6} V}{3.908 \times 10^{-5} - 1.1604 \times 10^{-8} |T|} \right)^2 + \left[\frac{1}{10} \left(0.3 + 0.005 |T| \right) \right]^2 + \left(1.96 \frac{S_{T,RTD}}{\sqrt{N}} \right)^2} \quad °C
\end{aligned}
\tag{C.150}
$$

The bulk temperature is the sum of inlet and outlet nominal temperatures. Since it is a function of two lower level parameters, the method 3 is used to find the uncertainty in bulk temperature as follows.

$$
T_{g,b} = \frac{T_{g,i} + T_{g,o}}{2}
\tag{C.151}
$$

$$
U_{T_{g,b}} = \sqrt{\left(\frac{\partial T_{g,b}}{\partial T_{g,i}} U_{T_{g,i}} \right)^2 + \left(\frac{\partial T_{g,b}}{\partial T_{g,o}} U_{T_{g,o}} \right)^2}
\tag{C.152}
$$

Where,
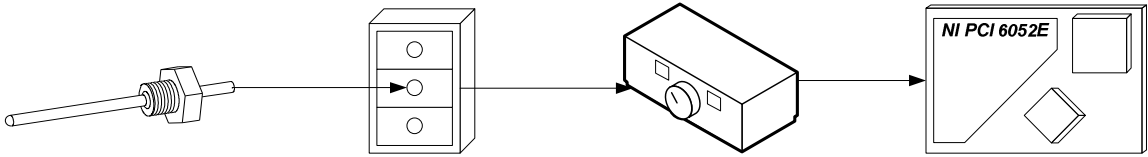
$$
\frac{\partial T_{g,b}}{\partial T_{g,i}} = \frac{1}{2}
\tag{C.153}
$$

$$
\frac{\partial T_{g,b}}{\partial T_{g,o}} = \frac{1}{2}
\tag{C.154}
$$

The difference between the glycol inlet and outlet temperatures (ΔT_g) is calculated by subtracting outlet temperature from the inlet. Since both of these temperatures have the same bias error contributions from DAQ components and RTD, they are cancelled by each other when subtracting one from the other. The inlet and outlet temperatures are however subject to different amounts of precision error resulting from different scatter in the data collected. As such, the uncertainty in the temperature difference is due to their individual precision errors only. The uncertainty in temperature difference is therefore calculated from the RSS of these precision errors as follows.

$$\therefore U_{\Delta T, Glycol} = \pm\sqrt{P_{DAQ}^2 + P_{RTD,i}^2 + P_{RTD,o}^2} = \sqrt{\left(1.96\frac{S_{T,RTD,i}}{\sqrt{N}}\right)^2 + \left(1.96\frac{S_{T,RTD,o}}{\sqrt{N}}\right)^2} \quad \text{(C.155)}$$

Table C.2: Summary of glycol temperature uncertainty calculation

RTD	Terminal Block	Signal Conditioner	DAQ Card
$B_{RTD} =$ $\pm\frac{1}{10}\left[\begin{array}{l}0.3+\\0.005\left\|T\left(°C\right)\right\|\end{array}\right]$ $P_{RTD} = \left(1.96\frac{S_{T,RTD,i}}{\sqrt{N}}\right)$ $U_{RTD} = \sqrt{B_{RTD}^2 + P_{RTD}^2}$	$B_{TB} = 0$ $P_{TB} = 0$ $U_{TB} = 0$	$B_1 = DNL$ $B_2 = Offset$ $U_{SCXI} = \sqrt{B_1^2 + B_2^2}$ *DNL*: Differential Non Linearity	$B_1 = LSB$ $B_2 = Relative$ $B_3 = DNL$ $B_4 = Offset$ $U_{DAQ\atop Card} = \sqrt{\begin{array}{l}B_1^2 + B_2^2\\+\\B_3^2 + B_4^2\end{array}}$
	$U_{DAQ} = B_{DAQ} = \sqrt{B_{DAQ-Card}^2 + B_{SCXI}^2} = 6.033\times10^{-6}V$		
	$U_{T,Glycol} = \pm\sqrt{U_{DAQ}^2 + U_{RTD}^2}$	$U_{\Delta T,Glycol} = \pm\sqrt{P_{RTD,i}^2 + P_{RTD,o}^2}$	

C.5 Uncertainty in air temperatures (inlet, outlet, bulk, ΔT$_a$)

The uncertainties in air temperature measurements using thermocouples alone are contributed by the bias, and random errors from three error groups. These error groups are (1) Instrument error, (2) Spatial variation error, and (3) Temporal variation error. Error group (2) applies here due to the fact that a total of 9 and 25 equally spaced thermocouples are used at the inlet and the exit of the test chamber, hence providing with a spatial temperature variation. Error group (3) is considered since the measurements are taken at 1 kHz sampling rate for a period of three to four minutes, which leads to a temporal temperature variation. In addition to the errors from these source groups, the DAQ component uncertainties also contribute to the overall uncertainties in temperature measurement. Detail methodology of this uncertainty estimation is provided in the following sections.
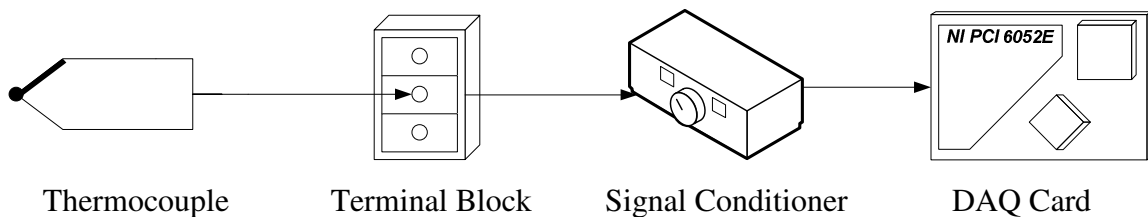
Figure C.2: Signal stream for thermocouple temperature measurement

C.5.1 Uncertainty inherent to air side thermocouples

Only error group (1) contributes to the bias error for the thermocouples. Since the thermocouples are well calibrated, the effect of uncalibrated thermocouple bias is greatly reduced from the measurements. Therefore the bias error from error group (1) is assumed to be 0.1 °C, as follows.

$$B_1 = 0.1\,^{\circ}C \tag{C.156}$$

It is also assumed that all inlet and outlet thermocouples are calibrated to the same extent, and as such, there is no significant difference in bias error between them. Therefore error group (2) does not contribute to bias error.

$$B_2 = 0\,^{\circ}C \qquad (C.157)$$

Also, since error group (3) deals with temporal variation, there is no bias error contribution from this group as well.

$$B_3 = 0\,^{\circ}C \qquad (C.158)$$

The bias index is therefore as follows.

$$B_{Thermocouple} = \sqrt{B_1^2 + B_2^2 + B_3^2} \qquad (C.159)$$

C.5.2 Random errors in air temperature measurement

The error groups (2), and (3) account for the spatial and temporal variations in temperature measurements. These are the contributors of random/precision errors in temperature measurement using thermocouples. Error group (1) deals with design stage uncertainty, and therefore does not provide any precision error.

$$P_1 = 0 \qquad (C.160)$$

The contribution to random error from error group (2), based on $N = 180,000 \sim 240,000$ readings from $M = 9$ inlet, and $M = 25$ outlet thermocouples is given as follows.

$$P_2 = \frac{S_T}{\sqrt{M}} \qquad (C.161)$$

Where,

$$S_T = \sqrt{\frac{\sum_{m=1}^{M}\left(\overline{T}_m - \left\langle \overline{T} \right\rangle\right)^2}{M-1}} \tag{C.162}$$

$$\left\langle \overline{T} \right\rangle = \frac{1}{M}\sum_{m=1}^{M}\overline{T}_m \tag{C.163}$$

$$\overline{T}_m = \frac{1}{N}\sum_{n=1}^{N}T_{mn} \tag{C.164}$$

$$\nu_2 = M - 1 \tag{C.165}$$

ν_{28} : Degree of freedom associated with this precision error

$\overline{T}_m$: Mean of 180,000~240,000 reading from a particular thermocouple

$\left\langle \overline{T} \right\rangle$: Mean of individual thermcouple means at the inlet and outlet respectively

S_T : Standard Deviation of individual thermcouple means at the inlet/outlet respectively

The contribution to random error from error group (3), based on the total number of temperature samples collected from 9 inlet and 25 outlet thermocouples is given as follows.

$$P_3 = \frac{\left\langle S_{T,Pooled} \right\rangle}{\sqrt{MN}} \tag{C.166}$$

Where,

$$S_{T,Pooled} = \sqrt{\frac{\sum_{m=1}^{9}\sum_{n=1}^{N}\left(\overline{T}_{mn} - \left\langle \overline{T} \right\rangle\right)^2}{M(N-1)}} \tag{C.167}$$

$$\nu_3 = M(N-1) \tag{C.168}$$

ν_3 : Degree of freedom associated with this precision error

$S_{T,Pooled}$: Pooled Standard Deviation of based on total thermocouples and samples

The precision index is therefore as follows.

$$P_{Thermocouple} = \sqrt{P_1^2 + P_2^2 + P_3^2}$$ (C.169)

C.5.3 Overall uncertainty in air temperature measurement

The overall uncertainty in temperature measurement has contribution from both the thermocouples alone and also the DAQ system uncertainties.

The precision index is composed of elements that have different degree of freedom. The degree of freedom for the precision index is computed through Welch-Satterthwaite formula as follows.

$$\nu = \frac{\left(\sum_{i=1}^{3} P_i^2 \right)^2}{\sum_{i=1}^{3} \left(P_i^4 / \nu_i \right)} = \frac{\left(P_2^2 + P_3^2 \right)^2}{\dfrac{P_2^4}{\nu_2} + \dfrac{P_3^4}{\nu_3}}$$ (C.170)

and, $$t_{\nu,95} = 1.96 \quad [N > 1000]$$ (C.171)

Once the degree of freedom for precision index is determined, the uncertainty of measurement for the thermocouples alone (discounting DAQ system), is found through RSS of the bias and precision index as follows.

$$U_{Thermocouple} = \sqrt{B_{Thermocouple}^2 + \left(t_{\nu,95} P_{Thermocouple} \right)^2}$$ (C.172)

Using the sensitivity of the T-type thermocouples, the uncertainty of the DAQ components can be translated from voltage to $°C$ as follows.

$$K_{Thermocouple} = 43 \times 10^{-6} \, V\!\!\Big/\!_{°C}$$ (C.173)

$$U_{DAQ} = \pm 6.033 \times 10^{-6} V = \frac{6.033 \times 10^{-6} V}{K_{Thermocouple}} = \frac{6.033 \times 10^{-6} V}{43 \times 10^{-6} V/_{\circ C}} = 0.14 \, ^{\circ}C \qquad (C.174)$$

Hence the overall uncertainty in the nominal inlet and outlet air temperature acquired is therefore calculated through RSS of the individual uncertainties of the thermocouples and DAQ component by the following.

$$U_{T_a} = \sqrt{U_{DAQ}^2 + U_{Thermocouple}^2} \qquad (C.175)$$

The bulk temperature is the sum of inlet and outlet nominal temperatures. Since it is a function of two lower level parameters, the method 3 is used to find the uncertainty in bulk temperature as follows.

$$T_{a,b} = \frac{T_{a,i} + T_{a,o}}{2} \qquad (C.176)$$

$$U_{T_{a,b}} = \sqrt{\left(\frac{\partial T_{a,b}}{\partial T_{a,i}} U_{T_{a,i}}\right)^2 + \left(\frac{\partial T_{a,b}}{\partial T_{a,o}} U_{T_{a,o}}\right)^2} \qquad (C.177)$$

Where,

$$\frac{\partial T_{a,b}}{\partial T_{a,i}} = \frac{1}{2} \qquad (C.178)$$
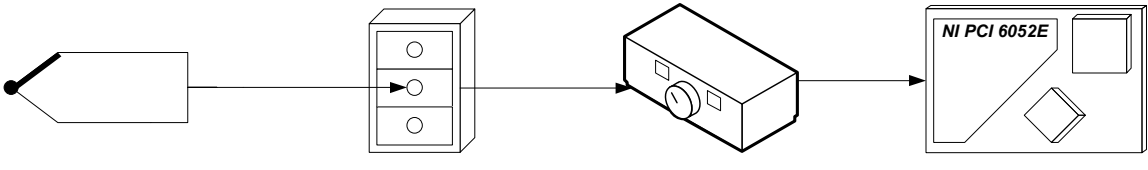
$$\frac{\partial T_{a,b}}{\partial T_{a,o}} = \frac{1}{2} \qquad (C.179)$$

The difference between the air inlet and outlet temperatures (ΔT_a) is calculated by subtracting the outlet temperature from the inlet. Since both of these temperatures have the same bias error contributions from DAQ components and thermocouples, they are cancelled by each other when subtracting one from the other. The inlet and outlet temperatures are however subject to different amounts of precision error resulting from different scatter in the data collected. As such, the uncertainty in the temperature

difference is due to their individual precision errors only. The uncertainty in difference in air temperature is therefore calculated from the RSS of these precision errors as follows.

$$U_{\Delta T} = \sqrt{P_{DAQ}^2 + P_{Thermocouple}^2} \qquad (C.180)$$

Table C.3: Summary of air temperature uncertainty calculation

Thermocouple	Terminal Block	Signal Conditioner	DAQ Card
$B_1 = P_1 = Instrumental$	$B_{TB} = 0$	$B_1 = DNL$	$B_1 = LSB$
$B_2 = P_2 = Spatial$	$P_{TB} = 0$	$B_2 = Offset$	$B_2 = Relative$
$B_3 = P_3 = Temporal$	$U_{TB} = 0$	$U_{SCXI} = \sqrt{B_1^2 + B_2^2}$	$B_3 = DNL$
$B = \sqrt{B_1^2 + B_2^2 + B_3^2}$			$B_4 = Offset$
$P = \sqrt{P_1^2 + P_2^2 + P_3^2}$			
$\nu = \dfrac{\left(P_2^2 + P_3^2\right)^2}{\dfrac{P_2^4}{\nu_2} + \dfrac{P_3^4}{\nu_3}}$		*DNL*: Differential Non Linearity	$U_{DAQ \atop Card} = \sqrt{\begin{array}{c} B_1^2 + B_2^2 \\ + \\ B_3^2 + B_4^2 \end{array}}$
$U_{Therm} = \sqrt{B^2 + \left(t_{\nu,95} P\right)^2}$			
	$U_{DAQ} = B_{DAQ} = \sqrt{B_{DAQ-Card}^2 + B_{SCXI}^2} = 6.033 \times 10^{-6} V$		
$U_{T,Air} = \pm\sqrt{U_{DAQ}^2 + U_{Therm}^2}$		$U_{\Delta T,Air} = \sqrt{P_{DAQ}^2 + P_{Therm}^2}$	

C.6 Uncertainty in glycol pressures

The uncertainties in glycol pressure measurements are contributed by the bias errors of the pressure measurement sensors (*i.e.* PTDs), the random errors due to scatter of the data collected, as well as the DAQ component uncertainties. Detail methodology of this uncertainty estimation is provided in the following sections.

| PTD | Terminal Block | Signal Conditioner | DAQ Card |
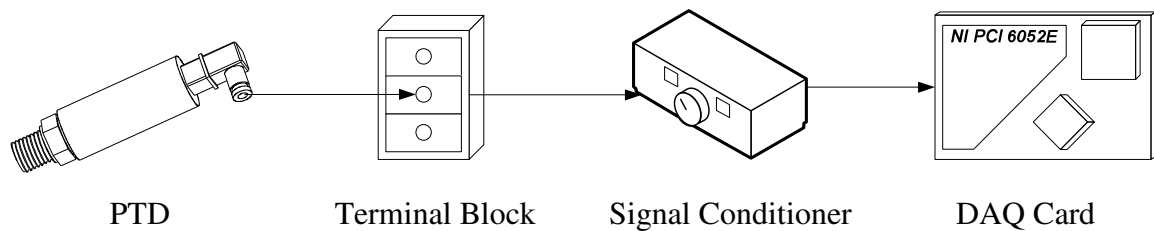
Figure C.3: Signal stream for PTD pressure measurement

C.6.1 Uncertainty inherent to liquid side PTDs

The bias error associated with the inlet and outlet PX series PTDs are supplied by their manufacturer Omega Engineering.

Based on the available information the bias error for the inlet pressure transducer has four individual contributors. These are instrument accuracy (taking into account linearity, hysteresis, and repeatability), zero balance, span setting, and thermal effects. The bias error for the inlet PTD is therefore computed through RSS and is given as follows.

$$B_{PTD-inlet} = \pm\sqrt{B^2_{Accuracy} + B^2_{0-Offset} + B^2_{Span-Setting} + B^2_{Thermal-Effect}}$$

$$= \pm\sqrt{\left(\frac{0.25}{100}FSO\right)^2 + \left(\frac{2}{100}FSO\right)^2 + \left(\frac{1.5}{100}FSO\right)^2 + \left(\frac{0.04}{100}|T|FSO\right)^2}$$

$$= \pm\sqrt{6.3125\times10^{-4}\,FSO^2 + 1.6\times10^{-7}\,FSO^2\,|T|^2}$$

$$= \pm\sqrt{FSO^2\left(6.3125\times10^{-4} + 1.6\times10^{-7}\,|T|^2\right)} \qquad (C.181)$$

$$= \pm FSO\sqrt{6.3125\times10^{-4} + 1.6\times10^{-7}\,|T|^2}$$

$$= \pm5\sqrt{6.3125\times10^{-4} + 1.6\times10^{-7}\,|T|^2}\,V$$

Also based on the available information the bias error for the outlet pressure transducer has three individual contributors. These are instrument accuracy (takes into account linearity, hysteresis, and repeatability), zero balance, and span setting. The bias error for the outlet PTD is given as follows.

$$B_{PTD-Outlet} = \pm\sqrt{B^2_{Accuracy} + B^2_{0-Offset} + B^2_{Span-Setting}}$$

$$= \pm\sqrt{\left(\frac{0.25}{100}FSO\right)^2 + \left(\frac{2}{100}FSO\right)^2 + \left(\frac{1.5}{100}FSO\right)^2}$$

$$= \pm\sqrt{6.3125\times10^{-4}\,FSO^2} \qquad (C.182)$$

$$= \pm2.5125\times10^{-2}\,FSO$$

$$= \pm0.12562V$$

C.6.2 Random errors in glycol pressure measurement

The random errors in glycol inlet and outlet pressure measurement are found based on the scatter of the data. This random error is presented in terms of precision error. The precision error is found by knowing the following 3 information:

    (1) Total number of pressure samples collected.

    (2) Standard deviation of the pressure samples acquired.

    (3) Student t-distribution value based on the total number of samples.

Once this information is known the precision error in glycol inlet and outlet pressure measurement is found through the following equations.

$$P_{PTD-inlet} = \pm t_{N,95\%} S_{\bar{P}} \approx \pm 1.96 \frac{S_{p,PTD-inlet}}{\sqrt{N}} \quad [\because N \geq 1000] \tag{C.183}$$

$$P_{PTD-Outlet} = \pm t_{N,95\%} S_{\bar{P}} \approx \pm 1.96 \frac{S_{p,PTD-Outlet}}{\sqrt{N}} \quad [\because N \geq 1000] \tag{C.184}$$

C.6.3 Overall uncertainty in glycol pressure measurement (inlet, outlet, and bulk)

The overall uncertainty in glycol inlet and outlet pressure measurement due to PTD alone is therefore given by the RSS of bias and precision errors as follows.

$$
\begin{aligned}
U_{PTD-inlet} &= \pm \sqrt{B_{PTD-inlet}^2 + P_{PTD-inlet}^2} \\
&= \pm \sqrt{FSO^2 \left(6.3125 \times 10^{-4} + 1.6 \times 10^{-7} |T|^2\right) + \left(1.96 \frac{S_{p,PTD-inlet}}{\sqrt{N}}\right)^2} \\
&= \pm \sqrt{1.5781 \times 10^{-2} + 4 \times 10^{-6} |T|^2 + \left(1.96 \frac{S_{p,PTD-inlet}}{\sqrt{N}}\right)^2} \, V
\end{aligned}
\tag{C.185}
$$

$$
\begin{aligned}
U_{PTD-Outlet} &= \pm \sqrt{B_{PTD-Outlet}^2 + P_{PTD-Outlet}^2} \\
&= \pm \sqrt{6.3125 \times 10^{-4} FSO^2 + \left(1.96 \frac{S_{p,PTD-Outlet}}{\sqrt{N}}\right)^2} \\
&= \pm \sqrt{1.5781 \times 10^{-2} + \left(1.96 \frac{S_{p,PTD-Outlet}}{\sqrt{N}}\right)^2} \, V
\end{aligned}
\tag{C.186}
$$

Hence the overall uncertainty in the nominal inlet and outlet glycol pressure acquired is therefore calculated through RSS of the individual uncertainties of PTD and DAQ component by the following.

$$U_{PTD-inlet(+)DAQ-System[V]} = \pm\sqrt{U^2_{PTD-inlet} + U^2_{DAQ-System}}$$

$$= \pm\sqrt{\begin{array}{l} FSO^2\left(6.3125\times10^{-4} + 1.6\times10^{-7}|T|^2\right) \\ + \left(1.96\dfrac{S_{p,PTD-inlet}}{\sqrt{N}}\right)^2 + \left(6.033\times10^{-6}\right)^2 \end{array}} \quad V \qquad (C.187)$$

$$= \pm\sqrt{1.5781\times10^{-2} + 4\times10^{-6}|T|^2 + \left(1.96\dfrac{S_{p,PTD-inlet}}{\sqrt{N}}\right)^2} \quad V$$

$$U_{PTD-Outlet(+)DAQ-System[V]} = \pm\sqrt{U^2_{PTD-Outlet} + U^2_{DAQ-System}}$$

$$= \pm\sqrt{\begin{array}{l} 6.3125\times10^{-4}FSO^2 \\ + \left(1.96\dfrac{S_{p,PTD-Outlet}}{\sqrt{N}}\right)^2 + 6.033\times10^{-6} \end{array}} \quad V \qquad (C.188)$$

$$= \pm\sqrt{1.5787\times10^{-2} + \left(1.96\dfrac{S_{p,PTD-Outlet}}{\sqrt{N}}\right)^2} \quad V$$

The sensitivity of the inlet and outlet PTD measurement (Pressure/Voltage) is taken from the slope of pressure-voltage calibration curve provided by the manufacturer is given below.

$$K_{PTD-inlet} = 20.773 kPa/V \qquad (C.189)$$
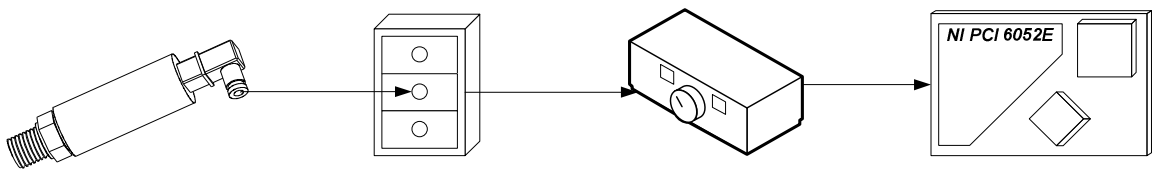
$$K_{PTD-Outlet} = 6.895 kPa/V \qquad (C.190)$$

Using the sensitivity of the PTDs, the combined uncertainty of inlet side with DAQ components and outlet side with DAQ components can be translated from voltage to kPa as follows.

$$U_{PTD-inlet(+)DAQ-System[kPa]} = \pm K_{PTD-inlet} U_{PTD-inlet+DAQ-System[V]}$$

$$= \pm 20.773 \sqrt{\begin{array}{l} FSO^2 \left(6.3125 \times 10^{-4} + 1.6 \times 10^{-7} |T|^2\right) \\ + \left(1.96 \dfrac{S_{p,PTD-inlet}}{\sqrt{N}}\right)^2 + \left(6.033 \times 10^{-6}\right)^2 \end{array}} \quad kPa \quad (C.191)$$

$$= \pm 20.773 \sqrt{\begin{array}{l} 1.5781 \times 10^{-2} + 4 \times 10^{-6} |T|^2 \\ + \left(1.96 \dfrac{S_{p,PTD-inlet}}{\sqrt{N}}\right)^2 \end{array}} \quad kPa$$

$$U_{PTD-Outlet(+)DAQ-System[kPa]} = \pm K_{PTD-Outlet} U_{PTD-Outlet+DAQ-System[V]}$$

$$= \pm 6.895 \sqrt{\begin{array}{l} 6.3125 \times 10^{-4} FSO^2 \\ + \left(1.96 \dfrac{S_{p,PTD-Outlet}}{\sqrt{N}}\right)^2 + \left(6.033 \times 10^{-6}\right)^2 \end{array}} \quad kPa \quad (C.192)$$

$$= \pm 6.895 \sqrt{1.5781 \times 10^{-2} + \left(1.96 \dfrac{S_{p,PTD-Outlet}}{\sqrt{N}}\right)^2} \quad kPa$$

Table C.4: Summary of glycol pressure uncertainty calculation

PTD	Terminal Block	Signal Conditioner	DAQ Card
$B_1 = Accuracy$	$B_{TB} = 0$	$B_1 = DNL$	$B_1 = LSB$
$B_2 = 0 - Offset$	$P_{TB} = 0$	$B_2 = Offset$	$B_2 = Relative$
$B_3 = Span$	$U_{TB} = 0$	$U_{SCXI} = \sqrt{B_1^2 + B_2^2}$	$B_3 = DNL$
$B_4 = Thermal$			$B_4 = Offset$
$B_{PTD} = \sqrt{\begin{array}{c} B_1^2 + B_2^2 \\ + \\ B_3^2 + B_4^2 \end{array}}$		*DNL*: Differential Non Linearity	$U_{\substack{DAQ \\ Card}} = \sqrt{\begin{array}{c} B_1^2 + B_2^2 \\ + \\ B_3^2 + B_4^2 \end{array}}$
$P_{PTD} = \left(1.96 \dfrac{S_{p,PTD}}{\sqrt{N}} \right)$			
$U_{PTD} = \sqrt{B_{PTD}^2 + P_{PTD}^2}$			
	$U_{DAQ} = B_{DAQ} = \sqrt{B_{DAQ-Card}^2 + B_{SCXI}^2} = 6.033 \times 10^{-6} V$		
$U_{p,inlet,Glycol} = \pm K_{PTD-inlet} \sqrt{U_{DAQ}^2 + U_{PTD,i}^2}$		$U_{p,outlet,Glycol} = \pm K_{PTD-outlet} \sqrt{U_{DAQ}^2 + U_{PTD,o}^2}$	

C.7 Uncertainty in air pressures

The uncertainties in air pressure measurements (both differential and dynamic pressures) derive contributions from the bias errors of the pressure measurement sensors (*i.e.* DPTDs), random errors due to scatter of the data collected, as well as the DAQ component uncertainties. Detail methodology of this uncertainty estimation is provided in the following sections.

| DPTD | Terminal Block | Signal Conditioner | DAQ Card |
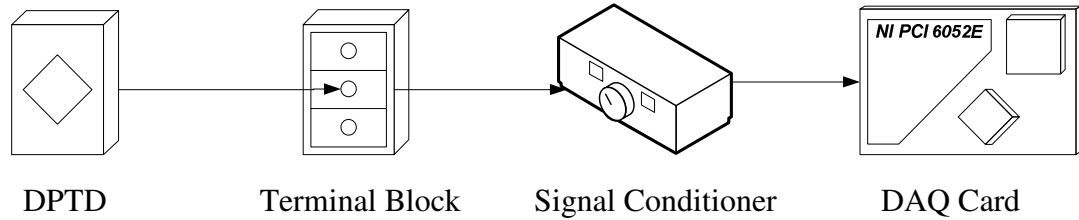
Figure C.4: Signal stream for DPTD pressure measurement

C.7.1 Uncertainty inherent to air side differential PTDs

The bias error associated with the PX series DPTDs used in differential and dynamic pressure measurements have been supplied by their manufacturer Omega Engineering. The same pressure transducer of different range of utilized to measure these pressures.

Based on the available information the bias error for the Pitot tube dynamic pressure measurement DPTD (range 0-1" H_2O) has two individual contributors. These are instrument accuracy (taking into account linearity, hysteresis, and repeatability), and thermal effects. The bias error for the inlet PTD is therefore computed through RSS and is given as follows.

$$
\begin{aligned}
B_{Pitot} &= \pm \sqrt{B_{Accuracy}^2 + B_{Thermal\_Effect}^2} = \pm \sqrt{\left(\frac{1}{100}FS\right)^2 + \left(\frac{0.02}{100}|T|FS\right)^2} \\
&= \pm \sqrt{1 \times 10^{-4} FS^2 + 4 \times 10^{-8} |T|^2 FS^2} \qquad \text{(C.193)} \\
&= \pm \sqrt{0.01 + 4 \times 10^{-6} |T|^2} \quad V
\end{aligned}
$$

Since the differential pressure measuring DPTD is almost identical with the exception of range (range 0-5" H_2O), it has the same two individual contributors with different magnitude of contribution in terms of pressure but not voltage. These contributors are instrument accuracy (takes into account linearity, hysteresis, and repeatability), and thermal effect. The bias error for the differential pressure measuring DPTD is given as follows.

$$B_{\Delta P,HX} = \pm\sqrt{B_{Accuracy}^2 + B_{Thermal\_Effect}^2} = \pm\sqrt{\left(\frac{1}{100}FS\right)^2 + \left(\frac{0.02}{100}|T|FS\right)^2}$$

$$= \pm\sqrt{1\times10^{-4}\,FS^2 + 4\times10^{-8}\,|T|^2\,FS^2} \qquad \text{(C.194)}$$

$$= \pm\sqrt{0.01 + 4\times10^{-6}\,|T|^2}\quad V$$

C.7.2 Random errors in air pressure measurement

The random errors in air dynamic and differential pressure measurement are found based on the scatter of the data. This random error is presented in terms of precision error. The precision error is found by knowing the following 3 information:

    (1) Total number of pressure samples collected.

    (2) Standard deviation of the pressure samples acquired.

    (3) Student t-distribution value based on the total number of samples.

Once this information is known the precision error in air dynamic and differential pressure measurement is found through the following equations.

$$P_{Pitot} = \pm t_{N,95\%}S_{\bar{P}} \approx \pm1.96\frac{S_{Pitot}}{\sqrt{N}} \quad [\because N \geq 1000] \qquad \text{(C.195)}$$

$$P_{\Delta p,HX} = \pm t_{N,95\%}S_{\bar{P}} \approx \pm1.96\frac{S_{\Delta p,HX}}{\sqrt{N}} \quad [\because N \geq 1000] \qquad \text{(C.196)}$$

C.7.3 Overall uncertainty in air pressure measurement

The overall uncertainty in air dynamic and differential pressure measurement due to the respective DPTD alone is therefore given in volts by the RSS of bias and precision errors as follows.

$$U_{Pitot,[V]} = \pm\sqrt{B_{Pitot}^2 + P_{Pitot}^2}$$
$$= \pm\sqrt{\left(0.01 + 4\times10^{-6}|T|^2\right) + \left(1.96\frac{S_{Pitot}}{\sqrt{N}}\right)^2} \quad V \qquad (C.197)$$

$$U_{\Delta p,HX,[V]} = \pm\sqrt{B_{\Delta p,HX}^2 + P_{\Delta p,HX}^2}$$
$$= \pm\sqrt{\left(0.01 + 4\times10^{-6}|T|^2\right) + \left(1.96\frac{S_{\Delta p,HX}}{\sqrt{N}}\right)^2} \quad V \qquad (C.198)$$

Hence the overall uncertainty in the nominal dynamic and differential air pressure acquired is therefore calculated through RSS of the individual uncertainties of the respective DPTD and DAQ component by the following.

$$U_{Dynamic-Pressure} = \pm\sqrt{U_{Pitot}^2 + U_{DAQ}^2}$$
$$= \pm\sqrt{\left(0.01 + 4\times10^{-6}|T|^2\right) + \left(1.96\frac{S_{Pitot}}{\sqrt{N}}\right)^2 + 3.6397\times10^{-11}} \quad V \qquad (C.199)$$

$$U_{Differential-Pressure} = \pm\sqrt{U_{\Delta p,HX}^2 + U_{DAQ}^2}$$
$$= \pm\sqrt{\left(0.01 + 4\times10^{-6}|T|^2\right) + \left(1.96\frac{S_{\Delta p,HX}}{\sqrt{N}}\right)^2 + 3.6397\times10^{-11}} \quad V \qquad (C.200)$$

The sensitivity of the dynamic and differential DPTD measurement (Pressure/Voltage) is taken from the slope of pressure-voltage calibration curve and is given below.

$$K_{Pitot} = 24.49\frac{Pa}{V} \qquad (C.201)$$

$$K_{\Delta p,HX} = 125.5\frac{Pa}{V} \qquad (C.202)$$

Using their respective sensitivities, the combined uncertainties of the dynamic pressure DPTD with DAQ components, and differential pressure DPTDs with DAQ components can be translated from voltage to kPa as follows.
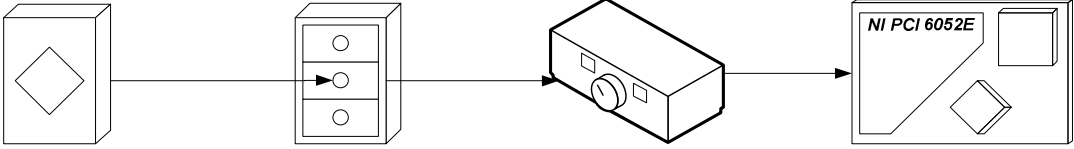
$$U_{Dynamic-Pressure,[Pa]} = \pm K_{pitot} U_{Dynamic-Pressure,[V]}$$
$$= \pm 24.49 \sqrt{\left(0.01 + 4\times10^{-6}|T|^2\right) + 3.6397\times10^{-11} + \left(1.96\frac{S_{Pitot}}{\sqrt{N}}\right)^2} \; Pa \quad \text{(C.203)}$$

$$U_{Differential-Pressure,[Pa]} = \pm K_{\Delta p,HX} U_{Differential-Pressure,[V]}$$
$$= \pm 125.5 \sqrt{\left(0.01 + 4\times10^{-6}|T|^2\right) + 3.6397\times10^{-11} + \left(1.96\frac{S_{\Delta p,HX}}{\sqrt{N}}\right)^2} \; Pa \quad \text{(C.204)}$$

Table C.5: Summary of air pressure uncertainty calculation

DPTD	Terminal Block	Signal Conditioner	DAQ Card
$B_1 = Accuracy$	$B_{TB} = 0$	$B_1 = DNL$	$B_1 = LSB$
$B_2 = Thermal$	$P_{TB} = 0$	$B_2 = Offset$	$B_2 = Relative$
$B_{DPTD} = \sqrt{B_1^2 + B_2^2}$	$U_{TB} = 0$	$U_{SCXI} = \sqrt{B_1^2 + B_2^2}$	$B_3 = DNL$
$P_{DPTD} = \left(1.96\frac{S_{DPTD}}{\sqrt{N}}\right)$			$B_4 = Offset$
$U_{DPTD} = \sqrt{\begin{array}{c}B_{DPTD}^2 \\ + \\ P_{DPTD}^2\end{array}}$		*DNL*: Differential Non Linearity	$U_{\substack{DAQ \\ Card}} = \sqrt{\begin{array}{c}B_1^2 + B_2^2 \\ + \\ B_3^2 + B_4^2\end{array}}$
	$U_{DAQ} = B_{DAQ} = \sqrt{B_{DAQ-Card}^2 + B_{SCXI}^2} = 6.033\times10^{-6}V$		
$U_{Dynamic-Pressure} = \pm K_{pitot}\sqrt{U_{DAQ}^2 + U_{DPTD,Dyn}^2}$		$U_{Differential-Pressure} = \pm K_{\Delta P,HX}\sqrt{U_{DAQ}^2 + U_{DPTD,Diff}^2}$	

C.8 Uncertainty in glycol flow rate

The voltage response of the digital flow meter correlated well with the mass flow rate obtained through bucket and stop watch method. Therefore the uncertainty resulting from digital flow meter can be taken to be the uncertainty in glycol flow rate. The uncertainties in glycol flow rate measurements are contributed by the bias errors of the flow measurement sensors (*i.e.* digital flow meter), random errors due to scatter of the data collected, as well as the DAQ component uncertainties. Detail methodology of this uncertainty estimation is provided in the following sections.
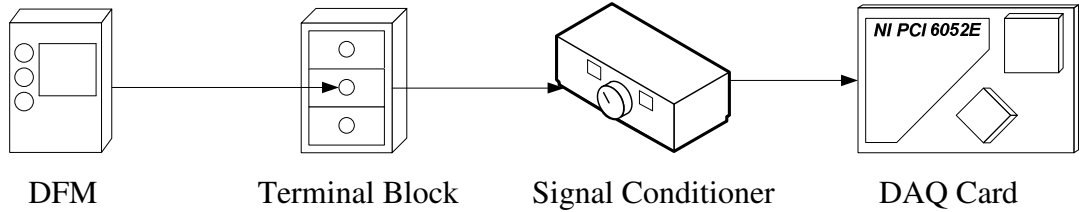
Figure C.5: Signal stream for digital flow meter flow measurement

C.8.1 Uncertainty inherent to liquid side Digital Flow Meter (DFM)

The bias error associated with the DFM is supplied by its manufacturer Proteus Industries.

Based on the available information the bias error for the DFM has two individual contributors. These are instrument accuracy (taking into account linearity, hysteresis, and repeatability), and linearity. The bias error for the DFM is therefore computed through RSS and is given as follows.

$$B_{DFM} = \pm\sqrt{B_{Accuracy}^2 + B_{Linearity}^2} = \pm\sqrt{\left(\frac{1}{100}FS\right)^2 + \left(\frac{1.5}{100}FS\right)^2}$$

$$= \pm\sqrt{3.25\times10^{-4}FS^2} = \pm0.018FS$$

(C.205)

C.8.2 Random errors in glycol volume flow rate measurement

The random errors in glycol flow rate measurement are found based on the repeatability information provided by the manufacturer as well as the scatter of the data. This random error is presented in terms of precision error. The precision error is found by knowing the following 3 information:

(1) Total number of flow rate samples collected.

(2) Standard deviation of the flow rate samples acquired.

(3) Student t-distribution value based on the total number of samples.

Once this information is known the precision error flow rate measurement is found through the following equations.

$$P_{DFM,1} = \pm P_{Repeatibility} \tag{C.206}$$

$$P_{DFM,2} = \pm t_{N,95\%} S_{\overline{V_{DFM}}} \approx \pm 1.96 \frac{S_{\overline{V_{DFM}}}}{\sqrt{N}} \quad [\because N \geq 1000] \tag{C.207}$$

$$P_{DFM} = \pm \sqrt{P_{DFM,1}^2 + P_{DFM,2}^2} = \pm \sqrt{\left(\frac{1}{100} FS\right)^2 + \left(1.96 \frac{S_{\overline{V_{DFM}}}}{\sqrt{N}}\right)^2} \tag{C.208}$$

C.8.3 Overall uncertainty in glycol volume flow rate measurement

The overall uncertainty in glycol flow rate measurement due to the DFM alone is therefore given by the RSS of bias and precision errors as follows.

$$U_{DFM} = \pm\sqrt{B_{DFM}^2 + P_{DFM}^2}$$

$$= \pm\sqrt{\left(\frac{1}{100}FS\right)^2 + \left(\frac{1.5}{100}FS\right)^2 + \left(\frac{1}{100}FS\right)^2 + \left(1.96\frac{S_{\overline{V_{DFM}}}}{\sqrt{N}}\right)^2}$$

$$= \pm\sqrt{4.25\times10^{-4}\,FS^2} \qquad \left[\because N \geq 180000 \text{ and } \frac{S_{\overline{V_{DFM}}}}{\sqrt{N}} \approx 0\right]$$

$$= \pm 2.062\times10^{-2}\,FS$$

(C.209)

Hence the overall uncertainty in the nominal glycol flow rate acquired in volts is therefore calculated through RSS of the individual uncertainties of DFM and DAQ component by the following.

$$U_{Flow\,Rate[V]} = \pm\sqrt{U_{DFM}^2 + U_{DAQ}^2}$$

$$= \pm\sqrt{4.25\times10^{-4}\,FS^2 + 3.6397\times10^{-11}}$$

(C.210)
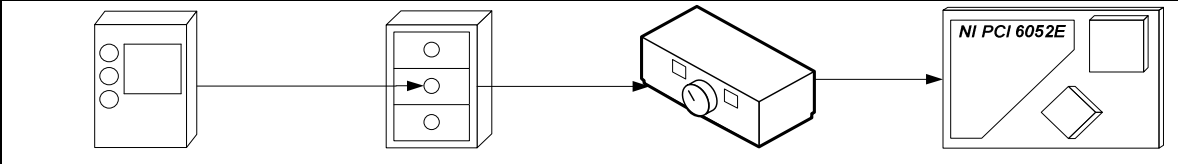
The sensitivity of flow meter measurement (Volume flow rate/Voltage) is calculated from the following equations.

$$K_{DFM} = \frac{\partial \dot{\forall}_{LPM}}{\partial V_{DFM}} = 1.792V_{DFM} - 0.3264 \quad \left|\frac{LPM}{V}\right|$$

(C.211)

Using the sensitivity of the DFM, the combined uncertainty of the DAQ components and flow meter can be translated from voltage to liters per minute (LPM) as follows.

$$U_{Flow\,Rate[LPM]} = \pm K_{DFM}U_{Flow\,Rate[V]}$$

$$= \pm(1.792V_{DFM} - 0.3264)\sqrt{4.25\times10^{-4}\,FS^2 + 3.6397\times10^{-11}}$$

(C.212)

Table C.6: Summary of glycol flow rate uncertainty calculation

DFM	Terminal Block	Signal Conditioner	DAQ Card
$B_1 = Accuracy$	$B_{TB} = 0$	$B_1 = DNL$	$B_1 = LSB$
$B_2 = Linearity$	$P_{TB} = 0$	$B_2 = Offset$	$B_2 = Relative$
$B_{DFM} = \sqrt{B_1^2 + B_2^2}$	$U_{TB} = 0$	$U_{SCXI} = \sqrt{B_1^2 + B_2^2}$	$B_3 = DNL$
$P_1 = Repeatability$			$B_4 = Offset$
$P_2 = \left(1.96 \dfrac{S_{DFM}}{\sqrt{N}}\right)$			
$P_{DFM} = \sqrt{P_1^2 + P_2^2}$		*DNL*: Differential Non Linearity	$U_{\substack{DAQ \\ Card}} = \sqrt{\begin{array}{c} B_1^2 + B_2^2 \\ + \\ B_3^2 + B_4^2 \end{array}}$
$U_{DFM} = \sqrt{\begin{array}{c} B_{DFM}^2 \\ + \\ P_{DFM}^2 \end{array}}$			

$$U_{DAQ} = B_{DAQ} = \sqrt{B_{DAQ-Card}^2 + B_{SCXI}^2} = 6.033 \times 10^{-6} V$$

$$U_{Flow\,Rate[LPM]} = \pm K_{DFM}\sqrt{U_{DAQ}^2 + U_{DFM[V]}^2}$$

C.9 Uncertainty in fluid thermophysical properties

The fluid thermophysical properties are determined at the respective fluid bulk temperatures. The uncertainties in the fluid basic thermophysical properties involved the use of method 2. These basic physical properties include fluid density, viscosity, specific heat, and thermal conductivity. The fluid Prandtl number is a dimensionless number which is also found in many property tables mainly because its evaluation depends on fluid and fluid state only. It is therefore deemed appropriate to include it in this section. Since the Prandtl number is function of other fluid properties its uncertainty is determined through method 3.

C.9.1 Uncertainty in glycol density

The uncertainty in glycol density is estimated through the following equation.

$$U_{\rho_g} = \frac{1}{2}\left|\left[\rho_g @ T_{b,g,max}\right] - \left[\rho_g @ T_{b,g,min}\right]\right| \qquad \text{(C.213)}$$

C.9.2 Uncertainty in glycol viscosity

The uncertainty in glycol viscosity is estimated through the following equation.

$$U_{\mu_g} = \frac{1}{2}\left|\left[\mu_g @ T_{b,g,max}\right] - \left[\mu_g @ T_{b,g,min}\right]\right| \qquad \text{(C.214)}$$

C.9.3 Uncertainty in glycol specific heat

The uncertainty in glycol specific heat is estimated through the following equation.

$$U_{c_{p,g}} = \frac{1}{2}\left|\left[c_{p,g} @ T_{b,g,max}\right] - \left[c_{p,g} @ T_{b,g,min}\right]\right| \qquad \text{(C.215)}$$

C.9.4 Uncertainty in glycol thermal conductivity

The uncertainty in glycol thermal conductivity is estimated through the following equation.

$$U_{k_g} = \frac{1}{2}\left|\left[k_g @ T_{b,g,max}\right] - \left[k_g @ T_{b,g,min}\right]\right| \qquad \text{(C.216)}$$

C.9.5 Uncertainty in glycol Prandtl number

The expression for the glycol Prandtl number is given as follows.

$$\mathrm{Pr}_g = \frac{\mu_g c_{p,g}}{k_g} \tag{C.217}$$

Its uncertainty is calculated as follows.

$$U_{\mathrm{Pr}_g} = \pm \sqrt{\left(\frac{\partial \mathrm{Pr}_g}{\partial \mu_g} U_{\mu_g}\right)^2 + \left(\frac{\partial \mathrm{Pr}_g}{\partial c_{p,g}} U_{c_{p,g}}\right)^2 + \left(\frac{\partial \mathrm{Pr}_g}{\partial k_g} U_{k_g}\right)^2} \tag{C.218}$$

Where,

$$\frac{\partial \mathrm{Pr}_g}{\partial \mu_g} = \frac{c_{p,g}}{k_g} \tag{C.219}$$

$$\frac{\partial \mathrm{Pr}_g}{\partial c_{p,g}} = \frac{\mu_g}{k_g} \tag{C.220}$$

$$\frac{\partial \mathrm{Pr}_g}{\partial k_g} = -\frac{\mu_g c_{p,g}}{k_g^2} \tag{C.221}$$

C.9.6 Uncertainty in air density

The uncertainty in air density is estimated through the following equation.

$$U_{\rho_a} = \frac{1}{2}\left| \left[\rho_a @ T_{b,a,max}\right] - \left[\rho_a @ T_{b,a,min}\right] \right| \tag{C.222}$$

C.9.7 Uncertainty in air viscosity

The uncertainty in air viscosity is estimated through the following equation.

$$U_{\mu_a} = \frac{1}{2} \left| \left[\mu_a @ T_{b,a,max} \right] - \left[\mu_a @ T_{b,a,min} \right] \right| \qquad \text{(C.223)}$$

C.9.8 Uncertainty in air specific heat

The uncertainty in air specific heat is estimated through the following equation.

$$U_{c_{p,a}} = \frac{1}{2} \left| \left[c_{p,a} @ T_{b,a,max} \right] - \left[c_{p,a} @ T_{b,a,min} \right] \right| \qquad \text{(C.224)}$$

C.9.9 Uncertainty in air thermal conductivity

The uncertainty in air thermal conductivity is estimated through the following equation.

$$U_{k_a} = \frac{1}{2} \left| \left[k_a @ T_{b,a,max} \right] - \left[k_a @ T_{b,a,min} \right] \right| \qquad \text{(C.225)}$$

C.9.10 Uncertainty in air Prandtl number

The expression for the air Prandtl number is given as follows.

$$\mathrm{Pr}_a = \frac{\mu_a c_{p,a}}{k_a} \qquad \text{(C.226)}$$

Its uncertainty is calculated as follows.

$$U_{\mathrm{Pr}_a} = \pm \sqrt{\left(\frac{\partial \mathrm{Pr}_a}{\partial \mu_a} U_{\mu_a}\right)^2 + \left(\frac{\partial \mathrm{Pr}_a}{\partial c_{p,a}} U_{c_{p,a}}\right)^2 + \left(\frac{\partial \mathrm{Pr}_a}{\partial k_a} U_{k_a}\right)^2} \qquad \text{(C.227)}$$

Where,

$$\frac{\partial \mathrm{Pr}_a}{\partial \mu_a} = \frac{c_{p,a}}{k_a} \qquad \text{(C.228)}$$

$$\frac{\partial \mathrm{Pr}_a}{\partial c_{p,a}} = \frac{\mu_a}{k_a} \qquad \text{(C.229)}$$

$$\frac{\partial \mathrm{Pr}_a}{\partial k_a} = -\frac{\mu_a c_{p,a}}{k_a^2} \qquad \text{(C.230)}$$

C.10 Uncertainty in mass flow rates

The mass flow rate of both glycol and air are functions of several lower level parameters. The steps for determining the glycol and air mass flow rate based on method 3 is documented in this section.

C.10.1 Uncertainty in glycol mass flow rate

The expression for the glycol mass flow rate is given as follows.

$$\dot{m}_{g,HX} = \dot{\forall}_g \, \rho_g \qquad \text{(C.231)}$$

Its uncertainty is calculated as follows.

$$U_{\dot{m}_{g,HX}} = \pm \sqrt{\left(\frac{\partial \dot{m}_{g,HX}}{\partial \rho_g} U_{\rho_g}\right)^2 + \left(\frac{\partial \dot{m}_{g,HX}}{\partial \dot{\forall}_g} U_{\dot{\forall}_g}\right)^2} \qquad \text{(C.232)}$$

Where,

$$\frac{\partial \dot{m}_{g,HX}}{\partial \rho_g} = \dot{\forall}_g \tag{C.233}$$

$$\frac{\partial \dot{m}_{g,HX}}{\partial \dot{\forall}_g} = \rho_g \tag{C.234}$$

C.10.2 Uncertainty in air mass flow rate

The uncertainty in air mass flow is determined by first determining the air flow velocity. The expression for the air flow velocity is given as follows.

$$V_a = \sqrt{\frac{2\Delta p_{Dynamic}}{\rho_a}} \tag{C.235}$$

Its uncertainty is calculated as follows.

$$U_{V_a} = \pm \sqrt{\left(\frac{\partial V_a}{\partial \Delta p_{Dynamic}} U_{\Delta p_{Dynamic}}\right)^2 + \left(\frac{\partial V_a}{\partial \rho_a} U_{\rho_a}\right)^2} \tag{C.236}$$

Where,

$$\frac{\partial V_a}{\partial \Delta p_{Pitot}} = \frac{1}{\sqrt{2\rho_a \Delta p_{Dynamic}}} \tag{C.237}$$

$$\frac{\partial V_a}{\partial \rho_a} = -\frac{1}{2}\frac{\sqrt{2\Delta p_{Dynamic}}}{\rho_a^{3/2}} \tag{C.238}$$

Once the uncertainty in air flow velocity is determined the uncertainty in air mass flow rate is also determined through method 3.

The expression for the air mass flow rate is given as follows.

$$\dot{m}_a = \dot{m}_{a,HX} = \rho_a V_a A_{Min,a} \qquad \text{(C.239)}$$

Its uncertainty is calculated as follows.

$$U_{\dot{m}_a} = \pm \sqrt{\left(\frac{\partial \dot{m}_a}{\partial \rho} U_{\rho_a}\right)^2 + \left(\frac{\partial \dot{m}_a}{\partial V_a} U_{V_a}\right)^2 + \left(\frac{\partial \dot{m}_a}{\partial A_{Min,a}} U_{A_{Min,a}}\right)^2} \qquad \text{(C.240)}$$

Where,

$$\frac{\partial \dot{m}_a}{\partial \rho_a} = V_a A_{Min,a} \qquad \text{(C.241)}$$

$$\frac{\partial \dot{m}_a}{\partial V_a} = \rho_a A_{Min,a} \qquad \text{(C.242)}$$

$$\frac{\partial \dot{m}_a}{\partial A_{Min,a}} = \rho_a V_a \qquad \text{(C.243)}$$

C.11 Uncertainty in Reynolds numbers

The Reynolds number of both glycol and air are functions of several lower level parameters. The use of method 3 for determining the glycol and air mass flow rate is documented in the following section.

C.11.1 Uncertainty in glycol Reynolds number

The expression for the glycol Reynolds number is given as follows.

$$\text{Re}_g = \frac{\dot{m}_{g,HX}}{51\pi\mu_g D_{MC}} \qquad \text{(C.244)}$$

Its uncertainty is calculated as follows.

$$U_{\text{Re}_g} = \pm \sqrt{\left(\frac{\partial \text{Re}_g}{\partial \dot{m}_{g,HX}} U_{\dot{m}_{g,HX}}\right)^2 + \left(\frac{\partial \text{Re}_g}{\partial \rho_g} U_{\rho_g}\right)^2 + \left(\frac{\partial \text{Re}_g}{\partial D_{MC}} U_{D_{MC}}\right)^2} \qquad \text{(C.245)}$$

Where,

$$\frac{\partial \text{Re}_g}{\partial \dot{m}_{g,HX}} = \frac{1}{51\pi\mu D_{MC}} \qquad \text{(C.246)}$$

$$\frac{\partial \text{Re}_g}{\partial \rho_g} = -\frac{\dot{m}_{g,HX}}{51\pi\mu_g^2 D_{MC}} \qquad \text{(C.247)}$$

$$\frac{\partial \text{Re}_g}{\partial D_{MC}} = -\frac{\dot{m}_{g,HX}}{51\pi\mu_g D_{MC}^2} \qquad \text{(C.248)}$$

C.11.2 Uncertainty in air Reynolds number

The uncertainty in air Reynolds number is determined by first determining the air mass velocity (also known as mass flux). The expression for the air mass velocity is given as follows.

$$G_a = \frac{\dot{m}_a}{A_{Min,a}} \qquad \text{(C.249)}$$

Its uncertainty is calculated as follows.

$$U_{G_a} = \pm \sqrt{\left(\frac{\partial G_a}{\partial \dot{m}_a} U_{\dot{m}_a}\right)^2 + \left(\frac{\partial G_a}{\partial A_{Min,a}} U_{A_{Min,a}}\right)^2} \qquad \text{(C.250)}$$

Where,

$$\frac{\partial G_a}{\partial \dot{m}_a} = \frac{1}{A_{Min,a}} \tag{C.251}$$

$$\frac{\partial G_a}{\partial A_{Min,a}} = -\frac{\dot{m}_a}{A_{Min,a}^2} \tag{C.252}$$

Once the uncertainty in air flow mass velocity is determined the uncertainty in air Reynolds number is also determined through method 3. The expression for the air side Reynolds number is given as follows.

$$\text{Re}_a = \frac{G_a D_{Hyd,a,HX}}{\mu_a} \tag{C.253}$$

Its uncertainty is calculated as follows.

$$U_{\text{Re}_a} = \pm \sqrt{\left(\frac{\partial \text{Re}_a}{\partial G_a} U_{G_a} \right)^2 + \left(\frac{\partial \text{Re}_a}{\partial D_{Hyd,a,HX}} U_{D_{Hyd,a,HX}} \right)^2 + \left(\frac{\partial \text{Re}_a}{\partial \mu_a} U_{\mu_a} \right)^2} \tag{C.254}$$

Where,

$$\frac{\partial \text{Re}_a}{\partial G_a} = \frac{D_{Hyd,a,HX}}{\mu_a} \tag{C.255}$$

$$\frac{\partial \text{Re}_a}{\partial D_{Hyd,a,HX}} = \frac{G_a}{\mu_a} \tag{C.256}$$

$$\frac{\partial \text{Re}_a}{\partial \mu_a} = -\frac{G_a D_{Hyd,a,HX}}{\mu_a^2} \tag{C.257}$$

C.12 Uncertainty in heat transfer rates

The following sections discuss the uncertainty analysis of heat transfer rates for both glycol, and air side, as well as their average heat transfer rate based on method 3. The determination of the heat transfer rate and associated uncertainty level indicates the soundness of heat balance and transfer from one fluid to another.

C.12.1 Uncertainty in glycol heat transfer rate

The glycol heat transfer rate is a function of glycol mass flow rate, specific heat and temperature differential between the inlet and outlet temperatures acquired by the RTDs. The expression for the glycol heat transfer rate is given as follows.

$$\dot{Q}_g = \dot{m}_g \, c_{p,g} \left(T_{g,i} - T_{g,o} \right) \tag{C.258}$$

Its uncertainty is calculated as follows.

$$U_{\dot{Q}_g} = \pm \sqrt{ \left(\frac{\partial \dot{Q}_g}{\partial \dot{m}_g} U_{\dot{m}_g} \right)^2 + \left(\frac{\partial \dot{Q}_g}{\partial c_{p,g}} U_{c_{p,g}} \right)^2 + \left(\frac{\partial \dot{Q}_g}{\partial \Delta T_g} U_{\Delta T_g} \right)^2 } \tag{C.259}$$

Where,

$$\frac{\partial \dot{Q}_g}{\partial \dot{m}_g} = c_{p,g} \Delta T_g \tag{C.260}$$

$$\frac{\partial \dot{Q}_g}{\partial c_{p,g}} = \dot{m}_g \, \Delta T_g \tag{C.261}$$

$$\frac{\partial \dot{Q}_g}{\partial \Delta T_g} = \dot{m}_g \, c_{p,g} \tag{C.262}$$

C.12.2 Uncertainty in air heat transfer rate

The air heat transfer rate is calculated in similar manner as glycol since they are also composed of parameters similar to the air side. The expression for the air heat transfer rate is given as follows.

$$\dot{Q}_a = \dot{m}_a \, c_{p,a} \left(T_{a,o} - T_{a,i} \right) \tag{C.263}$$

Its uncertainty is calculated as follows.

$$U_{\dot{Q}_a} = \pm \sqrt{ \left(\frac{\partial \dot{Q}_a}{\partial \dot{m}_a} U_{\dot{m}_a} \right)^2 + \left(\frac{\partial \dot{Q}_a}{\partial c_{p,a}} U_{c_{p,a}} \right)^2 + \left(\frac{\partial \dot{Q}_a}{\partial \Delta T_a} U_{\Delta T_a} \right)^2 } \tag{C.264}$$

Where,

$$\frac{\partial \dot{Q}_a}{\partial \dot{m}_a} = c_{p,a} \Delta T_a \tag{C.265}$$

$$\frac{\partial \dot{Q}_a}{\partial c_{p,a}} = \dot{m}_a \, \Delta T_a \tag{C.266}$$

$$\frac{\partial \dot{Q}_a}{\partial \Delta T_a} = \dot{m}_a \, c_{p,a} \tag{C.267}$$

C.12.3 Uncertainty in average heat transfer rate

The average heat transfer rate is the function of the two aforementioned heat transfer rates. The expression for the average heat transfer rate is given as follows.

$$\dot{Q} = \frac{\dot{Q}_g + \dot{Q}_a}{2} \tag{C.268}$$

Its uncertainty is calculated as follows.

$$U_{\dot{Q}} = \pm \sqrt{\left(\frac{\partial \dot{Q}}{\partial \dot{Q}_g} U_{\dot{Q}_g}\right)^2 + \left(\frac{\partial \dot{Q}}{\partial \dot{Q}_a} U_{\dot{Q}_a}\right)^2} \tag{C.269}$$

Where,

$$\frac{\partial \dot{Q}}{\partial \dot{Q}_g} = \frac{1}{2} \tag{C.270}$$

$$\frac{\partial \dot{Q}}{\partial \dot{Q}_a} = \frac{1}{2} \tag{C.271}$$

C.13 Uncertainty in log mean temperature difference

The log mean temperature difference is logarithmic average of temperature difference between the hot and cold fluids at both ends of the heat exchanger. It is a function of two temperature differentials; namely ΔT_1, and ΔT_2. Therefore uncertainty calculations for log mean temperature difference requires first calculating the uncertainty in these temperature differentials.

The expression for ΔT_1 is given as follows.

$$\Delta T_1 = T_{g,i} - T_{a,o}$$ (C.272)

Its uncertainty is calculated as follows.

$$U_{\Delta T_1} = \pm \sqrt{\left(\frac{\partial \Delta T_1}{\partial T_{g,i}} U_{T_{g,i}} \right)^2 + \left(\frac{\partial \Delta T_1}{\partial T_{a,o}} U_{T_{a,o}} \right)^2}$$ (C.273)

Where,

$$\frac{\partial \Delta T_1}{\partial T_{g,i}} = 1$$ (C.274)

$$\frac{\partial \Delta T_1}{\partial T_{a,o}} = -1$$ (C.275)

The expression for ΔT_2 is given as follows.

$$\Delta T_2 = T_{g,o} - T_{a,i}$$ (C.276)

Its uncertainty is calculated as follows.

$$U_{\Delta T_2} = \pm \sqrt{\left(\frac{\partial \Delta T_2}{\partial T_{g,o}} U_{T_{g,o}} \right)^2 + \left(\frac{\partial \Delta T_2}{\partial T_{a,i}} U_{T_{a,i}} \right)^2}$$ (C.277)

Where,

$$\frac{\partial \Delta T_2}{\partial T_{g,o}} = 1$$ (C.278)

$$\frac{\partial \Delta T_2}{\partial T_{a,i}} = -1 \qquad\qquad (C.279)$$

Once the uncertainties and nominal values of ΔT_1, and ΔT_2 are known, the expression for the log mean temperature difference is given as follows.

$$\Delta T_{LM} = \frac{\Delta T_1 - \Delta T_2}{\ln\left(\dfrac{\Delta T_1}{\Delta T_2}\right)} \qquad\qquad (C.280)$$

Its uncertainty is calculated as follows.

$$U_{\Delta T_{LM}} = \pm \sqrt{\left(\frac{\partial \Delta T_{LM}}{\partial \Delta T_1} U_{\Delta T_1}\right)^2 + \left(\frac{\partial \Delta T_{LM}}{\partial \Delta T_2} U_{\Delta T_2}\right)^2} \qquad\qquad (C.281)$$

Where,

$$\frac{\partial \Delta T_{LM}}{\partial \Delta T_1} = \frac{\ln\left(\dfrac{\Delta T_1}{\Delta T_2}\right) - \left(1 - \dfrac{\Delta T_2}{\Delta T_1}\right)}{\left[\ln\left(\dfrac{\Delta T_1}{\Delta T_2}\right)\right]^2} \qquad\qquad (C.282)$$

$$\frac{\partial \Delta T_{LM}}{\partial \Delta T_2} = \frac{-\ln\left(\dfrac{\Delta T_1}{\Delta T_2}\right) - \left(\dfrac{\Delta T_1}{\Delta T_2} - 1\right)}{\left[\ln\left(\dfrac{\Delta T_1}{\Delta T_2}\right)\right]^2} \qquad\qquad (C.283)$$

.

C.14 Uncertainty in thermal resistances

This section illustrates the uncertainties overall thermal resistances as well as the glycol side thermal resistance, and wall (conductive aluminum, which interfaces between glycol and air) by using method 3. Uncertainties in these thermal resistances will indicate the soundness of air side Nusselt number and heat transfer coefficient evaluated.

C.14.1 Uncertainty in total thermal resistance

The uncertainty in total thermal resistance is a function of crossflow correction factor, log mean temperature difference and average heat transfer rate. The expression for the total thermal resistance is given as follows.

$$R_{total} = \frac{1}{UA} = \frac{F \Delta T_{LM}}{\dot{Q}} \tag{C.284}$$

Its uncertainty is calculated as follows.

$$U_{R_{total}} = \pm \sqrt{\left(\frac{\partial R_{total}}{\partial F} U_F\right)^2 + \left(\frac{\partial R_{total}}{\partial \Delta T_{LM}} U_{\Delta T_{LM}}\right)^2 + \left(\frac{\partial R_{total}}{\partial \dot{Q}} U_{\dot{Q}}\right)^2} \tag{C.285}$$

Where,

$$\frac{\partial R_{total}}{\partial F} = \frac{\Delta T_{LM}}{\dot{Q}} \tag{C.286}$$

$$\frac{\partial R_{total}}{\partial \Delta T_{LM}} = \frac{F}{\dot{Q}} \tag{C.287}$$

$$\frac{\partial R_{total}}{\partial \dot{Q}} = -\frac{F \Delta T_{LM}}{\dot{Q}^2} \tag{C.288}$$

C.14.2 Uncertainty in wall thermal resistance

The wall thermal resistance is function of microchannel internal diameter, external diameter (taken as the slab height), combined length of all microchannels and thermal conductivity of aluminum. The uncertainty in thermal conductivity of aluminum is taken as zero. The expression for the wall thermal resistance is given as follows.

$$R_{wall} = \frac{\ln\left(\dfrac{D_{o,MC}}{D_{i,MC}}\right)}{2\pi k_{Aluminium} L_{HT,MC,HX}} \tag{C.289}$$

Its uncertainty is calculated as follows.

$$U_{R_{wall}} = \pm \sqrt{\left(\frac{\partial R_{wall}}{\partial D_{o,MC}} U_{D_{o,MC}}\right)^2 + \left(\frac{\partial R_{wall}}{\partial D_{i,MC}} U_{D_{i,MC}}\right)^2 + \left(\frac{\partial R_{wall}}{\partial L_{HT,MC,HX}} U_{L_{HT,MC,HX}}\right)^2} \tag{C.290}$$

Where,

$$\frac{\partial R_{wall}}{\partial D_{o,MC}} = \frac{1}{D_{o,MC}\left(2\pi k_{Aluminium} L_{HT,MC,HX}\right)} \tag{C.291}$$

$$\frac{\partial R_{wall}}{\partial D_{i,MC}} = -\frac{1}{D_{i,MC}\left(2\pi k_{Aluminium} L_{HT,MC,HX}\right)} \tag{C.292}$$

$$\frac{\partial R_{wall}}{\partial L_{HT,MC,HX}} = -\frac{\ln\left(\dfrac{D_{o,MC}}{D_{i,MC}}\right)}{2\pi k_{Aluminium} L_{HT,MC,HX}^2} \tag{C.293}$$

C.14.3 Uncertainty in glycol side thermal resistance

The glycol side thermal resistance is evaluated based on glycol heat transfer coefficient as well as combined inner surface area of all microchannels in the heat exchanger. The expression for the glycol thermal resistance is given as follows.

$$R_g = \frac{1}{h_g A_{HT,in,MC,HX}} \tag{C.294}$$

Its uncertainty is calculated as follows.

$$U_{R_g} = \pm \sqrt{\left(\frac{\partial R_g}{\partial h_g} U_{h_g}\right)^2 + \left(\frac{\partial R_g}{\partial A_{HT,in,MC,HX}} U_{A_{HT,in,MC,HX}}\right)^2} \tag{C.295}$$

Where,

$$\frac{\partial R_g}{\partial h_g} = -\frac{1}{h_g^2 A_{HT,in,MC,HX}} \tag{C.296}$$

$$\frac{\partial R_g}{\partial A_{HT,in,MC,HX}} = -\frac{1}{h_g A_{HT,in,MC,HX}^2} \tag{C.297}$$

C.15 Uncertainty in fluid Nusselt number & heat transfer coefficient

In this present study the evaluation of glycol Nusselt number is followed by glycol heat transfer coefficient. In contrast, the air side Nusselt number evaluation follows the air heat transfer coefficient. All four of these parameters are function of other parameters, and their uncertainty analysis based on method 3 is shown in the following sections.

C.15.1 Uncertainty in glycol Nusselt number

Glycol Nusselt is a function of glycol Péclet number, microchannel diameter and the combined heat transfer length of all the microchannels in the heat exchanger. As such, their uncertainties are first evaluated prior to evaluating uncertainty in Nusselt number.

The expression for the glycol Péclet number is given as follows.

$$Pe_g = \text{Re}_g \, \text{Pr}_g \tag{C.298}$$

Its uncertainty is calculated as follows.

$$U_{Pe_g} = \pm \sqrt{\left(\frac{\partial Pe_g}{\partial \text{Re}_g} U_{\text{Re}_g} \right)^2 + \left(\frac{\partial Pe_g}{\partial \text{Pr}_g} U_{\text{Pr}_g} \right)^2} \tag{C.299}$$

Where,

$$\frac{\partial Pe_g}{\partial \text{Re}_g} = \text{Pr}_g \tag{C.300}$$

$$\frac{\partial Pe_g}{\partial \text{Pr}_g} = \text{Re}_g \tag{C.301}$$

The uncertainties in microchannel diameter as well as the combined length of all microchannels in the heat exchanger have been found earlier, and are also documented in appendix B. The uncertainty in glycol Nusselt number can proceed based on this information. The expression for the glycol side Nusselt number is given as follows.

$$Nu_g = \sqrt[3]{3.66^3 + 1.61^3 \left(\frac{Pe_g D_{MC}}{L_{HT,MC,HX}} \right)} \tag{C.302}$$

Its uncertainty is calculated as follows.

$$U_{Nu_g} = \pm \sqrt{\left(\frac{\partial Nu_g}{\partial Pe_g} U_{Pe_g} \right)^2 + \left(\frac{\partial Nu_g}{\partial D_{MC}} U_{D_{MC}} \right)^2 + \left(\frac{\partial Nu_g}{\partial L_{HT,MC,HX}} U_{L_{HT,MC,HX}} \right)^2} \qquad \text{(C.303)}$$

Where,

$$\frac{\partial Nu_g}{\partial Pe_g} = \frac{1.61^3}{3} \left[3.66^3 + 1.61^3 \left(\frac{Pe_g D_{MC}}{L_{HT,MC,HX}} \right) \right]^{-\frac{2}{3}} \left(\frac{D_{MC}}{L_{HT,MC,HX}} \right) \qquad \text{(C.304)}$$

$$\frac{\partial Nu_g}{\partial D_{MC}} = \frac{1.61^3}{3} \left[3.66^3 + 1.61^3 \left(\frac{Pe_g D_{MC}}{L_{HT,MC,HX}} \right) \right]^{-\frac{2}{3}} \left(\frac{Pe_g}{L_{HT,MC,HX}} \right) \qquad \text{(C.305)}$$

$$\frac{\partial Nu_g}{\partial L_{HT,MC,HX}} = -\frac{1.61^3}{3} \left[3.66^3 + 1.61^3 \left(\frac{Pe_g D_{MC}}{L_{HT,MC,HX}} \right) \right]^{-\frac{2}{3}} \left(\frac{Pe_g D_{MC}}{L_{HT,MC,HX}^2} \right) \qquad \text{(C.306)}$$

C.15.2 Uncertainty in glycol heat transfer coefficient

The glycol heat transfer coefficient is a function of glycol Nusselt number, thermal conductivity, and microchannel hydraulic diameter. The expression for the glycol heat transfer coefficient is given as follows.

$$h_g = \frac{Nu_g k_g}{D_{MC}} \qquad \text{(C.307)}$$

Its uncertainty is calculated as follows.

$$U_{h_g} = \pm \sqrt{\left(\frac{\partial h_g}{\partial Nu_g} U_{Nu_g} \right)^2 + \left(\frac{\partial h_g}{\partial k_g} U_{k_g} \right)^2 + \left(\frac{\partial h_g}{\partial D_{MC}} U_{D_{MC}} \right)^2} \qquad \text{(C.308)}$$

Where,

$$\frac{\partial h_g}{\partial Nu_g} = \frac{k_g}{D_{MC}}$$

(C.309)

$$\frac{\partial h_g}{\partial k_g} = \frac{Nu_g}{D_{MC}}$$

(C.310)

$$\frac{\partial h_g}{\partial D_{MC}} = -\frac{Nu_g k_g}{D_{MC}^2}$$

(C.311)

C.15.3 Uncertainty in air heat transfer coefficient

The uncertainty evaluation for air side heat transfer coefficient requires first evaluating total, wall, and glycol side thermal resistances, as well as the fin efficiency and total air side heat transfer surface area. Their uncertainties have been evaluated previously with the exception of fin efficiency.

The expression for the fin efficiency is given as follows.

$$\eta_{Fin} = \frac{\tanh(ML)}{ML}$$

(C.312)

Its uncertainty is calculated as follows.

$$U_{\eta_{Fin}} = \pm \sqrt{\left(\frac{\partial \eta_{Fin}}{\partial M} U_M\right)^2 + \left(\frac{\partial \eta_{Fin}}{\partial L} U_L\right)^2}$$

(C.313)

Where,

$$\frac{\partial \eta_{Fin}}{\partial M} = \frac{ML\mathrm{sech}^2(ML) - \tanh(ML)}{M^2 L}$$

(C.314)

$$\frac{\partial \eta_{Fin}}{\partial L} = \frac{ML\mathrm{sech}^2(ML) - \tanh(ML)}{L^2 M}$$

(C.315)

The uncertainty in air side heat transfer coefficient can proceed based on this information. The expression for the air side heat transfer coefficient is given as follows.

$$h_a = \frac{1}{\eta_a A_{HT,a,HX} \left[R_{total} - R_{wall} - R_g \right]} \tag{C.316}$$

Its uncertainty is calculated as follows.

$$U_{h_a} = \pm \sqrt{ \begin{array}{l} \left(\dfrac{\partial h_a}{\partial \eta_a} U_{\eta_a} \right)^2 + \left(\dfrac{\partial h_a}{\partial A_{HT,a,HX}} U_{A_{HT,a,HX}} \right)^2 \\[3mm] + \left(\dfrac{\partial h_a}{\partial R_{total}} U_{R_{total}} \right)^2 + \left(\dfrac{\partial h_a}{\partial R_{wall}} U_{R_{wall}} \right)^2 + \left(\dfrac{\partial h_a}{\partial R_g} U_{R_g} \right)^2 \end{array} } \tag{C.317}$$

Where,

$$\frac{\partial h_a}{\partial \eta_a} = -\frac{1}{\eta_a^2 A_{HT,a,HX} \left[R_{total} - R_{wall} - R_g \right]} \tag{C.318}$$

$$\frac{\partial h_a}{\partial A_{HT,a,HX}} = -\frac{1}{\eta_a A_{HT,a,HX}^2 \left[R_{total} - R_{wall} - R_g \right]} \tag{C.319}$$

$$\frac{\partial h_a}{\partial R_{total}} = -\frac{\eta_a A_{HT,a,HX}}{\left[\eta_a A_{HT,a,HX} \left[R_{total} - R_{wall} - R_g \right] \right]^2} \tag{C.320}$$

$$\frac{\partial h_a}{\partial R_{wall}} = \frac{\eta_a A_{HT,a,HX}}{\left[\eta_a A_{HT,a,HX} \left[R_{total} - R_{wall} - R_g \right] \right]^2} \tag{C.321}$$

$$\frac{\partial h_a}{\partial R_g} = \frac{\eta_a A_{HT,a,HX}}{\left[\eta_a A_{HT,a,HX} \left[R_{total} - R_{wall} - R_g \right] \right]^2} \tag{C.322}$$

C.15.4 Uncertainty in air Nusselt number

The air side Nusselt number is a function of air side heat transfer coefficient, thermal conductivity, and hydraulic diameter. The expression for the air-side Nusselt number is given as follows.

$$Nu_a = \frac{h_a D_{Hyd,a,HX}}{k_a} \tag{C.323}$$

Its uncertainty is calculated as follows.

$$U_{Nu_a} = \pm \sqrt{\left(\frac{\partial Nu_a}{\partial h_a} U_{h_a} \right)^2 + \left(\frac{\partial Nu_a}{\partial D_{Hyd,a,HX}} U_{D_{Hyd,a,HX}} \right)^2 + \left(\frac{\partial Nu_a}{\partial k_a} U_{k_a} \right)^2} \tag{C.324}$$

Where,

$$\frac{\partial Nu_a}{\partial h_a} = \frac{D_{Hyd,a,HX}}{k_a} \tag{C.325}$$

$$\frac{\partial Nu_a}{\partial D_{Hyd,a,HX}} = \frac{h_a}{k_a} \tag{C.326}$$

$$\frac{\partial Nu_a}{\partial k_a} = -\frac{h_a D_{Hyd,a,HX}}{k_a^2} \tag{C.327}$$

C.16 Uncertainty in effectiveness

Effectiveness for present study is defined by a function of average heat transfer rate, glycol mass flow rate, and specific heat, as well as the temperature difference between the temperatures of both fluids at their respective inlets. The temperature differential here is subject to total uncertainties associated with acquiring these temperatures since different sensors are utilized. The expression for the effectiveness is given as follows.

$$\varepsilon = \frac{\dot{Q}}{\dot{Q}_{max}} = \frac{\dot{Q}}{\left(\dot{m}\,c_p\right)_{min} \Delta T_{max}} = \frac{\dot{Q}}{\left(\dot{m}\,c_p\right)_g \left(T_{g,i} - T_{a,i}\right)} \qquad (C.328)$$

Its uncertainty is calculated as follows.

$$U_\varepsilon = \pm \sqrt{\begin{array}{l}\left(\dfrac{\partial \varepsilon}{\partial \dot{Q}} U_{\dot{Q}}\right)^2 + \left(\dfrac{\partial \varepsilon}{\partial \dot{m}_g} U_{\dot{m}_g}\right)^2 + \left(\dfrac{\partial \varepsilon}{\partial c_{p,g}} U_{c_{p,g}}\right)^2 \\[4mm] + \left(\dfrac{\partial \varepsilon}{\partial T_{g,i}} U_{T_{g,i}}\right)^2 + \left(\dfrac{\partial \varepsilon}{\partial T_{a,i}} U_{T_{a,i}}\right)^2\end{array}} \qquad (C.329)$$

Where,

$$\frac{\partial \varepsilon}{\partial \dot{Q}} = \frac{1}{\dot{m}_g\, c_{p,g} \left(T_{g,i} - T_{a,i}\right)} \qquad (C.330)$$

$$\frac{\partial \varepsilon}{\partial \dot{m}_g} = -\frac{\dot{Q}}{\dot{m}_g^{\,2}\, c_{p,g} \left(T_{g,i} - T_{a,i}\right)} \qquad (C.331)$$

$$\frac{\partial \varepsilon}{\partial c_{p,g}} = -\frac{\dot{Q}}{\dot{m}_g\, c_{p,g}^2 \left(T_{g,i} - T_{a,i}\right)} \qquad (C.332)$$

$$\frac{\partial \varepsilon}{\partial T_{g,i}} = -\frac{\dot{Q}}{\dot{m}_g\, c_{p,g} \left(T_{g,i} - T_{a,i}\right)^2} \qquad (C.333)$$

$$\frac{\partial \varepsilon}{\partial T_{a,i}} \frac{\dot{Q}}{\dot{m}_g\, c_{p,g} \left(T_{g,i} - T_{a,i}\right)^2} \qquad (C.334)$$

C.17 Uncertainty in Number of Transfer Unit (NTU)

The expression for the *NTU* is given as follows.

$$NTU = \frac{UA}{C_{min}} \tag{C.335}$$

Its uncertainty is calculated as follows.

$$U_{NTU} = \pm \sqrt{\left(\frac{\partial NTU}{\partial UA} U_{UA} \right)^2 + \left(\frac{\partial NTU}{\partial C_{min}} U_{C_{min}} \right)^2} \tag{C.336}$$

Where,

$$\frac{\partial NTU}{\partial UA} = \frac{1}{C_{min}} \tag{C.337}$$

$$\frac{\partial NTU}{\partial C_{min}} = -\frac{UA}{C_{min}^2} \tag{C.338}$$

C.18 Uncertainty in air side heat convection Colburn factor

The evaluation of uncertainty associated with Colburn factor first requires computation of uncertainties in Stanton number. The Stanton number is a function of air side heat transfer coefficient, mass velocity, and specific heat. The expression for the Stanton number is given as follows.

$$St_a = \frac{h_a}{G_a c_{p,a}} \tag{C.339}$$

Its uncertainty is calculated as follows.

$$U_{St_a} = \pm \sqrt{\left(\frac{\partial St_a}{\partial h_a} U_{h_a}\right)^2 + \left(\frac{\partial St_a}{\partial G_a} U_{G_a}\right)^2 + \left(\frac{\partial St_a}{\partial c_{p,a}} U_{c_{p,a}}\right)^2} \qquad \text{(C.340)}$$

Where,

$$\frac{\partial St_a}{\partial h_a} = \frac{1}{G_a c_{p,a}} \qquad \text{(C.341)}$$

$$\frac{\partial St_a}{\partial G_a} = -\frac{h_a}{G_a^2 c_{p,a}} \qquad \text{(C.342)}$$

$$\frac{\partial St_a}{\partial c_{p,a}} = -\frac{h_a}{G_a c_{p,a}^2} \qquad \text{(C.343)}$$

Once the uncertainty in Stanton number is evaluated, the analysis of uncertainty in Colburn factor for convective heat transfer can proceed. The expression for the Colburn factor is given as follows.

$$j_a = St_a \, Pr_a^{2/3} \qquad \text{(C.344)}$$

Its uncertainty is calculated as follows.

$$U_{j_a} = \pm \sqrt{\left(\frac{\partial j_a}{\partial St_a} U_{St_a}\right)^2 + \left(\frac{\partial j_a}{\partial Pr_a} U_{Pr_a}\right)^2} \qquad \text{(C.345)}$$

Where,

$$\frac{\partial j_a}{\partial St_a} = Pr_a^{2/3} \qquad \text{(C.346)}$$

$$\frac{\partial j_a}{\partial Pr_a} = \frac{2}{3} St_a \, Pr_a^{-1/3} \qquad \text{(C.347)}$$

C.19 Uncertainty in air side friction factor

The evaluation of uncertainty associated with air side friction factor first requires computation of uncertainties in air density at the inlet and outlet. Uncertainties for all other required parameters for this analysis have been computed previously.

The uncertainty for air density at inlet is estimated as per method 2.

$$U_{\rho_{a,i}} = \frac{1}{2} \left| \left[\rho_{a,i} @ T_{a,i,max} \right] - \left[\rho_{a,i} @ T_{a,i,min} \right] \right| \tag{C.348}$$

The uncertainty for air density at outlet is also estimated as per method 2.

$$U_{\rho_{a,o}} = \frac{1}{2} \left| \left[\rho_{a,o} @ T_{a,o,max} \right] - \left[\rho_{a,o} @ T_{a,o,min} \right] \right| \tag{C.349}$$

Once this information is known, the analysis of uncertainty in air side friction factor can be evaluated. The expression for the air side friction factor is given as follows.

$$f_a = \left(\frac{A_{Min,a}}{A_{HT,a,HX}} \right) \left(\frac{\rho_{a,b}}{\rho_{a,i}} \right) \left[\frac{2\Delta p_{a,HX} \rho_{a,i}}{G_a^2} - \left(1 + \sigma_a^2 \right) \left(\frac{\rho_{a,i}}{\rho_{a,o}} - 1 \right) \right] \tag{C.350}$$

Its uncertainty is calculated as follows.

$$U_{f_a} = \pm \sqrt{ \begin{aligned} &\left(\frac{\partial f}{\partial A_{Min,a}} U_{A_{Min,a}} \right)^2 + \left(\frac{\partial f}{\partial A_{HT,a,HX}} U_{A_{HT,a,HX}} \right)^2 + \left(\frac{\partial f}{\partial \rho_{m,a}} U_{\rho_{a,b}} \right)^2 \\ &+ \left(\frac{\partial f}{\partial \rho_{in,a}} U_{\rho_{a,i}} \right)^2 + \left(\frac{\partial f}{\partial \rho_{out,a}} U_{\rho_{a,o}} \right)^2 + \left(\frac{\partial f}{\partial \Delta p_{a,HX}} U_{\Delta p_{a,HX}} \right)^2 \\ &+ \left(\frac{\partial f}{\partial G_a} U_{G_a} \right)^2 + \left(\frac{\partial f}{\partial \sigma_a} U_{\sigma_a} \right)^2 \end{aligned} } \tag{C.351}$$

Where,

$$\frac{\partial f_a}{\partial A_{Min,a}} = \left(\frac{1}{A_{HT,a,HX}}\right)\left(\frac{\rho_{a,b}}{\rho_{a,i}}\right)\left[\frac{2\Delta p_{a,HX}\rho_{a,i}}{G_a^2} - \left(1+\sigma_a^2\right)\left(\frac{\rho_{a,i}}{\rho_{a,o}}-1\right)\right] \qquad \text{(C.352)}$$

$$\frac{\partial f_a}{\partial A_{HT,a,HX}} = -\left(\frac{A_{Min,a}}{A_{HT,a,HX}^2}\right)\left(\frac{\rho_{a,b}}{\rho_{a,i}}\right)\left[\frac{2\Delta p_{a,HX}\rho_{a,i}}{G_a^2} - \left(1+\sigma_a^2\right)\left(\frac{\rho_{a,i}}{\rho_{a,o}}-1\right)\right] \qquad \text{(C.353)}$$

$$\frac{\partial f_a}{\partial \rho_{a,b}} = \left(\frac{A_{Min,a}}{A_{HT,a,HX}}\right)\left(\frac{1}{\rho_{a,i}}\right)\left[\frac{2\Delta p_{a,HX}\rho_{a,i}}{G_a^2} - \left(1+\sigma_a^2\right)\left(\frac{\rho_{a,i}}{\rho_{a,o}}-1\right)\right] \qquad \text{(C.354)}$$

$$\frac{\partial f_a}{\partial \rho_{a,i}} = \left(\frac{A_{Min,a}}{A_{HT,a,HX}}\right)\left\{\begin{array}{l}\left(\left(-\frac{\rho_{a,b}}{\rho_{a,i}^2}\right)\left[\frac{2\Delta p_{a,HX}\rho_{a,i}}{G_a^2} - \left(1+\sigma_a^2\right)\left(\frac{\rho_{a,i}}{\rho_{a,o}}-1\right)\right]\right) \\ -\left(\frac{\rho_{a,b}}{\rho_{a,i}}\right)\left[\frac{2\Delta p_{a,HX}}{G_a^2} - \left(1+\sigma_a^2\right)\left(\frac{1}{\rho_{a,o}}\right)\right]\end{array}\right\} \qquad \text{(C.355)}$$

$$\frac{\partial f_a}{\partial \rho_{a,o}} = \left(1+\sigma_a^2\right)\left(\frac{A_{Min,a}}{A_{HT,a,HX}}\right)\left(\frac{\rho_{a,b}}{\rho_{a,o}^2}\right) \qquad \text{(C.356)}$$

$$\frac{\partial f_a}{\partial \Delta p_{a,HX}} = \left(\frac{A_{Min,a}}{A_{HT,a,HX}}\right)\left(\frac{\rho_{a,b}}{\rho_{a,i}}\right)\left[\frac{2\rho_{a,i}}{G_a^2}\right] \qquad \text{(C.357)}$$

$$\frac{\partial f_a}{\partial G_a} = \left(\frac{A_{Min,a}}{A_{HT,a,HX}}\right)\left(\frac{\rho_{a,b}}{\rho_{a,i}}\right)\left[-\frac{4\Delta p_{a,HX}\rho_{a,i}}{G_a^3}\right] \qquad \text{(C.358)}$$

$$\frac{\partial f_a}{\partial \sigma_a} = -2\sigma_a\left(\frac{A_{Min,a}}{A_{HT,a,HX}}\right)\left(\frac{\rho_{a,b}}{\rho_{a,i}}\right)\left(\frac{\rho_{a,i}}{\rho_{a,o}}-1\right) \qquad \text{(C.359)}$$

Based on the equations presented in this appendix the nominal values and the uncertainties all the parameters are calculated. The uncertainties for few of the important fluid flow and heat transfer parameters are expressed as a percentage of their nominal values in Table C.7. In order to avoid partiality towards any of the particular operating conditions in this study, a trial run is selected for illustration and analysis of results. The trial operating condition is set at $25\,^{\circ}C$, and $3-11\,m/s$. From the results of uncertainty analysis at this temperature, it is evident that for a given temperature, the uncertainty relative to nominal value in key fluid flow and heat transfer parameter on the air side increases with a decrease in air velocity. This is to be expected as air and heat flow uniformity, and distribution is enhanced at higher flow rates. The highest uncertainties are found for air side Nusselt number and Colburn j factor. For the glycol side parameters, the change in relative uncertainty is absent. Once again, this is to be expected since the glycol side operating condition is not altered along with the air side.

Table C.7: Uncertainties of key parameters as percentages of nominal value

Operating Conditions	$25\,^{\circ}C$ $3\,m/s$	$25\,^{\circ}C$ $5\,m/s$	$25\,^{\circ}C$ $7\,m/s$	$25\,^{\circ}C$ $9\,m/s$	$25\,^{\circ}C$ $11\,m/s$
Key Parameters	Uncertainties as percentage of nominal value				
$\Delta p_{Dynamic}$	4.86	4.59	4.30	4.01	3.83
$\Delta p_{a,HX}$	3.14	3.01	2.84	2.63	2.54
$T_{a,b}$	0.29	0.32	0.37	0.44	0.52
$T_{g,b}$	0.20	0.21	0.21	0.22	0.23
$\dot{m}_g$	0.73	0.73	0.73	0.73	0.73
V_a	2.43	2.30	2.15	2.01	1.91
$\dot{m}_a$	2.22	2.14	2.04	1.95	1.90
Re_g	3.56	3.57	3.56	3.56	3.57
Re_a	3.15	3.10	3.03	2.97	2.93
$\dot{Q}_g$	0.73	0.73	0.73	0.73	0.73
$\dot{Q}_a$	2.57	2.40	2.26	2.14	2.06
$\dot{Q}$	1.33	1.28	1.20	1.15	1.11
ΔT_{LM}	5.54	4.55	3.84	3.31	2.90
Nu_g	0.00	0.00	0.00	0.00	0.00
h_g	3.48	3.48	3.48	3.48	3.48
η_{Fin}	0.99	0.97	0.96	0.95	0.94
η_a	0.89	0.87	0.86	0.85	0.84
h_a	7.91	6.63	5.72	5.07	4.55
Nu_a	8.07	6.82	5.95	5.32	4.83
ε	1.73	1.63	1.54	1.47	1.41
NTU	5.84	4.89	4.22	3.72	3.35
j_a	8.36	7.13	6.27	5.65	5.17
f_a	6.48	6.31	6.10	5.89	5.78

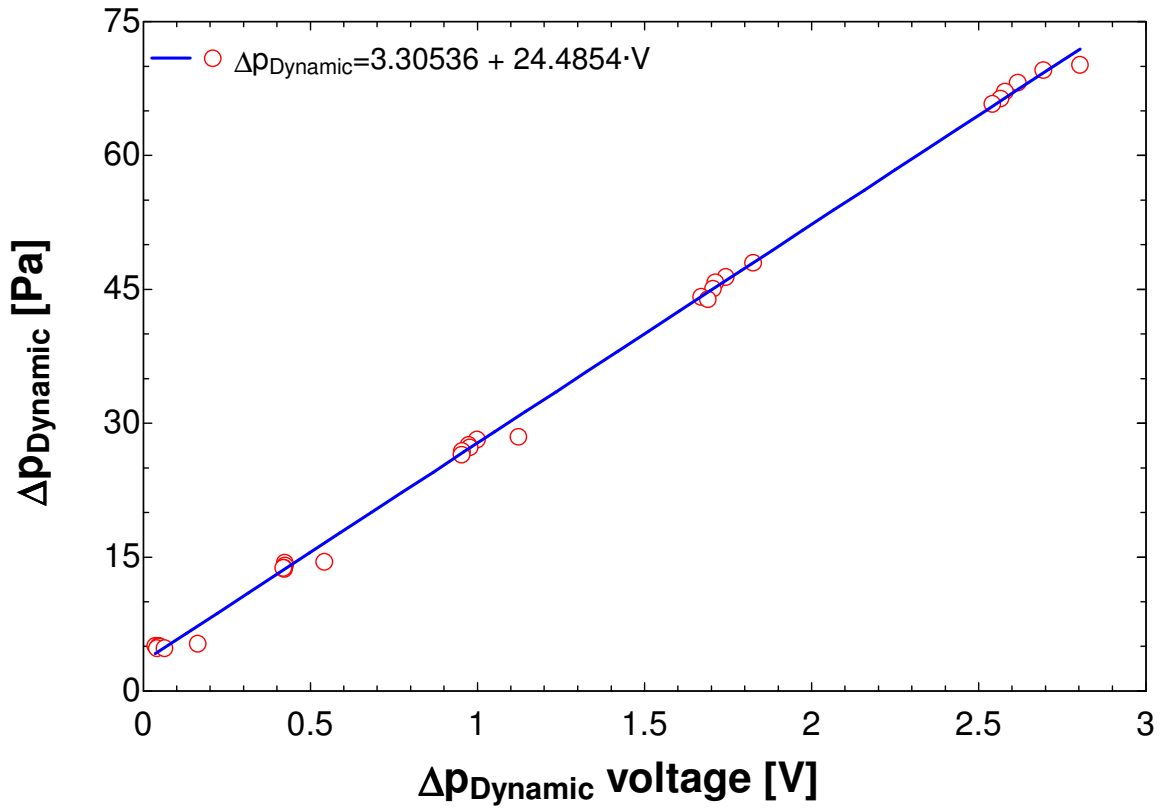# Appendix – D: Calibration Curves and Equations

Figure D.1: Calibration curve for PX277-01D5V (DPTD)

Based on the data for PX277-01D5V used in measurement of dynamic pressure with Pitot static tube:

Calibration Equation: $\Delta p_{Dynamic} = 24.49V + 3.31$

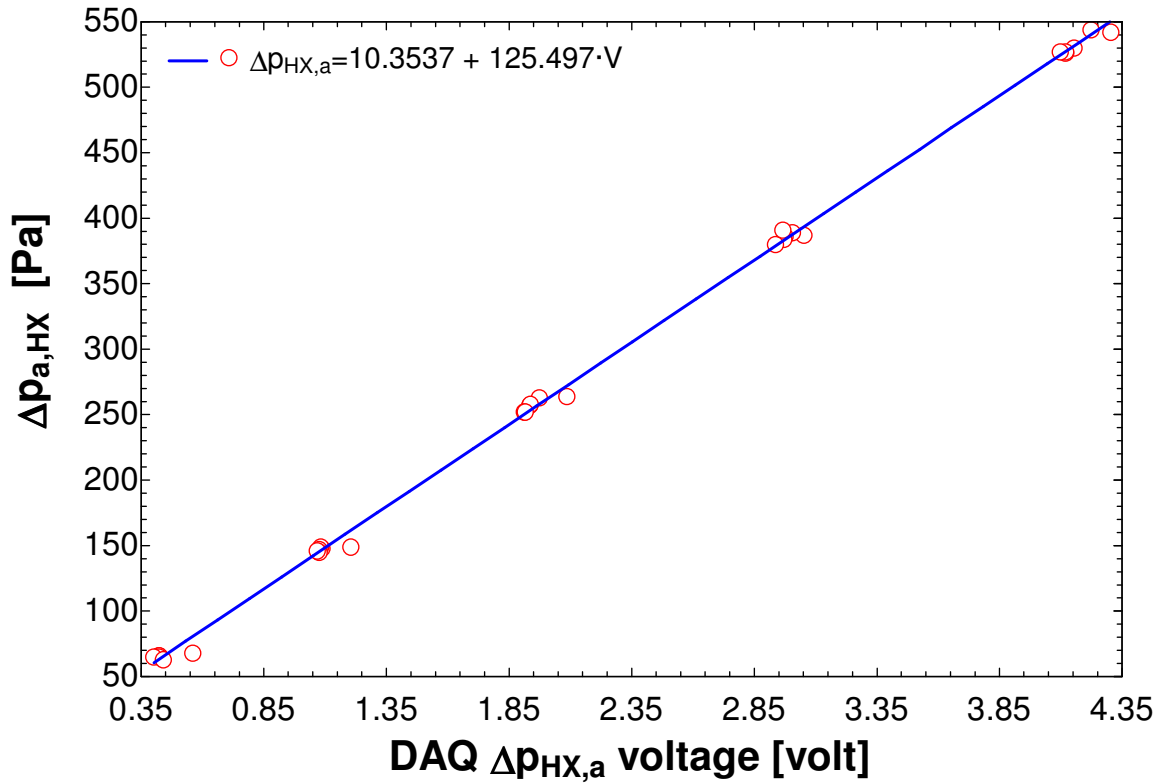Sensitivity: $K = 24.49 \dfrac{Pa}{V}$

Figure D.2: Calibration curve for PX277-05D5V (DPTD)

Based on the data for PX277-05D5V used for measurement of air side pressure drop across heat exchanger:

Calibration Equation: $\Delta p_{a,HX} = 125.5V + 10.35$

Sensitivity: $K = 125.5 \dfrac{Pa}{V}$

Appendix – E: Permission from FlowKinetics, Re: Fig 3.12

The following is the email transcript for permission to include the FlowKinetics Flow and Pressure Acquisition System as Figure 3.12 in the thesis.

INBOX Message   1/6/2011 7:54 PM

From: FlowKinetics LLC <inform@flowkinetics.com>

Subject: Re: Seeking permission to include copyrighted material

Date: Thu, 06 Jan 2011 15:06:49 -0600

To: Faisal Siddiqui <siddiqy@uwindsor.ca>

```
Faisal,

You can include the material as requested.

Best regards,

Sam Galls, Ph.D.
Vice President
FlowKinetics LLC
email: inform@flowkinetics.com
Web: www.flowkinetics.com


On 1/5/2011 10:18 PM, Faisal Siddiqui wrote:

    Dear Sir/Madam

    This is Faisal SIDDIQUI, a graduate student from University of Windsor,
    Canada. I am contacting you to seek permission to include the following
    material within the electronic version of my Masters thesis to better
    illustrate my experimental setup:

    *Fig. A1 FKT series components*, (from the manual file for FKT 3DP1A
    named: FKTSeriesManual.pdf)

    If you are not the rights holder for this material I would be grateful
    if you would advise me who to contact.

    The thesis will be made available within the University of Windsor's
    online Thesis and Dissertations repository
    (http://web4.uwindsor.ca/units/leddy/leddy.nsf/ThesesAndDissertations!OpenForm).
    The repository is non-commercial and openly available to University of
    Windsor student/staff community.

    Thank you very much.

    Sincerely

    Faisal SIDDIQUI
    MASc. Mechanical Engineering Candidate
    University of Windsor
```

https://webmail1.uwindsor.ca/Session/905455-hwevOKF6ruzNgFJilEJe...   1 of 1

Vita Auctoris

Faisal Siddiqui was born in Rajshahi, Bangladesh in the winter of 1985. In 1999, he moved to Perth, Australia with his family. There he graduated from Willetton Senior High school in 2002. After briefly studying Computer Science in Curtin University of Technology, and University of Notre Dame Australia, he migrated to Canada in summer of 2004. He immediately resumed his undergraduate studies and obtained a Bachelor of Applied Science (B.A.Sc.) degree in Mechanical Engineering in 2008 from University of Windsor, Ontario. He is currently a candidate for Degree of Master of Applied Science (M.A.Sc.) in Mechanical Engineering at the University of Windsor.